An innovative approach for magnetic solid supports handling in droplet microfluidics

Marco Serra

THÈSE DE DOCTORAT

de l'Université de recherche Paris Sciences et Lettres
PSL Research University

Préparée à l'Institut Curie

An innovative approach for magnetic solid supports handling in droplet microfluidics

Ecole doctorale n°564

PHYSIQUE EN ILE DE FRANCE (PIF)

Spécialité: Physique

COMPOSITION DU JURY :

M. BAROUD Charles
Ecole Polytechnique, Président

Mme. DITTRICH Petra
ETH Zurich, Rapporteur

M. BARET Jean-Christophe
Université de Bordeaux, Rapporteur

Mme. JULLIEN Marie-Caroline
ESPCI, Examinateur

Mme. DE CREMOUX Patricia
Hôpital Saint-Louis, Examinateur

M. FERRARO Davide
Università di Padova, Invité

M. VIOVY Jean-Louis
Institut Curie, Directeur de thèse

Mme. DESCROIX Stéphanie
Institut Curie, Co-directrice de thèse

Soutenue par Marco **SERRA**
le 19 Janvier 2018

Dirigée par **Jean-Louis VIOVY**
Stéphanie DESCROIX

institutCurie PSL RESEARCH UNIVERSITY PARIS

Table of Contents

Introduction

Droplet microfluidics is recently experiencing a tremendous growth in the bioanalytical field, as attested by both the increasing number of existing lab-scale protocols implemented and by the completely new directions in diagnostic and research opened, based on this technology. This is due to the wide set of functionalities currently available in the droplet microfluidic toolbox (i.e., droplet generation, merging, splitting, sorting, cell encapsulation,…), fostering the implementation of homogeneous (liquid/liquid) processes. Recently, innovative strategies for the development of heterogeneous (typically solid/liquid) reactions have been proposed. This step, crucial in many biochemical protocols, is conventionally performed based on the manipulation of a functionalized solid-phase support, binding the target molecule.

The aim of my PhD work has been to answer the demand for an integrated microfluidic concept devoted to solid supports handling in droplet, in order to combine the possibility to both extract an analyte of interest from a complex matrix and to exchange it between different media, with high throughput operations. We thus present the conception, fabrication and characterization of a novel droplet microfluidic approach based on the integration of a pair of soft magnetic components, placed adjacently to the main droplet flowing microchannel and activated by an external permanent magnet.

Chapter 1 presents an overview of the existing technologies devoted to the handling of the solid support in different multi-phase and droplet microfluidic architectures (stationary, digital and continuous). In particular, the discussion will be focused on: i) the working principle and technological development of the solid support handling strategies and ii) applications, critically discussing

their level of maturity, which ranges from initial proof-of-concept to real clinical validations.

In my PhD work, we will focus on continuous droplet microfluidic systems, in which droplets are transported in a continuous pressure-driven flow of oil. Chapter 2 describes the magnetic tweezers technology, developed in our lab in 2012 and representing one of the state-of-the art technologies in the field, being the only device currently available in continuous droplet microfluidics to perform extraction and redispersion operations in droplets continuously flowing in a capillary. After recalling the working principle and the physics underlying this device, two recently developed projects will be presented illustrating the potential of this technology for clinical applications. The first one describes a droplet microfluidic platform for the purification of mRNA from a total RNA sample prior to an RT-qPCR step for breast cancer gene expression level determination. The second describes a single-step ELISA protocol for the detection of amyloid beta peptides, as biomarker of interest for Alzheimer disease.

Despite its interesting features, we aim at overcoming the current limitations of the magnetic tweezers technology, represented in particular by the processing velocity and the lack of scalability and parallelization. This will be achieved by developing a new generation of droplet microfluidic device to manipulate magnetic particles. To do so, an innovative droplet microfluidic concept for magnetic beads handling will be introduced in chapter 3, combining: i) the advantages of magnetic tweezers in terms of extraction/redispersion functionalities and purification efficiency; ii) the integration and high throughput processing, characterizing continuous droplet microfluidic systems.

This approach is based on the integration of a pair of soft magnetic components placed adjacently to a microchannel, and able to generate along the path of the droplet a strong and local magnetic force, attracting the magnetic particles in the capture region, defined by the volume between the soft magnetic components. In particular, the numerical simulations-assisted device conception will be presented, followed by the microfabrication workflow and the characterization of the device extraction and purification rates. Furthermore, we will also investigate how the device performances can be improved based on the control of the droplet fingering in the capture region. In particular, two strategies based on passive or active fashion will be developed and characterized. The former exploits a microfabricated pressure-driven hyperelastic component while the latter is based on a fine control of the hydraulic resistances ratio in two separated channels of the device. Furthermore, the second approach bring an additional functionality to the system, allowing in fact the clean-up of a target molecule from the original matrix, as described in Chapter 4. The developed device functionalities will be exploited for a first proof-of-concept application, demonstrating the on-chip clean-up and size selection steps of DNA fragments, representing a critical step for the preparation of nucleic acids libraries dedicated to next generation sequencing (NGS). In particular, the discussion will be conducted analysing the preparation workflow and stressing, in particular, the most critical steps for the protocol and extrapolating the technological aspects and challenges that in its in-droplet version should be integrated and considered. Chapter 5 focuses on the conception and microfabrication of an additional tool in the droplet microfluidic field: an innovative pinch valve technology characterized by no dead volume

and negligible back flow, suitable for droplet handling. Several proof-of-concept applications in multi-phase microfluidics will be presented. Finally, the conclusion and future perspectives of the project will be discussed.

Chapter 1

The power of solid supports in multiphase and droplet-based microfluidics: towards clinical applications

The content of this chapter is part of a critical review recently published in Lab on Chip journal (***Lab Chip***, 2017,**17**, 3979-3999).

1 Introduction

Microfluidic systems are currently undergoing an accelerated development, becoming key players in modern bioanalysis[1]. This is largely due to the advantages offered by the intrinsic properties of microfluidic devices, e.g.: reduction of sample volume, parallelization, assay time shortening and cost reduction. In the case of biological and bioanalytical applications, the ability of microfluidic devices to compartmentalize the bioassays into small volume reactors further allows multiplexing, reduction of contamination risks and high-throughput analysis. In conventional bioanalytical laboratories, compartmentalization is achieved by dispensing samples and reagents in independent tubes or microtiter plate wells. Microfluidics allows implementing smart compartmentalization using a wider range of approaches. As an example, different kinds of valves have been introduced[2,3], some of them are now present in commercially available products. However, despite their efficiency, these types of devices are costly and relatively complicated to produce and manipulate. In the last two decades, multiphase and droplet-based fluid systems have emerged as an alternative for microscale compartmentalization. For instance, placing immiscible phases close to each other on flat or patterned surfaces allows the generation of isolated compartments. This concept is named "Stationary Droplet Microfluidics". For biological applications, aqueous phases are typically separated by an oil phase or simply by air. As will be described in detail later, in these devices the solutions are typically manipulated by pipetting, avoiding external pressure or flow control systems. Therefore, even if this approach does not bring a dramatic reduction in reagent volumes as compared with conventional strategies, it results in simple and intuitive

microfluidic devices, facilitating the introduction of some of these systems in the market. Beyond this simple strategy, higher programmability of biological assays is provided by "Dynamic Droplet Microfluidics", in which actuation can be obtained by electrical potentials or pressure-driven flows. The former is primarily represented by Digital MicroFluidics (DMF) systems[4,5], allowing an independent control of discrete aqueous droplets, emulsified in oil or air, and placed on a solid surface. In these devices, the droplet actuation is usually controlled by the Electrowetting On Dielectric (EWOD) technology[6,7]: the application of an electrical potential to an array of electrodes patterned on a hydrophobic surface causes a local variation in surface wettability and leads to droplet displacement. On the other hand, what is probably the most common compartmentalization approach exploiting multiphase fluid systems is known with the general name of "Droplet Microfluidics"[8]. Here, in contrast with the DMF approach, two (or more) immiscible fluids are combined in microfluidic channels obtaining controlled emulsions of one phase inside the other. Typically, these droplet emulsions are generated by specific channel geometries, such as T-junctions and flow-focusing[9], or by pipetting robots[10], and are transported in a pressure-driven flow. For biological and bioanalytical applications, aqueous droplets are dispersed in oils containing specific surfactants[11]. In this way, as for DMF devices, each droplet can be considered as single virtual microreactor. This guarantees the stable compartmentalization of chemicals, biomolecules and even cells, while reducing, with respect to conventional lab-scale protocols, both the volume of the liquid necessary for the analysis and the contamination risks with the surrounding environment. Moreover, besides the compartmentalization itself, droplet microfluidics typically offers additional advantages as compared

with monophasic microfluidics, such as further volume reduction, faster mixing and shorter analysis time. In this review, to avoid misunderstanding with the discrete DMF systems, we will define this approach "Continuous Droplet Microfluidics". By using different approaches, both DMF and continuous droplet microfluidics allow different droplet operations, including merging, splitting, incubation, sorting and optical measurements[12]. Based on these functionalities, increasingly complex protocols have been implemented and some clinical applications presented[13,14].

Despite their already established potential, especially regarding clinical applications, the above multiphase and droplet-based fluidic devices are limited to liquid-liquid (homogenous) reactions, where the biomolecules of interest are dispersed or dissolved in an aqueous phase. To expand the range of possible assays (including the extraction, purification and low abundancy detection of nucleic acids, proteins or cells), new approaches that allow heterogeneous (typically solid-liquid) reactions have been explored. For this reason, several researchers have recently focused on the development of microfluidics strategies employing solid or gel particle suspensions in multiphase fluidic systems to improve the droplet-based toolbox and open the way to more complex bioanalytical applications. Indeed, the use of solid suspensions in biological and bioanalytical protocols is already a very common practice in conventional (non microfluidic) assays: solid particles are typically employed as support for nucleic acids, molecules or cell manipulations and/or detection. These applications harness two main advantages of solid particles: i) the possibility to functionalize their surface with a broad range of surface chemistries, providing a high versatility in terms of aggregation and adsorption properties, and allowing

various strategies for the covalent linking of ligands[15]; ii) the high surface to volume ratio, due to their micro/nanometric sizes, that guarantees an improved capture of targets[16]. In many cases, these particles present paramagnetic properties. The structures of paramagnetic beads can be very diverse, from a simple core of magnetic material (commonly magnetite Fe_3O_4 or maghemite y-Fe_2O_3), to a distribution of iron oxide particles in a polymer matrix or a polymer sphere coated with magnetic oxide[17,18]. A strong advantage of these particles is the possibility to manipulate them at a distance by an external magnetic field. In more detail, the key parameter for the manipulation of paramagnetic beads is the magnetic force $\boldsymbol{F_{mag}}$ that, considering the magnetic dipole approximation, can be written as $\boldsymbol{F_{mag}} \propto \left(\frac{Q}{\rho}\right) \boldsymbol{M}\, \boldsymbol{\nabla B}$ where Q is the amount of beads, ρ is their density, $\boldsymbol{M}$ is the magnetization of a single unit, and $\boldsymbol{B}$ is the local magnetic field[19]. In the case of a microfluidic system, $\boldsymbol{B}$ is typically generated by a permanent magnet or an electromagnet, which can be situated either outside of the device or integrated in it[20]. It is important to notice that, the magnetic properties of the beads being fixed, $\boldsymbol{F_{mag}}$ mainly depends on the quantity of beads and on the gradient of the magnetic field. Working at the microscales, sharper gradients can be obtained[21], yielding stronger forces that in the macroscopic world.

Due to these advantages, paramagnetic solid state supports gained a central role in bioanalytical methods: many existing protocols have been developed in a bead-based version and the amount of new assays implemented is increasing[22,23]. In these protocols, a suspension of paramagnetic beads coated with specific ligands is dispersed in the sample to bind specific molecules. Then, a magnet placed close to the liquid holder is used for their separation from the

initial solution (or supernatant) and removed for their dispersion in a new solution for washing or detection. This specific protocol is named magnetic solid-phase extraction (MSPE) and is typically used for achieving multi-step protocols like the enzyme-linked immunosorbent assay (ELISA)[24]; additionally, solid magnetic and non-magnetic particles could be exploited for bead-based detection. The integration of magnetic beads in monophasic microfluidic devices has been largely explored; in particular, the online and continuous separation of cells[25,26,27] as well as the integration of assays for proteins[28,29,30] and nucleic acids[31,32] extraction and detection have been implemented. The complexity of bead handling by magnetic fields at the microscale can be reduced by geometrically arranging the beads inside the device in such a way that their contact with the passing solution is maximized, avoiding the need of mixing steps or bead displacement[33,34]. Alternatively, other systems have focused on a continuous dynamical displacement of the beads, allowing a good mixing between beads and solution. This can be obtained with variations of the magnetic field polarity[35] or through fluidization phenomenon in the presence of a permanent magnet[36]. Demonstrations of the latter approach was implemented for the flow-through immunoextraction of bacteria[37] and protein biomarkers[38]. Therefore, considering the versatility and widespread use of functionalized magnetic beads in conventional macroscopic protocols as well as in monophasic microfluidic devices, their integration in multiphase microfluidic systems holds great promise. In fact, this new approach renders purification and pre-concentration steps achievable in a multiphase microfluidic format. This facilitates the integration of complex biomedical protocols and the development of reliable clinical assays in a microfluidic platform.

However, few considerations should be done on the physics underlying the implementation of magnetic-beads for solid-phase extraction protocols in multiphase microfluidic devices. Differently from the monophasic case, multiphase microfluidics involves the presence of an interface between two immiscible fluids, usually an aqueous solution and oil (or air). This interface is characterized by a capillary interfacial force, that for a spherical meniscus can be written $F_{int} \propto \gamma L$, where γ is the interfacial tension between the immiscible fluids and L is a representative length of the system, such as the radius of curvature of the meniscus[39]. Typical values of this force in microfluidic devices range between several tens and few hundreds of μN. The purification of an analyte of interest from a complex matrix requires, therefore, breaking this interface in order to separate or extract the particle-bound target. To facilitate that, surfactants, that reduce γ, can be used for decreasing the interfacial force. Therefore, in order to achieve the magnetic beads extraction, a magnetic force overcoming the interfacial force of the interface ($F_{mag} > F_{int}$) is required; this process is also named "direct magnetic extraction". If $F_{mag} < F_{int}$, the extraction of the magnetic particles cannot be achieved. However, hydrodynamic strategies can be exploited to induce droplet break-up[40], allowing magnetic separation also in this case, as it will be described later.

In this review, we will discuss the impact of the solid-phase support (colloidal suspensions, micrometric magnetic and non-magnetic beads and hydrogel particles) confined in multiphase and droplet-based fluidic systems. Due to the important amount of published research exploiting functionalized paramagnetic beads in multiphase microfluidic systems, most of this discussion will be focused on the technologies developed for their manipulation, discussing their level of

maturity for bioanalytical applications, which ranges from proofs of concept to real clinical validations. Furthermore, the advantages brought by a non-magnetic solid-phase support for the development of detection techniques in continuous droplet microfluidics will be discussed: based on the confinement of single functionalized micro- or nano-particles in droplets, a strong improvement in the limit of detection of low abundance molecules has been achieved. Finally, the recent advances of these systems for barcoding applications will be presented, opening completely new directions of research in diagnostics.

To facilitate reading, as illustrated in Fig.1, we divided the review into two main sections based on the microfluidic technology used. We first explore stationary droplet microfluidics, followed by the more complex dynamic approaches, which are divided in discrete digital microfluidics (DMF) and continuous droplet microfluidics. In contrast to stationary and DMF, in which the applications of solid-phase support mainly concern magnetic extraction, a wider variety of applications (extraction, detection and barcoding) have been implemented in continuous droplet microfluidics and will thus be presented in separated paragraphs. Despite all of these approaches are still active fields of research, this structure roughly reflects the chronological order in which solid-phase supports emerged in multiphase microfluidic systems.

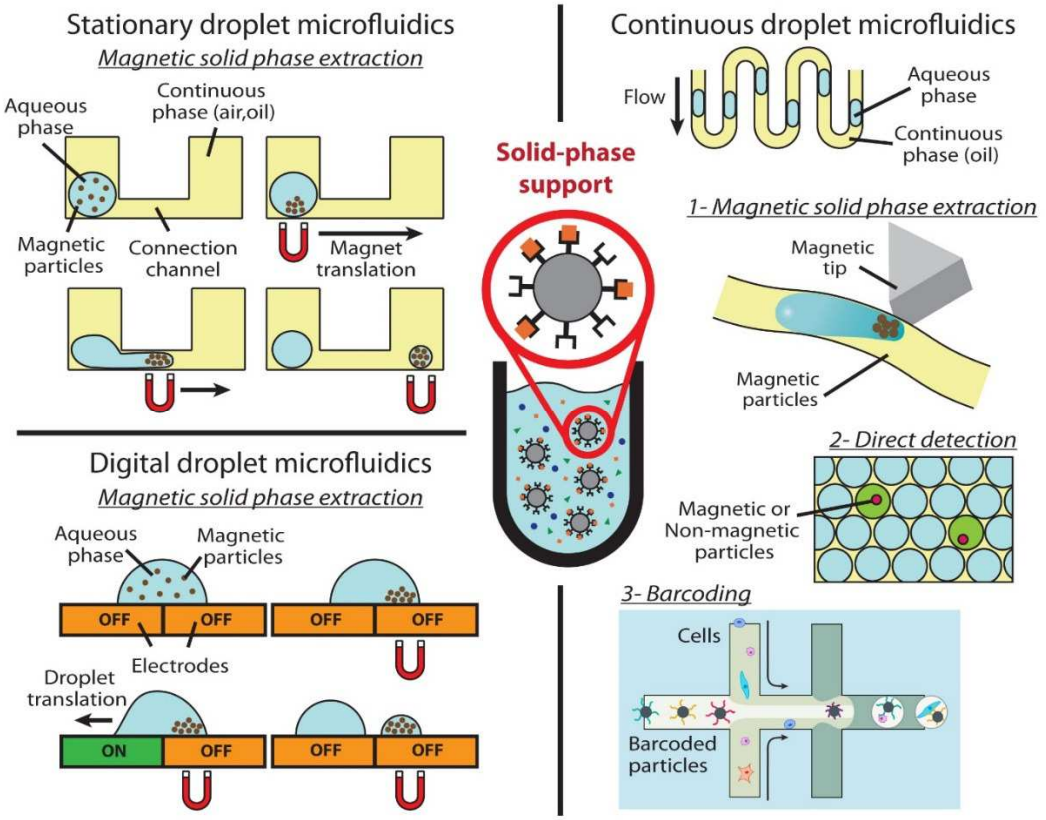

Figure 1: Overview of the main domains of multi-phase and droplet-based microfluidics (stationary, digital and continuous droplet microfluidics) combined with solid-phase support for specific binding of target molecules. *Depending on the microfluidic approach and nature of the suspension, the fields of applications can be divided into magnetic solid phase extraction, direct detection and barcoding (Adapted with permission from*[41]*. Copyright © 2015 Elsevier Inc.).*

2 Stationary droplet microfluidics and magnetic solid-phase extraction

The potential and future of microfluidic technologies to replace the conventional bioanalytical approaches relies on their analytical performance as well as on their acceptance by end-users. In this context, the compartmentalization of aqueous solutions keeping a format compatible with conventional tools (i.e., robots for liquid handling, microplate readers, multichannel pipettes, etc.), but

aiming at a reduction in reagent volumes and processing time is particularly relevant. The compartmentalization relies on the Stationary Microfluidics approach, where the extraction of an analyte of interest from a supernatant and its subsequent redispersion in another solution are based on the displacement of the functionalized magnetic solid-state support between fixed aqueous compartments. This can be performed thanks to two strategies, which will be discussed below: i) two immiscible fluids confined in adjacent reservoirs which are both in contact with the walls of the reservoir and through the shared meniscus between them; ii) an aqueous phase completely surrounded by an oil phase, forming a microliter droplet which is never in contact with the walls of the device. Interestingly, in either format there is no need for pressure or flow control systems, making these approaches particularly suitable for point-of-care (POC) devices.

2.1 Physically confined fluids defining a shared meniscus

The first stationary droplet microfluidics-based approach exploits capillary effects to confine loaded reagents in adjacent reservoirs or closed chambers, separated by an immiscible phase. The interface between the two phases acts as a valve allowing only magnetic particles to transit and be displaced between stationary liquids[42]. Initially, under the effect of the magnetic field, particles arrange in a cluster and move towards the interface. The magnetic pulling force acting on the cluster gradually deforms this meniscus, opening the valve. This creates a neck in the liquid thread, until pinch-off occurs and the aggregate of particles separates from the bulk of the initial sample. At this point, the cluster is transported in the immiscible phase region, while the valve immediately closes by capillary forces. Finally, the beads aggregate reaches the solution in the next

chamber and merges with it. This configuration reduces eventual hydrophobic and hydrophilic contaminants present in an aqueous reservoir to reach the next one, with a crossing of the immiscible liquids interface. As will be discussed in detail, either oil or air were proposed as the immiscible phase but, in spite of the differences in design and immiscible phase used, this process represents the common operating principle of the devices described below.

2.1.1 Oil as immiscible phase

Some stationary multiphasic microfluidic systems[43,44] rely on the "pinning" effect[45], leveraging the dominance of surface tension over gravity at the microscale. In fact, here, aqueous and oil reservoirs connected by geometrical constrictions can coexist side-by-side in a planar configuration as opposed to the density stratification phenomena observed at the macroscale. In order to exploit pinning effects, the plate preparation requires a careful pipetting sequence of aqueous and oil solutions. In particular, considering a sequence of connected reservoirs, at first, aqueous phases must be dispensed in every second well. As in the phaseguide concept[46,47], the presence of geometrical constrictions between the reservoirs causes an abrupt change in capillary pressure. This represents a virtual barrier for the aqueous/air meniscus, supporting its pinning and allowing better confinement of the aqueous phases. Then, to complete the loading process, the remaining reservoirs are loaded with an immiscible phase liquid (wax, oil), leading to the formation of stable aqueous/oil interfaces. It is worth noting that the interfacial energy between the two immiscible phases has an important role in the crossing process of functionalized magnetic particles. Indeed, excessively high surface energies would create too rigid interfaces, thus

permanently trapping the cluster and preventing its transfer. On the other end, a too low interfacial tension causes the transport of the extracted magnetic cluster diluted in a large volume of supernatant, consequently affecting the purification rate of the device. Further reducing the interfacial tension, the extraction process led to a bridging between separated aqueous wells and their consequent mixing. Interestingly, the condition for aqueous bridge formation were investigated as a function of water-oil, water-substrate and oil-substrate interfacial tensions[42]. Overall, due to the variable surfactant concentration in common biological buffer solutions, the appropriate choice for the immiscible phase and device geometry are fundamental to define the correct extraction of the particle cluster.

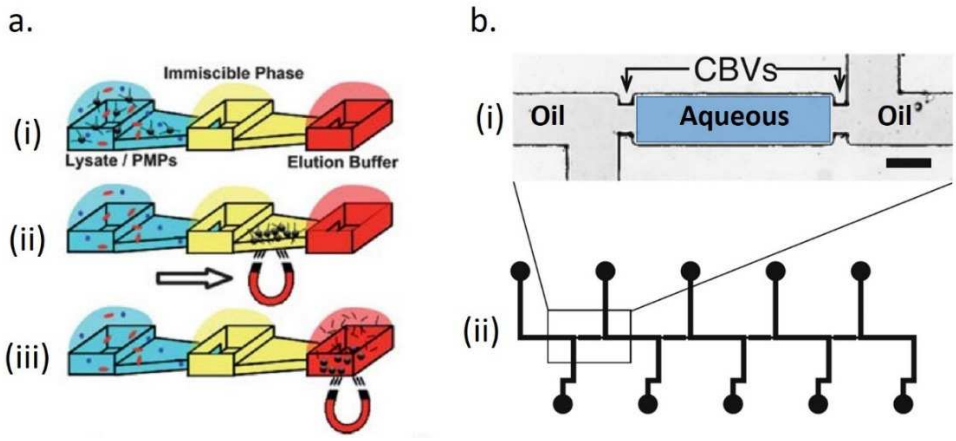

Figure 2: *a) the IFAST platform consists in a sequence of three wells connected by microchannels. The central well, hosting an immiscible oil phase, separates the aqueous phase wells, filled with cell lysate containing functionalized magnetic particles and elution buffer, respectively (i). An external magnet is used to draw the nucleic acids-bound particles through the immiscible phase (ii) and into the elution buffer (iii). (Reprinted with permission from[43]. Copyright © 2011 The Royal Society of Chemistry). b) The µIPELISA device consists of a closed microchannel characterized by a series of 4 elements joined horizontally (ii). Each element is composed of a central channel (for aqueous phase) and two lateral ones (for the*

immiscible phases), separated by capillary burst valves (CBVs) (i). Scale bar=400µm. (Adapted with permission from [44]. Copyright © 2010 Springer-Verlag).

Based on this concept, following the work of Sur and co-workers[48], Berry et al. recently developed immiscible filtration assisted by surface tension (IFAST)[43], a method in which adjacent reservoirs are connected by trapezoidal microfluidic channels (Fig. 2a). Using this device, the possibility of nucleic acids extraction and purification was first demonstrated[49,50]. Furthermore, increasing the number of connected reservoirs, IFAST immunoassay functionality was shown[51]. In particular, the possibility to use this technology to perform all the steps of a conventional ELISA. In detail, they investigated the detection of a prostate cancer biomarker (PSA for Prostate Specific Antigen), by making a proof of concept with recombinant PSA and, after that, by the successful application of the IFAST technology to a limited set of patient samples. Purification of target cell sub-populations from an aqueous sample was also demonstrated[52] . An improved version of this technology, the Vertical IFAST (VerIFAST) was later developed to integrate both cell isolation and intra- and extracellular staining[53]. The vertical configuration exploits the settling of non-target cells at the bottom of the reservoir to decrease non-specific carryover, thus to reach higher levels of target cells purity. Device potentialities were demonstrated performing standard histopathologic assays: cancer cells were captured from both mini-bronchoalveolar lavage (mBAL) and blood from six lung cancer patients. The on-chip staining allows to determine the expression level of two therapeutic targets, thyroid transcription factor-1 (TTF-1) and epidermal growth factor receptor (EGFR)[54].

Differently, arrays of micro-pillars separating adjacent chambers were introduced by Kim et al.[55] to create stable oil/water interfaces. In this work, a magnetic-beads based sandwich ELISA for the detection of Aβ oligomer was implemented. However, in order to prevent Aβ aggregation, synthetic oligomer mimicking standard protein (OMSP) were spiked in human serum plasma in the proof-of concept application.

The main limitations of these devices are the relatively high volume (≈10µL/reservoir) used during the assay, and the possible evaporation of the aqueous solution over long experimental times. In addition, these systems are prone to contamination issues due to exposure to open air. An interesting alternative was proposed by Chen et al.[44]. They reduced the volume of reagents by designing a microfluidic architecture in which the reservoirs are replaced by isolated plugs encapsulated in closed micro channels. The geometry of this system, named µIPELISA (microfluidic inverse phase enzyme-linked immunosorbent assay), is characterized by a sequence of 4 identical sectors where different aqueous plugs of reagents needed for the immunoassay are stored (see Fig.2b (i)). In particular, each sector is designed with a central chamber, where the aqueous liquid phase is stored (140nl in volume) and two lateral ones for the oil phase (see Fig.2b (ii)). Additionally, the chambers are separated by capillary burst valves (CBVs)[56], defined through a reduction in channel cross-sectional area. After having filled the water phase chambers by the ELISA reagents, the chambers separating the aqueous phase are filled by oil via additional side inlets, in order to generate the water/oil interfaces (see Fig. 2b). CBVs confine the reagents by capillary forces and are characterized by a semi open gate that allows the displacement of beads between adjacent

plugs joined horizontally. Finally, despite the reduction in volume and the prevention of reagent evaporation with respect to the previous system, the cartridge preparation requires careful and time-consuming operations, representing the main drawback of this device.

2.1.2 Air as an immiscible phase

In general, the presence of oil in the configurations mentioned above allows the formation of immiscible barriers between the aqueous plugs as well as the decrease of the interfacial tension with respect to a water/air case. Therefore, oil facilitates the extraction of the paramagnetic beads cluster and prevents cross-contaminations between separated aqueous phases. Despite its good compatibility with several biological protocols, however, the presence of an aqueous/oil interface can be a hindrance for some bioassays such as the purification and enrichment of proteins, because the adsorption of some proteins at the water-oil interface, or their surfactant-mediated transfer from droplet to droplet through the oil may be difficult to avoid in some situations. This led to the research of alternative fluids as the immiscible phase. In particular, air was found to be a good candidate as a substitute for oil.

An oil-free and low-resource setting device was proposed for the first time by Bordelon et al.[57] by injecting in a capillary the different reagents separated by air gaps (Fig. 3a). The interfacial tension between air and the aqueous solution acts as a valve, keeping individual reagent plugs fixed during the processing. The system was characterized with the sequential extraction, washing and elution of respiratory syncytial virus (RSV) RNA from infected HEp-2 cell

lysates. Furthermore, the same operations were performed for 7 positive and 7 negative nasal wash clinical samples. However, the setting-up of the system is complicated and the achieved recovery rates were lower than the ones obtained in tube with commercially available kits. Later, den Dulk et al.[42] proposed an integrated version of this system, making use of two microscope glass slides held at capillary distance and characterized by specific geometrical features and/or hydrophobic/hydrophilic surface patterning to confine the stationary aqueous solutions and to separate them by air. The versatility of this system was demonstrated by several proof-of concept applications, showing purification and enrichment of nucleic acids and of a biomarker protein (PSA) in buffer.

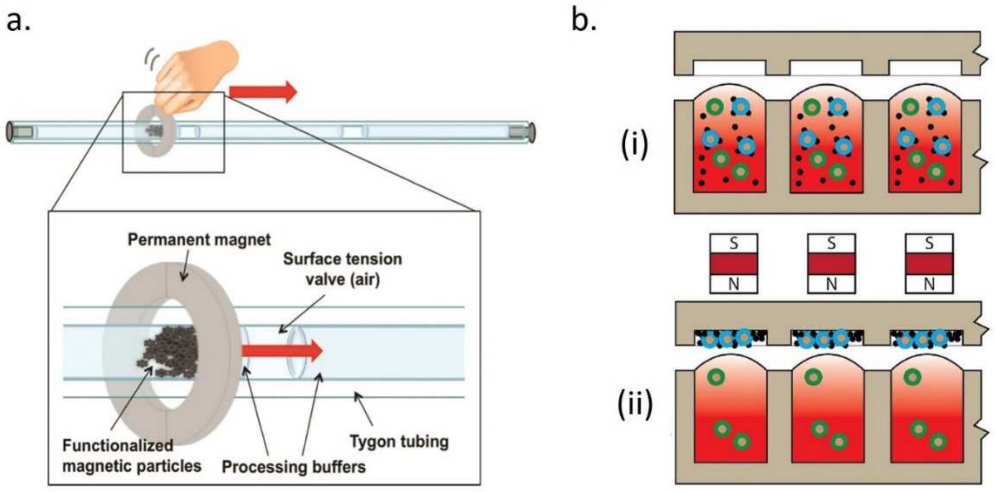

Figure 3: *a) Design of the oil-free extraction method developed by Bordelon et al.[57]. Individual processing solutions are held in place in a tubing and separated by air gaps (surface tension valve). Target RNA is adsorbed to functionalized magnetic particles and then pulled through successive processing solutions using a magnet. (Reprinted with permission from [57]. Copyright © 2011 American Chemical Society). b) Schematic of the AirJump system[58]. (i) A disposable elution plate is placed on top of a sample plate filled with functionalized beads (black), target analyte (blue) and non-target material (green). (ii) When introducing a magnet, the analyte, bound to the magnetic particles, "jumps" across the air*

gap and reaches the elution plate. (Reprinted with permission from [58]. Copyright © 2016 American Chemical Society).

More recently, Berry et al.[58] performed the magnetic separation vertically, rather than on a planar configuration: solutions were loaded in standard well plates and the magnetic particles, pulled upward by a magnetic force, traversed the liquid/air interface and were deposited in a disposable strip-based elution well, directly over the sample (Fig. 3b). During plate preparation, the sample well must be filled with solution, creating a slightly convex meniscus at the air interface. This geometry promotes the aggregation of the functionalized magnetic particles in a point prior to jumping. The extraction takes place when a critical mass of particles is reached, allowing to achieve a magnetic force higher than the surface tension. In this way, and taking advantage of the gravitational force, supernatant carryover is expected to be reduced, "excluding" non-specific molecules from the magnetic support. This "exclusion-based technology", called AirJump, is now commercialized by Gilson and is perfectly suited for low affinity targets, which can otherwise be lost with conventional washing steps. A complete extraction requires between 30 and 120s, but the same operation can be performed in parallel wells on the same plate. The beads recovery ranged from 77 to 87% depending on bead concentration. Based on this principle, a wide range of applications have been demonstrated, such as protein immunoprecipitation, viral RNA isolation and cell culture gene expression analysis; however, only HIV RNA extraction was performed on real patient samples. Later, an automated platform was developed, allowing the extraction of the analyte of interest and redispersion in a different well. These operations were based on the change in the mutual

distance between two permanent magnets placed on top of the elution wells and beneath the sample plate[59].

2.2 Dispersed water phase surrounded by oil

Other stationary systems rely on the manipulation of aqueous phase droplets suspended in oil in an open hydrophobic plate or well. As already mentioned, the presence of the completely surrounding oil has several advantages: it limits the possibility of contamination with the surface, prevents the evaporation of the aqueous solution, reduces the friction between the droplet and the surfaces and, finally, lowers the interfacial tension, thus facilitating droplet splitting. Additionally, as compared with the systems presented above, in which the aqueous phase is in direct contact with the device, here, the magnetic force controls not only the beads extraction but also the transport of the droplets. More specifically, under the influence of an external magnetic field, particles aggregate in a cluster, and the magnetic pulling force is then transferred to the water/oil interface, dragging the whole droplet in the desired direction. However, the transition between the transport and extraction regimes requires the introduction of an additional retention force to block the droplet and avoid further dragging: the parent droplet is immobilized in defined positions of the plate while the magnetic field assists in the particle cluster separation from the parent droplet. The retention force could be achieved by either i) confining the droplet by physical constraints (narrow channel[60,61,62], surface topographic features[63]), or ii) tuning the droplet friction with the substrate acting on droplet volume[64] or on the chemical properties of the substrate itself[65].

The first attempt to combine stationary droplet microfluidics with magnetic solid-phase extraction was reported in 2006 by Shikida et al.[60]. The device consisted in two wells completely filled with oil and separated by a mm-sized hydrophobic glass gate; each well contained, respectively, the sample droplet (50µl) with magnetic beads and the solution droplet for bead release (Fig. 4a). During the extraction process, the magnet displacement pulled the beads across the gate while a larger volume of the aqueous solution was trapped behind the gate, due to the geometrical constraint and the low wettability of the hydrophobic gate surface. A small daughter droplet containing the cluster of magnetic beads (≈30nl) was thus separated from the sample, moving towards the adjacent droplet where coalescence occurs and the beads were redispersed. Despite the relatively large volume processed here, two types of applications were achieved: heterogeneous enzyme assays[66] and the detection of enzyme-labelled DNA oligomers[67].

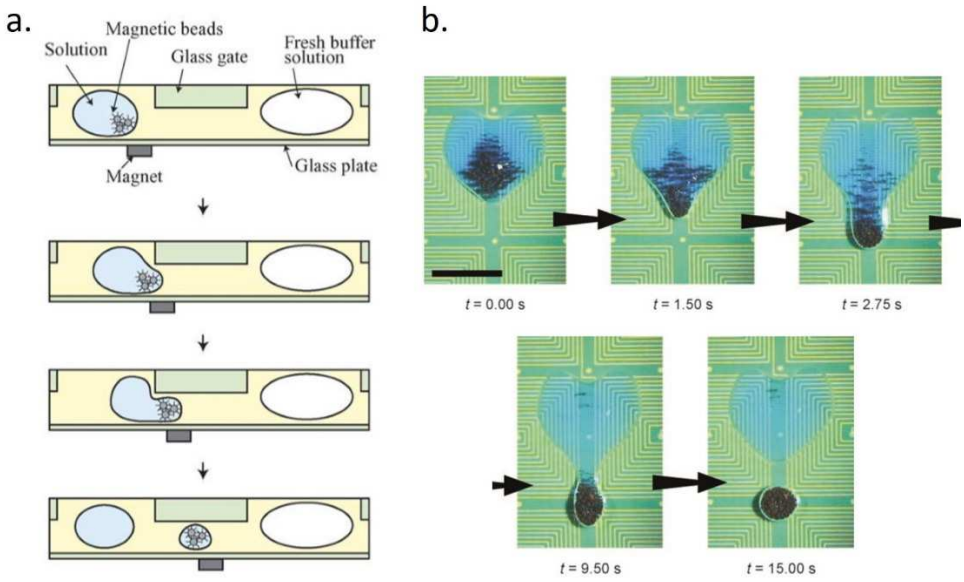

Figure 4: *(a) First example of magnetic separation device in droplet microfluidics, proposed by Shikida et al.[60]. The sample (containing functionalized magnetic beads) and reagent droplets, emulsified in oil, are separated by a hydrophobic glass gate. Under the influence of*

an external magnet, the magnetic force exerted on the beads is transferred to the water/oil interface. This, assisted by the low wettability of the gate surface, causes a droplet splitting: a compact cluster of magnetic particles separates from the original droplet, passing under the glass gate and reaching the next well, finally merging with the reagent droplet. (Reprinted with permission from[60]. Copyright © 2005 Elsevier). (b) Photographs of a droplet splitting sequence from Lehmann et al.[68]. A droplet containing a blue dye and magnetic beads is immobilized in a hydrophilic heart-shaped region. Activating the magnetic field by an array of magnetic coils results in the separation of a small cluster of magnetic beads from its parent droplet. Scale bar=3mm. (Adapted with permission from[68]. Copyright © 2006 Wiley-VCH Verlag GmbH & Co.).

Cui et al.[61] gave a first example of convincing clinical application based on a similar strategy, showing the isolation of influenza RNA from nasopharyngeal swab specimens. In particular, they compared the performance of their approach with conventional commercial kits, showing that the on-chip capture efficiency was higher and, moreover, that the chip purification did not compromise RNA integrity. However, their approach was less efficient when combined with qPCR, probably because of some carryover that negatively affected the downstream qPCR efficiency. More recently, Park et al.[62] automated and parallelized this approach, designing a microchannel-connected multiwell plate, named μCHAMP. This system presents a high processing capacity and ease of use, but it requires a specific microfabricated plate instead of conventional multi-well units. To date, it has been applied to synthetic Amyloid peptides, as model biomarkers of Alzheimer disease: parallel immunoassays were performed and a limit of detection (LOD) in the pg/mL was achieved. While this was a good sensitivity, these results must be confirmed with real patient samples. Alternatively, Zhang et al.[63] proposed an extraction assisted by surface topographic features. Here, the hydrophobic surface

contained pairs of extruded structures characterized by a narrow slit between them. The authors proposed a sample-to-answer platform integrating different analytical steps: cell lysis, DNA extraction, amplification and detection. To illustrate the potential of their approach, they successfully extracted DNA from whole blood and amplified the Rsf-1 gene, which is under evaluation as a future biomarker for ovarian cancer.

Instead of exploiting geometrical constraints, Lehmann et al.[65] created hydrophobic/hydrophilic patterns to block the aqueous droplets. Interestingly, rather than using a manual or mechanical displacement of a permanent magnet, in their device, a first instance of automated electronic control was proposed: the magnetic driving force was generated by a switchable array of magnetic coils. The hydrophobic Teflon surface was locally treated by oxygen plasma, leading to the creation of hydrophilic heart-shaped spots, where the pipetted aqueous droplet was positioned. The hydrophobic/hydrophilic boundary increases the slip friction[69] thus allows to immobilize the aqueous droplet, while the beads cluster pulls it to move in the direction of the applied field gradient. As a result of this forces interplay, the droplet splits, generating a daughter containing the magnetic beads cluster (Fig. 4b). Using sequential magnetic separation and merging steps between immobilized aqueous droplets, DNA purification[68] and on-chip detection of enzyme-labelled antibodies[70] were reported. However, this strategy is prone to contamination due to the possible non-specific adsorption of the droplet contents on the hydrophilic spots. In addition, the reduced number of droplets hosted on a plate and their careful pipetting in specific regions of the flat surface makes the system laborious, complex to automate and offering low-end throughputs.

A more versatile and surface contamination-free approach was presented by Pipper and co-workers[64]. They manipulated magnetic particles injected in microliter-size droplets, placed on a hydrophobic surface. The droplets are surrounded, but not covered, by a layer of silicone oil, generating a ring of immiscible phase around the droplet bottom. This decrease in oil loading increases the droplet friction with the substrate compared with the case of droplet completely immersed in oil. Consequently, the transport and splitting behaviours of a droplet, which are controlled by its interfacial tension and the frictional force, can be experimentally tuned by the volume of the droplet, thus without requiring any surface treatment. In particular, for a fixed oil loading, if the parent droplet volume is smaller than a critical value, it moves; otherwise, a small droplet containing the cluster of magnetic beads splits and it is pulled away from the parent droplet which is retained by friction. However, compared to the case of droplets completely surrounded by oil, this magnetic separation strategy requires a higher concentration of beads for droplet splitting. For more details, the reader can refer to Long et al.[71] for a comprehensive mathematical description of the interplay between magnetic, interfacial and frictional forces controlling the droplet transport and extraction regimes on open hydrophobic surfaces. The above approach does not require any surface treatment or additional microstructure to immobilize the droplet, but it risks to considerably increase the overall cost of a single analysis due to the amount of particles solution needed. The applicability of this device was shown by the detection of the avian influenza virus H5N1 from a throat swab sample; more specifically, viral RNA was isolated, purified, preconcentrated and subjected to a real-time RT-PCR protocol. Considering its simplicity and effectivity for the application

chosen, this device seems particularly well adapted for POC diagnostic. Later, a similar device was also applied for the extraction of monocytic cell line spiked in blood, their lysis, RNA purification and real time RT-PCR[72]. Despite this representing an interesting proof-of-concept, it can handle just a few microliters of sample per analysis, limiting the application concerning rare cells screening, in which milliliters volume of liquid are necessary.

In conclusion, the stationary droplet microfluidic systems discussed above present several advantages: they are compatible with standard laboratory tools, do not require particular microfluidic skills nor additional equipment (pressure controller, syringe pump, optical microscopes,…) as with most traditional microfluidic devices[73], and allow simple parallelization and automation. In our opinion, these systems represent mainly laboratory prototypes and the key issue for reaching commercialization is to achieve compatibility with conventional disposable units (in particular microtiter plates). This explains why the only commercial stationary droplet microfluidic product to our knowledge is EXTRACTMAN®, which is based on the previously discussed AirJump technology. As a matter of fact, the main contribution given by these devices is the automation of existing lab-scale protocols, simplifying and reducing manual operations, but without leading to strong improvements in term of reduction of reagents volumes, higher sensibility or sensitivity with respect to traditional macroscale methods. Indeed, stationary microfluidic devices suffer from poor mixing and washing efficiencies. In order to improve these key concepts for clinical diagnostic applications, dynamic droplet microfluidic approaches must be considered.

3 Dynamic droplet microfluidics

The approaches mentioned above share the possibility to perform magnetic separation through the displacement of functionalized magnetic beads between fixed aqueous solutions, assisted by an external magnet. In the next section, we will discuss about dynamic microfluidics approaches, characterized by a spatially fixed magnet position and either discrete droplet transport on an open plate (digital droplet microfluidics) or a continuous pressure-driven flow in microchannel networks (continuous droplet microfluidics).

3.1 Digital droplet microfluidics (DMF)

In DMF, the most common and flexible technology for the actuation of discrete aqueous emulsions (in oil or in air) on a substrate is represented by EWOD. The key principle of this concept is the electrically induced contact angle reduction between a droplet and the solid surface. This causes an asymmetric change in the interfacial tension of the droplet, leading to an inside pressure gradient that results in droplet motion. This is achieved, in both open and closed (sandwiched) DMF configurations[74], by the application of an electrical potential to an array of patterned electrodes coated with a hydrophobic insulator. From the fabrication point of view, clean room processes (lift-off, deposition, sputtering, etching, etc.) and facilities are required, which were traditionally developed for the production of micro and nano electronic devices[75].

Even if the DMF platforms were introduced about 20 years ago, the possibility to perform magnetic extraction in digital droplet microfluidics (DMF) was shown for the first time by Wang et al.[76] in 2007. In this work, the authors

added a control parameter to the system, performing droplet transport by EWOD technology while actuating the magnetic particles with a fixed permanent magnet. In this seminal work, a parent droplet (400nl), containing magnetic and non-magnetic particles, is surrounded by oil and placed between two parallel plates of an EWOD system. On the top plate, a fixed permanent magnet is present in order to attract the magnetic particles towards one droplet meniscus, next to the magnet. Once a compact cluster of magnetic particles is formed, the magnet is removed and the electrodes present in the bottom plate are activated. Consequently, the droplet elongates in a longitudinal direction, resulting in a splitting into two daughter droplets of identical volumes, one containing the magnetic particles cluster and the other mainly composed by non-magnetic ones. The reported performances regarding beads capture efficiency were quite good (about 92%), although not compatible with multiple-steps protocols. Furthermore, in this configuration, only about 50% of the initial droplet content is present in the daughter droplet, leading to very weak purification rates regarding bioassays applications.

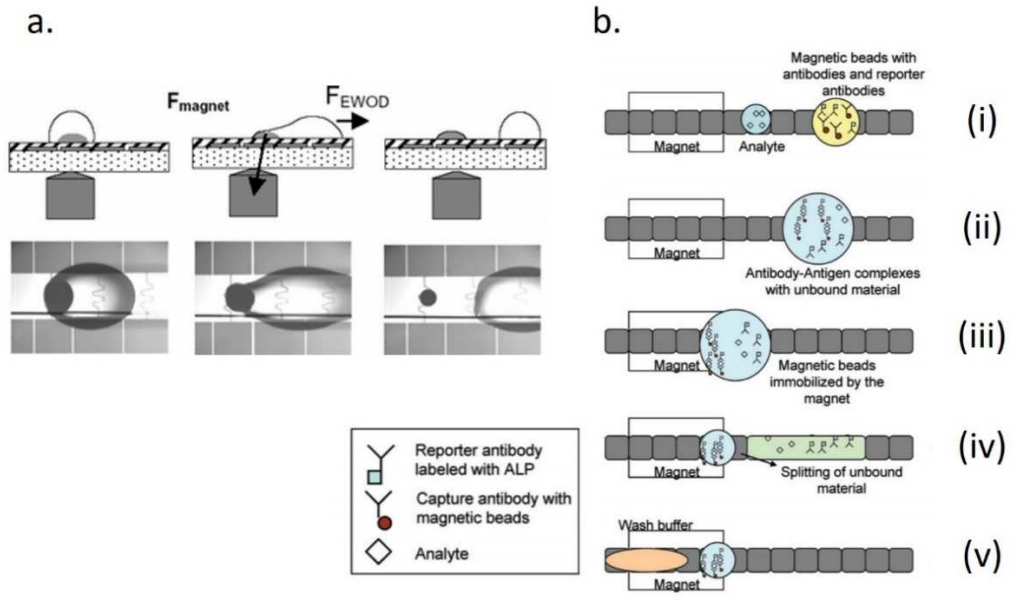

Figura 5: *(a) Magnetic solid phase extraction in DMF devices[77]. A permanent magnet is fixed underneath an EWOD plate. The magnetic force causes the concentration of the beads in a compact cluster retained by the magnet. Actuating the droplet by elettrowetting, it is possible to extract the magnetic beads from the parent droplet. (Reprinted with permission from[77]. Copyright © 2007 Springer-Verlag). (b) Protocol developed by Sista et al.[78] for the implementation of heterogeneous immunoassays on a DMF platform. It includes: (i) dispensing of reagents, (ii) incubation, (iii) immobilization of magnetic beads, (iv) supernatant removal and washing, (v) addition of fresh wash buffer. (Adapted with permission from[78]. Copyright © 2008 The Royal Society of Chemistry).*

To face this problem, better performances could be achieved based on the same driving forces but changing the operating principle, as described by Fouillet et al.[77]. Here, an open EWOD configuration is used and the permanent magnet, fixed beneath the chip, allows the creation of a compact cluster of beads in the bottom of the droplet. Differently from the work of Wang et al., here, the magnet is not removed before the electrodes activation and the droplet is asymmetrically actuated. As a consequence, the droplet stretches under the effect of magnetic and electrowetting forces: as soon as these forces are

equivalent and higher than the capillary force, the droplet splits and the particle cluster is extracted from the parent droplet, while the supernatant solution is pulled away (Fig.5a). The method was validated for bead concentrations from 2 to 10 mg/ml with 1 µl droplets, resulting in a capture efficiency of 99.8% and a concentration factor of 100x.

Once the combination of digital microfluidic and magnetic beads extraction was demonstrated, several groups optimized this approach and showed its potential for bioanalytical applications. Sista et al.[78] further enriched the toolbox of available operations in DMF to manipulate droplets containing functionalized magnetic beads. They showed magnetic beads retention, washing and resuspension, and demonstrated, for the first time in digital microfluidics, the possibility to perform a heterogeneous sandwich immunoassay. In particular, human insulin and interleukin-6 (IL-6) were chosen as target molecules, using samples of known concentration (Fig. 5b). Furthermore, they used a chemiluminescent detection and were able to quantify these proteins in less than 10 minutes, thus showing an important improvement as compared with conventional methods in tube. Later, the same group extended this work to the detection of Troponin-I spiked in whole blood samples and to the sample preparation for infectious disease pathogens (methicillin-resistance Staphylococcus aureus and Candida albicans) and for human genomic DNA[79]. Interestingly, these DMF technologies led to the creation of two companies: Advanced Liquid Logic and Baebies.

In addition, in order to increase the surface to volume ratio and to attenuate the variability of particle concentrations during droplet dispensing[77], a reduction in bead size was explored by Vergauwe et al.[80] showing, as a proof-of-concept,

the possibility to perform an ELISA-based assay to detect the presence of human immunoglobulin E (IgE) with 15 nm diameter paramagnetic particles. This group also demonstrated the use of magnetic particles as magnetic stirrers to improve the mixing of the droplet content; the interest of this strategy was evidenced by the resulting decrease in the LOD of IgGs, reaching concentrations down to the single-digit ng/mL range[81]. Interestingly, Wheeler's team[82] implemented the first oil-free magnetic beads-based immunoassay on a DMF device. Here, they reduced the surface tension of the water phase with air by including a surfactant (Pluronic L64) in all the reagent and sample solutions. In this way, droplet actuation in an air environment as well as the mitigation of protein fouling at the surface of the device were achieved. Furthermore, in the same work, the first competitive immunoassay in DMF was performed and a calibration curve was provided for standard solutions of 17β-estradiol (E2) as model analyte. Recently, this assay was shown as an interesting diagnostic tool for the personalized treatment of estrogen receptor (ER)-positive breast cancer. The study was performed on core needle tissue samples collected from fifteen breast cancer patients before and after treatment with aromatase inhibitor therapy, an increasingly popular treatment for post-menopausal ER-positive breast cancer[83]. The same team also developed a DMF immunoassay for the detection of rubella virus IgG and IgM, evaluating the assay performances with serum and plasma samples from a commercial antirubella performance panel (constituted by undiluted sample aliquots collected from individual donors). The obtained results were then compared with the ones from commercial RV antibody immunoassay[84]. Based on the technologies developed by this team, an open-source DMF instrument is now available (DropBot, by SCI-BOTS)[85].

Finally, the potential of the combination of magnetic particles manipulation and EWOD was also demonstrated for cells[86] and nucleic acids. In particular, regarding nucleic acid sample preparation and analysis, Rival et al.[87] implemented, for the first time, the complete process of transcriptome analysis, starting from the extraction of mRNA from a few cells up to RT-qPCR, on the same chip. The capability of this technology to manage multi-step protocols was also demonstrated by Kim et al.[88]. This group used a DMF device for the preparation of DNA libraries for Next-Generation Sequencing (NGS); a protocol that includes enzymatic transformations, washing, temperature-controlled amplification and size selection steps by magnetic beads actuation[89]. Furthermore, the programmability and versatility of these systems were proven by Kühnemund et al.[90], who implemented a complex bioassay called Circle-to-Circle Amplification (C2CA)[91]. This demanding molecular biology protocol integrates multiple steps of DNA extraction, digestion, ligation and isothermal amplification by rolling circle amplification (RCA)[92]. The good performance of this platform allowed the detection of 1 aM of synthetic Pseudomonas aeruginosa DNA with a linear dynamic range over 4 orders of magnitude.

It is important to underline that the several proof-of-concept and clinical applications that have been presented so far, together with the set of other tools already developed in DMF[93,94,95], are based on the same working principle. This undoubtedly demonstrates the versatility and easy re-configurability of this technology, which allows to achieve extraction and purification rates comparable to those obtained with conventional macroscale methods, while reducing the volume of reagents and strongly improving automation. Additionally, these devices are simple to handle once programmed. This

technology, however, presents several limitations: first of all, the microfabrication needed for the device production is complex, and requires technical skills as well as specific and costly facilities. Moreover, the fact that the liquids are not controlled by external pumping systems could represent a limitation if very small volumes (in the pL range) need to be manipulated, as in the cases of single cell or single molecule analysis. The throughput of the system is limited to the processing of a few droplets per second. All of these limitations are better overcome by continuous droplet microfluidics.

3.2 Continuous droplet microfluidics

3.2.1 Applications in magnetic solid phase extraction

Before 2010, the manipulation of solid-phase supports in droplets was limited to stationary microfluidic and DMF systems, suffering of low throughput and non-continuous processes. In that year, a droplet-based magnetic separation technique in a continuous microfluidic device was independently proposed by Pamme et al.[96] and Lombardi et al.[97], using magnetic nanoparticles and microparticles, respectively, dispersed in aqueous media. In particular, a parent droplet containing functionalized paramagnetic supports flows towards a T-shaped junction in the channel, where it breaks-up into two daughter droplets of equal volume (Fig. 6a). During the whole process, a permanent magnet is placed next to one of the two outlets. This leads to the accumulation of magnetic particles on one side of the droplet, resulting in the selective separation of magnetic particles into one of the daughter droplets. Furthermore, using this approach, the affinity of warfarin with human serum albumin (HSA) was investigated[97]. Regarding its performance, for magnetic beads

concentrations between 1 mg/mL and 3.3 mg/mL, a recovery rate of beads over 95% was reported. This approach allowed the reduction of droplet volumes (1.25nL) and the increase in throughput (few tens of droplets per second) with respect to previously reported systems. On the other hand, the symmetrical droplet splitting limits the purification rate: only half of the parent droplet volume is removed, while the other half is transferred to the daughter droplet enriched with particles.

Based on the hydrodynamic droplet splitting concept and on the magnetic manipulation of microparticles, a few approaches have been proposed in order to increase the purification efficiency, thus to have a higher enrichment in the daughter droplet containing magnetic beads. These methods rely on an asymmetric droplet splitting concept, achieved with different strategies. Pan and coworkers[98] developed a microfluidic device including sequential steps for magnetic separation and reagent addition. In this way, they showed the possibility to implement loading, washing and elution steps required for several complex bioassays. Since the split ratio is controlled by the difference in hydraulic resistance between the two outlet channels, this geometry allows to split the droplet slightly asymmetrically and leads to an improvement in purification efficiency with respect to the previous work. In particular, the daughter droplet consisted of about one third of the original parent volume (pL to nL range). In addition, the device was clinically validated implementing the extraction of hepatitis B virus (HBV)-DNA from serum samples. However, the purification efficiency still represented a limitation of the method: even after three separation steps, the final post-processed droplet contained an undesired 7% of the solution present in the original droplet. A similar geometry was

recently exploited in the work of Gao et al., in which the separation of a magnetic immunocomplex at an asymmetric bifurcation was coupled with a surface-enhanced Raman scattering (SERS)-based droplet sensor in order to quantify the expression of PSA protein[99]. Further, a different strategy to perform a magnetic particle-based immunoassay involving a single washing step was proposed by Lee et al.[100] (Fig. 6b). In this module, two trains of droplets (11 nl in volume) containing both the sample with magnetic beads and the washing buffer were generated in separate cross-junctions, and then synchronized by using a ladder-like channel network[101]. This enabled the following lateral merging of the droplets by electrocoalescence[102,103] at the entrance of an X-shape junction. Upon merging, the magnetic beads migrate perpendicularly to the flow direction, from one side of the merged droplet (containing the sample) to the other (containing the buffer) under the influence of an external magnetic field. Finally, at the exit of the X-shape junction, an asymmetric splitting is performed. This allows to minimize dilution in the daughter droplet containing the extracted beads and increases the washing efficiency. As a proof of concept, an immunoassay with streptavidin-coated magnetic particles and fluorescently labelled biotin was reported, showing a successful depletion of unbound biotin by a >25x factor in a single step.

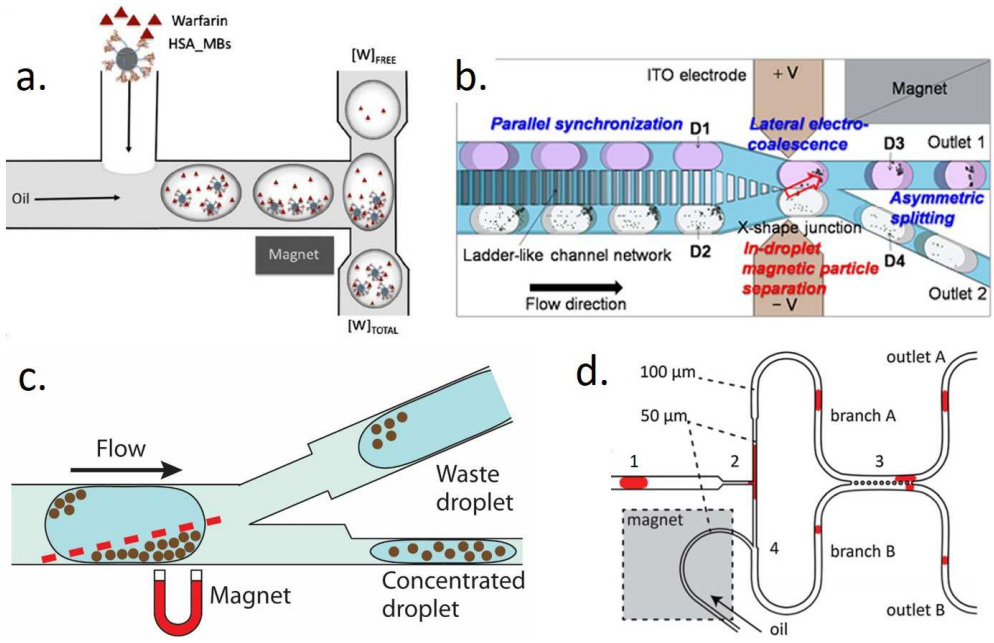

Figure 6: *(a) Schematics of the device proposed by Lombardi and Dittrich[97]. An aqueous solution containing magnetic beads coated with human serum albumin (HSA_MBs) binding warfarin is emulsified in oil. The generated droplets are symmetrically split at a T-junction but the side presence of an external magnet allows to concentrate the magnetic beads in half of the initial volume. (Reprinted with permission from[97]. Copyright © 2010 Springer-Verlag). (b) Workflow of the technology presented by Lee et al.[100]. The device includes several modules, including: (i) droplet generation; (ii) mixing; (iii) parallel synchronization; (iv) lateral electrocoalescence; (v) in-droplet magnetic particle separation; and (vi) asymmetrical lateral splitting. (Adapted with permission from[100]. Copyright © 2014 AIP Publishing LLC). (c) Schematics of the asymmetric splitting work developed by Brouzes et al.[104] An external magnet is used to concentrate the functionalized magnetic beads in the bottom region of the droplet. The device is characterized by two branches of different hydraulic resistances and by the introduction of an initial symmetrical box to tune the splitting profile of the droplet (dashed red line). This strategy favors the capture of particles in the lower front part of the droplet while reducing the retained volume going towards the rear of the droplet, devoid of beads. (d) Design of the microfluidic device developed by Verbruggen et al.[105]. Particle suspension and sample solution are injected into the oil flow, to form a droplet (1). These are split asymmetrically at a T-junction, characterized by narrow channels to improve the splitting (2). The two branches of the T-junction are connected downstream through a pillar region in order to equalize and keep the pressure constant*

during the splitting process (3). The droplet split ratio is tuned by an additional oil flow (4) (Adapted with permission from[105]. Copyright © 2014 Springer-Verlag).

Brouzes et al.[104] concentrated the functionalized magnetic beads, through an external magnet, in the lower front corner of a droplet and designed a splitting fork optimized for the extraction of the beads-rich regions. The authors introduced in the front end of a 1:3 asymmetric splitting fork, a symmetrical box by modifying the channels cross-section (Fig. 6c). At the beginning of the splitting process, the symmetrical box allows to split the front of the droplet at its midpoint, retaining the magnetic beads present in the lower front part of the droplet; then, the following difference in cross-sections gradually decreases, due to capillary forces, the retained volume going towards the rear of the droplet, devoid of beads. A throughput of 15 droplets per second with an optimal capture efficiency of 98.1% was reported but, in general, both bead retention and enrichment ratios decreased as the droplet velocity increased. Indeed, in this case, the tuning of the splitting profile by capillary effects is not possible anymore, since the systems dynamics are dominated by viscous forces. In addition, increasing the working velocity, the capture efficiency is reduced due to the droplet internal flows, limiting the concentration of beads in a compact cluster inside the droplet. Finally, since the splitting process requires a droplet confinement in the channel, sequential purifications to increase the final purity are not possible because it would imply a reduction of channel size at each step, causing a dramatic increase in the overall hydraulic resistance of the system. A different method was presented by Verbruggen et al.[105]. Here, the asymmetric splitting is not controlled by geometrical parameters but rather by adding a continuous phase inlet into one of the branch channels, as proposed

by Yamada et al.[106]. Furthermore, these authors exploit a regular T-junction with the narrow split and loop concepts[107] (Fig. 6d). In this configuration, the splitting branches are reconnected downstream and an array of posts is fabricated in the recombination region, preventing separate trains of processed droplets from contacting and merging. The loop has the advantage to keep the hydrodynamic resistances in the two branches independent from the presence and accumulation of daughter droplets, allowing a stable droplet splitting ratio over time. The presence of an additional oil flow controls the volumetric flow-rates distributed into each branch channel and enables a precise tuning of the volume ratio of the daughter droplets. This makes the system flexible, especially during the optimization step of a bioassay. The performance of the device was evaluated for a DNA extraction assay: the optimized design and flow-rate for the additional inlet[108,109] resulted in a magnetic beads separation efficiency of 98% in a single step for a 1:9 asymmetric splitting regime. This represented an upper limit for the separation rate of the system; in fact increasing the ratio up to 1:19, the separation efficiency decreased to 83%. On the other hand, the 1:19 splitting regime guaranteed a higher purification rate with respect to the 1:9 configuration. In conclusion, this system improved the performance in terms of purification and extraction efficiency with respect to previous techniques based on the same concept. According to the application of interest, a splitting regime has to be chosen, as a compromise between capture efficiency and purification rate.

In continuous droplet microfluidic devices presented so far, the redispersion of the extracted magnetic beads cluster in a second droplet (e.g. for achieving an additional reaction) required a merging step between these two droplets. Ways

to achieve such merging are known[103,110], but controlling the contact of the droplets to be merged requires additional circuitry and synchronization, thus complicated networks of microchannels with integrated valves[111] or synchronization modules[101]. Therefore, some typical biological protocols, such as washing steps or immunoassay reactions, might be difficult to integrate. Additionally, an increased throughput of the system might be obtained to the detriment of the extraction and purification rates, resulting in purification efficiencies lower than with conventional methods. Other approaches based on a direct magnetic extraction, similar to those developed for DMF-based devices, can meet these needs. Here, the separation of the magnetic particles cluster is not induced by droplet splitting at a channel junction, but by a balance between the viscous drag force pushing the droplet forward, the capillary forces tending to keep the droplet's integrity, and the magnetic force retaining the plug of magnetic particles. In particular, within a reference frame moving at the droplet velocity, at the approach of a magnet, an extraction is possible if the magnetic force overcomes the interfacial forces and if both these forces are themselves overcome by the viscous drag forces on the main droplet. In particular, as described in the introduction, the magnetic force is proportional to the magnetic flux density gradient and to the mass of the magnetic bead cluster, while the capillary force depends on the interfacial tension[112,113]. Following this idea, Gu et al.[114] developed a solid-phase extraction method for picoliter-scale droplets. In order to help the magnetic beads pass through the water-oil interface, micrometer-scale ferromagnetic particles were introduced in the droplet system. Under the influence of an external field, these particles act like small magnets in the droplet, attracting functionalized magnetic beads and self-

assembling with them in a cluster structure. In this way, an increase in magnetic force can be achieved and the sequential magnetic beads extraction and exchange between different droplets in a deterministic train was reported. In particular, as a proof of concept, a single-cell DNA purification from human lung carcinoma was performed. This strategy allowed a high enrichment rate with respect to previously reported systems since, as a result of the extraction process, a subdroplet containing the bead-cluster was generated. Furthermore, due to the hydrophilic surfaces of the ferromagnetic particles and of the paramagnetic beads, the magnetic cluster carried only a small amount of aqueous solution, which also helped to avoid eventual cross-contaminations. On the other hand, this ferromagnetic particle-assisted extraction limits the versatility of the system: the permanent magnetization induced in ferromagnetic particles prevent the possibility to perform multiple trapping-release sequences, as required in many analytical protocols. In contrast, higher programmability and versatility could be achieved by the magnetic tweezers technology[19,115]. In this system, two soft ferromagnetic tips terminating in an edge faced each other across a capillary filled with oil (Fig. 7a,i), in which confined aqueous droplets flowed (Fig. 7a,ii). The body of each tip was placed inside a tunable electric coil. The resulting magnetic tweezers generated a strong and local magnetic flux density gradient along the path of the droplet, contributing to a magnetic force able to concentrate the magnetic particles in a compact cluster (Fig. 7a,iii) and to extract them from the parent droplet (Fig. 7a, iv) with a low carryover of supernatant and a high separation efficiency (99% of the total droplet volume). As in [114], the extracted aggregate was kept inside an aqueous solution, preventing its contact with the continuous phase

and the capillary walls (Fig. 7a,v). Furthermore, the carryover of supernatant was mainly limited to the porosity of the packed bead cluster. After the extraction process, two different actuation sequences were demonstrated. In a first one, the cluster was retained by the magnetic tweezers during the passage of one or several washing droplets. In this way, a spontaneous coalescence occurred, the cluster of particles was diluted in the washing solution while the beads remained confined in the magnetic trap, allowing the removal of residual solution contained in the aggregate and at its surface. Second, after the merging of a new droplet with the aggregate (Fig. 7a, vi-vii), the beads could be released by switching off the magnetic field (Fig. 7a,viii).

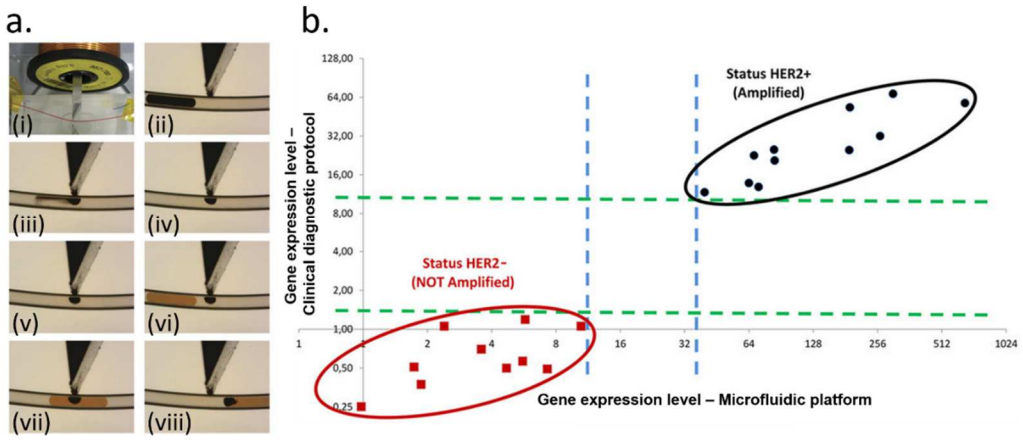

Figure 7: *(a) Sequence of images showing the magnetic tweezers technology. (i) The magnetic tweezers are composed by a pair of paramagnetic tips, adjacent to a microchannel (colored in red) and activated by magnetic coils. (ii-iv) Switching ON the electric current in the coil, the generated magnetic force allows the confinement of paramagnetic particles in a compact cluster and their extraction against the droplet interfacial force. (v) The extracted cluster is kept immobile in the continuous oil flow. (vi-viii) The particles are then redispersed, upon merging, in a coming droplet (colored in orange), switching OFF the electric current in the coil. (b) Results obtained in the clinical validation of the droplet microfluidic platform based on the magnetic tweezers technology. Graph in Logarithm scale (base 2) of the HER2 expression level obtained by the clinical diagnosis protocol versus the one resulting by the*

droplet microfluidic platform. Samples disclosed a posteriori as HER2- samples are plotted in red, and HER2+ ones in black. The dashed lines help to identify the excluded zone between the two populations: blue for the droplet platform, green for the hospital[10]. (Adapted with permission from[10]. Copyright © 2016 Nature Publishing Group).

Using a series of tweezers, several sequential exchanges of particles among droplets containing different solutions are possible. For example, Ferraro et al. showed the possibility of using the magnetic tweezers for RNA purification from breast cancer clinical samples followed by RT-qPCR[10]. In particular, the protocol aimed at quantifying the expression of the HER2 gene. Patients with HER2 overexpression are eligible for targeted therapy that can drastically improve their overall survival but may be deleterious for other patients[116]. The gene expression levels determined by the microfluidic approach were in full agreement with the ones obtained by conventional clinical diagnosis (Fig.7b), showing an identical segregation of 21 patient samples in two populations characterized by an overexpressed (black circles) and normal (red squares) HER2 status, respectively. Based on a similar platform, a Chromatin ImmunoPrecipitation (ChIP) protocol[117] including sequential chromatin extraction, DNA elution and purification steps was implemented[118]. Furthermore, recently, a single-step immunoassay for amyloid-β peptides determination was shown[119].

In conclusion, this technology, that led to the creation of the company INOREVIA, represents interesting performances in terms of extraction and purification efficiencies and its potentialities were shown in relevant clinical applications. The use of capillaries, however, limited miniaturization and parallelization.

3.2.2 Applications in detection

In the previous sections, we discussed the use of magnetic beads as a solid state support for the extraction and purification of analytes of interest. Functionalized micro and nanoparticles, magnetic or not, also have interesting applications in detection, allowing the rapid quantification of low abundance species.

As an example, Teste et al. employed magnetic particles for the direct detection of a specific analyte, by immuno-agglutination inside droplets[120]. This is a one-step bioassay based on the aggregation of beads coated with polyclonal antibodies, in the presence of a target biomolecule. In this work, the aggregation was promoted by the magnetic concentration of paramagnetic particles by the magnetic tweezers technology presented in the previous paragraph. In this proof of concept with a streptavidin/biotin assay, a relatively high throughput was achieved (around 300 assays/h) with a limit of detection in the pM range. However, this droplet based agglutination assay is ten times less sensitive than conventional tests.

As already discussed for stationary microfluidic and DMF devices, solid-state supports have been employed for ELISA protocols. In detail, in conventional ELISAs, color/fluorescent measurements are used for detection reading and taken from the total substrate region, resulting in local positive signal intensities being diffused into the whole working volume and weaker actually measured signals. This, in turn, may render the detection of biomarkers having concentrations below the pM range very difficult (if at all possible). Indeed, these methods are not sensitive enough to answer the clinical demand of strategies able to quantify concentrations of biomarkers present in biological

fluids in the 10^{-12}-10^{-16}M range[121], important for diagnostic and follow-up of neurological diseases[122], cancer[123] and early stage infections[124]. In this direction, the new frontier in biomarker analysis is represented by single-molecule counting or digital detection[125]. Different from ensemble measurements, resulting in an analogic signal increasing with the concentration of the target analyte, digital measurements rely on counting binary (signal/no signal) readouts coming from single molecules. The sensitivity thus depends on independent reactions, but neither on signal/noise ratios nor on intensity. A mandatory step for digital counting is the confinement of the single molecule (and the bound micro or nanoparticles if used as the solid support) in small volume compartments (picoliter to femtoliter scale), in order to achieve a locally high concentration. Among the different compartmentalization approaches proposed[126], continuous droplet microfluidics offers interesting advantages, especially in terms of processing time and binding kinetics. In the following, two strategies for the quantification of low abundance biomarkers with a combination of droplets and magnetic support will be discussed, namely digital ELISA and digital direct detection. In particular, in digital ELISA, the color/fluorescent intensity produced by an enzymatic reaction is confined into a small interrogation volume of the substrate surrounding the beads. On the other hand, in digital direct detection no enzymatic reaction is performed and a high intensity signal is achieved in specific spots on the bead surface due to a fluorescently tagged antibody.

Inspired by the SIngle MOlecule Array (SIMOA) concept[121], Shim et al. presented in 2013 a single molecule-counting ELISA in femtoliter droplets, paving the way for the development of highly sensitive immunoassays in droplet

microfluidics[127]. In their work, single protein molecules were captured and labelled on 1 μm polystyrene beads, forming immunocomplexes as in conventional bead-based ELISA. More in detail, in the case of low abundance biomarkers, the target-to-beads ratio was small (typically less than 1:1) and, as a consequence, the distribution of beads containing labelled immunocomplexes was Poissonian, i.e. only a minority of beads will have one target protein molecule associated, while the majority of beads will have zero target molecule. After that, single beads were encapsulated in femtoliter droplets with a Fluorescein di-β-D-galactopyranoside (FDG) substrate and incubated in on-chip traps to measure their fluorescence signal. In particular, at the end of the experiment, three populations of droplets were observed: droplets containing no beads, droplets encapsulating a bead without immuno-complexes and droplets containing a bead with an immuno-complex showing a fluorescence signal corresponding to the active enzyme associated with the target analyte. The analyte concentration was obtained by the number of droplets expressing a fluorescent signal, normalized by the total number of droplets containing a bead (Fig. 8). Using this method as a proof-of concept, the detection of PSA protein spiked in buffer resulted in a LOD of 46 fM, two order of magnitude lower than the standard bulk ELISA one.

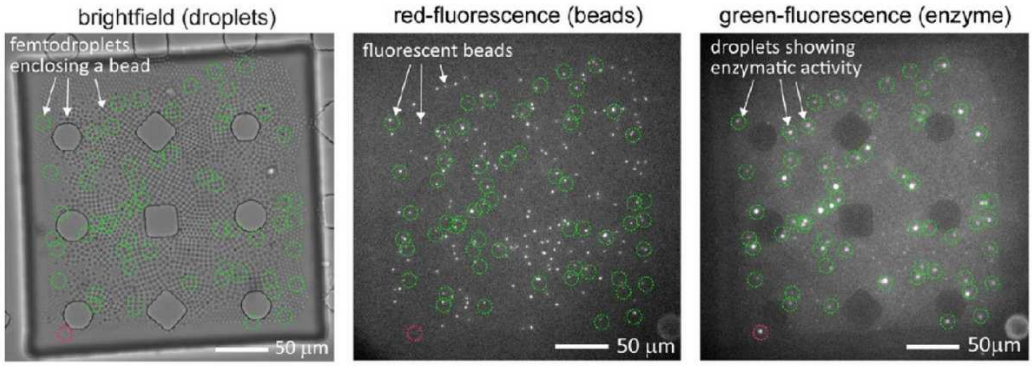

Figure 8: *Digital ELISA in femtoliter droplets for the detection of PSA protein[127]. Bright-field, red and green-fluorescence images of droplets after the ELISA protocol. In the red fluorescence image, bright spots represent capture antibody conjugated-beads while, in the green fluorescence image, they indicate droplets containing a bead and showing enzymatic activity. Furthermore, the red circle in the bottom left corner of each panel, shows the presence of a single droplet, exhibiting an enzymatic activity but not containing beads. This is due to the presence of unbound enzyme in the droplet. (Reprinted with permission from[127]. Copyright © 2013 American Chemical Society).*

On the other hand, direct digital detection methods in droplets were first exploited to profile cytokines molecules secreted by single T-cells. These proteins represent potential biomarkers and targets of interest in therapeutics and diagnostics. In this assay, implemented for the first time by Yarmush's group, an individual cell was encapsulated in a droplet containing fluorescent detection antibody and a single microparticle functionalized with an anti-Interleukin 10 (IL-10) antibody[128]. The binding of the secreted IL-10 with both the antibody grafted on the beads and the fluorescent detection antibody, led to a local increase of fluorescence intensity at the surface of the particles, allowing one-step single cell secretome analyses. Similarly, Chokkalingam et al. encapsulated single Jurkat T-cells in agarose droplets together with 500 nm polystyrene beads, functionalized to capture IL-2, TFN-alpha and IFN-gamma

cytokines[129]. After breaking the emulsion, the resulting agarose beads were stained with fluorescent antibodies, labelling the target proteins and enabling the following single-droplet detection by flow cytometer.

Later, Yarmush's team extended its previous work, developing a droplet-based platform for single cell-functional phenotyping[130]. Here, the stimulation of single dendritic cells (DC) for maturation was performed by lipopolysaccharide (LPS) and the resulting effects monitored for two phenotypic markers of DCs. In particular, the CD86 surface marker expression was measured by direct antibody based fluorescent labelling while the secreted IL-6 by bead-based immunoassay. Exploiting the advantages of droplet microfluidics, stimulation, secretion and time-resolved monitoring of single-live cell in population were performed in separated microenvironment and in a parallelized manner. Interestingly, in the same work, cell-cell communication was investigated in droplets, monitoring the surface biomarkers during T cell/DC interaction. Furthermore, the same team developed a droplet microfluidic platform for the detection of anti-tetanus ImmunoGlobulin(Ig)G in human serum samples[131]. In the clinical validation, performed with 500 adult immunized individuals, the device demonstrated the necessary sensitivity for IgG detection in human serum and an analysis time six-fold faster than standard ELISA.

Another interesting field of application for digital detection in droplet microfluidics is represented by monoclonal antibody screening. These antibodies have indeed an important role especially in cancer diagnosis and therapeutics, however one of the current main challenges is still to obtain monoclonal-antibodies with desirable functions. With this aim, for example, Mazutis et al. developed a platform for the high-throughput isolation of individual antibody-

secreting cells from a 10-fold excess of non-secreting cells[132]. In particular, antibodies secreted from mouse hybridoma at the single cell level were detected and, based on their fluorescence, the corresponding droplets were sorted by dielectrophoresis.

Colloidal metal nanoparticle (NPs) suspensions represent a further interesting tool for increasing the detection sensitivity of target molecules. They are already exploited in Surface-Enhanced Raman Spectroscopy (SERS), a promising detection technique for high-sensitive detection, and recently also in droplet microfluidic systems[133]. In fact, in SERS, the colloid support allows an important amplification of the low classical Raman signal due to a localized surface plasmon resonance between the excitation light beam, the analyte molecule and a noble metal nanostructure (typically Au, Ag, etc.). The coupling of SERS with droplet microfluidics brings interesting advantages, e.g., an improvement in repeatability and throughput, enhancement sample and colloidal suspension mixing, and avoidance of aggregates and sedimentation problems. Several applications in bioanalytical analysis have been shown; for example, the detection of Levofloxacin antibiotics[134], thiocyanate in real human serum and saliva samples[135] and PSA enzyme were demonstrated[99].

3.2.3 Barcoding applications

The most recent application of solid-phase support in continuous droplet microfluidics for diagnostic application is barcoding. As mentioned above, multiphase microfluidic devices allow high-throughput single-cell and single-molecule encapsulation and analysis. However, in these systems, the sequential

order of droplet generation is lost. Therefore, beyond the fundamental improvements brought to the biological community by digital-PCR[136], current and future generation analysis would require droplet indexing as a crucial step[137]. The principle of barcoding is to introduce a unique tag (or barcode) into a droplet for the univocal identification of the droplet itself, or its content. An example of barcoding can be achieved by varying the concentration of different fluorescent dyes, sometimes coated on solid micrometric beads[138]. This approach, however, only allows a few tens of combinations of distinguishable barcodes. To overcome this limitation, quantum dots (QDs) were introduced as fluorescent dyes[139]. In fact, these semiconductor nanoparticles present, in very narrow emission spectra, depending on their size, and can be excited by a wavelength. Therefore, compared with conventional molecular dyes, QDs allow a higher number of different barcodes combinations. For barcoding applications, these QDs were encapsulated in hydrogel microparticles produced by droplet microfluidic approaches. For example, by using flow-focusing and T-junctions microchannel geometries, in 2011 Ji et al. produced alginate QDs-doped microparticles, tuning on-demand the nanoparticles size and concentrations[140]. In the same period, Zhao et al. embedded different types of QDs in polymeric particles produced by double emulsion[141]. Additionally, they showed the possibility to integrate magnetic nanoparticles (MNPs), obtaining magnetic-tagged particles that could be easily handled by an external magnetic field. Lin et al.[142] proposed encapsulated MNPs as a barcode as well, by changing their concentration in a droplet and detecting the relative magnetoresistance with a miniaturized sensor. However, all the methods presented above are limited to a few hundreds of barcodes, insufficient for the typical throughput of droplet

generation in microfluidic devices (of the order of a few kHz). An alternative strategy of barcoding is the use of DNA oligonucleotides: considering the number of nucleotides that can be involved, the target capacity is then almost unlimited[137]. This approach requires downstream sequencing for detection, but it is nevertheless very promising. By exploiting this strategy, two similar techniques were recently presented, Drop-Seq[41] and *inDrop* (indexing droplets)[143], in which the sequencing of mRNA from thousands of single cells was achieved. Both consist in the preparation for sequencing of mRNA coming from thousands of cells, keeping a record of the original cell by oligonucleotide barcodes functionalized either on solid[143] or in hydrogel microparticles[144]. In both articles, proof-of-concept applications were shown: Drop-Seq was used for analysing 44,808 mouse retinal cells, identifying 37 different populations, while with inDrop, the authors studied the resulting heterogeneous population of embryonic stem cells after Leukemia Inhibitory Factor (LIF) withdrawal. However, for a deeper discussion comparing the performances and applications of these two promising technologies, we redirect the reader to other interesting reviews[145,146].

4 Conclusion

The power of solid-phase supports relies on two main properties: the possibility of surface functionalization with a wide range of chemistries and the micro/nanometric size, that guarantees a high surface/volume ratio favoring target capture.

The integration of solid-supports expanded the toolbox of available operations in microfluidic multiphase systems, conventionally limited to homogeneous

liquid-liquid reactions. This opened the way to more complex bioanalytical applications, including, for example, the extraction and purification of target analytes from complex matrices or the realization of multi-step protocols requiring efficient washing steps. Additionally, this will allow for more automated and user-friendly protocols, a prerequisite in particular for large scale diagnostic, security or environmental analyses.

The implementation of these magnetic solid-phase extraction protocols relies on the manipulation of functionalized magnetic particles through three main technologies: stationary, discrete digital (DMF) and continuous droplet microfluidics. The coupling of solid support with stationary microfluidic architectures offers the possibility to directly implement conventional protocols in microscale systems, leading to easy-to-use devices, compatible with conventional biological laboratory facilities and supporting the automation of existing protocols. This strategy, however, does not lead to a dramatic reduction in reagent consumption nor an increase in sensitivity.

DMF and continuous droplet microfluidics aim to overcome these barriers. Despite being limited by their low throughput, DMF devices allow extraction and purification efficiencies comparable with those of conventional lab scale protocols. Furthermore, these systems are highly flexible and the functionality of a DMF device can be easily tuned by modifying the actuation order of the electrodes, allowing the easier customization of new biological protocols starting from a generic device. Continuous droplet microfluidics allows a further decrease in sample volume and a higher throughput than previously described formats. These systems perform the enrichment of an analyte of interest and the magnetic tweezers technology, in particular, allows the transfer of magnetic

carriers between different matrices with a high purification rate, thus opening the possibility to implement multi-step protocols.

Each of the above approaches have their advantages and limitations, but overall the integration of magnetic manipulation in multiphase microfluidics opened the route to considerably increase the potential of this growing area of microfluidic, expanding it to multisteps protocols, and to direct operation with raw samples, a prerequisite for many clinical and analytical applications. This involves for instance the extraction and purification of nucleic acids, proteins or cells.

Overall, it is important to underline that the coupling of solid phase supports with continuous droplet microfluidics not only allows the miniaturization and integration of existing biomedical protocols but also paves the way for the development of completely new strategies for diagnostic and research. In fact, small droplet generation and high-throughput analysis, which are typical skills of continuous droplet microfluidics, allow the introduction of single-particles in droplets, yielding important results that could not be reached without the microfluidic contributions, such as the very low limit of detection in immunoassay applications or the efficient barcoding of single cells for consequent gene studies. Finally, the use of solid and hydrogel particles in droplet microfluidics, despite being in its infancy, holds strong promises regarding the high-throughput analysis of individual cells, and is expected to forge new paths in the fields of biology and medical sciences.

References

1 E. K. Sackmann, A. L. Fulton and D. J. Beebe, *Nature*, 2014, 507, 181–9.

2 K. W. Oh and C. H. Ahn, *J. Micromechanics Microengineering*, 2006, 16, R13–R39.

3 A. Yamada, R. Renault, A. Chikina, B. Venzac, I. Pereiro, S. Coscoy, M. Verhulsel, M. C. Parrini, C. Villard, J.-L. Viovy and S. Descroix, *Lab Chip*, 2016, 16, 4691–4701.

4 K. Choi, A. H. C. Ng, R. Fobel and A. R. Wheeler, *Annu. Rev. Anal. Chem.*, 2012, 5, 413–440.

5 M. J. Jebrail, M. S. Bartsch and K. D. Patel, *Lab Chip*, 2012, 12, 2452.

6 F. Mugele and J.-C. Baret, *J. Phys. Condens. Matter*, 2005, 17, 705–774.

7 E. Samiei, M. Tabrizian and M. Hoorfar, *Lab Chip*, 2016, 16, 2376–96.

8 M. T. Guo, A. Rotem, J. A. Heyman and D. A. Weitz, *Lab Chip*, 2012, 12, 2146.

9 P. Zhu, L. Wang, N. P. Macdonald, T. Lewis, R. M. Guijt, B. Paull, M. C. Breadmore, G. Grübel, J. Legrand, F. von Stetten, R. Zengerle and N. Paust, *Lab Chip*, 2017, 17, 34–75.

10 D. Ferraro, J. Champ, B. Teste, M. Serra, L. Malaquin, J.-L. Viovy, P. de Cremoux and S. Descroix, *Sci. Rep.*, 2016, 6, 25540.

11 J.-C. Baret, *Lab Chip*, 2012, 12, 422–33.

12 R. Seemann, M. Brinkmann, T. Pfohl and S. Herminghaus, *Rep. Prog. Phys.*, 2012, 75, 16601.

13 V. Taly, D. Pekin, L. Benhaim, S. K. Kotsopoulos, D. Le Corre, X. Li, I. Atochin, D. R. Link, A. D. Griffiths, K. Pallier, H. Blons, O. Bouché, B. Landi, J. B. Hutchison and P. Laurent-Puig, *Clin. Chem.*, 2013, 59.

14 C.-H. Chen, M. A. Miller, A. Sarkar, M. T. Beste, K. B. Isaacson, D. A. Lauffenburger, L. G. Griffith and J. Han, *J. Am. Chem. Soc.*, 2013, 135, 1645–1648.

15 K. Turcheniuk, a V Tarasevych, V. P. Kukhar, R. Boukherroub and S. Szunerits, *Nanoscale*, 2013, 5, 10729–10752.

16 B. Teste, F. Kanoufi, S. Descroix, P. Poncet, T. Georgelin, J.-M. Siaugue, J. Petr, A. Varenne and M.-C. Hennion, *Anal. Bioanal. Chem.*, 2011, 400, 3395–3407.

17 O. Philippova, A. Barabanova, V. Molchanov and A. Khokhlov, in *European Polymer Journal*, 2011, vol. 47, pp. 542–559.

18 M. A. M. Gijs, *Microfluid. Nanofluidics*, 2004, 1, 22–40.

19 A. Ali-Cherif, S. Begolo, S. Descroix, J.-L. Viovy and L. Malaquin, *Angew. Chemie Int. Ed.*, 2012, 51, 10765–10769.

20 N. Pamme, *Lab Chip*, 2006, 6, 24–38.

21 M. A. M. Gijs, F. Lacharme and U. Lehmann, *Chem. Rev.*, 2010, 110, 1518–1563.

22 M. F. Elshal, J. P. McCoy and Jr., *Methods*, 2006, 38, 317–23.

23 C. T. Lim and Y. Zhang, *Biosens. Bioelectron.*, 2007, 22, 1197–1204.

24 P. J. Tighe, R. R. Ryder, I. Todd and L. C. Fairclough, *PROTEOMICS - Clin. Appl.*, 2015, 9, 406–422.

25 K. Hoshino, Y.-Y. Huang, N. Lane, M. Huebschman, J. W. Uhr, E. P. Frenkel and X. Zhang, *Lab Chip*, 2011, 11, 3449.

26 B. D. Plouffe, M. Mahalanabis, L. H. Lewis, C. M. Klapperich and S. K. Murthy, *Anal. Chem.*, 2012, 84, 1336–1344.

27 J. Autebert, B. Coudert, J. Champ, L. Saias, E. T. Guneri, R. Lebofsky, F.-C. Bidard, J.-Y. Pierga, F. Farace, S. Descroix, L. Malaquin and J.-L. Viovy, *Lab Chip*, 2015, 15, 2090–2101.

28 B. Teste, F. Malloggi, J.-M. Siaugue, A. Varenne, F. Kanoufi, S. Descroix, J. Petr, A. Varenne and M.-C. Hennion, *Lab Chip*, 2011, 11, 4207.

29 J. Mok, M. N. Mindrinos, R. W. Davis and M. Javanmard, *Proc. Natl. Acad. Sci.*, 2014, 111, 2110–2115.

30 H. C. Tekin, M. Cornaglia and M. a M. Gijs, *Lab Chip*, 2013, 13, 1053–9.

31 S. Dubus, J. F. Gravel, B. Le Drogoff, P. Nobert, T. Veres and D. Boudreau, *Anal. Chem.*, 2006, 78, 4457–4464.

32 O. Strohmeier, S. Keil, B. Kanat, P. Patel, M. Niedrig, M. Weidmann, F. Hufert, J. Drexler, R. Zengerle and F. von Stetten, *RSC Adv.*, 2015, 5, 32144–32150.

33 S. Bronzeau and N. Pamme, *Anal. Chim. Acta*, 2008, 609, 105–112.

34 A. Le Nel, N. Minc, C. Smadja, M. Slovakova, Z. Bilkova, J.-M. Peyrin, J.-L. Viovy and M. Taverna, *Lab Chip*, 2008, 8, 294–301.

35 A. Rida and M. A. M. Gijs, *Anal. Chem.*, 2004, 76, 6239–6246.

36 I. Pereiro, S. Tabnaoui, M. Fermigier, O. du Roure, S. Descroix, J.-L. Viovy and L. Malaquin, *Lab Chip*, 2017, 17, 1603–1615.

37 I. Pereiro, A. Bendali, S. Tabnaoui, L. Alexandre, J. Srbova, Z. Bilkova, S. Deegan, L. Joshi, J.-L. Viovy, L. Malaquin, B. Dupuy, S. Descroix and H. H. Girault, *Chem. Sci.*, 2017, 8, 1329–1336.

38 T. D. Mai, I. Pereiro, M. Hiraoui, J.-L. Viovy, S. Descroix, M. Taverna and C. Smadja, *Analyst*, 2015, 140, 5891–5900.

39 P.-G. de Gennes, F. Brochard-Wyart and D. Quéré, in *Capillarity and Wetting Phenomena*, Springer New York, New York, NY, 2004, pp. 1–31.

40 M.-C. Jullien, M.-J. Tsang Mui Ching, C. Cohen, L. Menetrier and P. Tabeling, *Phys. Fluids*, 2009, 21, 72001.

41 E. Z. Macosko, A. Basu, R. Satija, J. Nemesh, K. Shekhar, M. Goldman, I. Tirosh, A. R. Bialas, N. Kamitaki, E. M. Martersteck, J. J. Trombetta, D. A. Weitz, J. R. Sanes, A. K. Shalek, A. Regev and S. A. McCarroll, *Cell*, 2015, 161, 1202–1214.

42 R. C. den Dulk, K. A. Schmidt, G. Sabatté, S. Liébana and M. W. J. Prins, *Lab Chip*, 2013, 13, 106–18.

43 S. M. Berry, E. T. Alarid and D. J. Beebe, *Lab Chip*, 2011, 11, 1747–53.

44 H. Chen, A. Abolmatty and M. Faghri, *Microfluid. Nanofluidics*, 2011, 10, 593–605.

45 D. Bonn, J. Eggers, J. Indekeu, J. Meunier and E. Rolley, *Rev. Mod. Phys.*, 2009, 81, 739–805.

46 P. Vulto, G. Medoro, L. Altomare, G. A. Urban, M. Tartagni, R. Guerrieri and N. Manaresi, *J. Micromechanics Microengineering*, 2006, 16, 1847–1853.

47 P. Vulto, S. Podszun, P. Meyer, C. Hermann, A. Manz and G. A. Urban, *Lab Chip*, 2011, 11, 1596.

48 K. Sur, S. M. McFall, E. T. Yeh, S. R. Jangam, M. A. Hayden, S. D. Stroupe and D. M. Kelso, *J. Mol. Diagn.*, 2010, 12, 620–8.

49 L. N. Strotman, G. Lin, S. M. Berry, E. a Johnson and D. J. Beebe, *Analyst*, 2012, 137, 4023–8.

50 S. M. Berry, A. J. LaVanway, H. M. Pezzi, D. J. Guckenberger, M. A. Anderson, J. M. Loeb and D. J. Beebe, *J. Mol. Diagn.*, 2014, 16, 297–304.

51 S. M. Berry, L. J. Maccoux and D. J. Beebe, *Anal. Chem.*, 2012, 84, 5518–23.

52 S. M. Berry, L. N. Strotman, J. D. Kueck, E. T. Alarid and D. J. Beebe, *Biomed. Microdevices*, 2011, 13, 1033–42.

53 B. P. Casavant, D. J. Guckenberger, S. M. Berry, J. T. Tokar, J. M. Lang, D. J. Beebe, D. M. Kelso, F. R. Haselton, T. J. Merkel, J. P. Ferrance, J. P. Landers, L. C. Martin, M. Toner, R. G. Tompkins, P. A. Efron and L. L. Moldawer, *Lab Chip*, 2013, 13, 391–396.

54 B. P. Casavant, L. N. Strotman, J. J. Tokar, S. M. Thiede, A. M. Traynor, J. S. Ferguson, J. M. Lang and D. J. Beebe, *Lab Chip*, 2014, 14, 99–105.

55 J. A. Kim, M. Kim, S. M. Kang, K. T. Lim, T. S. Kim and J. Y. Kang, *Biosens. Bioelectron.*, 2015, 67, 724–732.

56 H. Cho, H.-Y. Kim, J. Y. Kang and T. S. Kim, *J. Colloid Interface Sci.*, 2007, 306, 379–85.

57 H. Bordelon, N. M. Adams, A. S. Klemm, P. K. Russ, J. V Williams, H. K. Talbot, D. W. Wright and F. R. Haselton, *ACS Appl. Mater. Interfaces*, 2011, 3, 2161–8.

58 S. M. Berry, H. M. Pezzi, A. J. LaVanway, D. J. Guckenberger, M. A. Anderson and D. J. Beebe, *ACS Appl. Mater. Interfaces*, 2016, 8, 15040–15045.

59 D. J. Guckenberger, H. M. Pezzi, M. C. Regier, S. M. Berry, K. Fawcett, K. Barrett and D. J. Beebe, *Anal. Chem.*, 2016, 88, 9902–9907.

60 M. Shikida, K. Takayanagi, K. Inouchi, H. Honda and K. Sato, *Sensors Actuators B Chem.*, 2006, 113, 563–569.

61 F. R. Cui, J. Wang, S. M. Opal and A. Tripathi, *PLoS One*, 2016, 11, e0149522.

62 M. C. Park, M. Kim, G. T. Lim, S. M. Kang, S. S. A. An, T. S. Kim and J. Y. Kang, *Lab Chip*, 2016, 16, 2245–53.

63 Y. Zhang, S. Park, K. Liu, J. Tsuan, S. Yang and T.-H. Wang, *Lab Chip*, 2011, 11, 398–406.

64 J. Pipper, M. Inoue, L. F.-P. Ng, P. Neuzil, Y. Zhang and L. Novak, *Nat. Med.*, 2007, 13, 1259–1263.

65 U. Lehmann, S. Hadjidj, V. K. Parashar, C. Vandevyver, A. Rida and M. A. M. Gijs, *Sensors Actuators B Chem.*, 2006, 117, 457–463.

66 M. Shikida, K. Takayanagi, H. Honda, H. Ito and K. Sato, *J. Micromechanics Microengineering*, 2006, 16, 1875–1883.

67 H. Ito, K. Takayanagi, M. Okochi, M. Shikida, K. Sato and H. Honda, *J. Chem. Eng. JAPAN*, 2006, 39, 1296–1299.

68 U. Lehmann, C. Vandevyver, V. K. Parashar and M. A. M. Gijs, *Angew. Chemie Int. Ed.*, 2006, 45, 3062–3067.

69 N. Inagaki, K. Narushim, N. Tuchida and K. Miyazaki, *J. Polym. Sci. Part B Polym. Phys.*, 2004, 42, 3727–3740.

70 U. Lehmann, D. de Courten, C. Vandevyver, V. K. Parashar and M. A. M. Gijs, *Microelectron. Eng.*, 2007, 84, 1669–1672.

71 Z. Long, A. M. Shetty, M. J. Solomon and R. G. Larson, *Lab Chip*, 2009, 9, 1567–75.

72 J. Pipper, Y. Zhang, P. Neuzil and T.-M. Hsieh, *Angew. Chem. Int. Ed. Engl.*, 2008, 47, 3900–4.

73 D. Mark, S. Haeberle, G. Roth, F. von Stetten and R. Zengerle, *Chem. Soc. Rev.*, 2010, 39, 1153.

74 M. Abdelgawad and A. R. Wheeler, *Adv. Mater.*, 2009, 21, 920–925.

75 M. G. Pollack, R. B. Fair and A. D. Shenderov, *Appl. Phys. Lett.*, 2000, 77, 1725–1726.

76 Y. Wang, Y. Zhao and S. K. Cho, *J. Micromechanics Microengineering*, 2007, 17, 2148–2156.

77 Y. Fouillet, D. Jary, C. Chabrol, P. Claustre and C. Peponnet, *Microfluid. Nanofluidics*, 2008, 4, 159–165.

78 R. S. Sista, A. E. Eckhardt, V. Srinivasan, M. G. Pollack, S. Palanki and V. K. Pamula, *Lab Chip*, 2008, 8, 2188–96.

79 R. Sista, Z. Hua, P. Thwar, A. Sudarsan, V. Srinivasan, A. Eckhardt, M. Pollack and V. Pamula, *Lab Chip*, 2008, 8, 2091–104.

80 N. Vergauwe, D. Witters, F. Ceyssens, S. Vermeir, B. Verbruggen, R. Puers and J. Lammertyn, *J. Micromechanics Microengineering*, 2011, 21, 54026.

81 N. Vergauwe, S. Vermeir, J. B. Wacker, F. Ceyssens, M. Cornaglia, R. Puers, M. A. M. Gijs, J. Lammertyn and D. Witters, *Sensors Actuators B Chem.*, 2014, 196, 282–291.

82 A. H. C. Ng, K. Choi, R. P. Luoma, J. M. Robinson and A. R. Wheeler, *Anal. Chem.*, 2012, 84, 8805–12.

83 S. Abdulwahab, A. H. C. Ng, M. Dean Chamberlain, H. Ahmado, L.-A. Behan, H. Gomaa, R. F. Casper and A. R. Wheeler, *Lab Chip*, 2017, 17, 1594–1602.

84 A. H. C. Ng, M. Lee, K. Choi, A. T. Fischer, J. M. Robinson and A. R. Wheeler, *Clin. Chem.*, 2015, 61, 420–429.

85 R. Fobel, C. Fobel and A. R. Wheeler, *Appl. Phys. Lett.*, 2013, 102, 193513.

86 G. J. Shah, J. L. Veale, Y. Korin, E. F. Reed, H. A. Gritsch and C.-J. C. Kim, *Biomicrofluidics*, 2010, 4, 44106.

87 A. Rival, D. Jary, C. Delattre, Y. Fouillet, G. Castellan, A. Bellemin-Comte and X. Gidrol, *Lab Chip*, 2014, 14, 3739–49.

88 H. Kim, M. J. Jebrail, A. Sinha, Z. W. Bent, O. D. Solberg, K. P. Williams, S. A. Langevin, R. F. Renzi, J. L. Van De Vreugde, R. J. Meagher, J. S. Schoeniger, T. W. Lane, S. S. Branda, M. S. Bartsch and K. D. Patel, *PLoS One*, 2013, 8, e68988.

89 M. L. Metzker, *Nat. Rev. Genet.*, 2010, 11, 31–46.

90 M. Kühnemund, D. Witters, M. Nilsson and J. Lammertyn, *Lab Chip*, 2014, 14, 2983–2992.

91 F. Dahl, J. Banér, M. Gullberg, M. Mendel-Hartvig, U. Landegren and M. Nilsson, *Proc. Natl. Acad. Sci. U. S. A.*, 2004, 101, 4548–53.

92 A. Fire and S. Q. Xu, *Proc. Natl. Acad. Sci. U. S. A.*, 1995, 92, 4641–5.

93 E. Samiei, M. Tabrizian and M. Hoorfar, *Lab Chip*, 2016, 16, 2376–96.

94 M. G. Pollack, V. K. Pamula, V. Srinivasan and A. E. Eckhardt, *Expert Rev. Mol. Diagn.*, 2011, 11, 393–407.

95 H.-H. Shen, S.-K. Fan, C.-J. Kim and D.-J. Yao, *Microfluid. Nanofluidics*, 2014, 16, 965–987.

96 E. Al-Hetlani, O. J. Hatt, M. Vojtíšek, M. D. Tarn, A. Iles and N. Pamme, in *8th International Conference on the Scientific and Clinical Applications of Magnetic Carriers. AIP Conference Proceedings*, 2010, vol. 1311, pp. 167–175.

97 D. Lombardi and P. S. Dittrich, *Anal. Bioanal. Chem.*, 2011, 399, 347–352.

98 X. Pan, S. Zeng, Q. Zhang, B. Lin and J. Qin, *Electrophoresis*, 2011, 32, 3399–3405.

99 R. Gao, Z. Cheng, A. J. DeMello and J. Choo, *Lab Chip*, 2016, 16, 1022–1029.

100 H. Lee, L. Xu and K. W. Oh, *Biomicrofluidics*, 2014, 8, 44113.

101 B. Ahn, K. Lee, H. Lee, R. Panchapakesan and K. W. Oh, *Lab Chip*, 2011, 11, 3956.

102 C. Priest, S. Herminghaus and R. Seemann, *Appl. Phys. Lett.*, 2006, 89, 134101.

103 M. Chabert, K. D. Dorfman and J.-L. Viovy, *Electrophoresis*, 2005, 26, 3706–15.

104 E. Brouzes, T. Kruse, R. Kimmerling and H. H. Strey, *Lab Chip*, 2015, 15, 908–919.

105 B. Verbruggen, K. Leirs, R. Puers and J. Lammertyn, *Microfluid. Nanofluidics*, 2015, 18, 293–303.

106 M. Yamada, S. Doi, H. Maenaka, M. Yasuda and M. Seki, *J. Colloid Interface Sci.*, 2008, 321, 401–7.

107 J. Nie and R. T. Kennedy, *Anal. Chem.*, 2010, 82, 7852–7856.

108 B. Verbruggen, T. Tóth, Y. T. Atalay, F. Ceyssens, P. Verboven, R. Puers, B. Nicolai and J. Lammertyn, *Microfluid. Nanofluidics*, 2013, 15, 243–252.

109 B. Verbruggen, T. Tóth, M. Cornaglia, R. Puers, M. A. M. Gijs and J. Lammertyn, *Microfluid. Nanofluidics*, 2015, 18, 91–102.

110 X. Niu, S. Gulati, J. B. Edel, A. J. deMello, H. A. Stone and G. M. Whitesides, *Lab Chip*, 2008, 8, 1837.

111 M. A. Unger, H.-P. Chou, T. Thorsen, A. Scherer and S. R. Quake, *Science, 2000,* 288, *5463.*

112 C. N. Baroud, F. Gallaire, R. Dangla, A. Thomas, F. Chatelain, M. Y. Balakirev, F. Hollfelder, D. A. Weitz and L. Yobas, *Lab Chip*, 2010, 10, 2032.

113 B. Teste, N. Jamond, D. Ferraro, J.-L. Viovy and L. Malaquin, *Microfluid. Nanofluidics*, 2015, 19, 141–153.

114 S.-Q. Gu, Y.-X. Zhang, Y. Zhu, W.-B. Du, B. Yao and Q. Fang, *Anal. Chem.*, 2011, 83, 7570–7576.

115 D. Ferraro, Y. Lin, B. Teste, D. Talbot, L. Malaquin, S. Descroix and A. Abou-Hassan, *Chem. Commun.*, 2015, 51, 16904–16907.

116 E. A. Perez, A. C. Dueck, A. E. McCullough, M. M. Reinholz, K. S. Tenner, N. E. Davidson, J. Gralow, L. N. Harris, L. A. Kutteh, D. W. Hillman, R. B. Jenkins and B. Chen, *JNCI J. Natl. Cancer Inst.*, 2012, 104, 159–162.

117 T. S. Furey, *Nat. Rev. Genet.*, 2012, 13, 840–852.

118 B. Teste, J. Champ, A. Londono-Vallejo, S. Descroix, L. Malaquin, J.-L. Viovy, I. Draskovic and G. Mottet, *Lab Chip*, 2017, 17, 530–537.

119 T. D. Mai, D. Ferraro, N. Aboud, R. Renault, M. Serra, N. T. Tran, J.-L. Viovy, C. Smadja, S. Descroix and M. Taverna, *Sensors Actuators B Chem.*, 2017.

120 B. Teste, A. Ali-Cherif, J. L. Viovy and L. Malaquin, *Lab Chip*, 2013, 13, 2344–9.

121 D. M. Rissin, C. W. Kan, T. G. Campbell, S. C. Howes, D. R. Fournier, L. Song, T. Piech, P. P. Patel, L. Chang, A. J. Rivnak, E. P. Ferrell, J. D. Randall, G. K. Provuncher, D. R. Walt and D. C. Duffy, *Nat. Biotechnol.*, 2010, 28, 595–9.

122 D. Galasko, *J. Alzheimer's Dis.*, 2005, 8, 339–346.

123 P. R. Srinivas, B. S. Kramer and S. Srivastava, *Lancet Oncol.*, 2001, 2, 698–704.

124 J. M. Barletta, D. C. Edelman and N. T. Constantine, *Am. J. Clin. Pathol.*, 2004, 122, 20–27.

125 D. R. Walt, *Anal. Chem.*, 2013, 85, 1258–1263.

126 M. Cretich, G. G. Daaboul, L. Sola, M. S. Ünlü and M. Chiari, *Trends Biotechnol.*, 2015, 33, 343–351.

127 J. Shim, R. T. Ranasinghe, C. A. Smith, S. M. Ibrahim, F. Hollfelder, W. T. S. Huck, D. Klenerman and C. Abell, *ACS Nano*, 2013, 7, 5955–5964.

128 T. Konry, M. Dominguez-Villar, C. Baecher-Allan, D. A. Hafler and M. L. Yarmush, *Biosens. Bioelectron.*, 2011, 26, 2707–2710.

129 V. Chokkalingam, J. Tel, F. Wimmers, X. Liu, S. Semenov, J. Thiele, C. G. Figdor and W. T. S. Huck, *Lab Chip*, 2013, 13, 4740.

130 T. Konry, A. Golberg, M. Yarmush, D. Irimia and M. L. Yarmush, *Sci. Rep.*, 2013, 3, 1110–1115.

131 A. Golberg, M. L. Yarmush and T. Konry, *Microchim. Acta*, 2013, 180, 855–860.

132 L. Mazutis, J. Gilbert, W. L. Ung, D. A. Weitz, A. D. Griffiths and J. A. Heyman, *Nat. Protoc.*, 2013, 8, 870–891.

133 Y. Zhu and Q. Fang, *Anal. Chim. Acta*, 2013, 787, 24–35.

134 I. J. Hidi, M. Jahn, K. Weber, D. Cialla-May and J. Popp, *Phys. Chem. Chem. Phys.*, 2015, 17, 21236–42.

135 L. Wu, Z. Wang, S. Zong and Y. Cui, *Biosens. Bioelectron.*, 2014, 62, 13–18.

136 D. Pekin, Y. Skhiri, J.-C. Baret, D. Le Corre, L. Mazutis, C. Ben Salem, F. Millot, A. El Harrak, J. B. Hutchison, J. W. Larson, D. R. Link, P. Laurent-Puig, A. D. Griffiths and V. Taly, *Lab Chip*, 2011, 11, 2156.

137 N. Shembekar, C. Chaipan, R. Utharala and C. A. Merten, *Lab Chip*, 2016, 16, 1314–1331.

138 P. O. Krutzik and G. P. Nolan, *Nat. Methods*, 2006, 3, 361–368.

139 W. C. W. Chan and S. Nie, *Science, 1998,* 281, *5385.*

140 X.-H. Ji, W. Cheng, F. Guo, W. Liu, S.-S. Guo, Z.-K. He and X.-Z. Zhao, *Lab Chip*, 2011, 11, 2561.

141 Y. Zhao, H. C. Shum, H. Chen, L. L. A. Adams, Z. Gu and D. A. Weitz, *J. Am. Chem. Soc.*, 2011, 133, 8790–8793.

142 G. Lin, D. Makarov, M. Medina-Sánchez, M. Guix, L. Baraban, G. Cuniberti, O. G. Schmidt, *Lab Chip*, 2015, 15, 216–224.

143 A. M. Klein, L. Mazutis, I. Akartuna, N. Tallapragada, A. Veres, V. Li, L. Peshkin, D. A. Weitz and M. W. Kirschner, *Cell*, 2015, 161, 1187–1201.

144 R. Zilionis, J. Nainys, A. Veres, V. Savova, D. Zemmour, A. M. Klein and L. Mazutis, *Nat. Protoc.*, 2016, 12, 44–73.

145 D. Grün and A. van Oudenaarden, *Cell*, 2015, 163, 799–810.

146 M. Dhar, R. Khojah, A. Tay and D. Di Carlo, *Lab Chip*, 2015, 15, 4109–13.

Chapter 2

The magnetic tweezers technology: applications in nucleic acids and proteins analysis

In the previous chapter, we reviewed the use of the solid phase support in several biphasic microfluidic formats (e.g., stationary, digital and continuous), discussing about applications ranging from the magnetic solid-state extraction to the emerging direct detection and barcoding technologies dedicated to single cell analysis.

We will now focus on the magnetic solid-state extraction in continuous droplet microfluidics, going more into details on the magnetic tweezers technology developed in the lab by Anais Ali Cherif and S. Begolo[1]. We will briefly describe the technological peculiarities of this system and the physics underlying this concept. As briefly described in the previous chapter, the magnetic tweezers approach is perfectly suited to open the field of droplet microfluidic to biological and chemical protocols[1,2,3,4]. Among these, during my PhD I contributed in its application to nucleic acids analysis[5] and proteins detection[6]; both applications will be discussed in the following sections.

1 The magnetic tweezers

1.1 Technology and basic operations

The magnetic tweezers technology consists of a soft ferromagnetic core (AFK502 alloy, Ni/Fe-based), characterized by a sharp tip in close contact with a hydrophobic capillary (ID=300µm, OD=600µm) and with its other end inserted in a tunable electric coil (about 1000 loops of copper wire, 1 mm diameter). The capillary is filled with fluorinated oil and highly confined aqueous droplets (few hundreds nL in volume) are transported towards the tip by a continuous flow of oil. Applying an electric current to the coil (1A, 12V), a local magnetic field of about 0.15T is reached at the tip and a strong gradient (200T/m) is generated within the capillary. Adding a second passive tip, whose magnetization is induced by the first one that faces it across the capillary, the maximum magnetic field increases to 0.35T and the magnetic gradient results 500T/m[1].

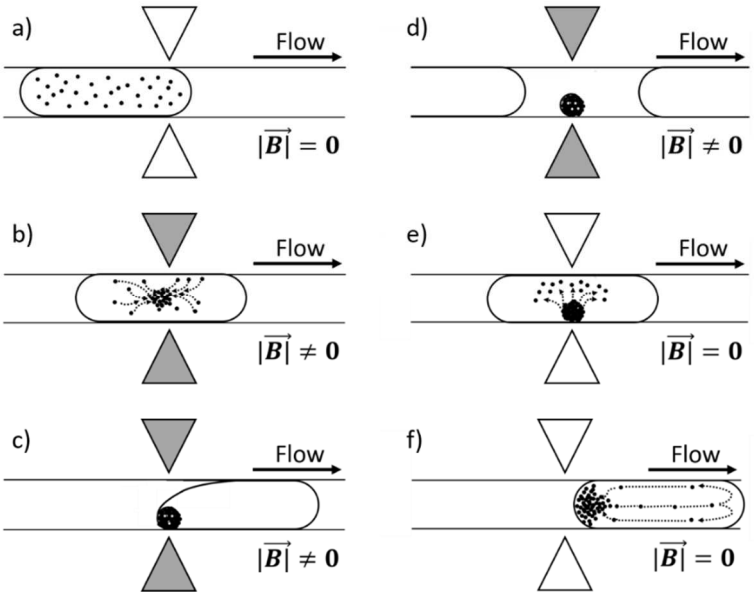

Figure 1: Scheme of the bead-handling step by the magnetic tweezers. *(a) The magnetic tweezers represented as triangles, face each other across a capillary in which droplets, loaded with magnetic particles, flow. (b) Switching ON the magnetic tweezers, the particles are confined in a compact cluster and extracted*

against the droplet interfacial force (c-d). The extracted cluster is kept immobile in the continuous oil flow. Two sequences of operation can then be performed. At first, maintaining the magnetic tweezers ON, the extracted cluster can be rinsed by the passage of a washing droplet. Alternatively, the particles can be redispersed, upon merging (e), in a coming droplet, switching OFF the electric current in the coil (f). The triangles representing the magnetic tweezers are gray when activated and white when inactived.

The magnetic force generated by these structures is able to attract the paramagnetic micrometric beads dispersed in an aqueous droplet, flowing in a microchannel (Fig.1a). Under the influence of the magnetic field, the beads form a densely packed cluster (Fig.1b) that is extracted against the capillary interfacial force of the droplet and is kept immobile in the oil flow (Fig.1c-d). The extraction efficiency has been demonstrated to be around 98%, for carrier oil flow-rates lower than 0.07µL/s. The extracted cluster is kept within an aqueous subdroplet so it is never in contact with the oil or the channel walls. Furthermore, the volume of liquid present in this subdroplet is around 1nL therefore the extraction process is highly efficient considering the volume ratio of the subdroplet compared to the mother droplet volume (around 100 to 200 nL). Following the extraction, two different actuation sequences can be adopted. In the first one, the magnetic field is maintained in the ON state during the passage of one (or several) rinsing droplet, to exchange the liquid that is initially present in the sub-droplet. Upon merging, the supernatant surrounding the particle cluster is further diluted in the washing solution while the particles stay confined in the magnetic trap. With this procedure, the residual liquid in the extracted subdroplet and at the beads surface is further removed. Alternatively, when a second droplet reaches the cluster, spontaneous coalescence with the magnetically trapped subdroplet occurs (Fig.1e), switching off the magnetic

field, the beads can be released in the following droplet (Fig.1f). Exploiting these three functions (bead extraction, rinsing and resuspension), any bead-based protocol can be implemented: functionalized magnetic beads are used as a solid-phase support to extract and purify an analyte of interest from a complex matrix with a low carryover of supernatant, obtaining indeed extraction and purification efficiencies comparable with those of macroscopic protocols. Furthermore, as will be shown in the following paragraphs, a series of magnetic tweezers can be used to perform sequential extraction and redispersion sequences within different media in a droplet train.

To conclude, it is worth noting that the washing step and the redispersion of the extracted magnetic cluster relies on the possibility to perform merging between the extracted cluster and the coming droplet. Differently from conventional droplet microfluidics systems, where surfactants are designed to prevent droplet merging[7], here, perfluorodecanol is used to create stable emulsion in fluorinated oil in a highly confined state, preventing also wall contamination[8]. The use of fluorinated oil decreases the PDMS swelling problem as well as the diffusion of molecules from the aqueous to the continuous oil phase, avoiding thus cross-contaminations problem[7].

1.2 The physical conditions for extraction

As briefly discussed in the introduction chapter, direct magnetic extraction relies on a subtle balance between the magnetic forces F_{mag} acting on the magnetic particle cluster and the interfacial force F_{int}, which tends to keep the droplet integrity. Before my PhD, Ali Cherif et al. experimentally investigated

the extraction regime, defined by the condition $F_{mag} > F_{int}$, as a function of the magnetic particles load, the induction current and the droplet velocities[1]. Fig. 2a presents a phase diagram describing the splitting behavior for 100nL droplets, containing a particle load ranging from 0.1µg to 1µg, for different electric current values supplied to the coil. Two regimes can be distinguished: i) a droplet splitting regime (open circles), corresponding to the condition $F_{mag} > F_{int}$ and leading to the extraction of the magnetic beads cluster; ii) a droplet disengagement regime ($F_{mag} < F_{int}$), in which no extraction happens and the bead cluster is carried away in the initial droplet (full circles).

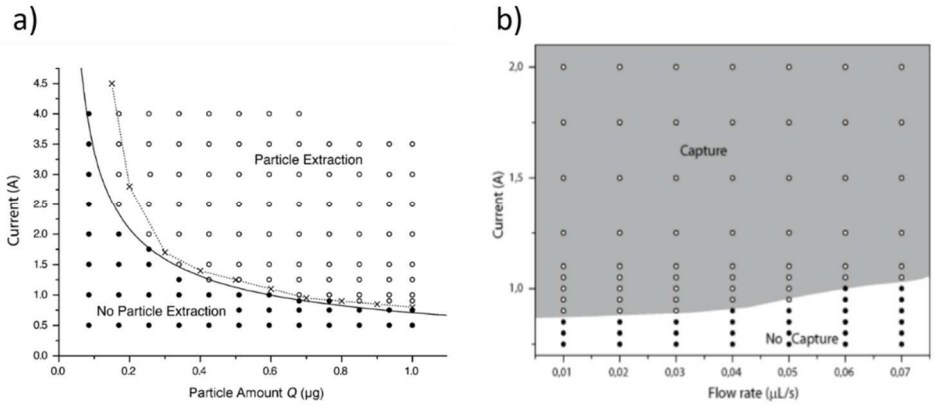

Figure 2: Phase diagrams of the extraction conditions for different electric current values in the coil as a function of (a) the particle load and (b) the flow-rate[1]. *In both graphs, the conditions for beads extraction and no extraction are represented by open and full circles, respectively. In (a), crosses are numerical predictions for the transition threshold while solid line is a best fit to $Q^{-2/3}$. In (b) the study is performed for 100nL droplet and a fixed particle load of 1 µg, for droplet flow-rates ranging between 0.01 and 0.07 µl/s[1].*

They also reported a further phase diagram to study the effect of the droplet flow-rate on the bead extraction domain. As presented in Fig. 2b, the droplet velocity does not strongly influence the capture regime in the investigated range (between 0.01 and 0.07 µl/s). However, for relatively high droplet flow-rates, a

slight increase in the critical current is required to maintain beads extraction. In fact, in the droplet extraction frame above described, leading to the extraction condition $F_{mag} > F_{int}$, the effect of the oil viscous drag force was not took into account.

Although this effect is negligible in the range of flow-rates considered, some comments must be done in the limit case of higher droplet flow-rates, in which the time for the formation of an aggregate is comparable to the residence time that the droplet spends in the neighborhood of the magnetic tip, characterized by a strong and local magnetic force. The droplet flow-rate will define an upper time limit for the magnetic beads to reach their aggregate state while crossing the capture region, thus influence the extraction performance of the device. In particular, a partial extraction of magnetic particles or even a failure in magnetic trapping can be experienced.

Finally, the effect of the viscosity of the aqueous phase was neglected as at this stage only aqueous buffers will be considered. However, it is worth noting that the viscous force can prevent the complete extraction of the magnetic particles induced by the magnetic field as it may slow down or impede the formation of the compact cluster towards the magnetic trap.

2 Applications

Our magnetic tweezers technology is the core element of a droplet microfluidic platform that has been applied to the analysis of different types of biomarkers. During my PhD I contributed to two of them; the first one was reported by *Ferraro et al., 2016* (Annex 1) and deals with nucleic acids analysis. The second application was presented by *Mai et al., 2017* (Annex 2); in this case the

magnetic tweezer technology was used for peptides analysis. Both application will be further described in the following paragraphs. Of note, I did not personally drive both projects but I mainly contributed to them by developing all the aspects of the platform related to its automation. In particular, I conceived and installed a dedicated hardware to allow automated device operations and interfaced and controlled the different units by a LabVIEW code. The implemented script is based on an image-recognition process, analyzing in real-time the images captured by a camera, in correspondence of the magnetic tweezers tip and recognizing both the arrival of a droplet and the presence of magnetic beads in it. Based on these two image-recognition paths the control of the magnetic tweezers operations during the extraction of magnetic beads from a droplet and their redispersion in a different one can thus be achieved. Interestingly, the software allows high robustness and flexibility, and can be easily reconfigured according to the number, order and type of operations to be implemented in the platform. Furthermore, for the protein analysis project, I also extended the platform automation to the detection module, developing a LabVIEW program able to monitor the real-time fluorescence signal of a droplet, recorded by a home-made detection unit, and to perform signal processing operations in order to finally recognize the maximum intensity signal for each single droplet. This software represents a simple-read out for the platform and reduces the data post-processing time and the user intervention.

2.1 Nucleic acids analysis

Analyses of nucleic acids are routinely performed in hospital laboratories to detect gene alterations for cancer diagnosis and treatment decision. Among the different possible investigations, mRNA analysis provides information on abnormal levels of genes expression. However, the development of precision medicine, together with the multiplication of targeted therapies and associated biomarkers, demands nowadays for important improvements in the genetic analysis methods, allowing increased multiplexing and the implementation of more complex decision trees, without affecting the cost and the robustness of the assay. Furthermore, important efforts aim to develop minimally invasive approaches for diagnosis, thus leading to a reduction of the typical clinical samples.

In this framework, droplet microfluidics can represent a promising technique to fulfill the request for low-input volume and high throughput and multiplexing assays, associated with "precision medicine". In particular, our team presented a droplet microfluidic platform allowing a reliable clinical analysis of tumour tissue and drastically decreasing the contamination risk, representing the main limitation of standard protocol in diagnostic laboratories.

This fully automated system includes an mRNA purification step from a sample of total RNA, followed by reverse transcription (RT) and quantitative Polymerase Chain Reaction (qPCR). The developed protocol aims at the determination of the gene expression in cancer patients and focuses, in this work, on the Her2 (human epidermal growth factor receptor 2) gene, a major biomarker for breast cancer diagnosis. Importantly,

patients with Her2 overexpression are eligibile for target therapy that can improve their overall survival but may be deleterious for other patients. The platform was clinically validated with a cohort of 21 breast cancer samples and the obtained results were blindly compared with the established routine analysis used in the hospital.

2.1.1 Platform layout and operations

The developed platform includes three main components: a droplet generation and flow control system, a magnetic beads handling section and a thermal module (Fig.3). In this paragraph, the peculiarities and the functionalities of each of these units will be described in details.

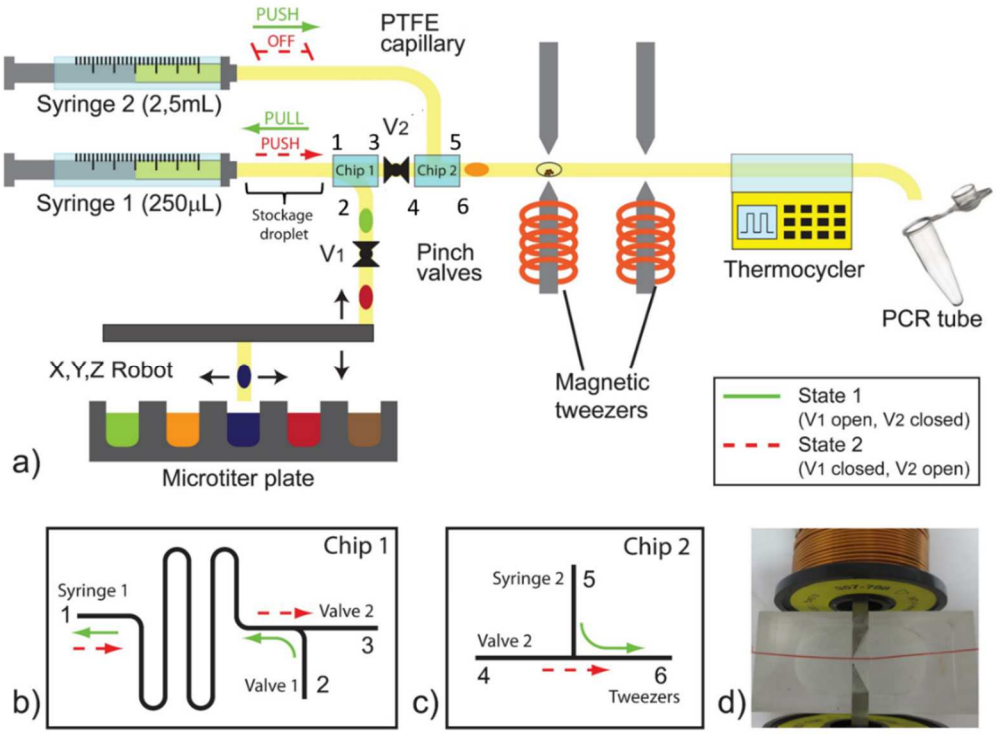

Figure 3: Scheme of the developed droplet microfluidic platform for nucleic acids analysis. *(a) The platform is composed of three main parts: the droplet generation module, the magnetic tweezers and the thermocycler. The droplet generation module combines a microtiter plate placed under an arm-robot, two syringes, two pinch-valves and two PDMS*

chips (b-c). At first, samples and reagents solutions are prepared in the microtiter plate. Syringe pump and pinch valves (V1 and V2) are software controlled thus making the system completely automated. The system continuously and alternatively switches between states 1 and 2, represented by green continuous line and red dashed line, respectively. During state 1, V1 is open, V2 is closed and a generated train of droplets, passing through V1 is stored in the serpentine of the PDMS chip 1. At the same time, syringe 2 pushes oil in the rest of the microfluidic circuit. Then, the system switches to state 2 (V1 closed and V2 open): syringe 2 is OFF and syringe 1 pushes the generated train of droplets beyond V2 and the PDMS chip 2. Finally, state 1 is reactivated for the next train. In this way, the system can work continuously: while a precision syringe is generating the droplet train, an high volume one is driving the previously generated sequences through the next modules of the platform. After their generation, droplets reach the magnetic tweezers composed by paramagnetic tips, adjacent to a microchannel (colored in red) and activated by magnetic coils (d). After the magnetic beads handling, the droplets are driven to the adapted thermocycler for the Reverse Transcription and are finally collected in standard PCR tubes to perform the final step in a conventional qPCR machine.

Droplet generation and flow control units

The platform front-end is represented by the droplet generation system: a motorized arm, coupled with a syringe pump equipped with a high-precision syringe, controls the position of a pipetting capillary on a standard microtiter plate (MTP) and allows the programmable sampling of desired volume of samples and reagents. The generated droplets (250nL in volume) are highly confined in the capillary and the pipetting of an aqueous solution is followed by the one of a fluorinated oil plug so that the generated droplets are kept equally spaced by oil, reducing the inter-droplet contamination risk. Differently from other droplet microfluidic platforms, for example the one dedicated to "digital PCR"[9] where all the droplets are pooled together in a chamber, here the generated droplet sequence keeps its initial order and spacing, and the

content of each single droplet can be thus univocally identified by the corresponding position in the sequence, without need for internal tag. Furthermore, the solutions in the MTP are protected by a layer of light mineral oil. Due to its density (0.838 g/mL at 25 °C) being lower than water (about 1 g/mL at 25 °C) and fluorinated FC-40 oil (1.855 g/mL at 25 °C), mineral oil stays on top of the samples and reagents solutions during the pipetting step, preventing evaporation problems[8] and insulating the RNA samples by reducing the risk of contamination and degradation by RNAases from the external environment.

The flow control of the platform is designed to generate a train of droplets while the previously generated trains are processed in the rest of the platform at a constant speed, controlled by an additional high-volume syringe pump. Fig.3 shows a schematic description of the platform and of the connection used for continuous droplet generation and processing operations. Interestingly, two PDMS device connectors (Fig.3b-c), operating as switching and storage junction, coupled with two pinch valves allow the creation of two independent fluidic circuits, alternatively activated so that the generation of a train of droplets is performed while the previous generated sequence is pushed in the rest of the platform.

Magnetic beads handling and thermal modules

Leaving the generation branch, the droplets are transported through a PTFE capillary in a continuous flow of oil to reach the magnetic beads handling. This module represents the core of the platform and it is composed of two magnetic tweezers. For the implementation of the mRNA extraction and purification

protocol, the composition of the droplet sequence and the performed operations are illustrated in Fig.4. The first droplet contains oligo-dT functionalized magnetic beads suspended in their storage buffer (Fig. 4b). Acting on the first magnetic tweezer (Fig.4c), the magnetic particles are extracted and released in a second droplet containing the total RNA sample (Fig.4d). Due to the beads functionalization, the mRNA hybridizes on the magnetic beads surface (Fig.4e) and, after 5 minutes incubation, a second magnetic tweezers is used to capture beads, allowing thus the extraction of mRNA captured on the surface of the beads. The extracted cluster is kept immobile in proximity of the tweezers' tip and it is then rinsed by a washing buffer droplet to remove contaminants and other interfering compounds (Fig.4f). The mRNA is finally redispersed in the droplet containing the RT-qPCR mix (Fig.4g).

In a typical run, 45 trains of droplets were continuously generated and processed, allowing the analysis in triplicate of two genes of interest from 7 total RNA samples and with three negative controls. Interestingly, the magnetic tweezers operations described above are fully automated and controlled by a dedicated National Instrument LabVIEW code, synchronizing the magnetic field actuation with the droplet passage. Furthermore, the programmability of the droplet generation system allows the production of sequential trains of droplets having customized composition thus allowing the screening of multiple samples and genes combinations.

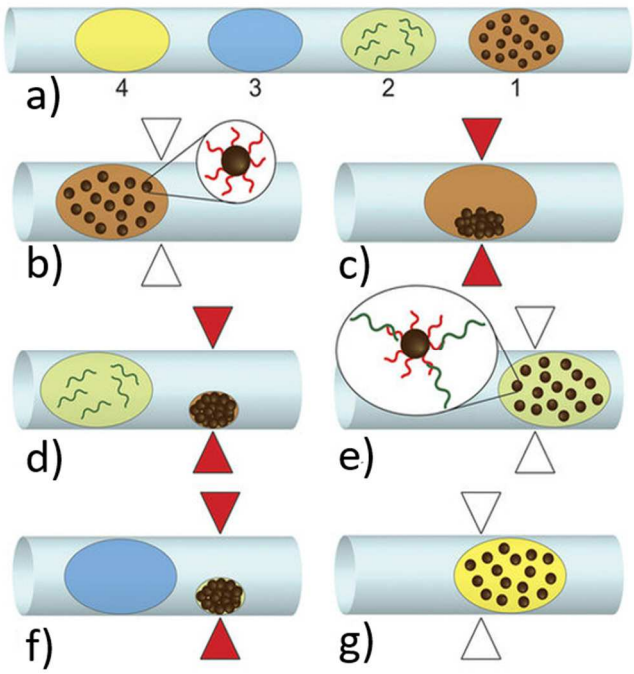

Figure 4: *(a) Scheme of the typical composition of the droplet sequence (droplet train) for the RT-qPCR assay: 1) oligo-dT functionalized magnetic beads, 2) Total RNA sample, 3) washing buffer and 4) RT-PCR enzyme mix. (b-g) Workflow of beads and droplet manipulation during the protocol: the functionalized magnetic beads dispersed in an aqueous droplet flowing in a channel (b) are transferred (c) to the one containing the Total RNA sample (d). During 5minutes incubation, the mRNA hybridizes on the bead surfaces (e). The m RNA-bound magnetic beads are then captured and kept immobile in proximity of the tweezers tip during the passage of the rinsing droplet (f) and they are finally released in the RT-PCR mix droplet (g). The ON state of the tweezers is represented by red triangles.*

In the next step, the droplets containing the purified mRNA, mixed with reverse transcriptase, polymerase and primers, flow in a temperature-controlled module kept at 50°C for 5 minutes. In this way, the synthesis (Reverse-transcription) of the complementary DNA (cDNA) from the RNA template can be performed directly in droplets. This operation was implemented with a commercial thermocycler equipped with a flat plate for glass slides. In particular, on top of the thermocycler, an aluminum part is placed, including a groove in which the PTFE capillary is installed. The generated cDNA strands contained in the droplets are used as a template for the following PCR process. At this stage of the project, these droplets are collected in standard PCR tubes, pre-loaded with

TaqMan probe mix, and the qPCR is performed in a conventional instrument (SmartCycler, by Cepheid).

2.1.2 Platform validation

Calibration curves with cell lines for Her2 and TBP genes

In general, during a qPCR run, the evolution in the amount of a target sequence or gene is monitored as a function of the thermal cycles, by measuring the increase of a fluorescent signal during amplification. In a typical curve resulting from this reaction, the threshold cycle (Ct) is the cycle number at which the fluorescent signal generated by the reaction rises above the background baseline. Interestingly, the Ct is inversely proportional to the original relative expression level of the gene of interest, i.e. lower Cts indicate higher gene expression levels than high Ct values. The platform was first validated considering two genes of interest: HER2, a major biomarker for breast cancer[10], and TBP (TATA-binding protein), a "house-keeping" gene, having a low variability in its expression in breast cancer cells, thus usually chosen in clinics as a reference to validate the RNA sample quality. The first evaluation of the platform performances was performed with sample of RNA extracted from different cell lines. The total RNA sample was extracted from two human breast cancer cell lines: MCF7, presenting a normal expression level of Her2, and SKBR3, which has an overexpression of this gene.

Calibration curves were performed for TBP and Her2 genes using total RNA quantities ranging from 1.5 ng/drop to 15 pg/drop. It is worth noting that the smallest concentration of total RNA used in this series is comparable with the

total RNA content of a single cell (about 20pg). The results obtained for MCF7 and SKBR3 cell lines are reported in Fig. 5a,b. Each curve is the average of a triplicate of the same experiment repeated three times, starting from the same MTP. The vertical error bars are given by the standard deviation of the triplicate (CV<1%) while the horizontal bars for the RNA/droplet concentrations are evaluated by the error propagation on the droplet volume. Calibration curves present a linear tendency in the investigated range ($R^2 > 0.96$). As expected, the level of TBP gene expression does not differ significantly between the two cell lines. On the contrary, Her2 gene in the MCF7 and SKBR3 cell lines present a normal (Her2-) and overexpressed (Her2+) status, as can be noticed by the difference (about 5 units) in the expression level (Ct values). In addition, the curves were found parallel and the PCR efficiencies (*Eff*), derived as the curve's slopes, are found between 97 and 99%. These experiments also confirm the absence of cross-contaminations between droplets: although all the train of droplets flow consequently in the same capillary and contain initial RNA concentrations ranging over two order of magnitude, no divergence from the linear behavior is found.

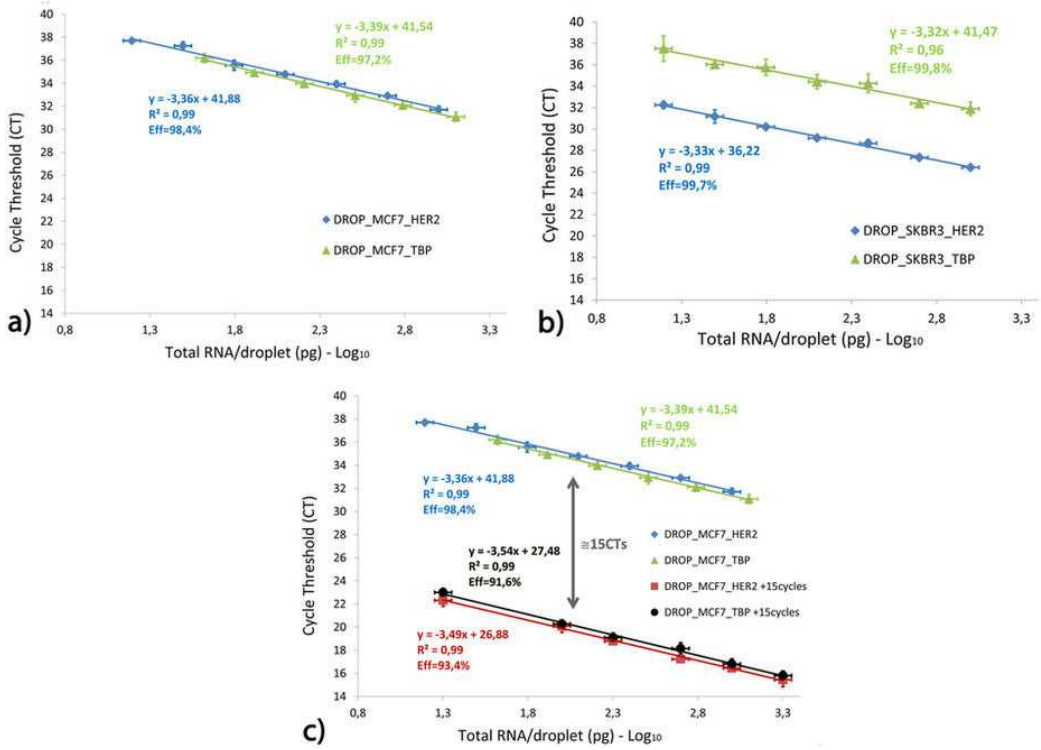

Figure 5: Calibration curves *performed with Total RNA extracted from (a) MCF7 and (b) SKBR3 cell lines for two genes: HER2, a major biomarker in breast cancer (in blue), and TBP, a "housekeeping" gene (in green). The obtained Cycle Threshold (Ct) are plotted in Logarithmic scale as a function of the Total RNA concentration. The efficiency Eff of the qPCR amplification process is indicated for each curve below the fit parameters and it is extracted from the slope of the linear fit. (c) Comparison between the calibration curves for Total RNA extracted from MCF7 cell line with (red and black points and fit) and without (blue and green points and fits) 15 PCR pre-amplification cycles. As expected, the pre-amplification cycles result in a shift of about 15Cts between the two curves. Error bars are not visible when they are smaller than the data point.*

Additional experiments were performed to evaluate the possibility to perform inline mRNA purification, reverse transcription and DNA amplification completely in droplets. Here, after the extraction of the mRNA from the Total RNA sample of MCF7 cells and the RT, the droplet trains are arrested in the thermal module and were subjected to 15 PCR cycles. The droplets were then

transferred to a conventional qPCR machine for a typical analysis run. This hybrid method, including two steps of thermal cycling (in droplet and in the machine) was chosen to guarantee a more reliable comparison and quantitative validation. The final readout using the qPCR machine allowed a comparison (with and without pre-amplification cycles) independent from the apparatus and the sensitivity of the detection. The results shown in Fig. 5c present the two calibration curves obtained with and without the pre-amplification cycles. The two curves have similar slopes and, within the experimental error, an effective shift by 15 Cts identifies the addition of 15 pre-amplification cycles to the protocol with respect to the case in which no pre-amplification is performed. These results allow us to conclude that, compared to the routine qPCR analysis in the machine, the in-droplet thermal cycling do not cause loss or degradation problem for enzymes and/or DNA fragment and it does not interfere with the performance of the qPCR process.

In conclusion, these proof-of-concept experiments demonstrated the possibility to perform inline mRNA extraction and purification, followed by RT-qPCR in the same platform and in highly confined droplets without cross-contamination problems, loss of reproducibility, quality and performances.

Clinical validation with breast cancer samples

Finally we demonstrated the potential of our approach for diagnosis application. The platform was validated using 21 total RNA samples extracted from percutaneous biopsies of breast cancer patients of Saint-Louis Hospital (Paris). This represents a quite large population with respect to other works in the same

domain presenting a validation with only few patient samples, or limiting their validation to the use of spiked standards. All the samples were analyzed in a blind protocol and in parallel by classical RT-qPCR at the hospital (the workflow used daily in the diagnosis department of Saint Louis Hospital) and by the droplet microfluidic platform, coupled to a commercial thermocycler, as described before for the cell lines. The used Total RNA sample quantity was 20ng per test at the hospital and 250pg per test for the microfluidic platform. In both cases, the $2^{-\Delta\Delta Ct}$ method[11,12] was used as a relative quantification strategy for RT-qPCR data analysis. This method is based on the normalization of the expression level of a gene of clinical interest (HER2) with respect to two references: i) a gene having stable expression between individuals (TBP in our case); and ii) a sample not presenting a HER overexpression status (MCF7 cell lines for the droplet platform and a pre-defined set of samples for the hospital protocol). This procedure allows the reduction of the experimentally induced variations in gene expression, like RNA or DNA integrity and purity and/or differences in amplification between the two genes. The result of the normalization procedure, called Fold difference *Fd*, quantifies the difference in expression level between a patient sample and a control sample. The *Fd* threshold value separating a "normal" to an "overexpressed" state depends on the experimental procedure and has to be defined for a given platform on a heuristic way. As an example, in the diagnostic laboratory at the Saint-Louis Hospital, the *Fd* cut-off ratio was determined on a tumor training set using univariate partition method (XLSTAT software) and by correlation with Her2 expression level results obtained by ImmunoHistoChemistry (IHC). This procedure yields to a condition daily used in the hospital for the identification

of an overexpressed status for the sample, i.e., $Fd > 7$[13,14]. As discusses above, the relative nature of the Fd definition could led to a difference in the results obtained for the same sample by different platform protocols and, especially, references. In our case, the Fd values obtained in the droplet microfluidic platform were systematically higher than the one obtained at the hospital. Due to this intrinsic discrepancy, the Fd values obtained at the hospital and in our droplet platform were compared by correlation analysis, as previously proposed[11]. The two data sets show a good correlation, with a Pearson Correlation Coefficient of 0.84. Furthermore, they were plotted on a correlation graph (Fig. 6) and, interestingly, they show identical segregation of patients presenting a Her2 positive (black circles) and Her2 negative (red squares) expression. The proper identification of the two populations of normal and overexpressed Her2 tumors validates the correct characterization of the 21 patient samples by the microfluidic platform in the blind test.

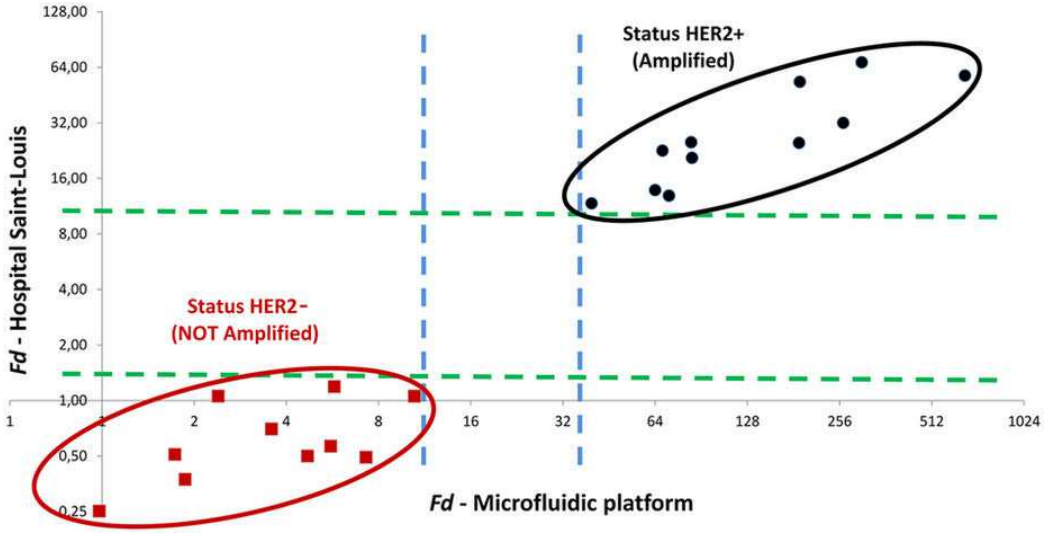

Figure 6: Correlation graph in Logarithmic scale (base 2) of the Fold difference (Fd) obtained by the Saint Louis Hospital versus the one obtained by the droplet microfluidic platform. *Samples disclosed a posteriori as presenting an HER2+ status are plotted in black while the HER2- ones in red. The dashed line represents a visual help to identify the excluded zone between the two sample populations: green for the hospital (1.5-11.71) and blue for the droplet platform (10.48-39.67).*

In conclusion, in this project a relevant clinical validation was presented for the first time in a continuous droplet microfluidic architecture, showing thus the high maturity of this platform platform and its potentialities for the implementation of further clinical assays.

2.2 Single-step ELISA immunoassay

After demonstrating the potential of our approach for nucleic acid analysis, we have been interested in the application of the magnetic tweezers technology in peptides analysis. In collaboration with the PNAS group at Université Paris Sud, we have recently developed a magnetic beads-based immunoassay for

the detection of the two well-established amyloid-β peptide biomarkers (*i.e.* monomeric Aβ 1-42 and Aβ 1-40) for Alzheimer's disease (AD) diagnosis[15,16].

For diagnosis of Alzheimer's disease (AD), the 42-amino acid long amyloid β (Aβ 1-42) peptide in cerebrospinal fluid (CSF) has been used as an established biomarker as the level of Aβ 1-42 peptide is decreased in the CSF of AD patients[17]. To improve the differential diagnostic power between AD and healthy subjects or to discriminate better AD from other neurodegenerative diseases, several research teams have proposed the use of Aβ 1-42 / Aβ 1-40 ratios[18,19] or other combinations of various Aβ isoforms[20,21]. Among the methods for tracing Aβ peptides in CSF, immunoassays, notably enzyme-linked immunosorbent assay (ELISA)[22], single molecule array (SiMoA)[23,24] and multi-analyte profiling assay (Luminex xMAP)[25,26] have been up to now the most practiced ones in clinical routine. Some considerations (if not drawbacks) should be nevertheless considered. While state of the art and costly ELISA instruments have been introduced for automated and/or routine analyses, conventional ELISA is still widely practised, especially outside the hospital context. The fact that several operations (analyte immunocapture, washing in-between steps, binding of detection antibodies and enzymatic detection) are required can lead to error accumulation. Furthermore, several dozen µL of sample are required for each analysis, which renders the detection of many analytes from the same biological sample not possible if only a limited sample volume (few µL for example) is available. In this context, miniaturization of the laborious conventional batch-based sandwich assays into microfluidic

platforms is of significant interest for the development of point-of-care (POC) devices and to increase the quality and accuracy of ELISA methods. For this purpose, we developed a novel magnetic bead-based immunoassay in which the capture antibodies grafted onto magnetic beads and the detection antibodies can simultaneously bind to monomeric β peptides in a single step (Fig.7). This method was employed for detection of Aβ 1-40 and Aβ 1-42 in CSF samples, which can be expanded for detection of established and potential Aβ-based biomarkers for early diagnosis of AD. This assay was validated with an artificial cerebrospinal fluid (CSF) sample from one healthy person and one AD patient. Then, the batch wise protocol was downscaled in a droplet microfluidic format exploiting the magnetic tweezers technology.

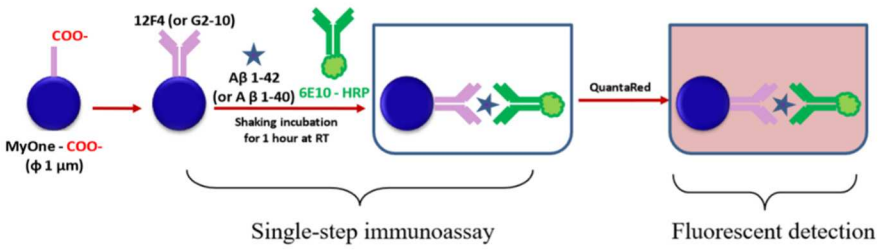

Figure 7: Protocol of magnetic-beads based immunoassays of Aβ 1-40 and Aβ 1-42 in batch mode.

2.2.1 Platform layout

An overview of the platform optimized for this protocol is sketched in Fig. 8b. The versatility and ease in reprogrammability of the droplet generation unit described in the previous paragraph makes it a convenient element for the

production of a deterministic sequence of droplets (train) devoted to any specific protocol.

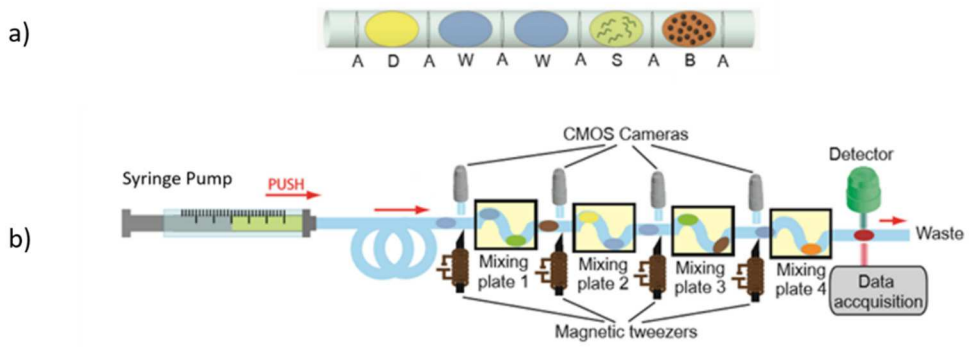

Figure 8: Developed setup for the implementation of the single-step ELISA assay for amyloid beta detection. *(a) Composition of the droplet sequence used in the ELISA immunoassay: magnetic beads droplet (B), sample droplet (S), washing buffer (W), detection droplet (D) and air bubbles (A). The droplets are emulsified in oil and they are highly confined in the channel. (b) Schematic drawing of the magnetic beads handling and detection units. A droplet generation module is used for droplet production, as previously described for nucleic acids assays. Droplet are then processed by a series of 4 magnetic tweezers, separated by mixing plates. A detection unit is added as platform read out to monitor the fluorescent signal directly in droplets continuously flowing in the microchannel.*

In particular, for the presented single-step ELISA immunoassay, each train is composed by five droplets (200nL each) with the following content (Fig.8a): i) antibodies-bound magnetic beads dispersed in a buffer solution (PBS 1x / 0.1% BSA / 0.1% Tween-20), ii) sample solution, iii-iv) washing solution (PBS 1x / 0.1% BSA / 0.1% Tween-20) and v) detection solution (chemifluorescent horseradish peroxidase substrate). In order to prevent any droplet merging during their transport along the platform, an air bubble (50nL) is inserted as a spacer between two aqueous droplets. In a trial, a series of 8 trains were

manipulated in the platform at a flow rate of about 0.13 µL/s. The train of droplets are then delivered to the magnetic-beads handling unit, including 4 pairs of magnetic tweezers. Controlling the on/off triggering of the tweezers, the beads can be trapped out of one droplet and released into a different one. In this way, the magnetic particles were transferred to the sample droplet (for single step immunoassay), then to the two washing droplets, and finally into the detection droplet containing the enzymatic substrate.

Furthermore, in order to perform this single-step beads-based immunoassay in a droplet microfluidic format, new features were implemented compared to the previously described platform for nucleic acid analysis (Fig.8b). The first element introduced in the platform is the mixing plate. This plate is a metallic holder characterized by a winding-shaped groove[15], serving as a holder for the PTFE capillary where droplets flow. Four mixing plates were inserted between magnetic tweezers to assist beads recirculation and to achieve an efficient mixing inside the droplet. Note that the absence of this component causes a sedimentation of magnetic particles in the bottom rear of the flowing droplet, leading to mediocre performances of immunoassay and beads washing.

Another interesting element integrated in this platform is a detection unit, placed downstream of the magnetic handling system. This platform read out allows the monitoring of the fluorescent signals from the detection droplets continuously flowing in the capillary. This low-cost detector is assembled by 3D printed parts and it is composed by an excitation light generated by a green LED (at 530nm), a silicon photodiode reading the emitted signal (at 570nm) and a system of basic optical elements (filters, mirrors, lenses), properly configured. The detected signal is processed at the pre-defined LED emitter

frequency (10kHz) by a custom-made lock-in amplifier, allowing a significant increase in the signal/noise ratio. Fluorescent readings were recorded with a data acquisition unit and a home-made LabVIEW software. This detection module simplifies the detection protocol: the data are real-time displayed and saved on a computer and the user intervention is limited to the collection of the data file to perform data analysis. This system is, thus, easy-to-use and strongly adapted to non-expert users, especially if compared with the less straightforward previous version[1] where fluorescence measurements were performed with a conventional epifluorescence microscope, equipped with a translation stage and a camera, and a further image processing step was required to obtain the final results.

2.2.2 Performances

Downscaling the batch wise protocol in a droplet microfluidic format allows a significant reduction (about 25x) in the volume required for each operation and consequently brings an important decrease in the samples and reagents consumption. Furthermore, a remarkable improvement in the operational time and analysis throughput was achieved: 8 samples were processed by the platform in less than one hour, instead of 2 hours per assay in batch mode. Fluorescent signals detected for different concentrations of Aβ 1-40 and Aβ 1-42 in droplets are reported in Fig. 9a and 9b, respectively. A very good linearity was achieved for both peptides (coefficient of determination $r^2 > 0.99$) and the limits of detection were found in the order of 0.5 – 1 nM, which is close to the detection limit needed for Aβ peptides, especially Aβ 1-42, in CSF samples. Furthermore, the sequential determination of Aβ 1-40 and Aβ 1-42 (2 nM each)

spiked in a CSF sample was investigated. In particular, two consecutive trains of droplet were generated, containing the same sample but differently functionalized magnetic beads, to achieve specific capture of Aβ 1-40 and Aβ 1-42, respectively. Fig. 9c reports the results obtained in duplicate for each peptide. A signal increase can be clearly observed between blank artificial CSF and samples spiked with Aβ peptides.

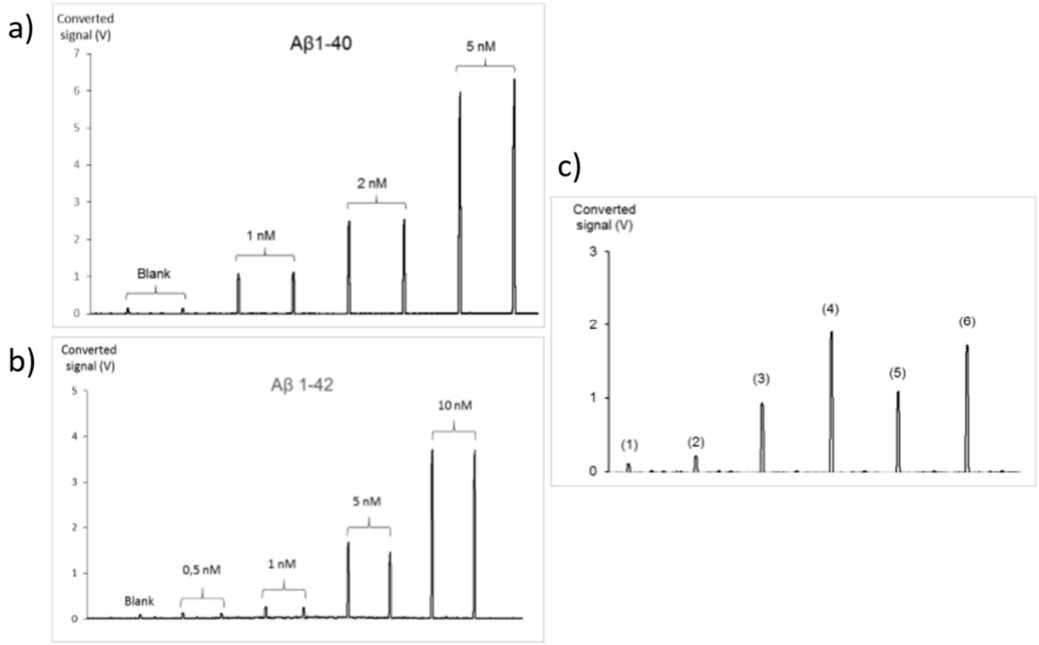

Figure 9: Fluorescent signal measured by the LED-based *detector for different concentrations of (a) Aβ 1-40 and (b) Aβ 1-42. (c)Fluorescent signals for sequential determination of a 2nM concentration of Aβ 1-40 (3-5) and Aβ 1-42 (4-6) spiked in an artificial CSF sample. (1) and (2) refers to a blank droplet (artificial CSF).*

Finally, this work represented the first droplet-based implementation of a single-step immunoassay protocol for monomeric Aβ peptides detection, showing interesting reduction in sample and reagent consumption and in processing time.

3 Critical overview

The magnetic tweezers technology discussed in this chapter provides the field of continuous droplet microfluidics with the possibility to perform the extraction of functionalized magnetic beads from a droplet and their redispersion in a different one, while they are continuously flowing in a microchannel. Interestingly, the versatility of this concept allows the droplet-based implementation of any protocol involving capture, washing and redispersion with extraction and purification efficiencies comparable or even superior to the one of macroscale protocols but with an important reduction in the sample and reagents volume needed. Another positive feature is the reduction of risks of human errors or contaminations, thanks to the fact that all the operations are fully-automated and performed under oil all-along the protocol. An additional value for this technology is the interfacing with a pipettor arm to generate sample and reagents droplets from a standard MTP. In fact this bring a lot of flexibility to the system due to the possibility to customize the order and content of droplets, thus to program different protocols into successive trains. As demonstrated for nucleic acids assays, any combination of sample versus mixes can be implemented allowing, for example, to screen the expression level of the same gene for several patient samples or to perform multi-biomarkers analysis on the same sample.

However, despite the fact that all the operations are performed in a PTFE capillary having sub millimetric size, the magnetic coil and the tip are in the order of tens of centimeters, thus limiting the portability of the system as well as the size of the droplet.

Furthermore, the system as existing is still limited in terms of flow-rate as its dynamic range is 0.01µL/s-0.13µL/s. Although, differently from other continuous microfluidic devices, the magnetic tweezers present the exclusive feature to perform a complete extraction and redispersion sequence, the typical droplet processing velocity in the system is about 1.8mm/s, ten times lower than other continuous droplet microfluidic systems, like the splitting fork of Brouzes et al.[27]. However, as discussed above, for a fixed value of magnetic force, the extraction performances depends on the velocity of the droplet flowing in the channel. Indeed, beyond a threshold value in droplet flow-rates, the time for the particle aggregation in a cluster becomes comparable to the one spent by the droplet in the neighborhood of the magnetic tweezers tip. As previously discussed, this will affect the extraction efficiency rate of the device and will define a range of optimal velocities to achieve capture efficiencies comparable with those of macroscopic protocols. Different strategies can be proposed to broaden this range, which are basically based on an increase of the magnetic force controlling the particle aggregation and their extraction from the droplet. Keeping the same geometry, a possible but impracticable (or, at least, non-convenient) way to improve this limit is to increase the current applied to the tweezers or increment the number of coils. Differently, a more elegant solution is represented by the miniaturization of this droplet microfluidic concept. Sharper magnetic field gradient can indeed be reached at the microscale, in parallel a gain in portability and parallelization can be achieved.

References

1 A. Ali-Cherif, S. Begolo, S. Descroix, J.-L. Viovy and L. Malaquin, *Angew. Chemie Int. Ed.*, 2012, **51**, 10765–10769.

2 D. Ferraro, Y. Lin, B. Teste, D. Talbot, L. Malaquin, S. Descroix and A. Abou-Hassan, *Chem. Commun.*, 2015, **51**, 16904–16907.

3 B. Teste, A. Ali-Cherif, J. L. Viovy and L. Malaquin, *Lab Chip*, 2013, **13**,2344–9.

4 B. Teste, J. Champ, A. Londono-Vallejo, S. Descroix, L. Malaquin, J.-L. Viovy, I. Draskovic and G. Mottet, *Lab Chip*, 2017, **17**, 530–537.

5 D. Ferraro, J. Champ, B. Teste, M. Serra, L. Malaquin, J.-L. Viovy, P. de Cremoux and S. Descroix, *Sci. Rep.*, 2016, **6**, 25540.

6 T. D. Mai, D. Ferraro, N. Aboud, R. Renault, M. Serra, N. T. Tran, J.-L. Viovy, C. Smadja, S. Descroix and M. Taverna, *Sensors Actuators B Chem.*, 2018, **255**, 2126–2135.

7 J.-C. Baret, *Lab Chip*, 2012, **12**, 422–33.

8 M. Morita, M. Matsumoto, S. Usui, T. Abe, N. Denkov, O. Velev and I. B. Ivanov, *Colloids and Surfaces*, 1992, **67**, 81–93.

9 D. Pekin, Y. Skhiri, J.-C. Baret, D. Le Corre, L. Mazutis, C. Ben Salem, F. Millot, A. El Harrak, J. B. Hutchison, J. W. Larson, D. R. Link, P. Laurent-Puig, A. D. Griffiths and V. Taly, *Lab Chip*, 2011, **11**, 2156.

10 A. C. Wolff, M. E. H. Hammond, D. G. Hicks, M. Dowsett, L. M. McShane, K. H. Allison, D. C. Allred, J. M. S. Bartlett, M. Bilous, P. Fitzgibbons, W. Hanna, R. B. Jenkins, P. B. Mangu, S. Paik, E. A. Perez, M. F. Press, P. A. Spears, G. H. Vance, G. Viale, D. F. Hayes, American Society of Clinical Oncology and College of American Pathologists, *J. Clin. Oncol.*, 2013, **31**, 3997–4013.

11 T. Yuen, E. Wurmbach, R. L. Pfeffer, B. J. Ebersole and S. C. Sealfon, *Nucleic Acids Res.*, 2002, **30**, e48.

12 K. J. Livak and T. D. Schmittgen, *Methods*, 2001, **25**, 402–408.

13 J. Jacquemier, F. Spyratos, B. Esterni, M.-J. Mozziconacci, M. Antoine, L. Arnould, S. Lizard, P. Bertheau, J. Lehmann-Che, C. B. Fournier, S. Krieger, F. Bibeau, P.-J. Lamy, M. P. Chenard, M. Legrain, J.-M. Guinebretière, D. Loussouarn, G. MacGrogan, I. Hostein, M. C. Mathieu, L. Lacroix, A. Valent, Y. M. Robin, F. Revillion, M. L. Triki, A. Seaume, A. V. Salomon, P. de Cremoux, G. Portefaix, L. Xerri, S. Vacher, I. Bièche and F. Penault-Llorca, *BMC Cancer*, 2013, **13**, 351.

14 J. Lehmann-Che, F. Amira-Bouhidel, E. Turpin, M. Antoine, H. Soliman, L. Legres, C. Bocquet, R. Bernoud, E. Flandre, M. Varna, A. de Roquancourt, L.-F. Plassa, S. Giacchetti, M. Espié, C. de Bazelaire, L. Cahen-Doidy, E. Bourstyn, A. Janin, H. de Thé and P. Bertheau, *Br. J. Cancer*, 2011, **104**, 1739–46.

15 M. R. Bringer, C. J. Gerdts, H. Song, J. D. Tice and R. F. Ismagilov, *Philos. Trans. A. Math. Phys. Eng. Sci.*, 2004, **362**, 1087–104.

16 N. R. Graff-Radford, J. E. Crook, J. Lucas, B. F. Boeve, D. S. Knopman, R. J. Ivnik, G. E. Smith, L. H. Younkin, R. C. Petersen and S. G. Younkin, *Arch. Neurol.*, 2007, **64**, 354.

17 C. Humpel, *Trends Biotechnol.*, 2011, **29**, 26–32.

18 K. Blennow and H. Hampel, *Lancet. Neurol.*, 2003, **2**, 605–13.

19 N. R. Graff-Radford, J. E. Crook, J. Lucas, B. F. Boeve, D. S. Knopman, R. J. Ivnik, G. E. Smith, L. H. Younkin, R. C. Petersen and S. G. Younkin, *Arch. Neurol.*, 2007, **64**, 354.

20 U. Haußmann, O. Jahn, P. Linning, C. Janßen, T. Liepold, E. Portelius, H. Zetterberg, C. Bauer, J. Schuchhardt, H.-J. Knölker, H. Klafki and J. Wiltfang, *Anal. Chem.*, 2013, **85**, 8142–8149.

21 M. Bibl, M. Gallus, V. Welge, H. Esselmann, S. Wolf, E. Rüther and J. Wiltfang, *J. Neural Transm.*, 2012, **119**, 805–813.

22 D. R. Lachno, B. A. Evert, K. Maloney, B. A. Willis, J. A. Talbot, M. Vandijck and R. A. Dean, *J. Alzheimers. Dis.*, 2015, **45**, 527–42.

23 L. Song, D. R. Lachno, D. Hanlon, A. Shepro, A. Jeromin, D. Gemani, J. A. Talbot, M. M. Racke, J. L. Dage and R. A. Dean, *Alzheimers. Res. Ther.*, 2016, **8**, 58.

24 S. Janelidze, E. Stomrud, S. Palmqvist, H. Zetterberg, D. van Westen, A. Jeromin, L. Song, D. Hanlon, C. A. Tan Hehir, D. Baker, K. Blennow and O. Hansson, *Sci. Rep.*, 2016, **6**, 26801.

25 A. Olsson, H. Vanderstichele, N. Andreasen, G. De Meyer, A. Wallin, B. Holmberg, L. Rosengren, E. Vanmechelen and K. Blennow, *Clin. Chem.*, 2005, **51**, 336–345.

26 J.-H. Kang, H. Vanderstichele, J. Q. Trojanowski and L. M. Shaw, *Methods*, 2012, **56**, 484–493.

27 E. Brouzes, T. Kruse, R. Kimmerling and H. H. Strey, *Lab Chip*, 2015, **15**, 908–919.

Chapter 3

An innovative approach for magnetic solid supports handling

In the previous sections, we discussed about the importance and interest for the manipulation of solid-state supports in droplet microfluidics. We focused, in particular, on the magnetic tweezers technology and discussed about two specific applications regarding nucleic acids and protein analysis, implemented using this system.

Here, we introduce a new droplet microfluidic concept for magnetic beads handling, combining: i) the advantages of magnetic tweezers in terms of extraction/redispersion functionalities and purification efficiency; ii) the integration and high throughput processing, characterizing continuous droplet microfluidic systems.

1 Introduction

Droplet microfluidics offers competitive advantages as compared to conventional methods or monophasic microfluidic systems, notably the possibility to aliquot samples and reagents into independent compartments in the microliter to femtoliter range, preventing undesired cross-contaminations problems, evaporations of solvents and adsorption onto channel surfaces[1]. Furthermore, droplet microfluidics is recently experiencing a tremendous growth in the bioanalytical field[2], as attested by both the increasing number of existing lab-scale protocols implemented[3,4] and by the completely new directions in diagnostic and research opened[5], based on this technology. These advances are mainly due to the wide set of functionalities available in the droplet toolbox, such as droplet generation[6], merging[7], splitting[8], sorting[9] and cell encapsulation[10]. However, unfortunately, a robust concept allowing the possibility to enrich or extract an analyte of interest from a complex matrix, a fundamental step in many biochemical protocols, is still lacking.

In current biochemical lab protocols, these extraction and purification steps are achieved either by interaction with a solid surface, as e.g. in chromatography or immufiltration, or through the dispersion of functionalized magnetic particles in the sample solution in order to bind target molecules. These particles can be trapped by a magnet placed next to the liquid holder while the supernatant is removed, and finally released in an elution buffer. However, these protocols are prone to contaminations and limited to relatively large volumes. Some automated solutions were proposed but they require specific robotic equipment and a strong consumption of consumable plasticware, thus remaining expensive to implement and operate.

In the last decade, several multi-phase microfluidic systems have been proposed for the manipulation of functionalized magnetic supports[11]. Historically, the first works on this topic are based on stationary microfluidic architectures, in which the extraction of a target analyte from a supernatant and the following redispersion in a different solution are based on the displacement of magnetic particles between fixed aqueous compartments, assisted by an external magnetic field. During the extraction process, the droplet is retained, for example, by introducing narrow channels or gates connecting adjacent reservoirs[12,13,14] , or by exploiting surface topographic features[15]. Other strategies were proposed, acting on the substrate wettability properties[16] or on droplet volume to tune its friction with the substrate itself[17]. Further approaches exploit capillary effects to confine solutions in adjacent reservoirs[18] or closed chambers[19] separated by an immiscible phase (oil or air[20,21]). The interface between the two phases acts as a valve[22], allowing magnetic particles to transit and be exchanged between different stationary liquids. Overall, these technologies allow simple parallelization and automation of existing lab-scale protocols but still suffer from the need for high reagents volume, and from poor mixing and washing efficiencies.

Better performances can be achieved by digital microfluidic (DMF) approaches[23,24], in which discrete droplets are transported on an array of electrodes. The introduction of a spatially fixed permanent magnet beneath the plate allows to confine the magnetic particles in a compact cluster, and to retain it while the droplet is actuated by elettrowetting forces, resulting in cluster extraction from the parent droplet[25,26,27]. DMF devices allow extraction and purification rates comparable with those of conventional lab-scale

protocols. They remain, however, limited by the complexity of fabrication of the microelectrodes array, by their relatively low throughput, and by a relatively high droplet volume (typically several µl) required for efficient droplet transport.

More recently, other technologies involving droplets in a continuous pressure-driven flow in a channel network were proposed. These approaches are mainly based on the hydrodynamic (symmetric or asymmetric) splitting of a droplet containing magnetic particles in an asymmetric magnetic field[28,29]. These devices allow the possibility to process few tens of droplets per second with effective beads enrichment in a single daughter droplet; however, they offer a limited purification rate, due to the inefficient removal of the supernatant fluid. Furthermore, the redispersion of the extracted magnetic cluster in another droplet, necessary e.g. for buffer exchange, cannot be directly accomplished by these systems and requires indeed additional modules to fully control and synchronize the contact of the droplets to be merged. Consequently, these devices allow the enrichment of a target analyte but limits the implementation of multi-steps protocols or those including washing stages. Other continuous droplet microfluidic approaches are more adapted to these needs, as is the case for the magnetic tweezers technology[30]. In particular, these are constituted by two soft ferromagnetic tips, activated by a magnetic coil and facing each other across a capillary in which aqueous droplets are transported in a continuous flow of oil. This concept is based on the generation of a strong and local magnetic force along the path of the droplet, able to overcome the interfacial tension, thus retaining the beads contained in it while the parent droplet continues its flow in the capillary. Switching off the magnetic coil, the beads

cluster can be then released in any coming droplet. This technology guarantees high programmability and versatility and allows the implementation of complex multi-steps protocols including specific extraction and washing steps, with performances comparable to conventional lab-scale methods[31,32,33,34]. However, the use of macroscale components limits miniaturization and parallelization. Furthermore, the throughput of the system is rather low (<0.5 Hz), as compared to other continuous droplet microfluidic approaches. In this panorama, a technology allowing to perform reliable extraction and redispersion processes, with performances comparable with those of lab-scale methods but guaranteeing faster processing times, is still highly desired.

Here, we report the conception, development and characterization of an innovative droplet microfluidic concept, based on the manipulation of magnetic particles on chip, for the extraction and purification of molecules of interest and for the implementation of multi-step protocols with high processing rates. Our innovative approach combines: i/ the deflection and confinement of magnetic particles through the integration of soft magnetic components adjacent to a microchannel (Fig.1) with ii/ the fast hydrodynamic-assisted droplet splitting, leading to the generation of a daughter droplet, enriched with particles and characterized by an extremely low carryover of supernatant. This sub-droplet is retained by soft magnets until redispersion in a new incoming droplet occurs. The implementation of this concept revealed new phenomena not present in previous ones, such as the droplet fingering inside the volume comprised between the magnetic elements. This phenomenon was studied, varying experimental conditions, and optimized to reach extraction and purification

efficiencies >95% at higher throughput than with earlier technologies based on microcapillaries.

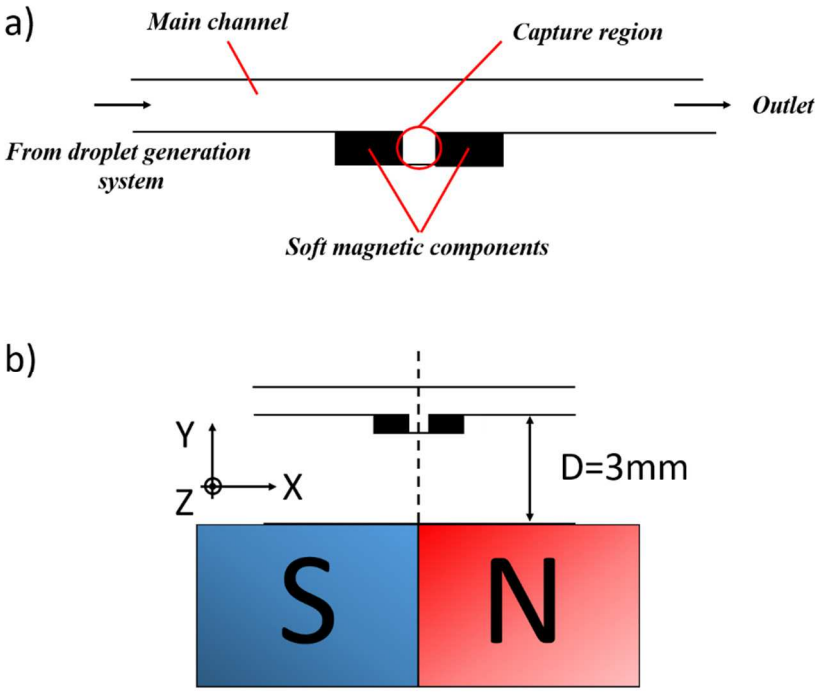

Figure 1: Sketch of the device overview (top view). *(a) A pair of soft magnetic components, fabricated in magnetic PDMS, are integrated adjacently to a microchannel (cross-section: 300µm x 200µm), where droplets flow. The portion of the channel between the soft magnetic components defines the capture region, where the extracted magnetic cluster will be accommodated. (b) The soft magnets are activated by an external permanent magnet, placed at a distance of 3mm in the vertical direction. Furthermore, the horizontal position of the magnet is defined in order to make the axis of symmetry of the magnetic components coincide with the one of the permanent magnet. Finally, the bottom plane of the soft magnets corresponds with the median XY plane of the magnet.*

2 Materials and methods

Our device is composed of two parts: the top one integrates the magnetic components, obtained by the "doctor blade" technique[35,36], while the bottom presents the microfluidic channels and a pocket were the soft magnets will be inserted (Fig.2). A brass mold was prepared by micromilling (Minitech Machinery). A CycloOlefinCopolymer (COC, 8007, Topas) replica was then fabricated by hot embossing of the brass mold (Fig.2a) using a hydraulic press (Scamex). For the fabrication of the top part, the COC replica presents two pocket shape structures, which will impose the design of the magnetic components. These pockets were filled with a mixture of Polydimethylsiloxane prepolymer (PDMS, Sylgard 184, Dow Corning, 1:10 base to curing agent ratio) and ferromagnetic iron particles (1-6um, GoodFellow). Different magnetic particles/PDMS pre-polymer w/w doping ratios were investigated, in particular 44.4%, 60% and 71.4% (Fig.2b). After degassing, the excess of magnetic PDMS was removed using a soft silicon blade in order to keep the pocket region of the master mold filled with the magnetic polymer (Fig.2c). At this point, a conventional pre-polymer mixture was poured on the master (Fig.2d) and the whole system was cured in an oven at 70°C for 48h. The resulting structures were then carefully peeled-off from the master. They consist in a flat PDMS layer of few millimeters with extruded micrometric magnetic structures (Fig.2e).

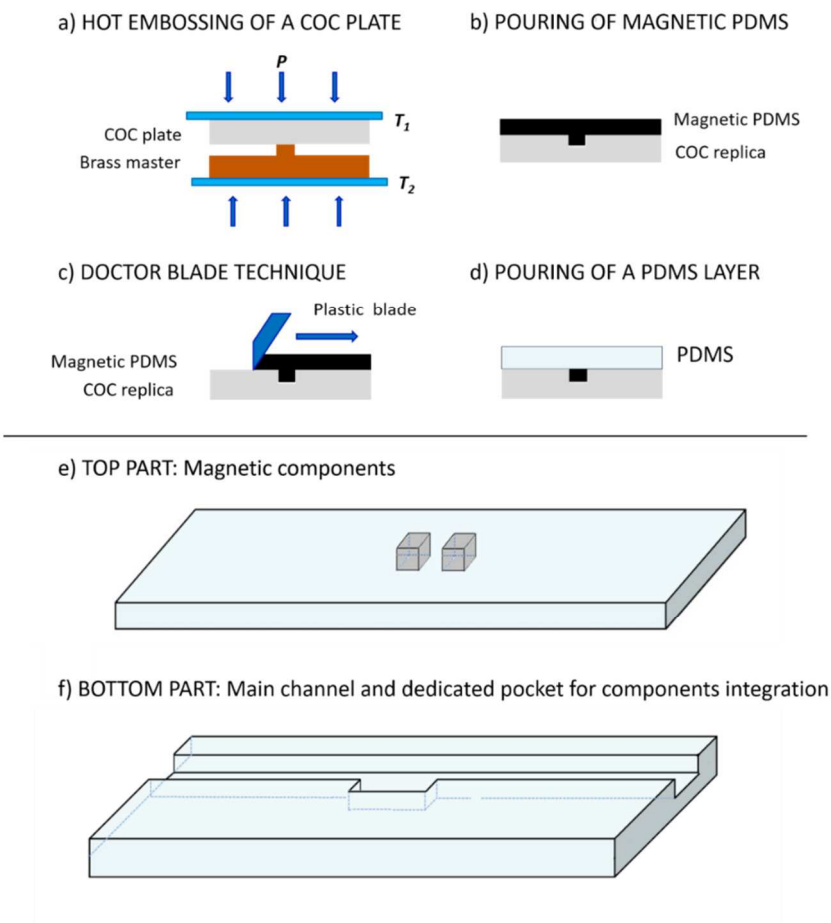

Figure 2: (a-d) Workflow of the integrated magnetic components fabrication. *A flat PDMS layer of few millimeters with extruded micrometric magnetic structures is obtained (e). These structures will be inserted in a dedicated pocket, designed in the bottom part of the device (fabricated by standard double replica molding with PDMS), and including also the main channel.*

The bottom part of the device was fabricated in PDMS by standard replica molding of the COC intermediate template (Fig.2f). Following an oxygen plasma treatment of both surfaces, the two parts were bonded together. To facilitate positioning and alignment of magnetic components in the dedicated pocket, a film of ethanol was dispersed on the activated bottom surface and the final device was then cured on a heating plate at 80°C for 20 min to allow

complete ethanol evaporation and to support the bonding of the surfaces. PTFE tubing (0.6mm OD, 0.3mm ID and 1.58 mm OD, 0.78mm ID, Sigma Aldrich) were then installed in the inlet and outlet of the device, respectively. Finally, the internal channel surfaces were treated with a solution of (Tridecafluoro-1,1,2,2-tetrahydrooctyl)trichlorosilane in FC-40 oil (5% v/v) for 20 min to improve the oil wetting, thus the droplet stability.

The set-up was completed by a further device, characterized by a circular pocket that connects the inlet and the outlet channels of the chip. This component is fabricated by double replica molding. At first, the design features, milled on a brass mold, were transferred to a COC plate by hot embossing. Then, a second replica molding of this COC master is performed either with PDMS (Sylgard 184, Dow Corning) or Ecoflex (00-50, by SMOOTH-ON). In the former case, Sylgard 184 PDMS in a 20:1 base to curing agent w/w formulation was used and subsequently cured at 70°C for 1h. On the other hand, Ecoflex was prepared by mixing equal weight parts of base and curing agent solutions. After degassing and pouring on the mold, this rubber was cured for 3h at room temperature, followed by a post-curing at 80°C for 2h and 100°C for 1h. Then, the demolded structures were bonded on a flat surface of the corresponding material, following an oxygen plasma treatment. PTFE tubing (0.6mm OD, 0.3 µm ID, Sigma Aldrich) were finally installed in the inlet and outlet of the device.

Discrete aqueous droplets (100nL volume) in a continuous oil phase (FC-40 oil + 2% perfluorodecanol) were generated using either a T-junction or a 1-arm motorized pipettor. The former was preferred during the characterization step of the device, in which a multiplicity of droplets with the same content is needed. The latter, instead, is used for the programmed sampling from a micro-

titer plate to generate a sequence of droplets with different contents. In particular, series of pairs of droplets were produced, the first containing a solution of magnetic beads (1µm diameter, Dynabeads MyOne, 10µg/µL), and the second a water sample without beads, separated by an oil gap. In both cases, syringe pumps (Cetoni) controlled the flow-rates for droplet production and pushed the generated droplets through the device at constant velocity. During the experiment, a NdFeB magnet (N52, size 20mm x 20mm x 30mm, magnetization direction through the thickness, by ChenYang technologies), installed on a linear translation stage (DDSM50, Thorlabs) was used to activate the integrated soft-magnetic structures. For droplets observation, a Macro Objective (MLH-10x) mounted on a CMOS camera (acA800-510um, by Basler) and white LED back light illumination (Schott Lighting and Imaging) were used. Data analysis was performed by ImageJ software and LabVIEW (National Instrument) home-made script.

3 Results and discussion

3.1 Device conception and numerical study

The presented approach allows the manipulation of functionalized magnetic beads in droplets through a pair of soft magnetic components, able to generate along the path of the droplet a specific magnetic force vector field, able to deflect the particles and to trap them out of the continuous oil flow. In this section, the device design will be presented, especially focusing on the numerical simulations-assisted optimization of the soft magnets geometry.

3.1.1 Device overview

The device design (Fig. 1) is characterized by a main channel (cross-section: 300µm x 200µm), crossing longitudinally the device and dedicated to the flow of confined droplets containing functionalized magnetic beads. The channel design was chosen in order to confine droplets having a volume between 80nL and 300nL. A pair of soft magnetic components are placed adjacently to the channel, facing each other and defining a channel side pocket dedicated to the extracted cluster (named the "*trap*") (Fig.1a). The soft-magnets were fabricated in magnetic PDMS (see Material and methods section), and their design will be discussed in the following section. The activation of the magnetic components is performed thanks to their magnetization by an external permanent magnet, placed with its direction of magnetization parallel to the main channel. In the ON state, the position of the permanent magnet is fixed and well-defined on a XY plane characterized by a horizontal and a vertical axis parallel and longitudinal, respectively, to the main channel (Fig.1b). In particular, the magnet is placed at a fixed vertical distance D=3mm from the main channel side (magnetic flux density at the magnet surface ≈0.5T), such that it is in contact with the device side. The horizontal position of the magnet is fixed to have the symmetry axis of the soft magnetic components coincident with the mid-point of the magnet side being in contact with the device. Furthermore, in the z direction, the bottom plane of the soft-magnets corresponds with the median XY plane of the permanent magnet.

3.1.2 Numerical simulations-assisted conception of integrated soft-magnetic structures

The introduction of soft-magnetic structures in proximity of a microfluidic channel has been shown to be an interesting method to generate local magnetic forces allowing to improve the deflection of magnetic particles in monophasic microfluidic systems[37,38]. However, working with multiphase systems, magnetic forces must not only deflect the particles, but also be intense enough to distort or break the droplet interface, in order to allow the particles to reach the *trap* and spatially confine them. In the magnetic dipole approximation, the generated magnetic force can be written as:

$$\mathbf{F_{mag}} \simeq \left(\frac{Q}{\rho}\right) \mathbf{M(B)}\, \nabla \mathbf{B}, \qquad (1)$$

where Q is the amount of beads, ρ is their density and M is the particle magnetization[30,39]. Furthermore, this force depends on the magnetic flux density $\mathbf{B}$ and its gradient, which are in turn affected by the shape of the soft-magnetic components, their mutual distance and the fabrication material. Systematic numerical simulations assisted the device conception, allowing to investigate the influence of these factors on the resulting magnetic force and to optimize it for applications involving droplet systems.

Finite-element simulations were performed using Comsol Multiphysics software in order to solve the static Maxwell's equation. A spherical surface, with a radius 10-fold the largest feature of the geometry, defines the simulation domain and its magnetic parameters are identified to those of air. The behavior of each magnetic element in the geometry is described by its magnetization curve. In particular, the NdFeB permanent magnet activating the structures presents a

maximum energy product of 52MGOe; a magnetization M of about $1 \cdot 10^6$ A/m was defined accordingly in the corresponding constitutive relation $B=\mu_0(H+M)$. Differently, for the soft magnetic components fabricated in various magnetic PDMS formulations, the B-H curves experimentally derived and reported in literature were considered[40]. However, in the range of magnetic field of interest for our device, these materials were assumed to be in the unsaturated, linear portion of the respective curves, thus characterized by the equation: $B=\mu_0\mu_r H$, where μ_r is the relative magnetic permeability of the material[41]. Furthermore, the slope of the curve varies as a function of the doping concentration of iron particles in PDMS pre-polymer. In particular, the relative magnetic permeability values set in the finite element study range from μr=1.301 to μr=1.883, corresponding to a Fe/PDMS ratio ranging between 44.4% to 71.4% w/w, respectively[42,43].

At first, three specific geometries for the soft magnetic components were investigated, resulting from a 200μm extrusion of a squared, triangular or trapezoidal-like design, respectively. These structures aim at focalizing the magnetic flux density streamlines in order to achieve a magnetic force vector field defining a *trap* able to deflect and retain the magnetic particles in the channel portion between the soft magnets. The two magnetic components, whose magnetic permeability is set to μr=1.883 for this study (corresponding to the highest Fe/PDMS ratio), are arranged along the same side of the channel and are activated by an external magnet. For each geometry, the magnetic flux density spatial distribution was evaluated in the neighbourhood of the magnetic components. The results for a median transversal plane of the devices are illustrated in Fig.3, a-c. The focusing effect resulting from the introduction of

the soft magnetic components generates, especially for squared and trapezoidal-like structures, a magnetic flux density more intense in the pocket between the soft magnets than in the main channel region; flux density maxima are localized around the sharp edges of the structures. Furthermore, independently from the structure geometry, the obtained magnetic flux density values are higher than 0.25T in the main channel. These values induce the saturation of the particles dispersed in the droplet[30] to a constant magnetization value, allowing, therefore, to maximise the contribution of this factor in the resulting magnetic force.

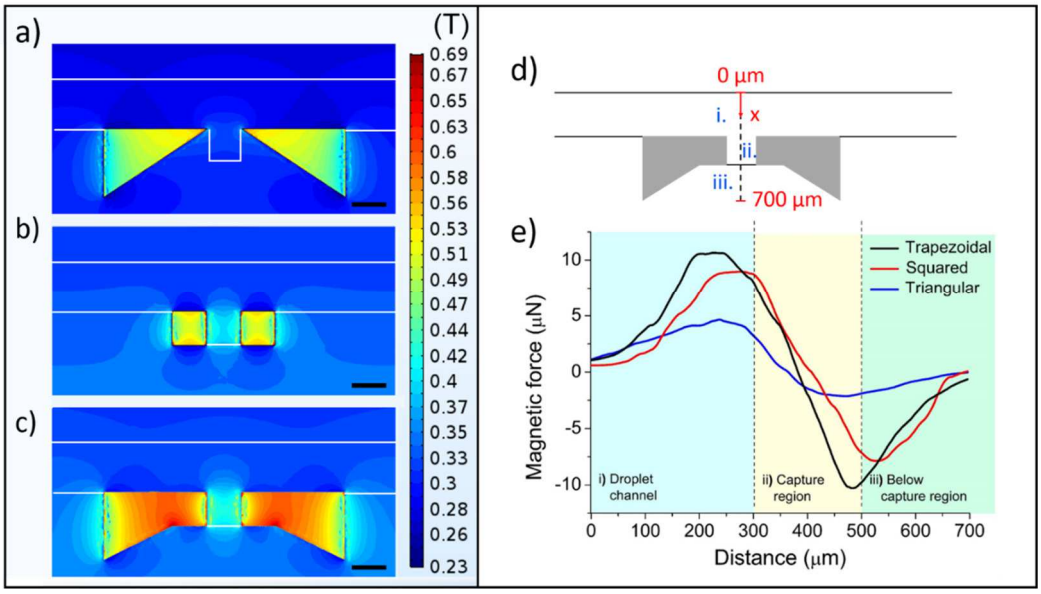

Figure 3: Numerical simulation-assisted soft magnets conception. *a-c) Spatial distribution of the magnetic flux density on a median device plane for three tested designs: triangular (a), squared (b) and trapezoidal (c). The intensity values are expressed in Tesla. Scale bar: 200µm. Independently from the design, these structures guarantee magnetic flux densities higher than 0.25T, thus allowing magnetic particles to reach their saturation value. (d) The generated magnetic forces were evaluated on the symmetry axis of the soft magnets, considering a reference frame in which positive values correspond to magnetic forces inwards the capture region, as indicated by the red arrow. Furthermore, three channel sections were defined, i.e. the droplet channel (i), the capture region (ii) and the zone below the trap (iii). Resulting magnetic forces for the investigated structures are reported in (e).*

The magnetic force magnitude acting on a 1µg cluster of particles was then evaluated, according to eqn. (1), for different soft-magnets designs. It is worth noting that we are considering here the particle cluster as a whole, and the final magnetic force is thus approximated as the sum over the individual contributions of each particle. This was supported by experimental observations of the aggregation process of magnetic beads, initially uniformly dispersed in a droplet, when subjected to an external permanent magnet. The resulting magnetic forces along the symmetry axis of these structures are shown in Fig. 3e. In order to identify the different device regions, the horizontal axis is separated into three sections, corresponding to the main channel, the capture region and the zone below the *trap* pocket (Fig. 3d). In the defined reference frame, a positive force indicates a magnetic force directed inwards the capture region, while the opposite case corresponds to a negative force. In the resulting trend for the three soft magnet designs, the magnetic force applied on the particles presents a maximum in the main channel and decreases in intensity approaching the capture region, reaching a zero value inside the *trap* pocket. Below this zone, a symmetrical tendency results in a force directed upward with an increasing intensity moving far away from the capture region. Although the magnetic force profile obtained for the different soft-magnetic structures is characterized by a similar trend, the trapezoidal-like structure allows to achieve a maximum force in the main channel of about 10.6 µN (corresponding to a maximum gradient of about 430 T/m), which is higher than those obtained for squared (about 8.5µN) and triangular structures (about 4.6µN).

Interestingly, the direction of the magnetic force vector field is exclusively defined by the magnetic flux density gradient and the integration of soft

magnetic components (and their geometry) generates a magnetic force distribution converging toward the capture region and inducing a focusing effect on the particles moving in the channel (Fig. 4a). Furthermore, a specific energetic landscape is achieved around the *trap*, characterized by two absolute minima in proximity of the centre of the soft magnets walls, delimiting the capture region. A third relative minimum can be identified in the middle of the *trap* (Fig. 4b. Note that the origin of the reference frame coincides with the centre of the capture pocket, as indicated in the inset). These minima represents equilibrium points for the deflected particles and allow, thus, their spatial confinement in the continuous oil flow. In particular, small clusters (corresponding to particle load of about few hundreds nanograms) will preferentially accommodate in one of the two absolute energy minima. Increasing the beads quantity, the cluster size varies accordingly and a larger portion of the capture region will be occupied. As a matter of fact, increasing its volume, the cluster will at first place transversally in the *trap*, assuming an elongated shape by bridging the region corresponding to the three minima, until filling the whole pocket for particle loads of few micrograms.

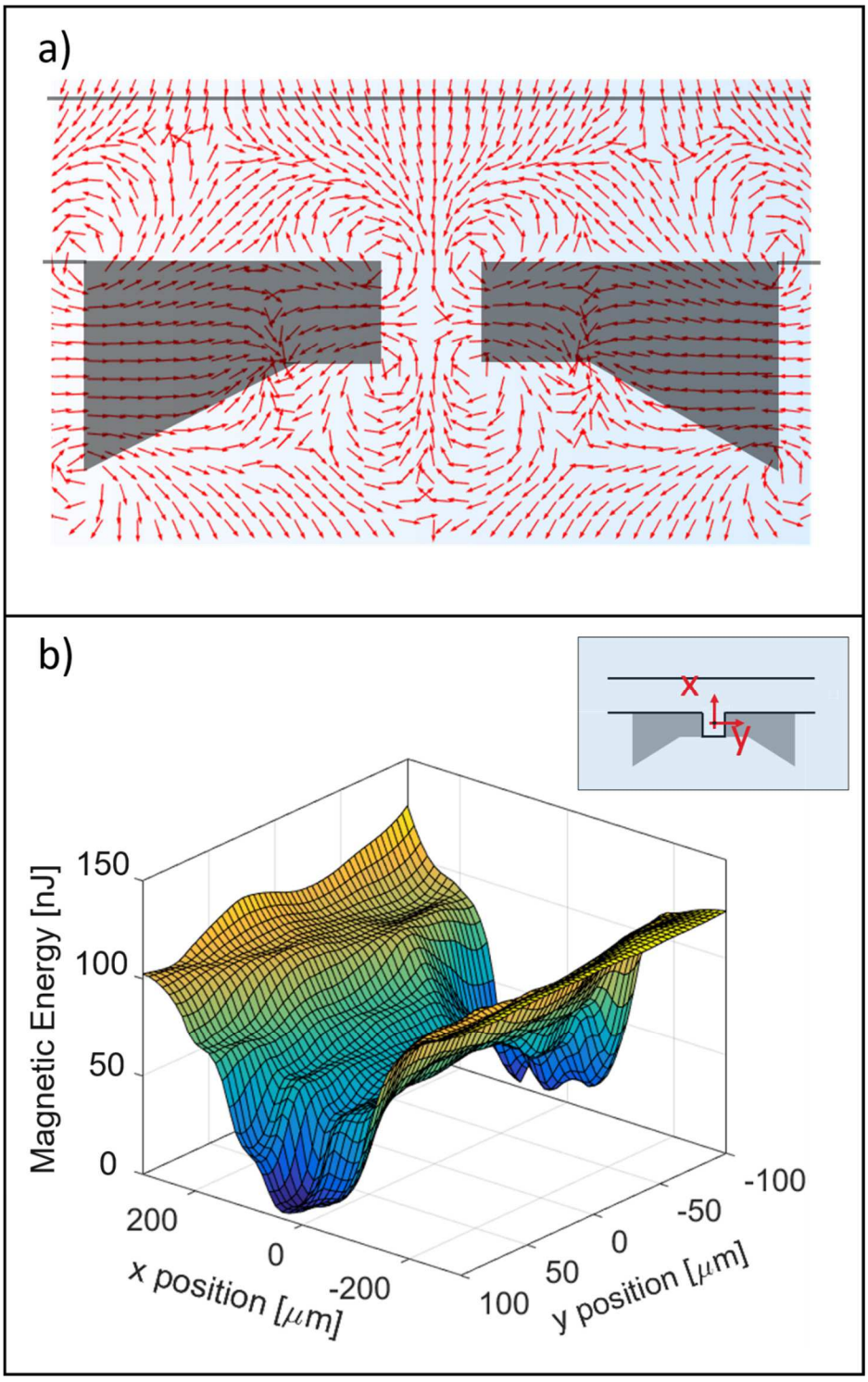

Figure 4: Direction of the magnetic force field vector and resulting magnetic energy landscape in the neighbourhood of the capture region. *(a) The integration of soft magnets allows to generate on the particles flowing in the channel a focusing effect towards the capture region. (b) As described in the inset, the reference frame's origin coincides with the*

middle of the trap and the x and y axis are directed as indicated. In particular, the points (0,100) and (0,-100) are the centre of the soft magnets faces, defining the capture region. The energetic landscape is characterized by 2 absolute minima, localized in correspondence of the centre of the soft magnets walls. A further relative minimum can be identified in the middle of the trap. The achieved energetic landscape allows the deflection of the particles from the continuous oil flow, and their spatial confinement in the trap. Interestingly, the cluster of particles will differently accommodate in the capture region according to its volume, as discussed in the main text.

Based on these considerations, the trapezoidal-like structure was chosen as the optimal one for magnetic particles extraction. Once fixed the soft magnets design, their mutual distance was optimized by numerical simulations as well. It is worth noting that this distance defines the size of the *trap* region, thus it sets an upper limit to the maximum amount of magnetic beads that can be accommodated. Consequently, since typical particles loads of interest for the applications are in the order of few hundreds of nanograms up to several micrograms, different gaps l ranging from 100µm to 400µm were considered (Fig. 5a) and the achieved magnetic force was evaluated in the symmetry axis of the magnetic pairs. In particular, the height and width of the curves' portion referred to the main channel region (0µm<x<300µm, blue background region in Fig. 5b) will be compared, in order to consider both the magnetic force intensity and its spatial range of influence. Overall, the force intensity decreases by increasing the gap between the magnetic components and assumes its maximum value in the channel (about 12.5 µN) for a gap of 100 µm (Fig. 5b). On the other end, with a 200µm gap the maximum magnetic force achieved is slightly smaller (about 10.6 µN) than previous case, but influences a larger

portion of the channel, as demonstrated by the wider positive peak. For these reasons, a 200µm gap was chosen as a compromise for the final design.

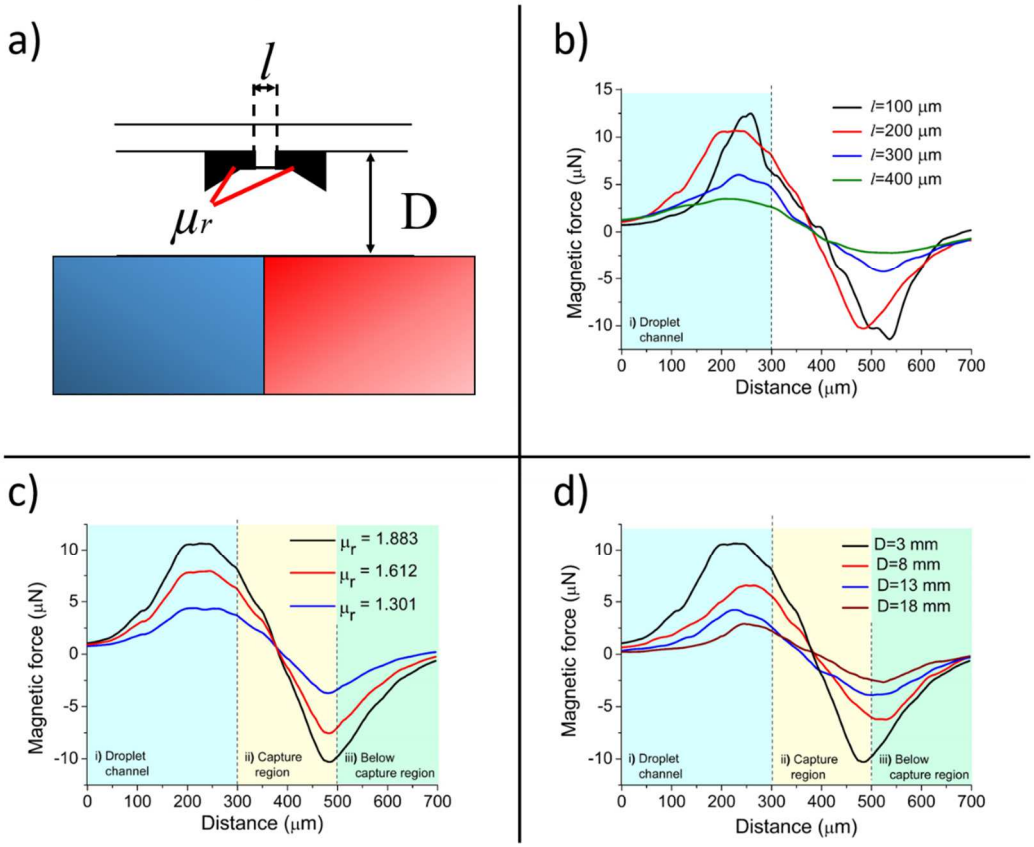

Figure 5: (a) Definition of the geometrical and material parameters considered in the device conception. *In the scheme, l is the gap between the soft magnets, µr their relative permeability and D the distance between the microstructures and the permanent magnet. In this part of the numerical study, the influence of these parameters was studied, evaluating the magnetic force in the symmetry axis of the soft magnetic components.* ***(b) Generated magnetic force for different gaps l in the trapezoidal-like soft-magnets design.*** *In the final device configuration, a 200µm gap was chosen as a compromise between the peak's height and its width, corresponding to the magnetic force intensity and its spatial influence, respectively.* ***(c) Effect of PDMS doping ratio on the magnetic force achieved.*** *Three magnetic PDMS formulations were tested, i.e. 44.4%, 60.0% and 71.4% Fe/PDMS w/w, corresponding to relative magnetic permeability of μ_r =1.301, 1.612 and 1.883, respectively. Interestingly, increasing µr from 1.301 to 1.883, the resulting magnetic force gained about a factor 2.* ***(d) Effect of the mutual distance D between the magnet and the integrated***

components on the magnetic force. *An increase in distance between 3 mm (ON state of the device) and 15mm, leads to a 5-fold decrease in the generated force. The distance D can be thus exploited to control the ON/OFF state of the device.*

The influence of iron powder concentration in the composite soft magnetic structures was further investigated. In fact, the doping concentration affects the relative magnetic permeability of the composite, thus the induced magnetic flux density. In this study, three doping ratios (Fe/PDMS) were considered, i.e. 44.4%, 60% and 71.4% w/w and the resulting magnetic force, evaluated in the symmetry axis of the soft-magnets, are reported in Fig. 5c. As expected, an increase in iron concentration, and the consequent gain in magnetic permeability, leads to the generation of higher magnetic forces. Interestingly, despite a small change in relative permeability (from μr=1.301 to μr=1.612), the resultant forces almost doubled, passing from to 4.5μN to 7.9μN, and reaching about 10.6μN for μr=1.883.

Finally, to complete the design optimization, the influence of the distance between the magnet and the soft-magnetic structures was investigated. Considering a XY plane characterized by a horizontal and a vertical axis parallel and longitudinal, respectively, to the main channel (Fig.1), the magnet horizontal position was kept fixed while different ordinates values D were considered, ranging from 3mm to 15mm (Fig.5a). As expected, the closer the magnet, the higher the achieved magnetic force (Fig. 5d). Increasing the magnet's distance to the upper value in the range considered, yielded a 5-fold drop in the generated force. Interestingly, as will be shown below, this strong dependence can be thus exploited to control the ON/OFF state of the soft magnetic components.

In conclusion, the presented numerical study assisted the conception of the soft-magnets geometry and of their fabrication material in order to optimize the achieved local magnetic force, perpendicular to the flow. Furthermore, in a static study, this force would exert a magnetic pressure of about 265 Pa, slightly higher but of the same order of magnitude as the Laplace pressure of the droplet meniscus (≃200 Pa) in a 200µm-side squared channel cross-section like the capture region. Altogether, the numerical simulations show that the magnetic force exerted through the soft magnet structures would be thus able to deflect the droplet interface, but would certainly not be intense enough to complete the extraction process. With this aim, a hydrodynamically-assisted droplet splitting at the junction between the main channel and the capture region was considered, exploiting the magnetically-driven deformation of the droplet meniscus in the *trap*, as described in the following section.

3.2 Experimental section

3.2.1 Extraction and redispersion processes

A confined droplet containing superparamagnetic particles (1µm diameter) is transported in the device microchannel by a continuous flow of oil (Fig. 6a). Under the combined effect of the external magnetic field and the internal recirculation flows, the particles sediment in the bottom rear of the droplet, forming a compact cluster (Fig. 6b). Approaching the integrated magnetic components, the cluster experiences a magnetophoretic force that attracts it towards the capture region, corresponding with the minima of the magnetic energy landscape for the bead-cluster (Fig. 6b). While reaching this point, the magnetic force acting on the particles deforms the droplet interface, resulting

in the generation of a small droplet finger, penetrating into the capture region and containing the cluster (Fig. 6c). As the rear meniscus of the droplet moves beyond the capture region, the bridge linking the main droplet body with the finger thins out (Fig. 6d). Simultaneously, a meniscus finger retreat process occurs, opposed by the magnetic force of the cluster. The latter keeps the interface in a steady deformed state, preventing the droplet to complete the finger retreat into the main channel and to recover its original shape[44]. As soon as the rear meniscus reach the upper right corner of the magnetic component, pinch-off of the droplet thread occurs and a smaller sub-droplet containing the particle cluster is split out of the initial one (Fig. 6e). The cluster is kept immobile in the capture region and, due to the hydrophilic nature of the beads, it remains surrounded by a layer of aqueous solution, so it is never in contact neither with oil nor with the microchannel and soft magnets walls. When a different droplet is carried by the continuous oil flow over the capture region, spontaneous coalescence with the magnetically-trapped cluster occurs (Fig. 6f), and switching off the magnetizing field allows the release of the beads and their dispersion inside the following droplet (Fig. 6g). In fact, differently from conventional droplet microfluidics systems, in which tensioactives aim at maximizing the steric repulsion between the surfactant molecules in order to prevent droplet merging, in this work perfluorodecanol is preferred, which guarantees the production of stable water phase droplets in fluorinated oil and prevents wall contamination but still allows the merging of droplets upon contact in a highly confined state[45].

Based on this sequence of operations, functionalized magnetic beads can be used to extract analytes of interest from a sample and to carry them between

different media, with a very low carryover of the initial matrix. Indeed, the volume of the extracted subdroplet containing the magnetic beads in a closed-pack configuration is of only few nanoliters (<3.5nL), as compared to the initial droplet volume (between 80nL and 200nL), thus providing a high purification rate from the supernatant fluid (>95% of the total droplet volume). In addition, the device showed effective capture (Fig.7, a-e) and release (Fig.7, f-h) operations for magnetic particle loads in a droplet ranging from 100ng to 10µg. Interestingly, the energetic landscape numerically-evaluated in the neighborhood of the capture region (cf. Fig.4b) was experimentally confirmed: as shown in Fig. 7i, the accommodation of the extracted cluster in the *trap* will change as a function of the particle load Q (thus of the cluster volume). In particular, the cluster is positioned in correspondence of the energy minimum at the soft magnets wall for low particles loads, and assumes a transversal elongated shape in the *trap* for increasing Q, until filling the whole capture pocket.

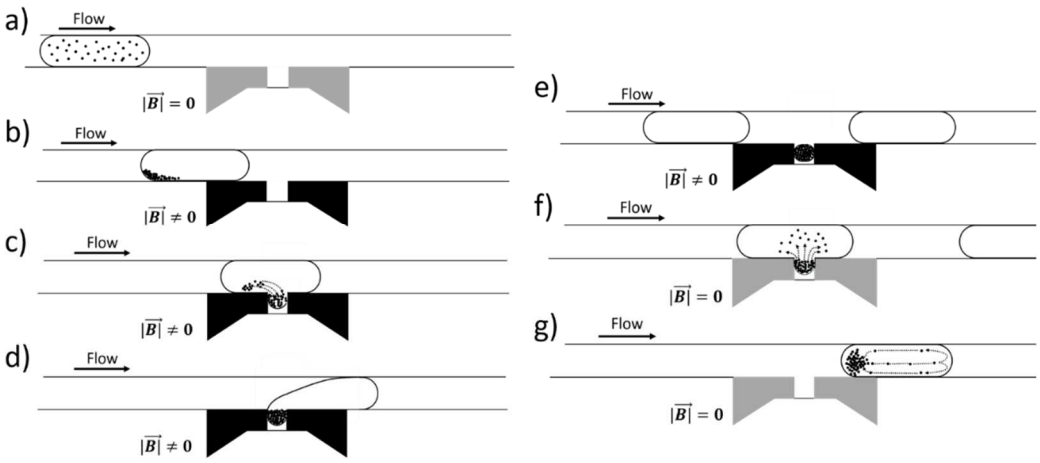

Figure 6: Sketch of the device functionality (top view). *The integrated soft magnetic components are illustrated in black when activated by an external magnetic field and in grey when they are passive. (a) A confined aqueous droplet containing functionalized magnetic*

particles, approaches the soft magnetic components. (b) Under the effect of the external magnetic field and due to the droplet internal recirculation flows, the particles sediment in the bottom rear of the droplet, forming a compact cluster. (c) The soft magnetic components generate a magnetophoretic force on the cluster, pushing them in the capture region and causing the generation of a small droplet meniscus inside this capture pocket. (d) As soon as the bottom rear of the droplet crosses the capture region, the bridge linking the finger with the main droplet body thins out until pinch-off occurs and (e) a daughter droplet containing the enriched cluster of particles is extracted from the parent drop. (f-g) Switching off the magnetic components, the beads can be released, upon merging, in a coming droplet.

Together with the purification rate, a further interesting parameter defining the performance of the device is the extraction efficiency as a function of the droplet velocity. This was evaluated for 100nL droplets containing a 1µg particle load and transported at constant oil flow-rates, ranging between 0.1 µL/s and 1.0 µL/s. Using the optimized design for the integrated soft magnets, three doping ratios of iron particles in PDMS (w/w) were investigated, i.e., 44.4%, 60% and 71.4% (Fig.8, each point is an average of 30 independent measurements performed on three devices characterized by the same doping ratio).

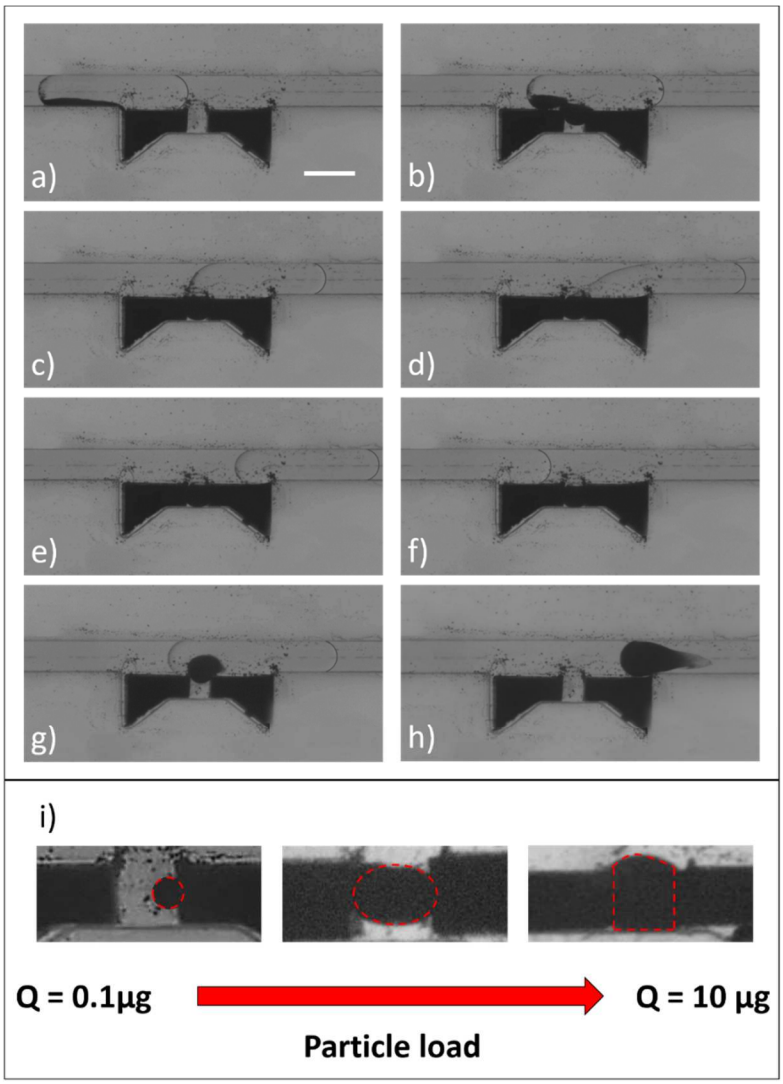

Figure 7: Image sequence of the extraction (a-e) and redispersion (f-h) processes in a 100nL containing a particle load of 1µg*. Scale bar: 0.5mm. Panel (i) focuses on the capture region and presents the different configurations chosen by the extracted cluster of magnetic particles in the capture region as a function of the increasing load Q (thus for increasing cluster volume). Interestingly, the simulation results about the energetic landscape achieved through the introduction of the soft magnets are experimentally confirmed.*

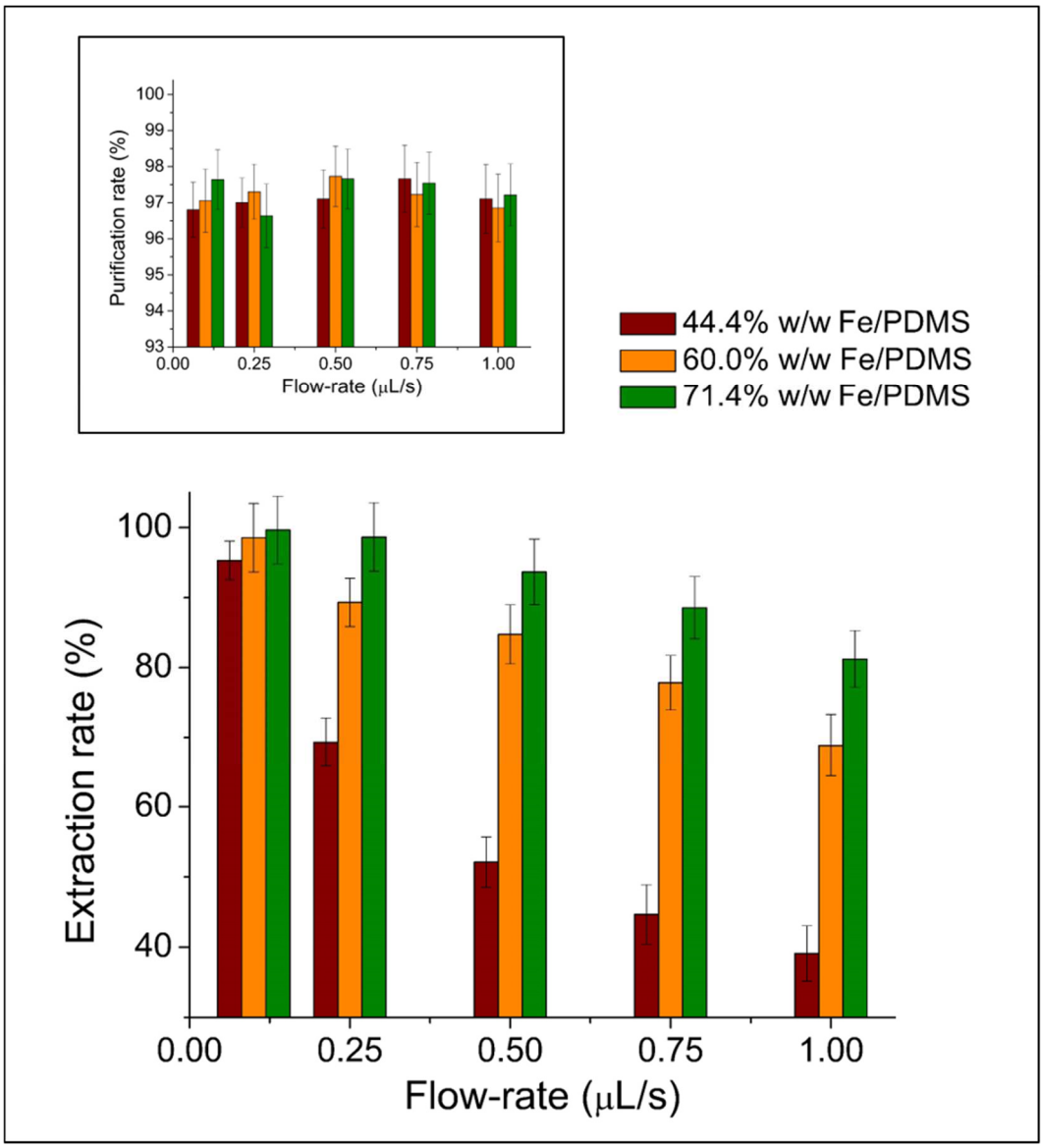

Figure 8: Extraction and purification efficiencies as a function of the carrier oil flow-rate for different magnetic PDMS doping concentrations. *In particular, 44.4% (brown), 60.0% (orange) and 71.4% (green) ratio were tested for the extraction of 1.0μg of magnetic particles confined in 100nL droplet. As shown by numerical simulations, an increase in doping concentration allows the generation of higher magnetic forces and results in better overall extraction performances. However, the reduction of the time window during which the cluster passes in front of the trap, together with the slowing down of its dynamics due to the resistance exerted by the droplet interface, cause a detriment in capture rates for high flow-rates. Independently from the PDMS doping ratio, the device shows purification rates higher than 95% (see figure inset).*

As predicted by numerical simulations, an increase in the doping ratio of the magnetic PDMS allows for higher magnetic forces. This is reflected by the higher extraction rates obtained with a 71.4% doping ratio (in green, Fig.8), with respect to 60.0% (orange) and 44.4% (brown) ones. Our results demonstrate that at low flow-rates (lower than 0.1 µL/s) extraction rates higher than 97% can be achieved whereas an increase of the droplet velocity decreases the particle extraction efficiency even for the highest doping ratio. This behavior is related to the interplay between the droplet drag force dynamics, pushing the cluster longitudinally in the channel, and the magnetic force, attracting the beads towards the *trap*, perpendicularly to the main flow. Indeed, focusing on the characteristic times related to these two dynamic events, in the range of flow-rates of interest, the rear droplet meniscus pushing the cluster spends typically between about 15ms and 120ms to cross the gap between the soft magnetic structures defining the capture region. In order to reach the *trap*, the particles cluster has to deform the droplet interface developing a finger thus its dynamics is slowed down by the droplet interfacial counterforce, resulting in a typical time to get into the *trap* ranging from about 50ms to 200ms, for a 71.4% and 44.4% doping ratio, respectively. Consequently, a part or the whole cluster is dragged away from the capture region before being trapped in it and keeps flowing in the parent droplet.

Finally, thanks to an optimized design of the soft magnet structures, the finite capture pocket demonstrates its ability to efficiently extract magnetic particles in droplet for flow-rates limited to 0.25µL/s. However, the volume of this finite capture pocket sets an upper limit to the maximum amount of beads that can be accommodated. Whether the cluster volume exceeds the pocket one, the

device extraction efficiencies would be affected, especially at high flow-rates, due to the portion of beads lost during the droplet pinch-off process at the junction between the capture pocket and the main channel.

3.2.2 Introduction of a pressure-driven variable volume component

The principle

In order to extend the range of flow-rates allowing a reliable device functionality and to go beyond the state-of-art processing velocity[32] (1.84 mm/s, by the magnetic tweezers technology), a straightforward solution would be to generate a controlled and magnetic force-independent droplet fingering inside the capture region. In this way, the particle cluster dynamics moving towards the *trap* is not slowed down by the opposing interfacial force, as described before. Furthermore, the intrinsic droplet fingering would also allow to deform the internal recirculation flows, thus supporting the cluster, magnetically confined at the bottom rear of the droplet, to enter inside the capture region. The finger length, however, should be finally tuned in order to avoid droplet break-up, or a reduction of the device purification rate.

The introduction of a pressure-driven component of variable volume, connected to the capture region, is an interesting and passive (i.e., not requiring any external pumping system) way to induce droplet fingering (Fig. 9). In particular, the pocket between the magnetic components was modified in length in order to define a secondary channel, perpendicular to the first one and externally connected by a PTFE tubing to an additional variable volume device.

To achieve this feature, the device, called *balloon*, is fabricated in a hyperelastic material (see Materials and Methods) and it is designed with a longitudinal channel of rectangular profile (200µm high, 300µm wide), that connects the inlet to the outlet of the device through an expansion in channel width defining a circular chamber. The outlet of this chip is connected to a pinch valve.

Once the whole circuitry is filled with oil, the valve is closed and kept in this state during the entire experimental workflow. Consequently, as for the case of the capture pocket, no steady state flow across the *trap* is possible. Nevertheless, in contrast to the previous configuration, the presence of a deformable unit allows a non-negligible flow of oil in the secondary channel, in response to a pressure gradient. This will induce, as described in details in the next paragraph, a fingering phenomenon in the droplet. Interestingly, the increase in pressure drop due to the presence of a confined droplet in a microchannel can be exploited to self-trigger its fingering in the capture region.

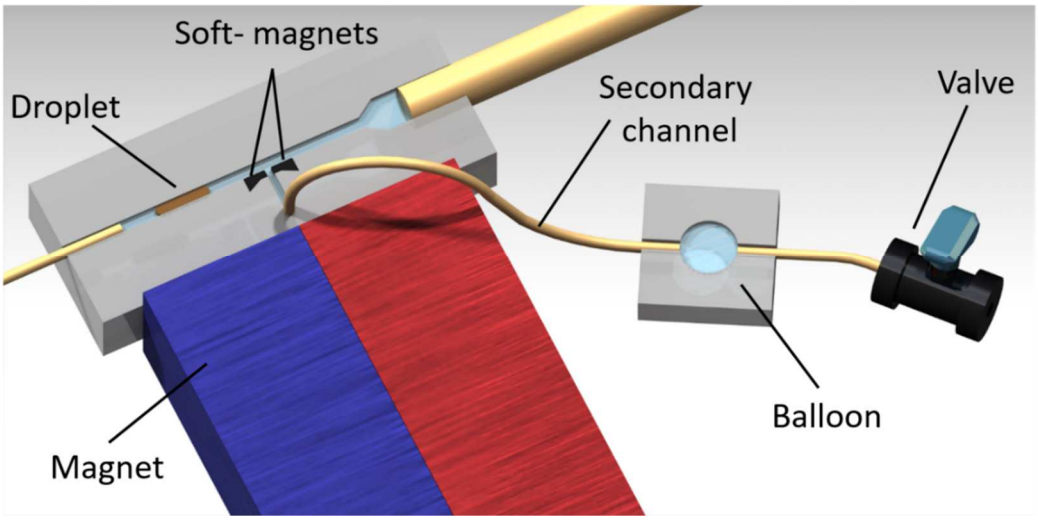

Figure 9: Final device configuration. *The pocket defined by the pair of soft magnets is extended in order to define a secondary channel, perpendicular to the main one. In this*

branch, a variable volume component, called balloon, is connected to the capture region through a PTFE tubing and its output is connected to a valve. Once the whole circuitry is filled with oil, the valve is closed and kept in this state during the entire experimental workflow in order to define a dead-end channel.

Flow-profile inwards a dead-end channel containing a variable-volume component

In order to investigate and characterize this droplet self-triggered fingering phenomenon, the magnetic components were not activated and a purely hydrodynamic study was performed. The droplets (100nL volume), generated by a T-junction geometry, were pushed at constant flow-rate (0.25µL/s) of carrier oil towards the main device, whose outlet was connected to a reservoir at the atmospheric pressure. Furthermore, a flow-meter was added in series to the secondary dead-end channel containing an Ecoflex *balloon* having a 1mm radius. The temporal flow-profile measurements during the crossing of a train of droplets (sampling time: 0.1s) was coupled to a synchronized video in order to have a biunivocal relation between the spatial position of the droplet and the measured flow-rate. A typical profile describing the flow-rate in the dead-end secondary channel is illustrated in Fig. 10a. When the system is in its rest position, i.e. no pressure is applied, the flow inward the secondary channel is zero. As soon as the train of droplets is pushed towards the chip, the flow-rate measured in the secondary channel suddenly increases, reaching a maximum depending on the pressure applied to the system (Fig. 10a, blue box).

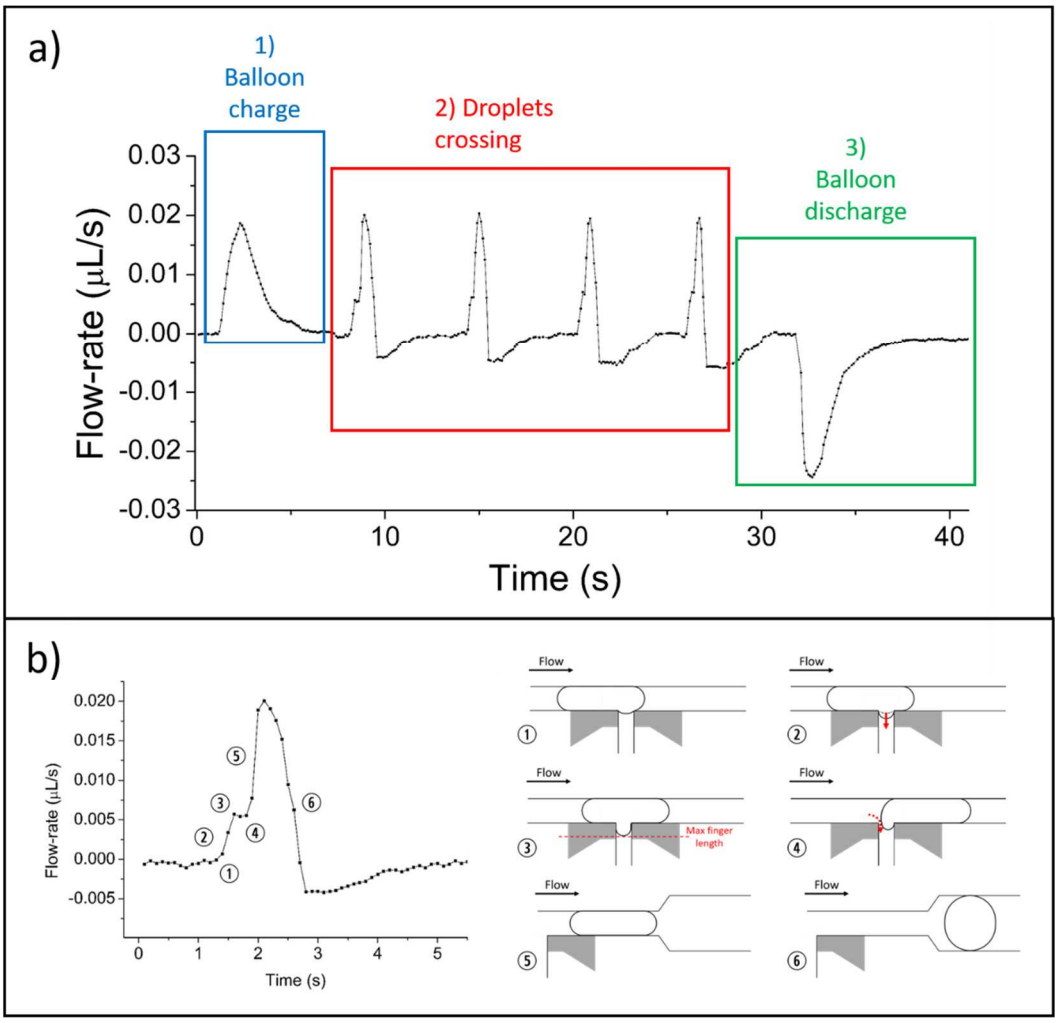

Figure 10: Measured flow profile in the secondary dead-end channel containing a balloon (Ecoflex, R=1mm) during the flow of four droplets in the main channel. *In the chosen reference frame, a flow inwards the capture region is indicated by a positive value while negative values correspond to flows outside the secondary channel. Three features of the curve are stressed by coloured rectangles: i) initial balloon charge due to the constant oil flow-rate pushing the droplet towards the chip (in blue); ii) passage of four droplets (refer to the main text for the features of the single droplet profile); iii) balloon discharge as the carrier flow is switched off.* ***b) Secondary channel flow profile during the crossing of a 100nL droplet transported by a carrier oil flow-rate of 0.25 µL/s.*** *Interestingly, the profile features were associated to the corresponding position of the droplet in the device, as indicated by the sketches in the left part of the panel.*

The volume of oil entering in the *balloon* then exponentially decreases in time, until reaching again a steady state around a zero inward flow. In this condition, the *balloon* is in an inflated state. The transient state, described by a peak in the inward flow-rate, separates in fact two steady phases of the *balloon* characterized by an absence of flow inward or outward: i) before the peak, a state corresponding to a rest position in the case of no applied pressure; ii) after the peak, an inflated state in which the maximum *balloon* membrane deformation, thus the final volume increase obtained, strongly depends on the applied pressure.

Due to the pressure-driven control of the volume increase in the *balloon*, the presence of a confined droplet in the main channel section beyond the junction with the secondary channel would give an additional pressure-drop contribution, thus causing an extra excitation to the *balloon* membrane. A focus on the effect of a single droplet on the flow profile in the secondary channel is shown in Fig. 10b. When the front meniscus of a confined droplet crosses the junction region between the main and the secondary channel, the flow-rate rises above the equilibrium baseline (Fig. 10b-1). In fact, as a portion of the confined droplet penetrates the section of the main channel after the junction, the hydraulic resistance in this section increases accordingly. Consequently, the droplet experiences a fingering phenomenon (Fig. 10b-2) until reaching a maximum finger length corresponding to a local maximum in the flow profile (Fig. 10b-3). The finger then moves backwards into the main channel in search of a lower energy state, as described by the slight decrease in inwards flow, until the back droplet meniscus opens a tunnel in the secondary channel (Fig. 10b-4). This, together with the presence of the whole confined droplet volume

"plugging" the channel after the junction, leads to a further increase in hydraulic resistance after the junction (Fig. 10b-5), thus to a larger volume of oil inflating the *balloon*. The presence of an increasing number of confined droplets in the section after the secondary channel could cause a dramatic increase in the hydraulic resistance of the branch, leading the *balloon* to an out of equilibrium inflated state. In this way, the obtained droplet deformation would depend on the position of the droplet in the train and an upper value for the number of processed droplets should be fixed in order to avoid a too high hydraulic resistance for the system, leading to the extreme case of *balloon* breaking. To guarantee an uniform deformation for different droplets and to make the system independent from the number of processed units, an 8-fold increase in channel cross-section was introduced after the junction in order to allow droplet de-confinement, therefore to minimize the contribution of the droplets in the hydraulic resistance of the channel after processing. As soon as the droplet is deconfined (Fig. 10b-6), the flow inwards the secondary channel decreases and the *balloon* subsequently deflates (negative portion of the curve) in order to restore its equilibrium position according to the applied pressure. In this way, a reproducible and homogeneous deformation for different droplets in a train can be achieved. Finally, stopping the flow, the *balloon* completely deflates as shown by the negative profile, symmetric to the one obtained during the initial inflation of the *balloon* (Fig. 10a, green box).

The presented *balloon* behaviour can be compared in an electric circuit analogy to a capacitor. The whole microfluidic network was then modelled using an electrical analogy. Interestingly, the developed circuit is able to simulate the dynamic presence of a droplet in a channel, reproducing the main features of

the previously described flow-profile measured in the secondary dead-end channel. (See Supplementary Note 1).

Fluid dynamics parameters controlling the finger length

The presence of a pressure-driven component of variable volume in the secondary channel led to a non-negligible flow inwards this dead-end section, thus to a droplet fingering phenomenon in this channel. Together with the pressure gradient, the maximum droplet finger length achieved depends on the pressure gradient, on the compliance of the *balloon*, and on the length L of the main channel section between the junction with the secondary channel and the transition to the larger cross-section (see Fig. 11a). In particular, exploiting the same experimental set-up (without flow-meter) and flow conditions as in the previous experiment, three lengths were investigated, namely L=0.5mm, 1mm and 2.5mm, and the respective droplet maximum finger lengths were measured. In each case, an average over 70 droplets was performed. The results, reported in Fig. 11b, show decreasing finger lengths corresponding to a reduction in the distance L. In fact, for L=0.5mm and L=1mm, the droplet front section enters in the deconfinement channel while its body experiences a fingering. This geometric change in the channel cross-section confining the droplet induces a difference in curvature radius between the front and the rear meniscus of the droplet, thus leading to a difference in Laplace pressure inside the droplet that will push it towards the larger cross-section channel and therefore interfere with the maximum droplet fingering reached. On the other hand, a distance L=2.5mm is sufficient to entirely confine a single 100nL droplet in a

homogenous section of the main channel during the complete fingering process and, for these reasons, was chosen as the final length in the device design. To allow a reproducible fingering between different droplets in a train, the oil gap between two droplets should be at least equal to 300nL, to allow deconfinenent of the previous droplet, and return of the *balloon* equilibrium position before the next droplet is processed. Longer channel length L would still avoid the influence of Laplace pressure, but the possibility to accommodate more than one droplet would complicate the hydrodynamic behaviour, and represents a hindrance for the control of the fingering phenomenon: the overall pressure in the section beyond the capture region would increase and higher oscillations between pressure levels are expected due to the variable number of droplets in this section.

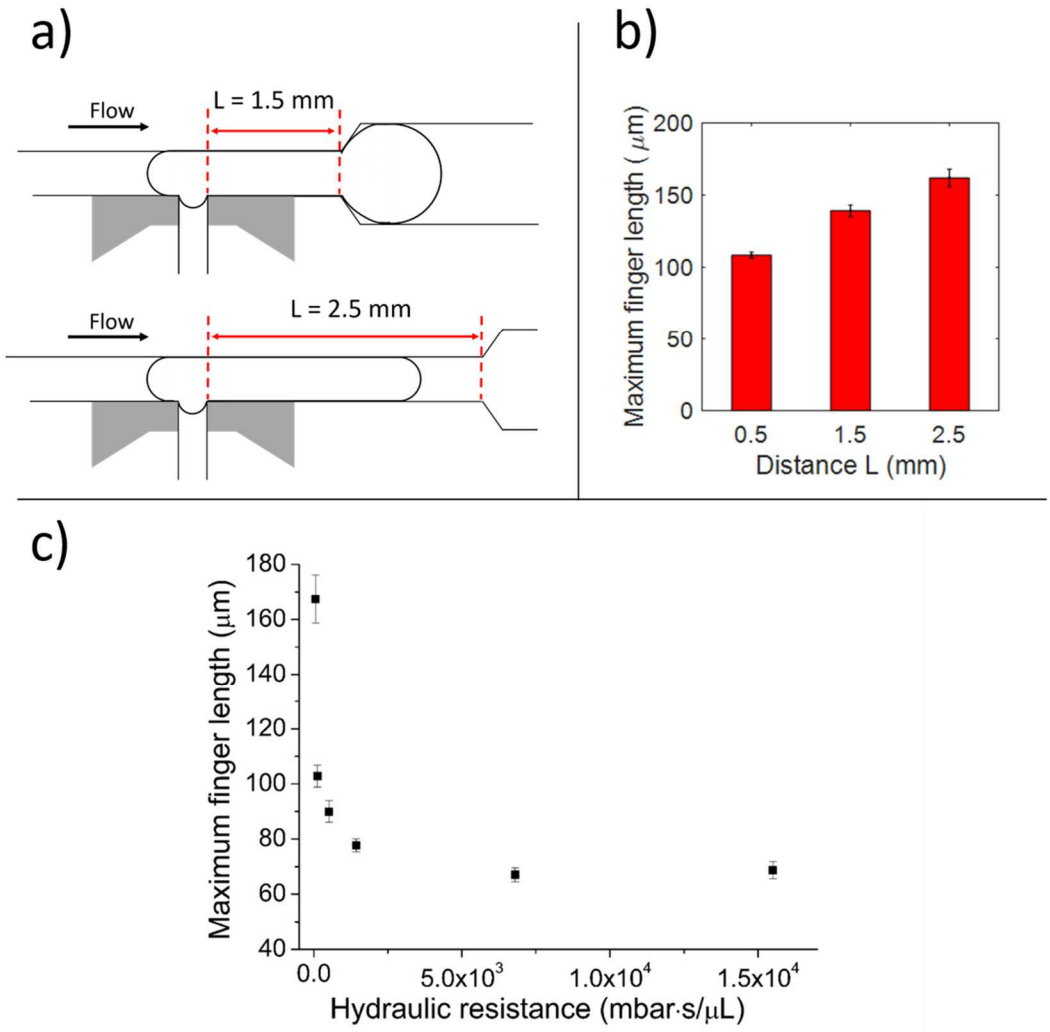

Figure 11: (a)-(b) Maximum droplet finger length as a function of different distance L between the capture region and the increase in channel cross-section. *In this study, 100nL droplet flowing at 0.25 μL/s were considered. An Ecoflex balloon (radius R=1mm) is included in the secondary channel. Internal droplet Laplace pressure influences negatively the achieved finger length for L shorter than 1mm.* ***(c) Effect of increasing hydraulic resistance values in the secondary dead-end channel on the fingering phenomenon.*** *An increasing hydraulic resistance results in decreasing maximum finger length until reaching the limit case in which the flow induced by the balloon presence is overridden by the high hydraulic resistance.*

The contribution of the secondary channel fluidic resistance on the droplet fingering was finally investigated. Droplets finger length was measured in different fluidic resistance conditions, achieved by installing tubing of increasingly smaller cross-section in series with the secondary channel. The results, reported in Fig. 11c, show that, as expected, an increase in channel fluidic resistance causes a decrease in droplet maximum finger length, leading to the extreme case in which the effect of the *balloon* is completely overridden by the hydraulic resistance. Therefore, the lower fluidic resistance tested (about 170 mbar $\cdot$ s/µL) was chosen as optimal for the final experimental set-up.

The definition of these design features allows to complete the hydrodynamic aspects of device conception. This geometry will be used for the following finger length characterization, in which the effect of different fabrication materials for the *balloon*, chamber radius and carrier oil flow-rates will be investigated.

Characterization of *balloon* properties

As previously described, the introduction of a variable volume component can induce a droplet fingering phenomenon in response to a pressure increase in the channel portion beyond the *trap*, due to the presence of the droplet itself, invading this section. The maximum finger length induced by the *balloon* has to be sufficiently long to define a volume penetrating in the capture region able to accommodate the entire cluster of particles and to allow them, at the same time, to reach the *trap* meeting no resistance from the droplet interface. A too long finger, however, would affect the purification efficiency of the device (retaining a volume larger than the magnetic aggregate's size) or cause an

undesired direct droplet break-up at the junction. To fulfil these conditions, the finger length has to be tuned as a function of the particle load in the droplet; for example, a droplet finger between 175µm and 200µm is required for a particle load of 1µg.

In order to quantify the effect of the *balloon* presence on the droplet fingering and to define the optimal *balloon* conditions for our aim, different materials and chamber sizes were investigated and compared with the case in which no variable-volume component is present in the dead-end secondary channel. In particular, chamber radius ranging between 1mm and 3.84mm were investigated and two elastomeric siloxanes materials were considered, PDMS in a 1:20 (w/w) base to curing agent formulation and Ecoflex (00-50 Shore hardness), characterized by a Young modulus of 0.50MPa and 0.26MPa, respectively. The study was performed in absence of magnetic field, to focus on the hydrodynamics of the system. In particular, 100nL droplets were pushed in the chip at different flow-rates for the continuous phase, ranging between 0.10µL/s and 1.00µL/s. The droplet finger evolution in time was measured by image processing and its maximum value was plotted against the carrier flow-rate. The results obtained for different *balloon* sizes and materials are shown in Fig. 12a. Each point is an average of 70 independent droplets.

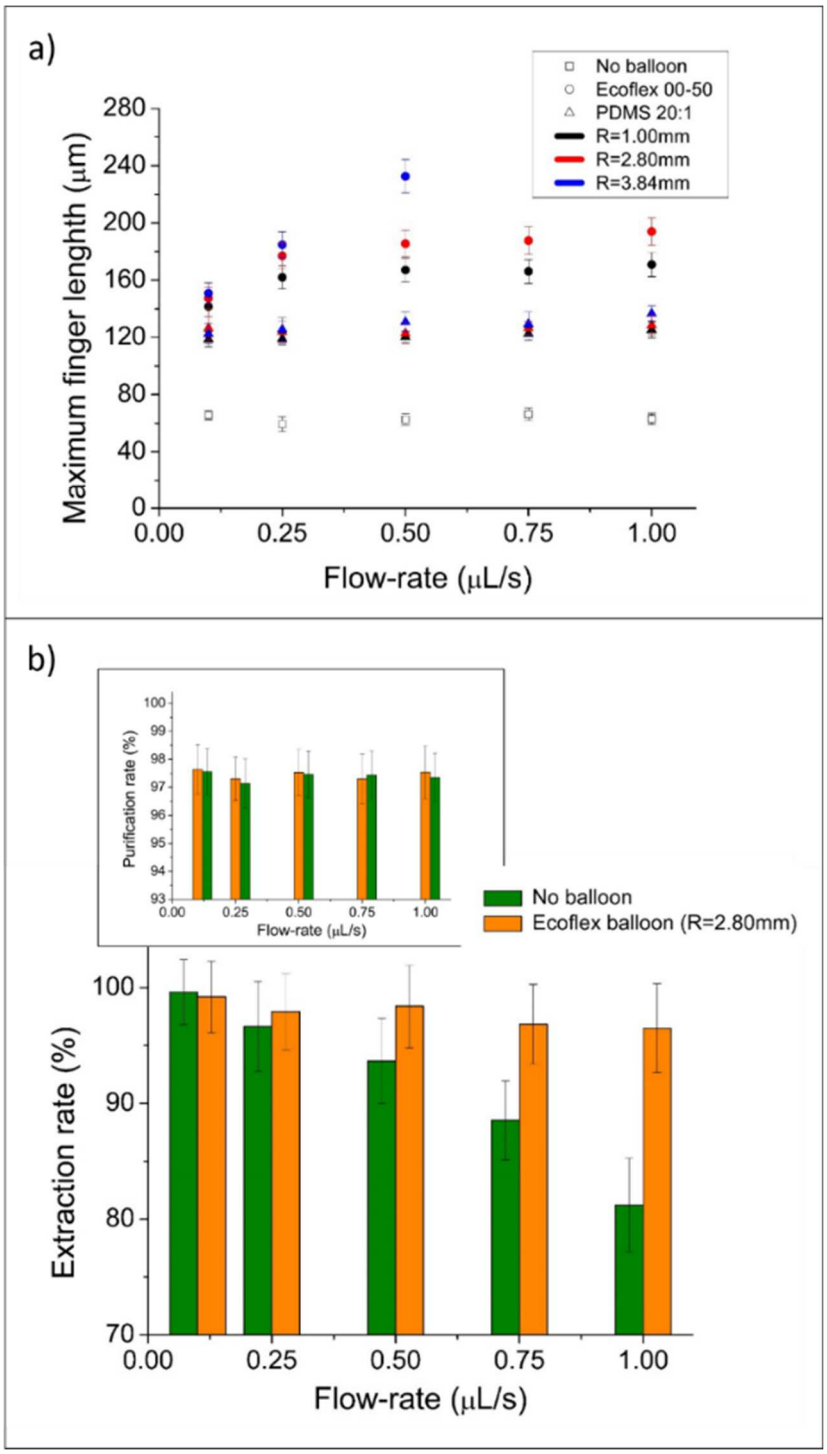

Figure 12: a) Maximum droplet finger length as a function of the carrier oil flow-rate achieved in different balloon conditions. *In particular, two fabrication materials, i.e. PDMS in a 20:1 base to curing agent formulation (represented as triangles) and Ecoflex 00-50 (represented by circles) were investigated. Furthermore, different chamber radius R were tested: R=1.00mm (black points), 2.80mm (red points) and 3.84mm (blue points). A negative*

control in absence of a balloon in the secondary channel was also performed. Ecoflex balloons systematically induce longer finger lengths than PDMS ones. The former material also shows increasing deformations as a function of the chamber radius, causing the direct droplet break-up for R=3.84 and flows higher than 0.5µL/s. Differently, considered chamber radii do not affect droplet fingering in the case of PDMS components. ***b) Extraction and purifications efficiencies for 100nL droplets containing a particle load of 1µg as a function of the carrier oil flow-rate.*** *The optimized setup, including a variable volume component characterized by a radius R=2.80mm, allows to reach extraction efficiencies higher than 97% for flow-rates up to 1.00 µL/s (orange bars). These performances were compared to the case in which no balloon is present in the secondary channel (green bars). In the inset, the purification efficiencies as a function of the carrier oil flow-rate were reported.*

Independently from the chamber radius and oil flow-rate, Ecoflex 00-50 as a fabrication material, due its lower elastic modulus, systematically presents larger droplet deformations (represented as full circles) with respect to 20:1 PDMS (represented by full triangles) from 1.2 to 1.7-folds depending on the flow-rate. Furthermore, the latter presents uniform finger lengths as a function of both the droplet flow-rates and the chamber radius considered, oscillating around 120µm. Differently, for a fixed flow rate, Ecoflex components led to a droplet finger increase as a function of the chamber size. Furthermore, for a radius of 1.00mm (black full circles) and 2.80mm (red full circles), the resulting deformations increase by raising the flow-rate from 0.10 µL/s to 0.25µL/s but keep a constant level beyond this value, achieving a deformation of about 165µm and 185µm, respectively. On the other hand, an Ecoflex chamber characterized by a radius of 3.84mm (blue full circles) causes an increasing finger length as a function of the carrier flow-rate and leads to a droplet direct break-up for flow rates higher than 0.50µl/s (not represented in the graph). A further negative control in absence of the *balloon* is also included (black empty circles). This aimed at the quantification of the contribution to droplet finger length given

by the elasticity of the secondary channel portion belonging to the main device and fabricated in 10:1 PDMS. As a result, an average constant droplet deformation of about 60µm was found.

In conclusion, the introduction of a variable volume component in the secondary dead-end channel leads to a significant contribution for the improvement of the fingering phenomenon. Its effect on the extraction and purification performances of the device will be discussed in the next section.

Final optimized device performances

Following the *balloon* characterization presented in the previous paragraph, a chamber with a radius of 2.80mm and fabricated in Ecoflex is chosen due to the achieved finger length, particularly adapted to a particle load of 1µg. Furthermore, based on the numerical simulations and on the previous capture rates results in the case of a capture pocket, a magnetic PDMS doping concentration of 71.4% was preferred to the other formulations investigated. These conditions were chosen to perform magnetic particles extraction in 100nL droplets, containing a particle load of 1µg and transported, as before, in a continuous flow of oil ranging between 0.10 µL/s and 1.00 µL/s. The extracted cluster will be then released in an incoming 100nL droplet containing water. As a comparison, the same experiment was repeated in the same conditions but in absence of the variable volume component in the secondary channel. The results, presented in Fig.12b, show that the coupling of the soft magnets with a variable volume component allows to reach extraction rate higher than 97% for carrier oil values up to 1.00 µL/s (orange bars), as compared to about 80%

in the absence of such component (green bars). Furthermore, no side effects on the purification rates are reported (see inset in Fig.12b), as is the case for other continuous droplet microfluidics systems[46]. Our passive *balloon* strategy offers, in fact, a 2.5x gain in the time spent by the magnetic cluster to reach the capture region, with respect to the case in which no variable volume component is present in the secondary channel (green bars). Finally, a maximum processing velocity of about 17mm/s, resulting in a throughput of few Hz, can be achieved by our system for the whole extraction and redispersion process, one order of magnitude faster than the performances obtained by the magnetic tweezers technology.

4 Conclusion

We presented a new droplet microfluidic concept, based on the manipulation of magnetic particles by a pair of integrated soft magnetic components, for the extraction and purification of molecules of interest and for the implementation of multi-steps protocols.

In our approach, a pair of soft magnets, whose design was optimized by numerical simulations, is able to generate an intense and local magnetic force along the path of the droplet. This confines the magnetic beads in a compact cluster and generates a magnetophoretic force attracting it in the *trap* region between the components. The particles exert a magnetic force on the droplet meniscus, causing its deformation and resulting in the generation of a droplet finger accommodating the cluster of particles. This magnetically-driven droplet configuration supported its hydrodynamically-assisted splitting, leading to the

generation of a daughter droplet, enriched with particles and characterized by an extremely low carryover of supernatant (<5% of the parent droplet volume) in the range of particle load between 100ng and 10µg.

Furthermore, the soft magnets were coupled to a pressure-driven variable volume component allowing a passive and controlled self-triggered droplet fingering in a dead-end channel. This strategy allowed avoiding the interfacial resistance of the water/oil meniscus, which slows down the cluster dynamics towards the capture region, thus negatively affecting the extraction rate for high flow-rates. This final device configuration extended the range of reliable device functionalities (capture efficiency>97%) up to 1.00µL/s, thus showing important improvement with respect to previous works. In particular, the achieved processing rate is one order of magnitude higher than the one of the magnetic tweezers technologies, chosen as paradigm for the state-of-the-art of this class of continuous droplet microfluidics devices allowing the implementation of the complete extraction and redispersion process. Despite, other continuous droplet systems still allow a higher throughput than our approach, this was obtained at the price of lower purification efficiencies. Furthermore, these systems are limited to enrichment protocols and do not allow the redispersion of beads in a new buffer. This complicates the implementation of numerous typical biological protocols in which buffer exchange is necessary, such as washing steps or immunoassay reactions.

A specific *balloon* configuration was selected as optimal for the flow conditions and beads loads took into account in this work; nevertheless, different materials or chamber sizes have been investigated and can be exploited to generate a deterministic finger length, adapted to the magnetic particle load in the droplet.

This confers a high flexibility to our device in a wide range of potential particle loads, by simply modifying the additional variable volume component.

In addition, this concept is also suitable to be further down-scaled for applications requiring smaller volume droplets. In this case, the channel dimensions should be resized accordingly in order to keep the droplet in a confined state. Furthermore, although the soft magnets design can be downscaled in order to maintain an effective magnetic force vector field distribution, the material and the consequent fabrication process should be modified in order to generate a higher magnetic force, able to deform the droplet meniscus.

Finally, we believe that the presented concept includes the main features required for the implementation of rapid and reliable extraction and enrichment multi-steps processes, and could represent a key technology for the down-scaling of further biochemical protocols in the future.

Supplementary information

4.1 Supplementary Note 1

The behaviour of the pressure-driven variable volume component can be easily understood by analogy with a capacitor. Aiming at the measure of the characteristic charge time of the *balloon*, the secondary channel branch of our microfluidic network was connected to a pressure controller while the other end was kept closed with a valve, after having filled the whole circuit with oil. Furthermore, a flow-meter (M, by Fluigent), was added in series to the channel to monitor the flow inwards the *balloon* while different pressures were applied at the inlet. The flow-rate corresponding to an applied pressure of 20mbar is reported in Fig.S1a) and Fig.S1b) for a PDMS and an Ecoflex component, respectively, both having a radius of 1mm. The resulting data sets were fitted with an exponential decay function and the characteristic times for the two components were extrapolated. In particular, a characteristic time of 0.41s and 1.43s were found for PDMS and Ecoflex, respectively. Interestingly, larger characteristic time corresponds to higher *balloon* capacitance, thus longer finger length achieved. This also implies a larger time needed for the fully discharge of the *balloon* during droplet crossing.

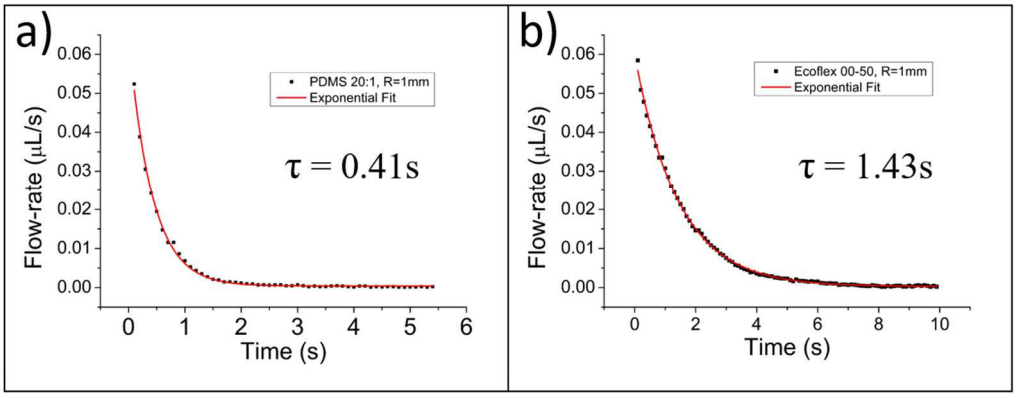

Fig. S1: Experimental data showing the time-resolved flow inwards the capture region during the balloon charge stage. *An Ecoflex 00-50 and PDMS balloons were investigated, both having a radius of 1mm. The red curves represent an exponential decay fit of the data points. A characteristic time for the charge process is deduced from the fitting.*

The fluidic/electric analogy *balloon*/capacitance was further extended by the definition of an equivalent electric circuit (in Fig. S2), which simulates the dynamic behaviour of the microfluidic network developed in this work during the crossing of a train of droplet. The labels on the circuit elements refer to the different sections and components of the microfluidic circuit.

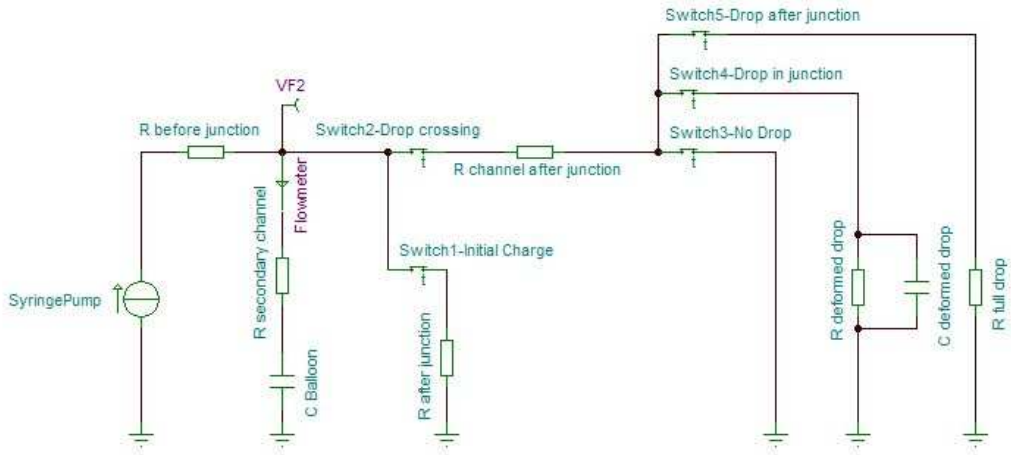

Fig. S2: Electric circuit modelling the microfluidic network of this work.

At time t=0, the Switch1 is closed while the Switch2 is open. The current flowing in the network charges the capacitor and the current value measured in the branch containing the capacitor decreases accordingly until reaching a steady equilibrium state in which the inwards current is zero, corresponding to the fully charged capacitor. When a droplet reaches the device, Switch1 opens while Switch 2 closes. The droplet crossing the capture region is separated in three independent stages, activated one by one sequentially and controlled by the Switch3, Switch4 and Switch5:

- ***Stage 1*** (Switch3 closed, Switch4 open, Switch 5open): the droplet is in the channel portion before the capture region. The network section beyond the *trap* is characterized by the hydraulic resistance of the channel "R channel after junction".
- ***Stage 2*** (Switch3 open, Switch4 closed, Switch 5open): the front droplet meniscus reaches the capture region and invades the section beyond the junction with the secondary channel. The portion of the droplet after the junction increases and, at the same time, the droplet experiences a fingering. These events are modelled by a parallel RC circuit (where R is "R deformed drop" and C corresponds to "C deformed drop") added in the branch controlled by Switch4.

- ***Stage 3*** (Switch3 open, Switch4 open, Switch 5 closed): the droplet rear meniscus crosses the capture region. The whole droplet volume is now in the channel portion beyond the junction with the secondary channel. A further contribution to the resistance of this branch is added (R full drop).

Once the droplet is deconfined, the system goes back to Stage 1 and these stages sequence is repeated. The simulated electric current profile measured in the branch of the circuit containing the capacitor is reported in Fig. S3a.

In conclusion, we presented here a simple model, based on an electrical analogy, to describe the flow inwards a secondary dead-end channel containing a variable volume component. The preliminary results show an estimated profile for the current in the secondary channel presenting the typical features of the flow profile generated by a droplet during its passage across the capture region junction (Fig. S3b). However, a short-term perspective will be to refine this model, especially focusing on the portion of the curve corresponding to the droplet deconfinement.

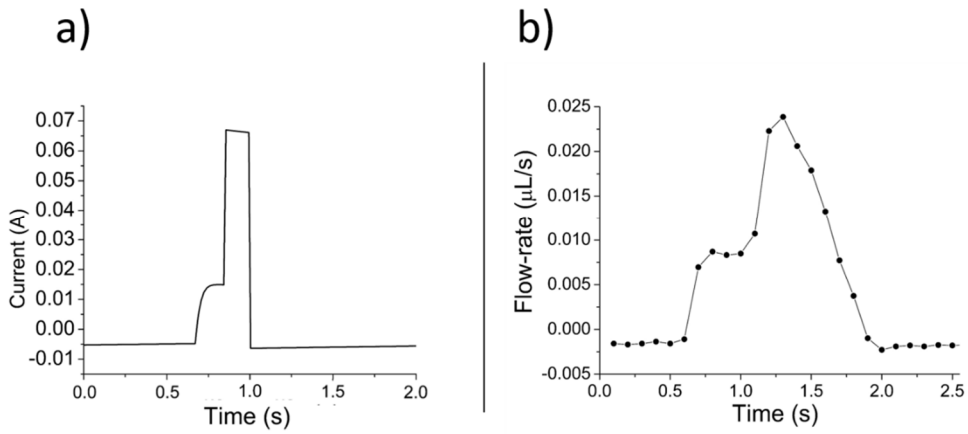

Fig.S3: Electric current profile in the branch containing the capacitor during the simulated crossing of a droplet (a) compared to the experimentally measured flow-rate (b) of Fig.10b.

References

1 S.-Y. Teh, R. Lin, L.-H. Hung and A. P. Lee, *Lab Chip*, 2008, **8**, 198.

2 L. Shang, Y. Cheng and Y. Zhao, *Chem. Rev.*, 2017, **117**, 7964–8040.

3 T. S. Kaminski, O. Scheler and P. Garstecki, *Lab Chip*, 2016, **16**, 2168–2187.

4 S. Mashaghi, A. Abbaspourrad, D. A. Weitz and A. M. van Oijen, *TrAC Trends Anal. Chem.*, 2016, **82**, 118–125.

5 N. Shembekar, C. Chaipan, R. Utharala and C. A. Merten, *Lab Chip*, 2016, **16**, 1314–1331.

6 P. Zhu and L. Wang, *Lab Chip*, 2017, **17**, 34–75.

7 M. Chabert, K. D. Dorfman and J.-L. Viovy, *Electrophoresis*, 2005, **26**, 3706–15.

8 R. Seemann, M. Brinkmann, T. Pfohl and S. Herminghaus, *Rep. Prog. Phys.*, 2012, **75**, 16601.

9 H.-D. Xi, H. Zheng, W. Guo, A. M. Gañán-Calvo, Y. Ai, C.-W. Tsao, J. Zhou, W. Li, Y. Huang, N.-T. Nguyen and S. H. Tan, *Lab Chip*, 2017, **17**, 751–771.

10 M. Chabert and J.-L. Viovy, *Proc. Natl. Acad. Sci. U. S. A.*, 2008, **105**, 3191–6.

11 M. Serra, D. Ferraro, I. Pereiro, J.-L. Viovy and S. Descroix, *Lab Chip*, 2017.

12 M. Shikida, K. Takayanagi, K. Inouchi, H. Honda and K. Sato, *Sensors Actuators B Chem.*, 2006, **113**, 563–569.

13 F. R. Cui, J. Wang, S. M. Opal and A. Tripathi, *PLoS One*, 2016, **11**, e0149522.

14 M. C. Park, M. Kim, G. T. Lim, S. M. Kang, S. S. A. An, T. S. Kim and J. Y. Kang, *Lab Chip*, 2016, **16**, 2245–53.

15 Y. Zhang, S. Park, K. Liu, J. Tsuan, S. Yang and T.-H. Wang, *Lab Chip*, 2011, **11**, 398–406.

16 U. Lehmann, S. Hadjidj, V. K. Parashar, C. Vandevyver, A. Rida and M. A. M. Gijs, *Sensors Actuators B Chem.*, 2006, **117**, 457–463.

17 J. Pipper, Y. Zhang, P. Neuzil and T.-M. Hsieh, *Angew. Chem. Int. Ed. Engl.*, 2008, **47**, 3900–4.

18 S. M. Berry, E. T. Alarid and D. J. Beebe, *Lab Chip*, 2011, **11**, 1747–53.

19 H. Chen, A. Abolmatty and M. Faghri, *Microfluid. Nanofluidics*, 2011, **10**, 593–605.

20 H. Bordelon, N. M. Adams, A. S. Klemm, P. K. Russ, J. V Williams, H. K. Talbot, D. W. Wright and F. R. Haselton, *ACS Appl. Mater. Interfaces*, 2011, **3**, 2161–8.

21 S. M. Berry, H. M. Pezzi, A. J. LaVanway, D. J. Guckenberger, M. A. Anderson and D. J. Beebe, *ACS Appl. Mater. Interfaces*, 2016, **8**, 15040–15045.

22 R. C. den Dulk, K. A. Schmidt, G. Sabatté, S. Liébana and M. W. J. Prins, *Lab Chip*, 2013, **13**, 106–18.

23 M. J. Jebrail, M. S. Bartsch and K. D. Patel, *Lab Chip*, 2012, **12**, 2452.

24 K. Choi, A. H. C. Ng, R. Fobel and A. R. Wheeler, *Annu. Rev. Anal. Chem.*, 2012, **5**, 413–440.

25 Y. Fouillet, D. Jary, C. Chabrol, P. Claustre and C. Peponnet, *Microfluid. Nanofluidics*, 2008, **4**, 159–165.

26 R. Sista, Z. Hua, P. Thwar, A. Sudarsan, V. Srinivasan, A. Eckhardt, M. Pollack and V. Pamula, *Lab Chip*, 2008, **8**, 2091–104.

27 A. H. C. Ng, K. Choi, R. P. Luoma, J. M. Robinson and A. R. Wheeler, *Anal. Chem.*, 2012, **84**, 8805–12.

28 D. Lombardi and P. S. Dittrich, *Anal. Bioanal. Chem.*, 2011, **399**, 347–352.

29 H. Lee, L. Xu and K. W. Oh, *Biomicrofluidics*, 2014, **8**, 44113.

30 A. Ali-Cherif, S. Begolo, S. Descroix, J.-L. Viovy and L. Malaquin, *Angew. Chemie Int. Ed.*, 2012, **51**, 10765–10769.

31 D. Ferraro, J. Champ, B. Teste, M. Serra, L. Malaquin, J.-L. Viovy, P. de Cremoux and S. Descroix, *Sci. Rep.*, 2016, **6**, 25540.

32 T. D. Mai, D. Ferraro, N. Aboud, R. Renault, M. Serra, N. T. Tran, J.-L. Viovy, C. Smadja, S. Descroix and M. Taverna, *Sensors Actuators B Chem.*, 2017.

33 D. Ferraro, Y. Lin, B. Teste, D. Talbot, L. Malaquin, S. Descroix and A. Abou-Hassan, *Chem. Commun.*, 2015, **51**, 16904–16907.

34 B. Teste, J. Champ, A. Londono-Vallejo, S. Descroix, L. Malaquin, J.-L. Viovy, I. Draskovic and G. Mottet, *Lab Chip*, 2017, **17**, 530–537.

35 B. Teste, N. Jamond, D. Ferraro, J.-L. Viovy and L. Malaquin, *Microfluid. Nanofluidics*, 2015, **19**, 141–153.

36 A. Sayah, V. K. Parashar, A.-G. Pawlowski and M. A. M. Gijs, *Sensors Actuators A Phys.*, 2005, **125**, 84–90.

37 D. W. Inglis, R. Riehn, R. H. Austin and J. C. Sturm, *Appl. Phys. Lett.*, 2004, **85**, 5093–5095.

38 N. Xia, T. P. Hunt, B. T. Mayers, E. Alsberg, G. M. Whitesides, R. M. Westervelt and D. E. Ingber, *Biomed. Microdevices*, 2006, **8**, 299–308.

39 S. S. Shevkoplyas, A. C. Siegel, R. M. Westervelt, M. G. Prentiss and G. M. Whitesides, *Lab Chip*, 2007, **7**, 1294.

40 J. Li, M. Zhang, L. Wang, W. Li, P. Sheng and W. Wen, *Microfluid. Nanofluidics*, 2011, **10**, 919–925.

41 J. Keyes, M. Junkin, P. K. Wong and J. P. Vande Geest, *Biomed. Microdevices*, 2009, **11**, 1259–67.

42 M. Faivre, R. Gelszinnis, J. Degouttes, N. Terrier, C. Rivière, R. Ferrigno and A.-L. Deman, *Biomicrofluidics*, 2014, **8**, 54103.

43 R. Zhou and C. Wang, *Microfluid. Nanofluidics*, 2016, **20**, 48.

44 L. Ménétrier-Deremble and P. Tabeling, *Phys. Rev. E*, 2006, **74**, 35303.

45 J.-C. Baret, *Lab Chip*, 2012, **12**, 422–33.

46 E. Brouzes, T. Kruse, R. Kimmerling and H. H. Strey, *Lab Chip*, 2015, **15**, 908–919.

Chapter 4

Towards library preparation for Next Generation Sequencing (NGS)

In the previous chapter, we presented the conception, fabrication and characterization of an innovative microfluidic device for the manipulation of solid-phase supports in droplet microfluidics based on the integration of a pair of soft magnets placed adjacently to a microchannel. We also exploited a droplet fingering phenomenon in the magnetic beads capture region to prevent the slow-down in the beads cluster dynamics while reaching the trap, due to the opposing droplet interfacial force. In particular, we demonstrated the possibility to induce and passively control this droplet self-triggered fingering phenomenon in a dead-end channel by the introduction of a pressure-driven variable volume component, leading to improved beads extraction performances of the device. Furthermore, we showed that the design and fabrication material of this additional component influence the maximum droplet finger length achieved. We thus evidenced that these parameters must be carefully chosen as a function of the magnetic particle load in a droplet to not affect negatively the purification efficiency of the device or to cause undesired droplet breaking. With

the same aim and based on the same principle, a more elegant solution will be presented in this chapter, where the fingering phenomenon in the capture region will be finely tuned by controlling the pressure applied on the main and secondary channel outlets. In this way, the range of processing velocities of our system will be slightly extended, while keeping optimal extraction and redispersion rates.

The second part of this chapter reports on the application of our pressure-controlled approach to libraries preparation for Next Generation Sequencing (NGS). This protocol represents a critical step for the following sequencing process, strongly influencing its outcomes. Although microfluidics can contribute to the workflow simplification, increasing both its throughput and automation while allowing sample volume reduction, only few works are presented based on this technology, especially concerning droplet systems[1,2,3]. Here, we will specifically focus on the most demanding step of this workflow, i.e. the clean-up and size selection processes based on Solid Phase Reversible Immobilization (SPRI)[4]. The implementation in a droplet-microfluidic format of this method, common to every NGS sample preparation, independently from the sequencing technology used and from the specific application, will be thus presented in this chapter. The critical points of this protocol and the specific skills to be considered in its microfluidic version will be evidenced, especially regarding the operative functionalities to be integrated and the handled reagents used in the protocol (viscous fluids, organic solvent). Preliminary results about the on-chip DNA clean-up and size-selection integration will be presented, and future perspective will be finally discussed.

1 A pressure controlled-tuning of the droplet fingering

In the previous chapter, an innovative approach for the manipulation of magnetic beads in droplet microfluidic has been presented. This strategy is based on the integration of a pair of soft magnetic components placed adjacently to microchannel to generate an intense and local magnetic force along the path of a droplet. This magnetic force is able to confine the magnetic beads contained in the droplet in a compact cluster and to attract it in the capture region between the magnetic components. The trapped cluster exerts a magnetic force on the droplet meniscus, causing the formation of a finger in the capture pocket, containing the particle aggregate. This magnetically-driven droplet deformation assisted its hydrodynamics splitting at the junction between the capture pocket and the main channel, leading to the extraction of the cluster of particles from the droplet with an extremely low carryover of supernatant. Nevertheless, in this process, the meniscus interfacial force opposes the magnetophoretic cluster dynamics towards the trap, thus affecting the extraction performances of the device especially for flow-rates higher than 0.5µl/s. The introduction of a pressure-driven variable volume component in a dead-end channel (perpendicular to the main one and defined as an extension of the capture pocket) has been presented as a passive and simple solution to induce the droplet self-triggered fingering in the capture region, showing significant improvements on the extraction performances of the device but not altering the purification rate. However, the geometrical and material properties of the variable-volume component must be tuned as a function of the magnetic particle load in the droplet, in order to achieve the respective optimal finger length.

Here we report an alternative strategy for the control of the droplet fingering that can be achieved by setting a constant hydraulic resistance ratio between the main and the secondary channel. In fact, the introduction of a valve to delimit the dead-end channel is not necessary anymore, thus, an additional outlet for the device is defined. Experimentally, the hydraulic resistance ratio can be tuned by connecting both outlets of the device to pressurized reservoirs (Fig.1), whose constant pressure value is set by a pressure controller (MFCS, by Fluigent). In particular, the main channel outlet is connected to a reservoir kept at the atmospheric pressure while a higher constant pressure is applied to the reservoir connected to the secondary channel.

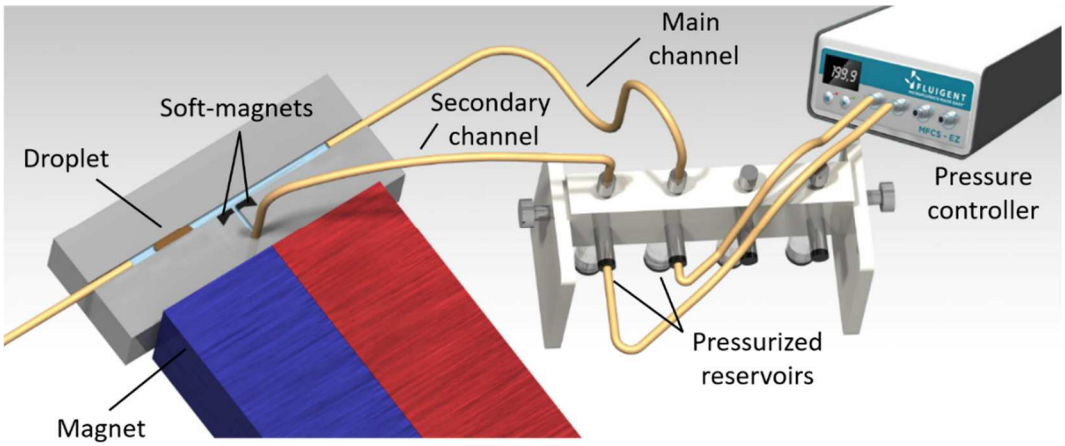

Figure 1: Improved version of the experimental setup. *The passive control, characterized by the presence of a pressure-driven variable volume component in the dead-end secondary channel delimited by the pinch valve, is now replace by an active control, achieved by connecting both outlet channels to two pressurized reservoirs, controlled by a pressure controller. In this way, the droplet splitting ratio can be precisely tuned.*

In this way, the splitting of the droplet can be precisely tuned to minimize the carryover of supernatant during the extraction. Fig. 2 shows an example of the effect of the applied pressure to the secondary channel on the extraction (in

green) and purification (in orange) efficiencies of 1µg of magnetic particles, loaded in a droplet (100nL volume) flowing at 0.8 µL/s. Increasing the applied pressure on the secondary channel, the purification efficiency increases until reaching maximum purification at a pressure of approximately 350mbar. As a matter of fact, for low applied pressures, the generated finger length will retain a larger volume than the magnetic cluster size, thus affecting the purification rate of the device. Beyond this value, the purification rate does not experience significant variations, as shown by the plateau region for pressures above 350mbar. On the other hand, the capture efficiency is not affected by the increase in pressure below 350mbar but it strongly decreases above this optimal value due to the limited finger length generated, causing a portion of the beads cluster to be dragged away from the capture region before being trapped in it; this portion keeps thus flowing in the parent droplet.

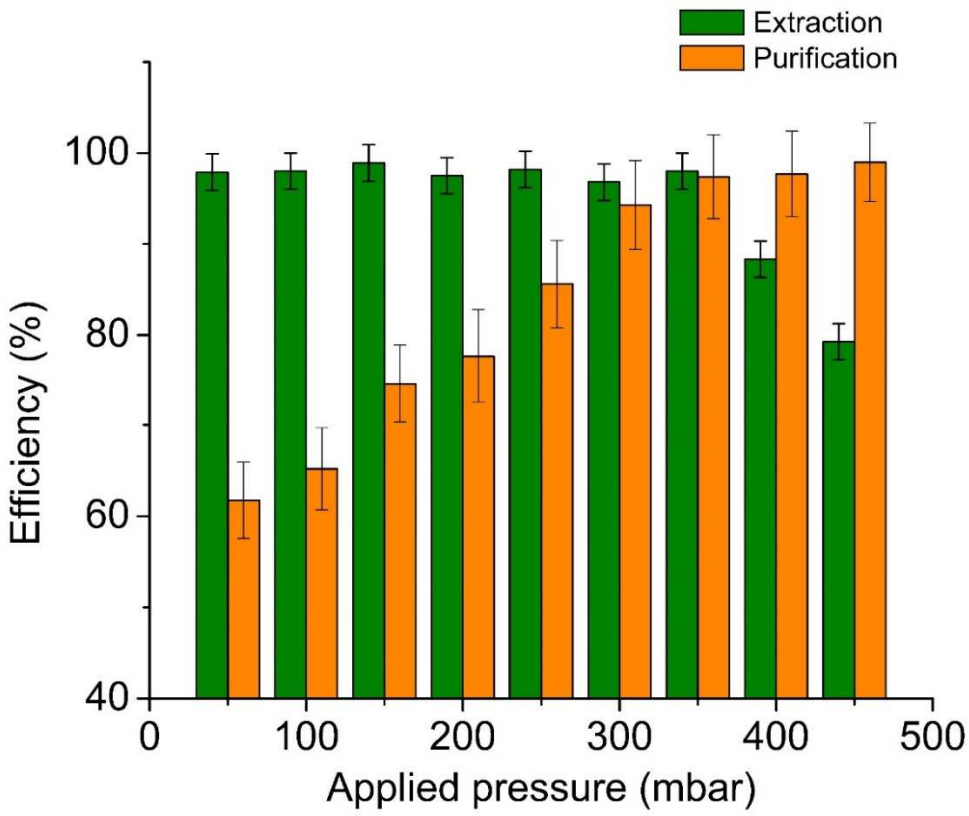

Figure 2: Effect of the applied pressure on the secondary channel on the extraction and purification efficiencies. *The data refers to a 100nL droplet flowing at 0.8 µl/s and containing a particle load Q=1µg. In these experimental conditions, 350mbar represents the optimal pressure to be applied to the secondary channel in order to maximize both the extraction and purification efficiencies.*

This characteristic behavior allows the biunivocal definition of an optimal pressure, that maximizes the device performances, associated to a specific carrier oil flow-rate. In particular, this study was performed for flow-rates ranging between 0.2µL/s and 1.6µL/s, and for 1µg of magnetic particles in the droplet. The resulting optimal pressures ranging between 90 mbar and 595 mbar (reported in Table 1) allows indeed to maximize the purification efficiency of the system (about 97%) and to make it independent from the oil flow-rate

transporting the droplet. These optimal values will be considered during the characterization of the device performance and for the implemented applications.

Table 1: *Optimized values for the secondary channel applied pressure as a function of the oil flow-rate in the secondary channel. The optimization process was performed considering 100nL droplet and a particle load of 1µg.*

Oil flow-rate in the main channel (µL/s)	**Applied pressure on the secondary channel (mbar)**
0.2	90
0.4	165
0.6	230
0.8	350
1.0	425
1.2	490
1.4	535
1.6	595

1.1 Extraction and purification efficiencies

The magnetic particle extraction and purification efficiencies were evaluated as a function of the carrier oil flow-rate for 100nL droplets loaded with 1µg particles. In particular, increasing flow-rates between 0.2µL/s and 1.6µL/s were applied; following the numerical and experimental results presented in the previous chapter, a magnetic particles/PDMS pre-polymer w/w doping ratio of 71.4% was preferred for the fabrication of the magnetic structures. In these conditions, the achieved beads capture efficiency is higher than 95% up to 1.2µL/s (Fig.3), significantly improving the maximum droplet processing

velocity with high extraction and purification performances (>95%) by a factor 2 and 12, with respect to other technologies devoted to simple magnetic separation[5] or allowing the whole extraction and release workflow[6], respectively. Furthermore, the achieved performances are comparable with those relative to the balloon, presented in the previous chapter.

Finally, the presented study confirms the possibility to replace the variable volume component by a pressure control of the device outlet, obtaining a more robust tuning of the droplet fingering with respect to the previous case without producing side effects on the purification or extraction rates of the device.

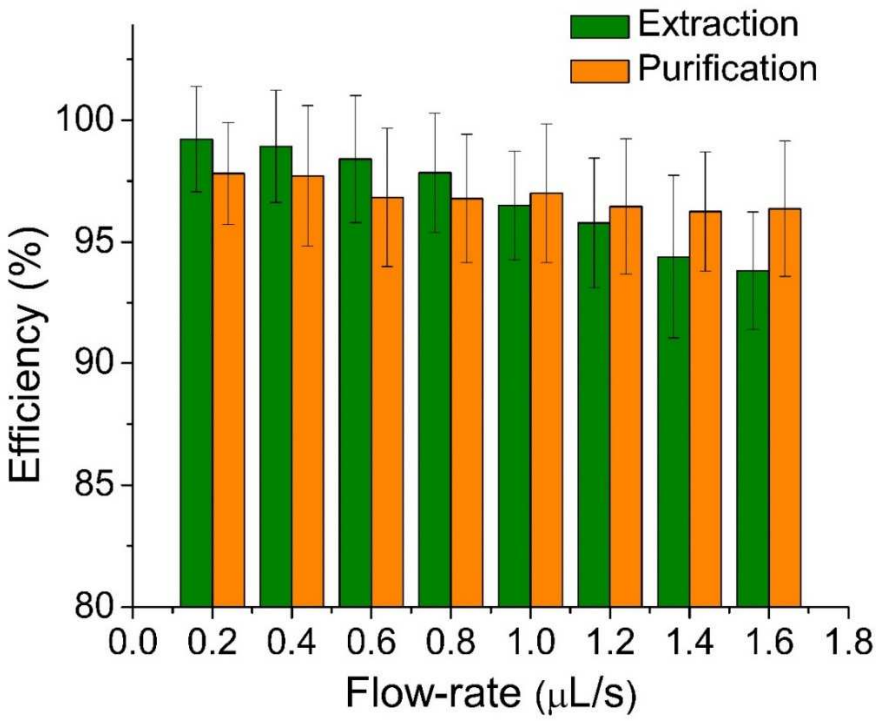

Figure 3: Extraction and purification performances as a function of the oil flow-rate for the 71.4% magnetic PDMS formulation, using the pressure-controlled approach. *It is worth noting that the extraction efficiency is higher than 90% and purification rate higher than 95% in the range of carrier oil flow-rates considered.*

2 The preparation of NGS libraries

So far, the conception, fabrication and characterization of an innovative droplet microfluidic concept was presented. From now on, the device functionalities above described will be exploited in an important and recent context, like the preparation of nucleic acids libraries for next generation sequencing applications.

2.1 Introduction

The development of next generation sequencing (NGS) represented a revolution in the genomics field, becoming a crucial tool in both biological and clinical research[7]. In the last decade, this technology, allowing the high-throughput and parallel sequencing of DNA fragments, showed steady improvements, resulting in costs dropping and in an exponential increase in number and range of sequencing applications[8]. Besides genome sequencing, NGS provides accurate information on the composition of complex DNA samples, representing thus a method of interest for all genomic applications, such as transcriptome analysis (RNA-Seq)[9], metagenomics[10,11], or profiling of methylated DNA (MeDip-seq)[12], or DNA-associated proteins (ChIP-Seq)[13]. Furthermore, new applications continue to be developed, together with wet lab and bioinformatics techniques, aiming at improving performance and addressing current limitations[14].

Before sequencing, the nucleic acids sample (RNA or DNA) is subjected to a series of enzymatic steps, commonly referred to as library preparation, in order to perform their conversion into a standard format compatible with a specific sequencing technology[15]. Despite the wide variety of NGS library preparation protocols, some common steps can be identified. In particular, the sequencing

library is at first prepared by the fragmentation of the DNA or cDNA sample (for RNA-sequencing), followed by the repair of the blunt ends and by the ligation at 3' and 5' extremities of adapters, containing the elements necessary for the immobilization on a solid surface (Fig.4). An alternative method, called tagmentation[16], combines fragmentation and ligation reactions into a single-step, thus increasing the efficiency of the library preparation process. These steps are usually followed by a size-selection step in order to remove free adapter and to select molecules in a specific range according to the machine specifications and to the sequencing applications. For example, for exome sequencing, more than 80% of human exomes are under 200bp in length[17]. Finally, libraries are amplified by Polymerase Chain Reaction (PCR). This step allows the successful enrichment of adapted fragments in order to achieve sufficient quantities of DNA for accurate quantification. Using specifically tailed primers, this step can also serve to introduce additional short sequences, or barcodes, in order to reduce the quantitative bias introduced by replication[18] (unique molecular identifiers[19], UMI) or to tag different samples, pooled in the same sequencing run[20]. A further sizing step is performed after the library construction in order to refine its size and to remove library preparation artefacts (like amplification errors), PCR primers and adaptor dimers (self-ligated adapters without a target library insert sequence). These will in fact consume a valuable space in the sequencing cell without generating useful data, thus affecting the sequencing efficiency. Importantly, the sequencing quality strongly depends on the library construction process. The latter should in fact guarantee the highest genomic coverage with the least amount of sequencing; therefore, a library with a balanced representation of all genomic area of

interest, both overly and low expressed, is required[21]. In this direction, important improvements have been made and are still ongoing, allowing the development of protocols for library preparations that more faithfully reproduce the starting nucleic acid sample, yielding higher quality in the resulting NGS data, thus facilitating their interpretation[22].

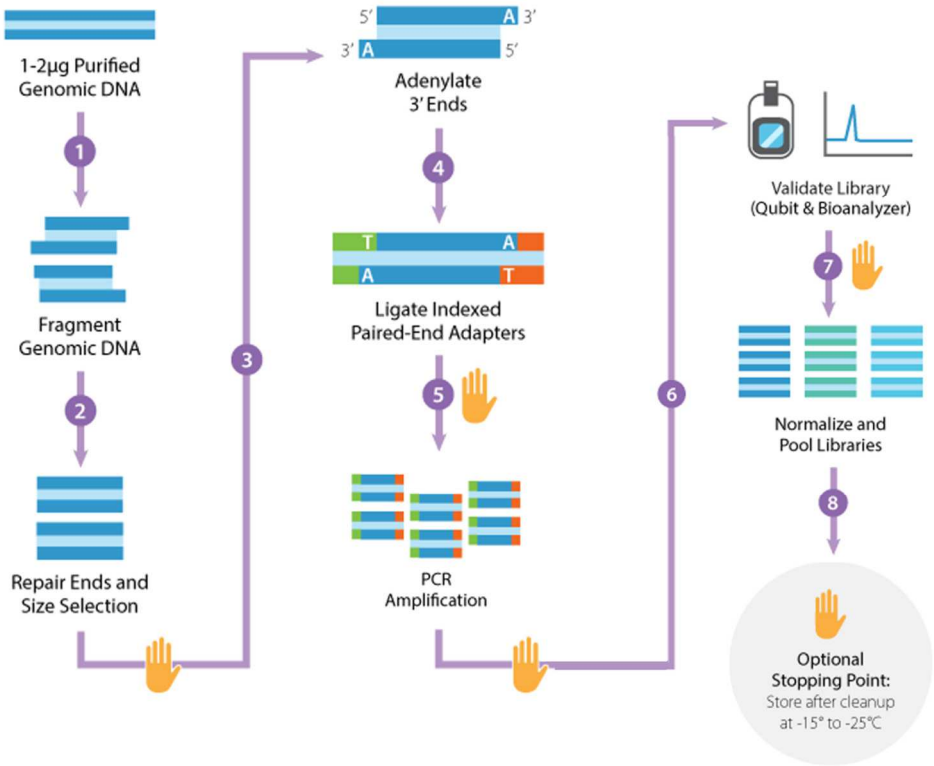

Figure 4: Example of NGS library preparation workflow. *This specific protocol refers to the Illumina TruSeq Nano DNA Library Prep Kit protocol (Image adapted from the Illumina manual).*

However, despite some proposed streamlined methods, like the tagmentation chemistry[23,24,25] described above, the preparation of template and properly formatted nucleic acids libraries still remains a multi-step process, whose main bottlenecks are the amount of time and resources required[21]. Few specific steps

of the protocol have been automated[26]; nevertheless, most of the preparation relies on manual and tedious operations. Robotic platforms represent possible solutions for automated and high-throughput library preparation, but they are not cost-effective for laboratories having limited demand. Moreover, they suffer from lack of flexibility in workflow customization, thus limiting the implementation of a wide variety of sample preparation protocols. In addition, the use of pipette, robotic or manual, limits the working volume and complicates the library preparation when the initial amount of sample is limited, as it may be the case in some clinical applications.

Microfluidics technology and architectures present specific features that could be valuable to answer these needs, like the precise control and manipulation of small volumes and the scalable automation, allowing an important reduction in the amount of input sample required and a considerable increase in the process throughput. However, only few microfluidic devices devoted to NGS sample preparation have been reported in literature so far. As an example, in single-phase microfluidics, microvalves integrated in a disposable PDMS chip have been exploited to implement a high-throughput library preparation workflow for genomic sequencing, now commercialized by Fluidigm[2,3]. This device enables a batch size up to 96 samples per device run and integrates all the step required for the Whole Genome Sequencing (WGS) sample preparation. In particular, this device includes several units devoted to cell lysis and DNA extraction, fragmentation and adaptors ligation by tagmentation, and the bead-based DNA purification steps required at multiple points of the sample preparation process. Differently, a droplet microfluidic approach was proposed by Kim et al.[1]. Their device is characterized by a central DMF hub, interfacing different peripheral

modules, constituted by capillaries and defining the different steps of the preparation protocol (depicted in different colours in Fig. 5). In particular, some tubing modules are coupled with external magnets and thermal blocks; multi-valve syringe pumps are used for the liquid handling in the device. Based on this platform the preparation protocol of human and bacterial genomic DNA samples were shown. Overall, this platform, characterized by a complex architecture, allows higher throughput with respect to manual protocol but does not integrate the cell lysis step and requires large input volume (in the microliter range).

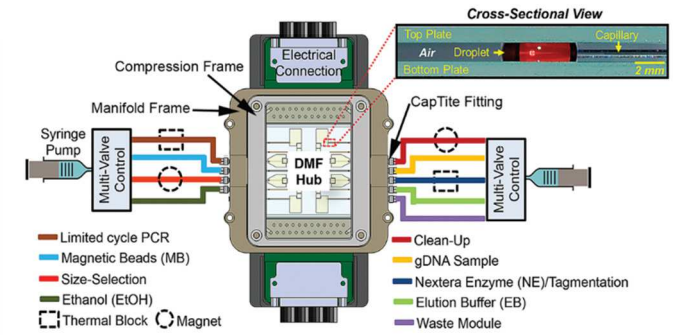

Figure 5: Top view of the system by Kim et al.[1] and side view of the DMF-capillary interface. *The different steps of the library preparation protocol are performed in separated tubing modules (defined with different colours), coupled with external*

In this context, we expect that better performances in term of throughput can be achieved with continuous droplet microfluidics devices, which recently gave important contribution showing single-cell[27,28] barcoding for NGS applications. However, the overall single-cell analysis workflow, characterized by a high-throughput cell and barcoding encapsulation, is later on slowed-down by the emulsion breaking and the manual in tube library construction, including sequential tagmentation, size-selection and thermal amplification steps.

Overall, despite the continuous droplet microfluidic modules devoted to merging and thermal amplification in multiphase systems have been widely demonstrated, a continuous droplet microfluidic device for DNA clean-up and size-selection has yet not been developed. This stage requires the implementation of both sequential capture/release sequences, including washing steps, and of the clean-up functionality, as discussed in the next paragraph.

2.2 Clean-up and size selection of DNA libraries for NGS applications

2.2.1 Overview

DNA size selection step has a major impact on the quality of the sequencing results. In particular, ineffective clean-up can waste sequencing capacity on low molecular weight material such as primer or adapter-dimers while imprecise sizing would affect the accuracy and complicates the data post-processing for sequences assembly. Overall, high-quality clean-up and size selection can improve sequencing efficiency, optimize the cost, facilitate and improve the reliability of the bioinformatics analysis and permits the sequencing of low and ultralow-input samples up to the single-cell level. However, each NGS technology requires different DNA input fragments to operate in an optimal way. For example, short-read sequencers, like Ion Torrent and Illumina systems require input DNA fragments in a specific range recommended by the manufacturer (overall, between 35 and 300 bp) in order to achieve an efficient sequencing[14]. On the other hand, other technologies like Oxford Nanopore or

Pacific Biosciences systems, produce read lengths in the thousands of bases per read and exploit the clean-up step to remove low molecular weight fragments focusing thus the sequencing capacity on the most amenable sequences to produce the longest reads[29].

In order to implement these clean-up and size selection protocols, different methods were proposed[26]. Among them, bead-based protocols represent a high-throughput and versatile approach; being also the most suggested technique by NGS suppliers in library preparation manuals. Besides, it is worth noting that this strategy is the most suitable and compatible with droplet microfluidic systems. Beads-based DNA purification protocols rely on solid-phase reversible immobilization method (SPRI)[4,30], in which carboxyl-coated magnetic microparticles can reversibly bind target DNA under high conditions of polyethylene glycol (PEG-8000) and salt concentrations. Briefly, DNA is a polar molecule, thus solvated in water. The sodium divalent cations, present in the buffer, shield the negatively charged phosphate of DNA backbone as well as the carboxylate functions at the surface of the beads. In these conditions the beads surface is no longer repulsive for DNA molecules. Introducing PEG in a DNA solution at saturating conditions, the DNA undergoes a structure transition, resulting in a compact random coil. When a hydrophilic molecule, like PEG, is added to the solution with specific salt concentration (Na^+), the DNA aggregates and precipitates out of solution from lack of solvation causing DNA to stick together and on the carboxylic beads present in the solution. The captured DNA can be then eluted by hydrating it with an aqueous solution (TE or water), allowing the DNA to restore its original shape in solution. In

these conditions, the DNA is repelled by the negative charge of the carboxyl-functionalized beads, allowing thus their extraction in the supernatant.

These elements and principles are the core components of several bead-based commercially available kit devoted to the DNA size selection and clean-up processes. Interestingly, the size of the target DNA can be tuned by controlling the PEG/NaCl concentration[31], i.e. varying the SPRI solution (containing these two molecules) to DNA sample volumes ratio. In particular, increasing the SPRI to DNA solution volume ratios (from about 1.5x to 2.5x, x being the initial volume of DNA sample), shorter fragments from the original sample will be captured on the beads while the precipitated fragments size will be longer when considering ratio to 1.0x or lower[29]. Based on this principle, a single SPRI step is exploited to clean-up from the solution fragments below a defined size (typically less than 100 bp, cf. Protocol 1). Furthermore, a tight DNA size range can be defined by performing a double size selection to define the upper and lower limit of the desired range (cf. Protocol 2 and Fig.6). In particular, at first a low concentration of SPRI solution is added to the sample, in order to bind to the beads the larger unwanted fragments that will be discarded. Next, in the resulting supernatant, the PEG and NaCl concentrations are increased by adding further SPRI solution, aiming at binding DNA fragments larger than the lower limit (Fig.6). The supernatant is then discarded, a beads washing step is performed and the target fragments are finally eluted.

Overall, the presented protocols describe the operations required to perform the clean-up and size selection protocols in-tube. However, the input fragments size depends on the sequencing machine used and on the desired application, thus the SPRI/DNA solution ratio must be adapted according to the insert size (i.e.,

the length of the sequence between adapters). In this work, the DNA size purification will be implemented considering the Agencourt AMPure XP (Beckman Coulter) solution; nevertheless, the presented device operations can be extended to any SPRI-based protocol devoted to DNA purification.

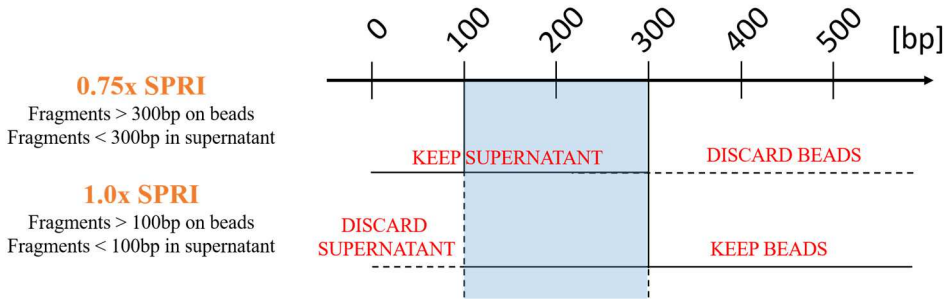

Figure 6: Workflow required for the double size-selection of a tight DNA range. *This scheme considers, as an example, the selection of DNA fragments between 100bp and 300bp.*

Protocol 1:

Clean-up using AMPure XP® Beads (Beckman Coulter, Inc.)

The following size selection protocol is for libraries with 100 bp insert from a 100 µl volume.

1. Vortex AMPure XP beads to resuspend.
2. Add 160 µl (1.6X) of resuspended AMPure XP Beads to the reaction. Mix thoroughly on a vortex mixer or by pipetting up and down at least 10 times.
3. Incubate for 5 minutes at room temperature.
4. Put the tube/PCR plate on an appropriate magnetic stand to separate beads from supernatant. After the solution is clear (about 5 minutes), carefully remove and discard the supernatant. Be careful not to disturb the beads that contain the DNA targets.
5. Add 200 µl of 80% freshly prepared ethanol to the tube/PCR plate while in the magnetic stand. Incubate at room temperature for 30 seconds, and then carefully remove and discard the supernatant.
6. Repeat Step 5 once.
7. Air dry beads for 5 minutes while the tube/PCR plate is on the magnetic stand with the lid open. **Caution: Do not overdry the beads. This may result in lower recovery of DNA target.**
8. Remove the tube/plate from the magnet. Elute the DNA target from the beads by adding 40 µl of 10 mM Tris-HCl or 0.1X TE.
9. Mix well on a vortex mixer or by pipetting up and down and incubate for 2 minutes at room temperature.
10. Put the tube/PCR plate in the magnetic stand until the solution is clear. Without disturbing the bead pellet, carefully transfer 32 µl of the supernatant to a fresh, sterile microfuge tube.

Protocol 2:

AMPure XP Bead-based Dual Bead Size-Selection for 100 bp inserts

The following size selection protocol is for libraries with 100 bp insert from a 100 µl volume.

1st Bead Selection to Remove Large Fragments:

This step is used to bind the large, unwanted fragments to the beads. The supernatant will contain the desired fragments.

1. Add 90 µl (0.9X) resuspended AMPure XP beads to 100 µl DNA solution. Mix well on a vortex mixer or by pipetting up and down at least 10 times.
2. Incubate for 5 minutes at room temperature.
3. Place the tube on a magnetic rack to separate the beads from the supernatant. After the solution is clear (about 5 minutes), carefully transfer the supernatant to a new tube **(Caution: do not discard the supernatant).** Discard beads that contain the large fragments.

2nd Bead Selection to Remove Small Fragments and to Bind DNA Target:
This step will bind the desired fragment sizes (contained in the supernatant from Step 3) to the beads. Unwanted smaller fragment sizes will not bind to the beads.

4. Add 15 µl (0.15X) resuspended AMPure XP beads to the supernatant, mix well and incubate for 5 minutes at room temperature.
5. Put the tube on a magnetic rack to separate beads from supernatant. After the solution is clear (approximately 3 minutes), carefully remove and discard the supernatant. Be careful not to disturb the beads that contain DNA targets **(Caution: do not discard beads)**.
6. Add 200 µl of 80% freshly prepared ethanol to the tube while in the magnetic stand. Incubate at room temperature for 30 seconds, and then carefully remove and discard the supernatant.
7. Repeat Step 6 once.
8. Keeping the tube on the magnetic rack, with the cap open, air dry the beads for 5 minutes.
   Caution: Do not overdry the beads. This may result in lower recovery of DNA target.
9. Remove the tube from the magnet. Elute DNA target from beads into 42 µ l sterile 0.1X TE. Mix well on a vortex mixer or by pipetting up and down, incubate for 2 minutes at room temperature.
10. Put the tube in a magnetic rack until the solution is clear, approximately 3 minutes. Transfer approximately 40 µl of the supernatant to a clean tube.

3 Droplet microfluidic implementation

The implementation of these complex protocols in a droplet microfluidic format is not straightforward and presents some constraints that need to be addressed, which includes the functionalities to be integrated and the handled reagents. In particular, the device should include extraction/redispersion sequences, clean-up processes (highlighted in yellow in the Protocol 1 and 2), and be able to deal with viscous fluids (highlighted in cyan in the Protocol 1 and 2) and hydro-organic solutions (highlighted in green in the Protocol 1 and 2). These points will be separately discussed in the following paragraphs, in order to describe the whole development workflow of a device dedicated to clean-up and size selection stages required during the preparation of DNA libraries devoted to any NGS technology.

3.1 An additional device functionality: magnetic beads clean-up

The droplet microfluidic concept discussed here was presented earlier in this chapter. In particular, in the upgraded version of the device, the variable-volume component has been removed and the fingering process is tuned fixing the ratio in hydraulic resistance between the main and secondary channels, both connected to a pressure controller. This approach allows higher flexibility and precision without detriment to the extraction and purification performances. Furthermore, following the cluster extraction process (Fig 7, a-e), the channel network design allows the implementation of a further functionality, together with the redispersion operation previously discussed (Fig.7, g-i). As a matter of fact, switching off the integrated magnetic components, the captured beads

cluster can be evacuated through the secondary channel while the parent droplet continues its flow in the main channel (Fig.7f). This allows both the clean-up of a target molecule from the original matrix and the possibility to perform further downstream process on the extracted cluster (e.g., optical detection, re-encapsulation,...) in a section of the microfluidic network distinct from the main channel.

Finally, a first technological bottleneck for the implementation of DNA size-selection and clean-up protocols in continuous droplet microfluidics was tackled, presenting a device combining the possibility to perform sequential exchanges of functionalized magnetic particles between different media with a low carryover of supernatant, the integration of washing steps and the implementation of any protocol requiring the clean-up of a specific molecule from the initial matrix. This clean-up functionality was thus made possible thanks to the new version of the droplet-based approach, in which the dead-end channel was replaced by an open-end channel.

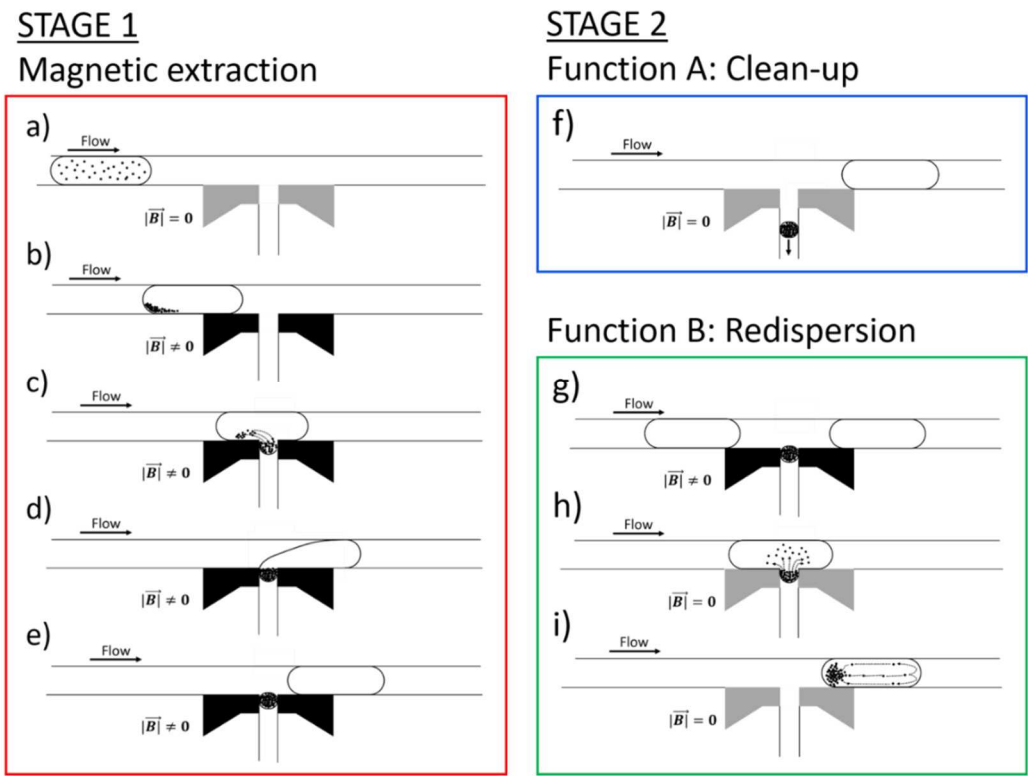

Figure 7: Overview of the available functionalities in the developed device. *Following the magnetic solid-phase extraction (a-e) presented in the previous chapter, two sequences of operations can be performed: clean-up (f) or redispersion (g-i).*

3.2 The effect of a viscous aqueous phase and of the particle load in the droplet

The SPRI method is based on the selective immobilization of DNA onto carboxyl-coated magnetic particles in presence of PEG and salt. In particular, the viscosity of the SPRI buffer, due to the PEG molecules in solution, and the concentration of magnetic carriers can both influence the implementation of this protocol in a droplet-microfluidic format. Therefore, in the following, these two properties of the buffer will be at first determined; then, a diagram describing the different operating domains for our device as a function of both

the aqueous phase viscosity and the magnetic particle load in the droplet will be presented.

3.2.1 The viscosity and magnetic beads concentration in the SPRI buffer

The AMPure XP solution is characterized by negatively charged magnetic beads (1µm diameter) dispersed in a matrix mainly containing the 20% (w/v) of PEG-8000 and 2.5M of sodium chloride. As previously discussed, this solution will be mixed with the DNA sample at different volume ratios in order to select specific DNA ranges for clean-up or size selection. In particular, in this study 0.8x and 1.8x ratios will be considered as representative values for lower and higher concentration of AMPure XP solution in DNA samples, respectively. At first, the viscosities of the pure and diluted solutions were experimentally measured in a temperature range of 15°C and 40°C (Fig. 8, each point is the average of three independent measurements. The error bars are not visible when smaller than the corresponding data point). The original solution presents a viscosity value of about 19.5mPa · s at room temperature (23°C), i.e. 20-fold higher with respect to that of PBS (+0.01% Tween20 + 0.09% NaN_3), in which functionalized paramagnetic particles are usually dispersed. On the other hand, the final solutions for the selection of DNA fragments of interest are characterized by viscosity values ranging between 4.4mPa · s and 8.0mPa · s. Furthermore, the concentration of the negatively charged magnetic particles in the solution is 1µg/µL, i.e. ten times lower than the Dynabeads MyOne solution used for the previous characterization of the droplet system performances.

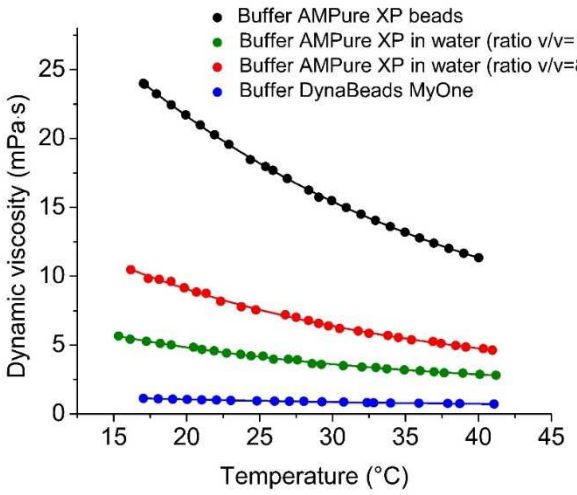

Figure 8: Experimentally measured dynamic viscosity values as a function of temperature for pure AMPure XP and Dynabeads MyOne buffers, and AMPure XP buffer solution in water at 8/10 and 18/10 v/v ratios. *Each point corresponds to an average of three measurements, performed with a rheometer (MCR 302, by Anton Paar). Interestingly, at room temperature, the AMPure XP buffer presents a dynamic viscosity 20-fold higher with respect to the one of DynaBeads MyOne buffer. Typical viscosity values for solutions used in the DNA size selection protocol range between 4.4mPa·s and 8.0mPa·s. The error bars are not visible when smaller than the corresponding data points.*

3.2.2 An operating diagram of the device

The extraction and purification performances of our device were evaluated for a typical system in which the aqueous phase presents a dynamic viscosity of about 1 mPa · s, i.e. equivalent to the one of water. However, as discussed before the implementation of a DNA purification protocol based on SPRI requires to handle relatively low amounts of beads (0.1µg), dispersed in an aqueous phase characterized by a dynamic viscosity ranging from 4.4 mPa · s to 8.0 mPa · s. Moreover, in biochemical and bioanalytical applications it is often important to deal with viscous biofluids, like blood, characterized by a viscosity a few times higher than water. With this aim, a more general study was performed to define

an operating diagram of our device as a function of the magnetic beads concentration and of the dynamic viscosity of the liquid in which they are dispersed.

In general, the introduction of a viscous force to the system causes an increase in the particles aggregation time, slowing down or preventing the magnetically-driven migration of beads (i.e., increasing the magnetophoresis time required to obtain a cluster), thus interfering with the formation of a compact cluster. Low throughput stationary and discrete digital droplet microfluidic systems suffer to a less extent of this issue. Indeed, despite the important increase in processing time, the droplet actuation step that leads to the cluster extraction is performed after a complete magnetic sedimentation of particles at the bottom of the immobile droplet is achieved. Exploiting these microfluidic architectures few assays based on viscous biofluids, especially whole blood samples, were implemented[32,33,34]. Differently, in the case of continuous droplet microfluidics systems the possibility to implement protocols involving viscous fluids was not yet demonstrated. In fact, in this microfluidic architecture, the droplets are transported in a continuous flow of carrier oil at a constant flow-rate, which defines a droplet crossing time under the influence of the magnetic field. This sets an upper time limit for the dispersed particles to achieve an aggregate state before the extraction occurs. The presence of a viscous media would thus slow down the aggregation dynamics and can affect the extraction performances of the device.

Given the complexity of this dynamical process, an empirical study was performed. In particular, we set the particles nature and the device geometrical and magnetic properties to investigate the impact of the dynamic viscosity of

the droplet aqueous solution (η) on the extraction process as a function of the magnetic particles load (Q) in the droplet. Hundred nL droplets were considered, transported by a constant flow rate of 0.25 µL/s, in order to set the droplet kinematics, therefore the crossing time of the beads under the influence of the magnetic field. The dynamic viscosity of the aqueous solution was varied considering different concentrations of glycerol in water, resulting in viscosities of the dispersed phase ranging between about 1 $mPa \cdot s$ and 22.5 $mPa \cdot s$. In the operating diagram presented in Fig. 9 several regimes have been identified, characterized by different force-interplay conditions involving: i) *the magnetic force exerted on a single particle*: $F_{mag} = \frac{V\chi}{\mu_0}(B \cdot \nabla B)$, where V is the volume of the superparamagnetic particle, χ its effective magnetic susceptibility and B the magnetic flux density; ii) *the droplet interfacial force*: $F_{int} \propto \gamma L$ (for a spherical meniscus), where γ is the aqueous/oil interfacial tension and L is a representative length of the system, such as the radius of curvature of the meniscus[35]; iii) *the viscous force on a magnetic particle moving through the aqueous solution*: $F_{vis} = 6\pi\eta Rv$ (with η the dynamic viscosity of the solution, R the radius of the bead and v the flow velocity relative to the object).

For low aqueous phase viscosities, the viscous forces contribution does not affect the formation of a compact cluster $(F_{mag} \gg F_{vis})$ and, although slowed-down for increasing η, the cluster can get formed and reach the capture region, driven by a magnetophoretic force. In this range, the device behavior is controlled by the interplay between the magnetic force exerted by the cluster $(F_{mag,cluster})$ and the interfacial force of the droplet. For low magnetic particles loads ($Q \leq 0.1\mu g$), the magnetic force is overcome by the droplet interfacial force, dragging the cluster away from the trap during the meniscus finger retreat process

($F_{mag,cluster} < F_{int}$, green empty circles in Fig. 9). On the other hand, for Q > 0.1µg the cluster is extracted from the parent droplet with an efficiency higher than 95% ($F_{mag,cluster} > F_{int}$, black full circles).

Increasing η, viscous forces starts playing an effective role in the system and the device performances are mainly limited by the incomplete particles aggregation before the extraction. The viscosity threshold above which viscous effects appear in the system (see dashed curve separating circles and triangles domains in Fig.9) does not occur for a constant η and increases as a function of the magnetic particles load in the droplet, reaching a plateau value of about 20mPa · s for particles amount higher than 0.7µg. For η>10 mPa · s, the behavior of the system is indeed controlled by the interplay between viscous forces and magnetic forces and two regimes can be distinguished as a function of Q. For particle load lower than 0.2µg, the magnetic force acting on a single particle or on a small assembly of few particles is not sufficient to overcome the viscous force in order to trigger particles aggregation, leading to the formation of a compact cluster ($F_{mag} < F_{vis}$, red empty triangles in Fig.9). The high dilution of the particles dispersed in a viscous aqueous droplet increases their average mutual distance, thus representing a further limiting factor affecting their aggregation. Increasing the particle quantity beyond 0.2µg, the magnetic force becomes slightly higher but of the same order of magnitude than the viscous one, allowing a slow sedimentation of particles that will occupy the lower longitudinal section of the droplet, not forming a compact cluster for the flow-rate considered ($F_{mag} \approx F_{vis}$, blue full triangles in Fig.9). While the droplet crosses the capture region, a part of the beads are trapped but the extraction efficiency is lower than 95%.

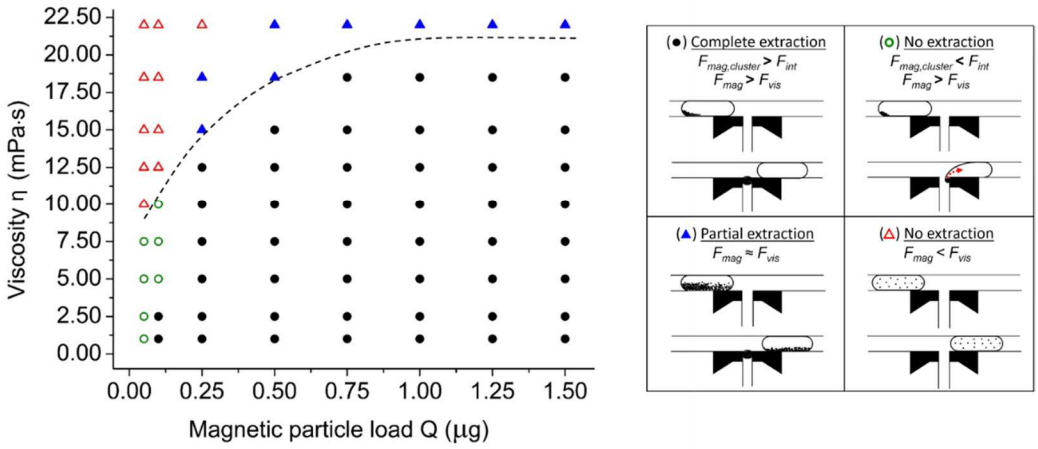

Figure 9: Operating diagram describing the effect of the magnetic particle load (Q) and of the aqueous phase solution viscosity (η) on the extraction rate of the system. *Different regimes can be identified and related to the interplay between the interfacial force on a single particle (F_{mag}) or on the compact cluster of beads($F_{mag,cluster}$), the interfacial force of the droplet (F_{int}) and the viscous force of the solution (F_{visc}), as indicated in the right panel. The full black circles represent the condition for an extraction regime, characterized by a bead retention efficiency higher than 95%. For low viscosities and magnetic particles load (empty green circles), the particles aggregate in a compact cluster but no extraction occurs because the magnetic force is overcome by the droplet interfacial force, dragging the cluster away from the trap during the meniscus finger retreat process. The dashed curve separating the circles and triangles domains represents the viscosity threshold above which viscous effects appear in the system. Above this line, viscous forces prevent the formation of a compact cluster, in the case of low particles load in the droplet (empty red triangles) or lead to a partial cluster formation and incomplete extraction of the particles (full blue triangles).*

This operating diagram gives a complete description of the possible regimes obtained during the extraction process as a function of both the droplet phase viscosity and the particle load dispersed in it. It is worth noticing that these regimes were described for a fixed droplet flow-rate. A decrease in droplet speed would allow a higher time that the droplet will spend under the influence of the magnetic field, showing thus improvements in capture performance for high

viscosities. The opposite happens when the droplet speed is increased and the beads aggregation time is limited accordingly. This is translated in the operating diagram by a shift upwards or downwards of the transition delimiting the arise of viscous effects in the system (see dashed curve in Fig.9).

In general, our device guarantees a large set of conditions in which the extraction process is successfully achieved with high extraction and purification efficiencies, especially in the viscosity range of interest for common biofluids (like whole blood[36], cerebrospinal fluid[37], urine, bile[38]…) presenting values below 6 mPa · s. However, for the in-drop implementation of the SPRI-based clean-up and size-selection protocols, a particle load of 0.1µg dispersed in aqueous phase characterized by a dynamic viscosity between about 4.4 mPa · s and 8.0 mPa · s is used. According to the operating diagram described above, the device would not allow the particle extraction to occur in these conditions, as experimentally confirmed. In fact, the decrease in the amount of magnetic carriers Q causes a reduction in the magnetic force acting on the cluster of particles, which is not intense enough to retain the particles against the interfacial force, as a consequence it is dragged away by the droplet meniscus. However, for a fixed dispersed phase viscosity in the range of interest, the diagram suggests the possibility to achieve the extraction conditions by increasing the particle load in the droplet (Fig. 10). This can be implemented in two ways: i) increasing the droplet volume; ii) introducing an additional amount of magnetic carrier in the SPRI solution. Since an important increase in the volume of a confined droplet can lead to droplet instability, especially at high flow-rates, the latter approach was preferred.

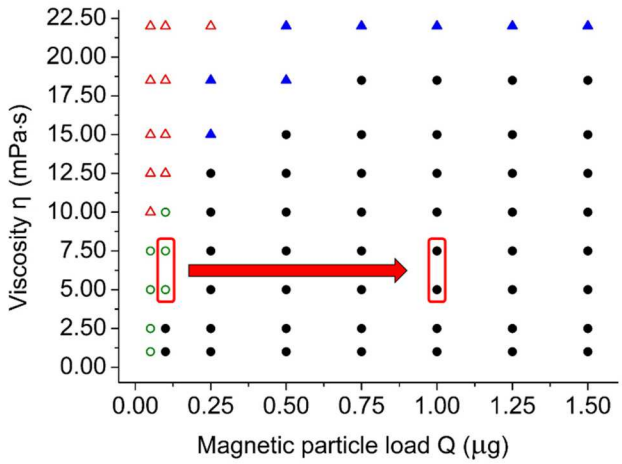

Figure 10: Transition in the operating diagram due to the introduction of an additional 1µg load of inert magnetic particles in the droplet. *Considering a 100nL droplet volume and standard conditions for SPRI-based clean-up and size-selection protocols (particle load of 0.1µg, dynamic viscosity between about 4.4 mPa·s and 8.0 mPa·s), the cluster extraction cannot happen. To support this operation, an additional amount of non surface-functionalized particles will be considered, in order to move in an extraction domain of the device.*

Nevertheless, the supplementary amount of beads has to exclusively contribute to the magnetic force, but at the same time must not interfere neither with the reactions on the beads surface nor with the device operations, limiting its flexibility as in the work of Gu et al.[39]. With this aim, surface inert polystyrene-based superparamagnetic particles (size: 1µm, by Sigma Aldrich) were chosen to support the magnetic extraction and were considered as an additional element for the reagents mix. In particular, a 1µg load was systematically added to the AMPureXP and sample DNA mix.

3.3 Washing with a solvent solution

Among the different difficulties of the commercial protocol of DNA size selection, the washing of the beads cluster with 80% ethanol represents the most critical step. In fact, following the washing, an air-dry step is suggested in

order to evaporate the ethanol solution. However, if the latter steps are performed inaccurately, i.e., not sufficient dry or overdry of the beads pellet, the elution step can be affected thus decreasing the efficiency of the DNA recovery. In order to determine the importance of the washing step in the protocol, the latter was implemented in batch, with and without the ethanol washing and no significant difference regarding both the DNA size selection and recovery rate were reported (Figure 11).

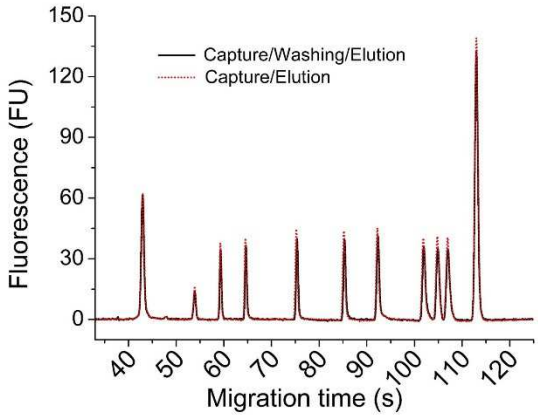

Figure 11: Electropherograms comparing two clean-up protocols in tube, with and without the washing step. *The black and the dashed red curves represents traces resulting from the protocol with and without washing, respectively. A AMPure XP/DNA sample ratio of 1.0x is used. The first and last peak are the internal standard of the BioAnalyzer.*

However, the washing step is required to improve the beads extraction as well as to remove the supernatant efficiently, specifically any excess of NaCl that might disrupt the downstream enzymatic steps in the PCR that follows. Note that our system is less prone to this type of contamination. Indeed, due to the high purification efficiency guaranteed by our device, the carryover of NaCl and other contaminants in the daughter droplet is approximately 3% with respect to the one of the original solution, allowing us to confidently skip the washing

step. Considering the release of the extracted cluster from the sample solution directly in the elution buffer, i.e. avoiding the washing step, the final concentration of NaCl contaminant in the elution droplet is about 50µM. According to Rossman et al., using a 170mM of NaCl would inhibit the PCR amplification, while using less than 102mM causes no inhibition[40]. Therefore, based on these comments, the washing step will be skipped in the following droplet proof of concept implementation in order to simplify the protocol.

Moreover, we also have to mention that our experiments have been performed using a DNA ladder (Gene Ruler, Low range DNA ladder, 0.5µg/µL, by Thermo Scientific) thus the washing step might be vital when handling real DNA samples. The latter emphasizes the need to perform more experiments with real DNA followed by PCR amplification. Preliminary experiments have been recently performed to demonstrate that 80% ethanol droplet can be integrated if required in the workflow without any stability issue.

3.4 On-chip implementation

In the previous sections, we evidenced and discussed the main constraints of the SPRI-based DNA clean-up and size-selection protocols, and the device functionalities required for the implementation of these processes in a continuous-droplet microfluidic architecture. In particular, a device gathering the possibility to perform both sequential extraction/redispersion operation and the clean-up of a target molecule from the original matrix has been presented. The handling of viscous fluids is a further requirement of the method. The influence of the dispersed phase viscosity and beads concentration was therefore investigated, presenting a diagram describing the different operating regimes of

our system. The introduction of an additional amount of magnetic particles was also proposed to assist the extraction of the particle cluster against the droplet interfacial force. Finally, the most critical stage, i.e. the ethanol washing, was discussed. Test in tube showed that the absence of this step does not influence the final DNA recovery, the latter being supported by the high purification efficiency of the device; thus, this step will be skipped in the current microfluidic implementation. Nevertheless, a short-term goal will be to deeply investigate this aspect, especially concerning its possible implication on the efficiency of the following PCR amplification.

Finally, to complete the experimental setup, this microfluidic device has been interfaced with a droplet generation module, composed by a pipetting robot (Rotaxys, by Cetoni), coupled with two syringe pumps (Nemesys, by Cetoni), two PDMS devices and pinch valves, as previously described (cf. chapter 2), guaranteeing continuous droplet generation and analysis. Based on this platform, the in-droplet implementation of both the clean-up and tight size selection process will be presented. In particular, both steps will be performed considering a DNA ladder (0.5µg/µL concentration) as a starting sample, characterized by sizes ranging between 25bp and 700bp.

3.4.1 The left-side size selection (Clean-up)

In libraries preparation, a single step AMPure XP process is usually exploited to remove fragments below a certain size from the solution. This is notably the case for long-read sequencers, where the low molecular weight fragments should be removed in order to focus the sequencing capacity on long DNA fragments.

Nevertheless, this step is also interesting for any sequencing preparation and can be repeated at multiple points of the protocol using slightly different AMPureXP/DNA ratio in order to remove specific waste fragments resulting from the fragmentation, end-repair, dA tailing, adaptor ligation or PCR amplification steps.

In order to define the lower limit of the selection, the target DNAs larger than a cut-off size are captured on the beads surface, thus a protocol including extraction, washing and elution of these long DNA molecules must be implemented in a droplet microfluidic format, as described in the following. As previously mentioned, the hydro-organic washing step will be skipped at this stage. As a proof-of-concept, in the current left side size-selection the AMPureXP solution and the DNA sample are mixed with a ratio 1.0x in order to capture DNA fragments larger than 100 bp on the beads.

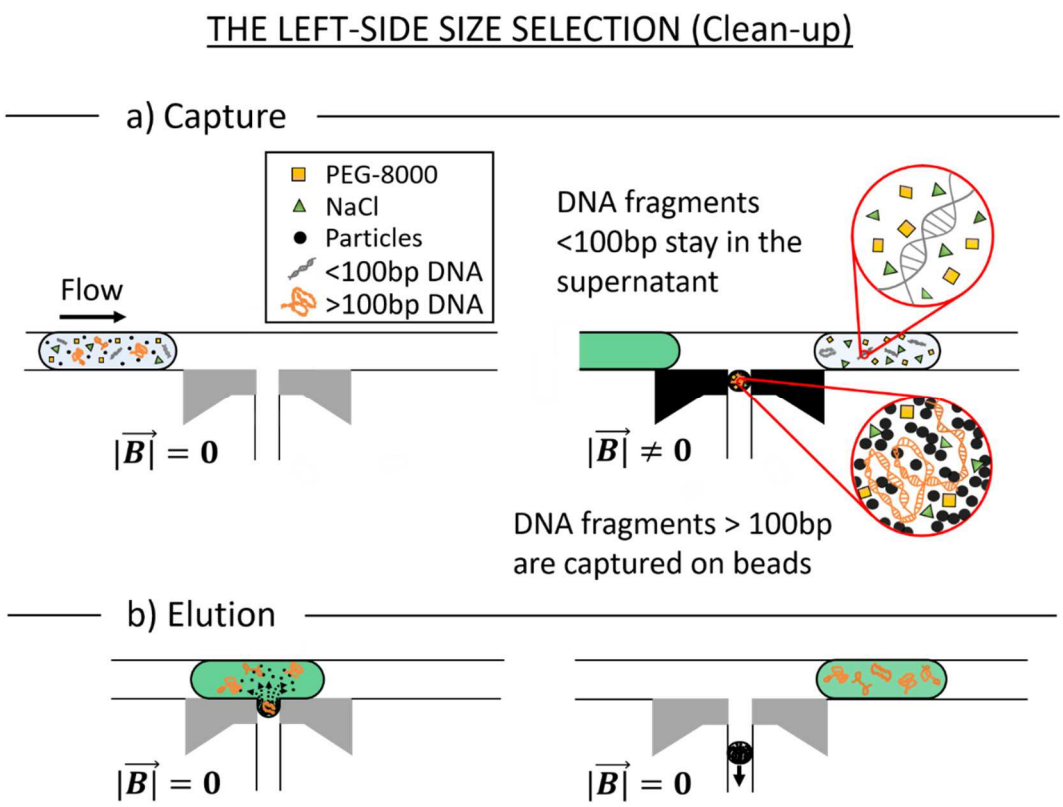

Figure 12: Droplet microfluidic implementation of the left-side size selection protocol. *(a) In order to define a left cut-off limit of 100bp, a droplet containing a mix of AMPure XP solution and DNA sample with a 1.0x ratio is considered. Therefore, the magnetic beads bind fragments larger than 100bp, while shorter fragments remain in the suspension. The soft magnets allows the extraction of the target DNA through the separation of the beads from the supernatant solution. (b) The extracted cluster will be released, upon merging, in a coming droplet containing the elution buffer (green droplet), by switching off the soft magnets. Once the elution performed, a second pair of magnetic components will be used to separate the eluted DNA from the magnetic beads, that will be discarded through a secondary channel. Grey structures indicate an OFF state of the device, while the ON state is represented in black.*

For the implementation of this protocol, the reagents are loaded in a 384-well microtiter plate and a train of two droplets (100nL in volume), separated by an oil gap, were sampled from it by the pipetting robot. The first droplet contains

the mix of the AMPureXP solution with the DNA sample at the defined ratio (1.0x) while the second is composed of an elution buffer (Tris-EDTA). The sample solution was enriched with an aliquot of inert superparamagnetic particles to assist the cluster extraction (about 1µg), as discussed above. Once the generation of the droplet train is completed, the pinch valves states are switched and the droplets are then pushed at a constant flow-rate towards the device. The distance between the generation and the first extraction stage is tuned in order to set the 5 minutes incubation time for the capture of the target DNA fragments onto the beads surface.

In order to implement this multi-step protocol, sequential extraction and release processes are performed using a series of soft magnets (Fig.12). In details, the magnetic beads bind the target DNA (larger than 100bp) and the soft magnets allow the purification of the solution by extracting the magnetic cluster, trapped in the region between the soft magnets, while the supernatant solution is discarded by being pushed away by the oil flow (Fig.12a, right panel). The beads are then released in the elution buffer by switching off the magnetic components (Fig.12b, left panel). The target DNAs, eluted from beads, are now dispersed in the buffer solution and a second pair of soft components is exploited to separate the solid-phase support from the supernatant solution containing the fragments with sizes of interest (Fig.12b, right panel). The magnetic particles are indeed trapped in the capture region and led to a waste outlet while the droplet containing the target fragments continue its flow towards the main outlet, where it will be collected in a tube containing 1mL of FC-40 oil and 5µL of Tris-EDTA buffer solution.

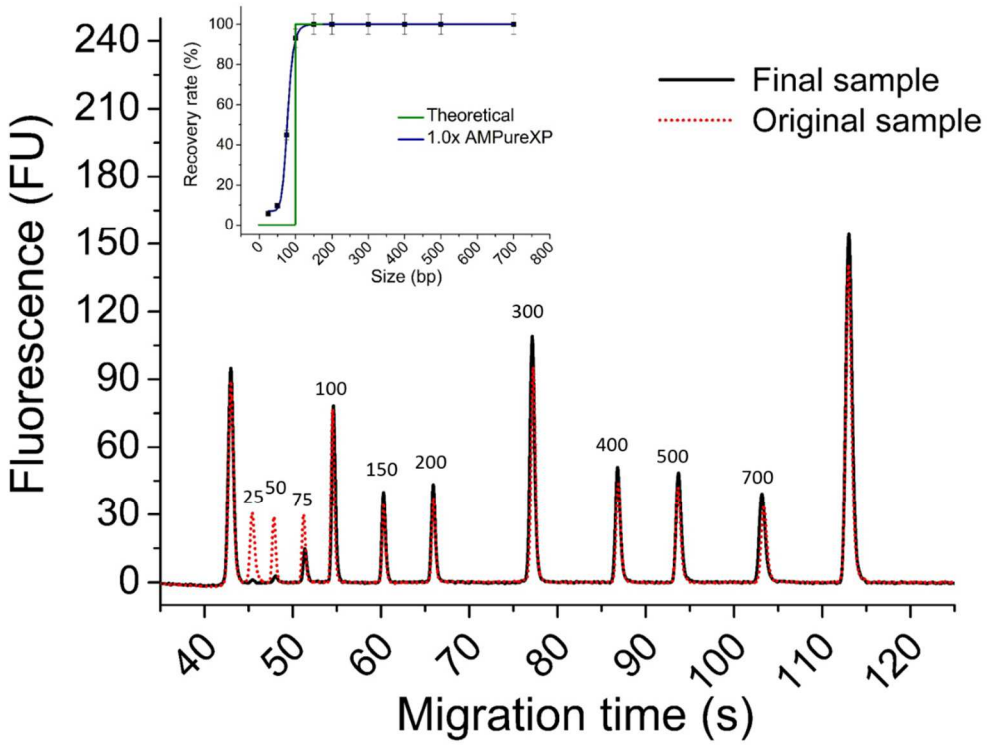

Figure 13: Electropherogram describing the results of the left-side size selection step performed in droplet. *Since an AMPure XP solution/DNA sample of 1.0x is used, fragments larger than 100bp are selected. The dashed red curves represents the trace of the original sample, while the black trace is the outcome from the final solution, after processing in droplet. The values on top of the peaks correspond to the DNA fragments length (bp). The first and last peak are the internal standard of the BioAnalyzer. In the inset, the recovery rate as a function of the fragment length. A slightly divergence between the theoretical curve (in green) and the obtained profile (in blue) is observed. Note that the blue curve does not represent a data interpolation, but rather a simple tracing to help the reader.*

The experiments were performed in triplicates and during each run five trains of droplets were processed. Finally, the resultant size distribution was confirmed by a BioAnalyzer run and a typical electropherogram trace is presented in Fig.13, showing the correct enrichment of the DNA fragments in the range of

interest obtained with our device (black line) versus the original sample (red dashed line). Furthermore, in order to define the cut-off profile, the intensity ratio of corresponding peaks before and after the clean-up step were evaluated, showing a slight deviation with respect to the ideal sharp transition at the cut-off size, as previously reported[41,42] (see Inset of Fig.13). The DNA concentration in the solution processed in droplet is measured by a QuBit assay and the resulting values were normalized with the corresponding in batch version, obtaining a rate of 93.85% with a CV of 5.64%.

3.4.2 Selection of a tight DNA size range (Double size selection)

Together with the clean-up protocol, short-read sequencers, like the Ion Torrent and Illumina technologies, require a tight DNA size range in the input, according to the manufacturer's specifications. This can be achieved by performing two sequential steps, as previously discussed, aiming at defining the upper and lower limit of the target DNA range. The first step of this double size selection was presented in the previous paragraph, while in order to perform the right-side size selection, the clean-up functionality of our device must be exploited, as will be discussed in the next paragraph.

The right-side size selection

In order to perform the right-side size selection, the magnetic beads binds the unwanted DNA fragments, while the supernatant solution contains the target

fragments. To demonstrate this functionality, a right cut-off limit of 300bp is fixed, thus an AmpureXP/DNA sample ratio of 0.75x is chosen.

As discussed before, an extra amount of inert (i.e, not surface functionalized) magnetic particles is added in the solution to support the following particle extraction from the droplet. The solution was then loaded in a 384-well microtiter plate and a train of 100nL droplets with uniform content was sampled from it by the pipetting robot (Fig.14, left panel). The droplets are then continuously processed by the device, following the operations previously described: the particle cluster is deflected towards the capture region and trapped by the soft magnets, allowing the extraction of the undesired DNA fragments (larger than 300bp in our case) and their enrichment in a tiny aqueous sub-droplet, while DNAs with target sizes remain in the parent droplet, that keeps flowing in the main channel (Fig.14, right panel). The soft magnets are switched OFF and the extracted sub-droplet is pushed towards a waste outlet via the secondary channel. The magnet position is then restored at the set distance for the activation of the integrated components, and the system is ready for processing the next droplet. Following the extraction, the resulting droplets are collected in a tube, as previously described.

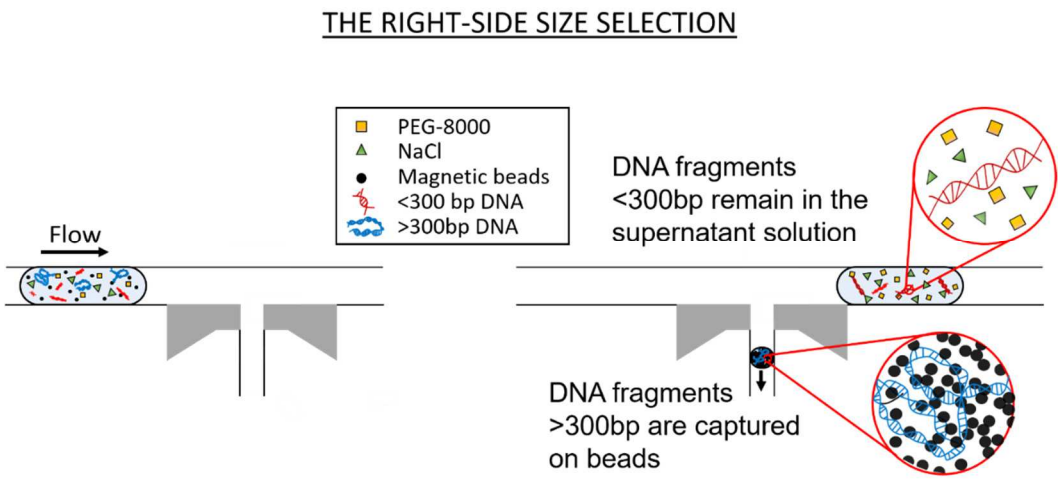

Figure 14: Droplet microfluidic implementation of the right-side size selection protocol. *(a) In order to define a right cut-off limit of 300bp, a droplet containing a mix of AMPure XP solution and DNA sample with a 0.75x ratio is considered. The undesired fragments, longer than 300bp, will be extracted from the original solution through the magnetic tweezers while the target DNA remain in the supernatant solution. By switching off the soft magnets, the captured cluster will be discarded. Grey structures indicate an OFF state of the device, while the ON state is represented in black.*

This right-side size selection protocol was performed in triplicate with a number of 40 droplets per run. The final size distribution was verified, by performing an Agilent BioAnalyzer run (Fig. 15), in which the electropherogram obtained from the purified DNA (black line) is compared to the one of the original solution (red dashed line). However, as in the previous case, a small variation with respect to the ideal cut-off profile is reported (Inset Fig.15). The final DNA concentration was also measured by a QuantiT dsDNA HS assay on the Qubit fluorometer. In particular, to quantitatively compare the resulting yields obtained in the integrated protocol versus the classical batch wise one, the ratio

between the recovered DNA concentration in droplet and in tube was estimated, and calculated to be 92.77% with a CV= 6.18%.

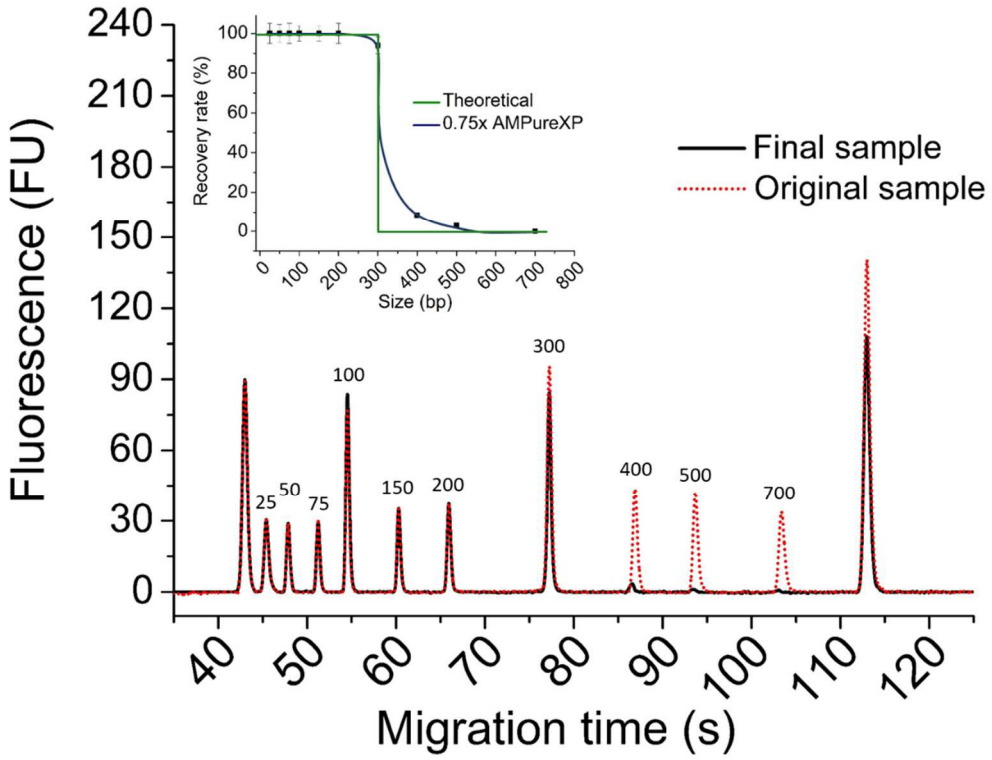

Figure 15: Electropherogram describing the results of the right-side size selection step performed in droplet. *Since an AMPure XP solution/DNA sample of 0.75x is used, fragments larger than 300bp are discarded. The dashed red curves represents the trace of the original sample, while the black trace is the outcome from the final solution, after processing in droplet. The values on top of the peaks correspond to the DNA fragments length (bp). The first and last peak are the internal standard of the BioAnalyzer. In the inset, the recovery rate as a function of the fragment length. A slightly divergence between the theoretical curve (in green) and the obtained profile (in blue) is observed. Note that the blue curve does not represent a data interpolation, but rather a simple tracing to help the reader.*

Overall protocol

The developed clean-up of unwanted DNA fragments and the capture and elution of the target ones can be sequentially performed in order to define a tight DNA range between 100bp and 300bp. With this aim, a right-side selection (capture/elution) using a 0.75x AMPureXP to remove DNA larger than 300bp was followed by left-side one (clean-up) with a 1.0x ratio to extract DNA larger than 100bp.

Again, the complex workflow that integrates both clean-up and extraction/redispersion steps was run in triplicate and the droplets were collected in tube for downstream analysis. To calculate yield, the purified DNA solution is run on an Agilent BioAnalyzer to confirm the selection of the correct range of DNA size of interest (Fig. 16). Furthermore, the concentration is also measured using a Qubit Assay, obtaining an 87.3% efficiency (CV=2.5%), evaluated as the ratio between the DNA concentration resulting from the in-tube and in droplet (4.05 ng/µL) protocols.

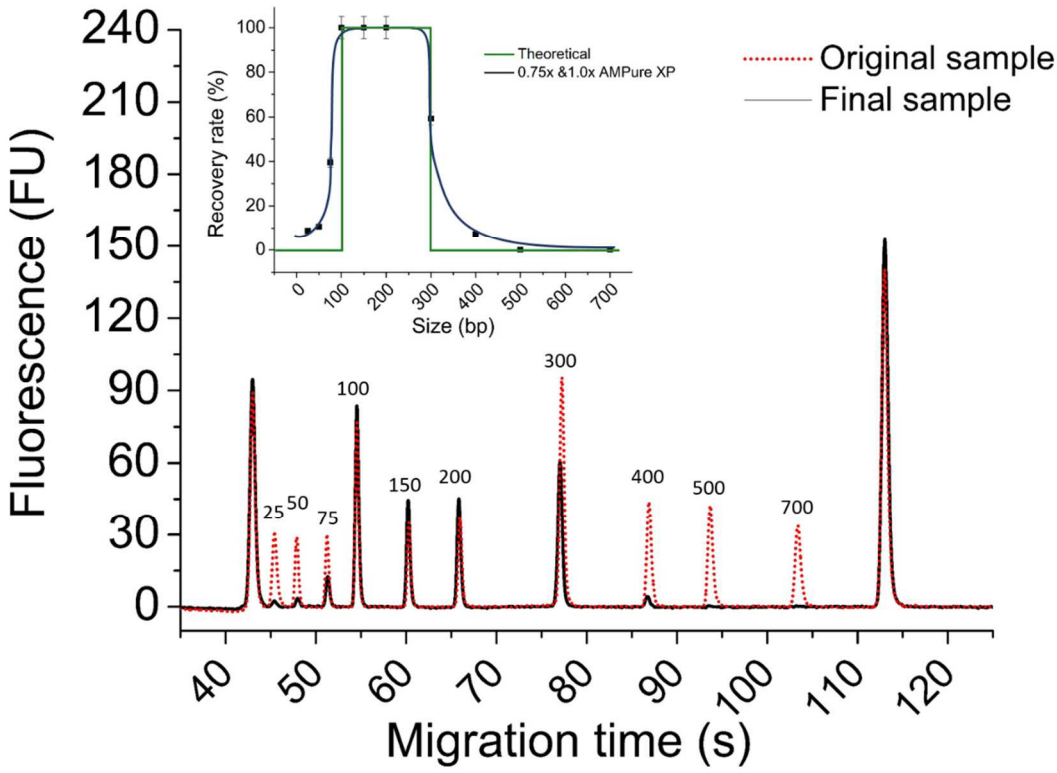

Figure 16: Electropherogram describing the results of the double-size selection step performed in droplet. *In this case, an AMPure XP solution/DNA sample of 0.75x is used to capture and discard fragments larger than 300bp; then, a ratio 1.0x is used to capture the target fragment between 100bp and 300 bp. The dashed red curves represents the trace of the original sample, while the black trace is the outcome from the final solution, after processing in droplet. The values on top of the peaks correspond to the DNA fragments length (bp). The first and last peak are the internal standard of the BioAnalyzer. In the inset, the recovery rate as a function of the fragment length. A slightly divergence between the theoretical curve (in green) and the obtained profile (in blue) is observed. Note that the blue curve does not represent a data interpolation, but rather a simple tracing to help the reader.*

Overall, for the first time we showed the possibility to implement clean-up and size selection steps on droplet continuously flowing in a microchannel with efficiencies comparable with conventional methods. Interestingly, starting from

a DNA ladder at a concentration of 0.5 µg/µL, and following the two in-droplet steps above described (including also the DNA dilution during droplet collection required for the DNA quality check), we were able to achieve a purified DNA volume of about 6µL at a concentration of about 4 ng/µL, i.e. in the range of standard sample concentration requirements for Illumina sequencers, considered as a reference. Nevertheless, a purified sample volume higher that 15µL is required, thus a 2.5x increase in the number of processed droplet with respect to the described implementation should be considered.

Furthermore, we showed that the introduction of an additional amount of inert superparamagnetic particles in the sample droplet does not obstacle neither the device operations, nor the DNA recovery rate, as shown by the electropherogram traces comparing the in-droplet and batch wise method (Fig.17)., the cut-off profile presents some divergences from the ideal sharp transition.

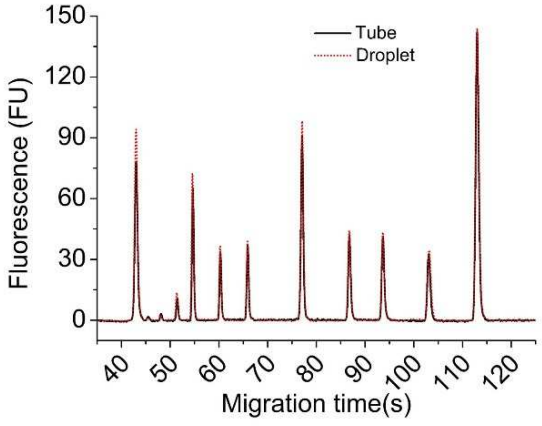

Figure 17: Electropherograms comparing the outcome of a clean-up protocol performed in tube *(black curve)* ***and in droplet*** *(dashed red curve).* ***An*** *AMPure XP/DNA sample ratio of 1.0x is used. The first and last peak are the internal standard of the BioAnalyzer.*

With our droplet method, a complete protocol of both clean-up and capture-elution steps takes less than 15 min (excluding the droplet collection step in tube). This duration, including the two incubation times of 5 minutes, is slightly shorter than those with conventional methods. However, it is worth noticing that for this first proof-of concept application we worked in the low-range of flow-rates (0.25µL/s) with respect to the platform potentialities, thus an important improvement in the overall workflow processing time is expected by simply increasing the carrier oil flow-rate.

Finally, although a method yielding DNA libraries with the majority of inserts in the 100-300bp size range was presented, this protocol can be easily adapted to the selection of any tight DNA range by modifying the AMPure XP concentration in the sample droplet.

4 Conclusion and perspectives

Despite the important efforts for workflow simplification, the preparation of reliable NGS DNA libraries is still a demanding process, whose quality will affect the sequencing results and the following bioinformatics data processing. The potential of microfluidics in sample preparation are well-known, nevertheless the possibility to exploit them for NGS libraries preparation is still an almost unexplored field, as proven by the low amount of articles discussing the NGS libraries preparation in microfluidics, especially in a droplet-based format.

Some steps of the protocol can be directly transported in droplet implementing merging or thermal steps while others, like the magnetic bead-based DNA size

selection or the clean-up step, require specific functionalities and constraints for their implementation in a multi-phase microfluidic format. With this aim, we extended here the capture/redispersion operations presented in the previous chapter, by the implementation of a clean-up functionality in our device thanks to pressure-controlled droplet approach. Furthermore, the manipulation of viscous fluids and the implementation of a washing step with a solvent solution were discussed. Successful preliminary data on DNA size selection and clean-up performed on a DNA ladder sample were presented. These results show DNA size distribution and recoveries compatible with the ones obtained with conventional methods, but using an integrated and automated platform, thus limiting the steps requiring human intervention. Furthermore, we also demonstrated that the addition of inert superparamagnetic beads, supporting the cluster extraction, does not alter the Solid Phase Reverse Immobilization process.

The slightly slower DNA recovery in the droplet format with respect to the in-tube method can be probably associated to the delicate collection of the processed droplet in tube and their transfer for BioAnalyzer and Qubit assay, causing probably some losses with respect to the original solution. This point represents a further technological aspect to be optimized in the future in order to improve the robustness of the system and to minimize the user's intervention. Furthermore, a deeper study about the impact of the washing step on the library preparation and sequencing outcome should be performed, in order to verify the assumption and hypothesis presented in this work. This step aims at removing contaminants in the droplet, especially NaCl, that could affect the efficiency of the following DNA amplification. Although the BioAnalyzer traces

do not show significant differences between a protocol performed in presence or in absence of the washing step, an interesting study would be to compare the results of PCR amplification performed on fragments selected with both protocols (with and without washing). The same should be done as a verification step of a capture/elution protocol, as presented in this chapter, in order to verify the assumption about the low concentration of NaCl in the extracted subdroplet, not influencing the PCR efficiency.

An upgrade on the sample should also be considered. In particular, the device reliability should be verified with DNA extracted from control cell lines typically used as reference standard for an NGS run. In this way, the robustness of the microfluidic integrated protocol can be validated directly by the sample quality control performed by the NGS machine.

Finally, although we focused here on a specific application, any bead-based protocol requiring sequential capture/release steps, including washing or clean-up step can be implemented in the developed device. The system is also versatile in terms of magnetic beads concentration and aqueous phase viscosity, thus representing a suitable for a wide range of sample preparation protocols.

References

1 H. Kim, M. J. Jebrail, A. Sinha, Z. W. Bent, O. D. Solberg, K. P. Williams, S. A. Langevin, R. F. Renzi, J. L. Van De Vreugde, R. J. Meagher, J. S. Schoeniger, T. W. Lane, S. S. Branda, M. S. Bartsch and K. D. Patel, *PLoS One*, 2013, 8, e68988.

2 S. Kim, J. De Jonghe, A. B. Kulesa, D. Feldman, T. Vatanen, R. P. Bhattacharyya, B. Berdy, J. Gomez, J. Nolan, S. Epstein and P. C. Blainey, *Nat. Commun.*, 2017, 8, 13919.

3 S. J. Tan, H. Phan, B. M. Gerry, A. Kuhn, L. Z. Hong, Y. Min Ong, P. S. Y. Poon, M. A. Unger, R. C. Jones, S. R. Quake and W. F. Burkholder, *PLoS One*, 2013, 8, e64084.

4 M. M. DeAngelis, D. G. Wang and T. L. Hawkins, *Nucleic Acids Res.*, 1995, 23, 4742–3.

5 E. Brouzes, T. Kruse, R. Kimmerling and H. H. Strey, *Lab Chip*, 2015, 15, 908–919.

6 A. Ali-Cherif, S. Begolo, S. Descroix, J.-L. Viovy and L. Malaquin, *Angew. Chemie Int. Ed.*, 2012, 51, 10765–10769.

7 K. V. Voelkerding, S. A. Dames and J. D. Durtschi, *Clin. Chem.*, 2009, 55, 641–658.

8 S. Goodwin, J. D. McPherson and W. R. McCombie, *Nat. Rev. Genet.*, 2016, 17, 333–351.

9 Z. Wang, M. Gerstein and M. Snyder, *Nat. Rev. Genet.*, 2009, 10, 57–63.

10 S. G. Tringe and E. M. Rubin, *Nat. Rev. Genet.*, 2005, 6, 805–814.

11 A. Escobar-Zepeda, A. Vera-Ponce de León and A. Sanchez-Flores, *Front. Genet.*, 2015, 6, 348.

12 W.-S. Yong, F.-M. Hsu and P.-Y. Chen, *Epigenetics Chromatin*, 2016, 9, 26.

13 T. S. Furey, *Nat. Rev. Genet.*, 2012, 13, 840–852.

14 S. E. Levy and R. M. Myers, *Annu. Rev. Genomics Hum. Genet.*, 2016, 17, 95–115.

15 S. R. Head, H. K. Komori, S. A. LaMere, T. Whisenant, F. Van Nieuwerburgh, D. R. Salomon and P. Ordoukhanian, *Biotechniques*, 2014, 56, 61–4, 66, 68, passim.

16 F. Syed, H. Grunenwald and N. Caruccio, *Nat. Methods | Appl. Notes, Publ. online 01 Oct. 2009; | doi10.1038/nmeth.f.269*, 2009.

17 M. K. Sakharkar, V. T. K. Chow and P. Kangueane, *In Silico Biol.*, 2004, 4, 387–93.

18 F. Erhard and R. Zimmer, *Nucleic Acids Res.*, 2015, 43, e136.

19 T. Kivioja, A. Vähärautio, K. Karlsson, M. Bonke, M. Enge, S. Linnarsson and J. Taipale, *Nat. Methods*, 2011, 9, 72–74.

20 C. Schlötterer, R. Tobler, R. Kofler and V. Nolte, *Nat. Rev. Genet.*, 2014, 15, 749–763.

21 S. R. Head, H. K. Komori, S. A. LaMere, T. Whisenant, F. Van Nieuwerburgh, D. R. Salomon and P. Ordoukhanian, *Biotechniques*, 2014, 56, 61–4, 66, 68, passim.

22 E. L. van Dijk, Y. Jaszczyszyn and C. Thermes, *Exp. Cell Res.*, 2014, 322, 12–20.

23 G. Robertson, M. Hirst, M. Bainbridge, M. Bilenky, Y. Zhao, T. Zeng, G. Euskirchen, B. Bernier, R. Varhol, A. Delaney, N. Thiessen, O. L. Griffith, A. He, M. Marra, M. Snyder and S. Jones, *Nat. Methods*, 2007, 4, 651–657.

24 D. Ramsköld, S. Luo, Y.-C. Wang, R. Li, Q. Deng, O. R. Faridani, G. A. Daniels, I. Khrebtukova, J. F. Loring, L. C. Laurent, G. P. Schroth and R. Sandberg, *Nat. Biotechnol.*, 2012, 30, 777–782.

25 J. D. Buenrostro, P. G. Giresi, L. C. Zaba, H. Y. Chang and W. J. Greenleaf, *Nat. Methods*, 2013, 10, 1213–1218.

26 M. A. Quail, Y. Gu, H. Swerdlow and M. Mayho, *Electrophoresis*, 2012, 33, 3521–3528.

27 E. Z. Macosko, A. Basu, R. Satija, J. Nemesh, K. Shekhar, M. Goldman, I. Tirosh, A. R. Bialas, N. Kamitaki, E. M. Martersteck, J. J. Trombetta, D. A. Weitz, J. R. Sanes, A. K. Shalek, A. Regev and S. A. McCarroll, *Cell*, 2015, 161, 1202–1214.

28 A. M. Klein, L. Mazutis, I. Akartuna, N. Tallapragada, A. Veres, V. Li, L. Peshkin, D. A. Weitz and M. W. Kirschner, *Cell*, 2015, 161, 1187–1201.

29 J. A. Reuter, D. V. Spacek and M. P. Snyder, *Mol. Cell*, 2015, 58, 586–597.

30 S. Fisher, A. Barry, J. Abreu, B. Minie, J. Nolan, T. M. Delorey, G. Young, T. J. Fennell, A. Allen, L. Ambrogio, A. M. Berlin, B. Blumenstiel, K. Cibulskis, D. Friedrich, R. Johnson, F. Juhn, B. Reilly, R. Shammas, J. Stalker, S. M. Sykes, J. Thompson, J. Walsh, A. Zimmer, Z. Zwirko, S. Gabriel, R. Nicol and C. Nusbaum, *Genome Biol.*, 2011, 12, R1.

31 K. R. Paithankar and K. S. Prasad, *Nucleic Acids Res.*, 1991, 19, 1346.

32 R. Sista, Z. Hua, P. Thwar, A. Sudarsan, V. Srinivasan, A. Eckhardt, M. Pollack and V. Pamula, *Lab Chip*, 2008, 8, 2091–104.

33 B. P. Casavant, L. N. Strotman, J. J. Tokar, S. M. Thiede, A. M. Traynor, J. S. Ferguson, J. M. Lang and D. J. Beebe, *Lab Chip*, 2014, 14, 99–105.

34 J. Pipper, Y. Zhang, P. Neuzil and T.-M. Hsieh, *Angew. Chem. Int. Ed. Engl.*, 2008, 47, 3900–4.

35 P.-G. de. Gennes, F. Brochard-Wyart and D. Quéré, *Capillarity and wetting phenomena : drops, bubbles, pearls, waves*, Springer, 2004.

36 J. A. Dormandy, in *Clinical Aspects of Blood Viscosity and Cell Deformability*, Springer London, London, 1981, pp. 67–78.

37 F. Yetkin, U. Kayabas, Y. Ersoy, Y. Bayindir, S. A. Toplu and I. Tek, *South. Med. J.*, 2010, 103, 892–895.

38 W. H. Reinhart, G. Näf and B. Werth, *Clin. Hemorheol. Microcirc.*, 2010, 44, 177–82.

39 S.-Q. Gu, Y.-X. Zhang, Y. Zhu, W.-B. Du, B. Yao and Q. Fang, *Anal. Chem.*, 2011, 83, 7570–7576.

40 L. Rossen, P. Nørskov, K. Holmstrøm and O. F. Rasmussen, *Int. J. Food Microbiol.*, 1992, 17, 37–45.

41 S. Rodrigue, A. C. Materna, S. C. Timberlake, M. C. Blackburn, R. R. Malmstrom, E. J. Alm and S. W. Chisholm, *PLoS One*, 2010, 5, e11840.

42 A. D. Sanders, E. Falconer, M. Hills, D. C. J. Spierings and P. M. Lansdorp, *Nat. Protoc.*, 2017, 12, 1151–1176.

Chapter 5

Microfluidic valve with zero dead volume and negligible back-flow for droplets handling

Together with the development of a device devoted to the manipulation of the solid supports in droplet microfluidics, during my PhD I also contributed to the conception and microfabrication of a microfluidic pinch valve dedicated to droplet handling. The content of this chapter is part of an article recently accepted for publication in *Sensor and Actuators B: Chemical (**doi:** 10.1016/j.snb.2017.12.002).*

Droplet microfluidics allows the implementation of several biochemical and bioanalytical protocols in microfluidic devices. However, this integration typically requires the use of microfluidic valves, which allow the control of different operations on the same channels network. Unfortunately, the valves commercially available are almost exclusively suitable for-single phase flow, and only one valve system compatible with multi-phase systems has been presented so far in the literature. We present here a new pinch-like valve that withstands high pressures (tested up to 4 bar), allows droplet manipulation and combines

the advantages of conventional pinch valves regarding the absence of dead volume, while making negligible the backflow generated (less than 2nL). The conception and design of the presented valve, based on numerical simulations, is performed by an optimized microfabrication strategy, combining PDMS soft-lithography and 3D printing technologies. The valves had been tested regarding their mechanical stability and proving their capability of allowing droplets passing through them, without any perturbation. Finally, the very small backflow volume generated during the actuation, has been exploited for various applications in droplets microfluidics, like droplet handling, droplet-on-demand generation and sorting.

1 Introduction

Droplet microfluidics has emerged as a key innovating technology in the field of biotechnology, notably for biological and biomedical applications[1,2]. This was made possible by the wide range of functionalities available in droplets microfluidics: generation[3], merging, splitting, trapping[4], solid phase manipulation[5], etc. These tools fostered the implementation of complex protocols in multi-phase microfluidics, in which droplets are flown in different parts of complicated circuits of microchannels and several steps can be performed in parallel (e.g.: heating, optical measurement, etc.)[2,6,7]. Despite this potential, droplet manipulation remains a challenging task. In fact, the presence of droplets in a channel causes local variations in the hydraulic resistance of the microfluidic system[8], leading to possible pressure drops[9] or uncontrolled flows in other parts of the circuit. So far, however, only relatively simple fluidic architectures and workflows have been implemented in microfluidics. The integration of complex protocols most often requires the use of valves to isolate different parts of the circuit. Many valves dedicated to microfluidics have been introduced in the literature in the last two decades; however, most of them can operate only with single phase flows[10–13] and very few of them are suitable for droplet-based applications. Cybulski et al.[14] recently discussed the potential use of different types of valves for droplet manipulations, pointing out the limiting factors of the existing technologies. Most of the valves, either commercially available or reported in the literature, are characterized by modifications in the channel wettability and/or by sharp geometrical changes that could lead to the instability of the droplets menisci, causing their breaking. Besides, in some cases, a chamber representing a finite "dead volume" is present in the actuation

region, between the inlet and the outlet of the valves. This is, for example, the case for solenoid valves. This dead volume, having cross-sectional dimensions larger than those of the incoming channels, can trap droplets or induce their splitting. Besides the world of droplet microfluidics, they also induce problems for other suspensions often used in microfluidics, like cells, particles or colloids. Nowadays, in general, three types of valves have been used for droplet handling: pneumatic membrane valves, gate valves and pinch valves. Pneumatic valves had been introduced by Unger et al.[15] in 2000: they are based on a multilayer PDMS device in which two channels are separated by a thin membrane. In this system, the valve actuation relies on the application of a pneumatic pressure to the elastomeric membrane via one of the two channels, causing a compression of the other one in which the liquids of interest flow. The original development of this type of valve in PDMS devices[16] led to its diffusion in the microfluidic community and, recently, to a commercial system for genomic applications (Fludigm IFC device). However, this type of valve entails a multi-step fabrication requiring clean-room facilities. Furthermore, this fully integrated system is not convenient during the development and prototyping stages of a complicated microfluidic platform, in which external valves are preferred for sake of simplicity in fabrication and control.

These limitations may be partially overcome by the use of a gate valve, in which a small portion of a microchannel is slid or rotated with respect to an original position, in order to be aligned or not with the main channel that transports the liquid. This operating principle prevents any pressure pulse to occur during opening and closing processes. A commercially available gate valve is the “slider valve” by Takasago Fluidic Systems[17]. However, probably because of the large

diameter of the internal via, it is not suitable for multi-phases flows and, in fact, its compatibility with droplet manipulations has not yet been demonstrated. Recently, inspired by these systems and by the work of Wang et al.[18], Cybulski et al.[14] proposed a customized gate valve showing, for the first time, successful application to droplet manipulations. Using capillaries and sheets made in Teflon and optimizing the fabrication protocol, these authors achieved a valve that allows the passage of droplets without perturbation during open/close operations. In addition, these valves can be easily integrated into a modular droplet microfluidic platform. The droplets suspension is in contact exclusively with Teflon surfaces, preventing any instability. However, this capability has been achieved at the cost of simplicity in the fabrication process. These valves involve multiple precisely manufactured layers, assembled and sealed together by rubber silicon O-rings. Therefore, the production of these devices requires specific mechanical skills, which are more related to a mechanical workshop than to microfluidics facilities. Any defect in the fabrication and alignment of the layers, or in tube placing and cutting could lead to malfunctioning in the system. Thus, despite of its definite advantages for droplet microfluidics, this system is not suitable for low-resource setting or nontechnical environments; additionally, the design and fabrication complexity induces significantly high production costs.

Finally, pinch valves can also be used for droplet microfluidics applications[2]. Their simple working principle is based on the compression of an elastic tubing by applying a local mechanical pressure generated by an external actuator, which clamps the tubing itself. Thus, since the liquids are flown in a smooth and monolithic channel, pinch valves do not present any dead volume and

droplets can generally pass through them without being perturbed. As a drawback, however, the valve actuation changes the volume of the tube, thus generates upon closing an unwanted back-flow that typically involves a volume ranging between hundreds of nL and few µL. This back-flow can affect the droplets motion or even cause their breaking, notably if the distance between the compressed region and the droplet is limited. Therefore, although pinch valves probably represent the simplest strategy for droplets manipulation in complex microfluidic platforms, they have been discarded so far.

Here, we report the conception, development and characterization of a new and simple external microfluidic pinch-like valve, optimized for droplet microfluidics applications. The aim of this valve is to combine the absence of dead volume, typical of pinch valves, with a negligible back-flow volume generated during opening and closing processes. Additionally, in order to make the microfabrication possible in conventional microfluidic laboratories, standard soft-lithography is used, complemented with the versatility of 3D printing, ensuring high resolution, rapid manufacturing time and ease of learning[19]. Analyzing the closing operation of a pinch valve, the displaced volume is related with the size of the actuator and to the cross-section of the tubing used. Therefore, in order to reduce the contribution of these two factors, we designed and microfabricated by stereolithographic 3D printing customized actuators having different sizes and geometries. Then, numerical simulations were performed to evaluate the volume of liquid displaced during the valve actuation for different tubing diameters. These results suggested that a negligible back-flow volume (less than 2nL) can be achieved working with tubing having diameters of tens of microns. Unfortunately, this optimal working range does

not match with commercially available products. Therefore, we developed a process for the production of monolithic tubing-like PDMS microfluidic device, based on soft-lithography[20] and scaffold-wire removal strategy[21,22]. The pinch-like valve obtained by combining this PDMS chip with the 3D printed actuator, was characterized from the mechanical and hydrodynamic point of view. Finally, this valve was exploited in different applications involving droplets manipulation and requiring precise valve actuation.

2 Materials and methods

In this section, at first, the different consumable materials and equipment used during the entire work will be presented; then, the fabrication strategies developed to obtain the final microfluidic valve will be described and discussed in detail.

2.1 Material and solvents

The microfluidic device was prepared by soft-lithography of Polydimethylsiloxane (PDMS) Sylgard 184 Elastomer Kit (by Dow Corning), combined with wire removal technique, using tungsten metallic wires (diameters: 25, 35, 50, 80µm, by Good Fellow). PTFE tubing (by Sigma-Aldrich) having 0.3/0.6 mm internal/external diameter was used for inlet and outlet connection of the valve. Then, a stereolithographic 3D printer (by DWS) and a photosensitive acrylate-urethane based nano-filled ceramic resin (DL-260, by DWS – Digital wax)[23] was used for preparing the lithographic mold and some parts of the final valve. During the device validation, water phase droplets

were dispersed in FC-40 oil (by Fluorinert, 3M) with 2% (w/w) of Krytox-PEG (by Ran Biotechnologies) surfactant and both syringe pumps (neMESYS, by Cetoni GmbH) and pressure controller (MFCS, by Fluigent) equipped by flow meter (M type, by Fluigent) were used for flow control. Finally, the PDMS valve was externally controlled by a solenoid frame actuator (Radiospares, No. 347-652) supplied by portable batteries connected in series with a toggle manual switch. However, during the characterization steps, valves were activated by the solid-state relays NI-6525 (by National Instruments), controlled by a customized LabVIEW software.

2.2 Fabrication methods

2.2.1 Fabrication and optimization of the actuator tip by 3D printing

As mentioned above, the back-flow volume displaced during the actuation of conventional pinch valves mainly depends on: i) the internal diameter of the capillary in which the liquid flows and ii) the surface of the clamped region or, equivalently, on the size of the actuator tip. In order to minimize the latter contribution, we designed and fabricated a specific tip with optimized shape and sizes by 3D printing. The actuator has a cylindrical body and contains a threaded blind hole (diameter 4mm) in the center of one of its base. The other side of the actuator tip accommodates a semispherical geometry ending up into a microscale structure, representing the only component of the actuator in contact with the elastic capillary. This microscale structure is characterized by a constant cross-section, whereas its size and shape, as well as the material and manufacturing process, have been optimized as a compromise between the

technical requirements (minimize the contact surface with the tubing) and the fabrication steps (develop an easy and reliable printing process in order to achieve a robust structure, resistant to the actuation process). As shown in Fig. 1, three geometries for the tip cross-section have been investigated: (a) triangular, (b) squared and (c) hemispherical. After having tested different tip sizes, we optimized and fixed three design features for the structures under investigation: height α=0.6mm, length β=3 mm and thickness ℓ=0.25mm (see insets Fig. 1a,b,c). Smaller tips resulted in fact too fragile for the final applications, since they could break even by handling. Comparing the three geometries, ideally, the triangular shape would minimize the contact surface, reducing it to a line having a thickness of the order of tens of microns. We observed, however, that this geometry causes tube cutting after a few actuation loops. The hemispherical cross-section was finally preferred to the squared one, because it causes a smaller back-flow volume without damaging the tubing. In order to reach these dimensions, the resolution of the 3D printing process was also optimized: 35µm layers and a rigid ceramic material (see Materials and solvents paragraph) were used. Fig. 1d shows a SEM image (TM 3030, by Hitachi) of the 3D printed tip. The tip body is screwed at one end of the frame solenoid plunger (see Fig. 1e), where a threaded rod is glued, giving the possibility and versatility to easily remove and change the tip.

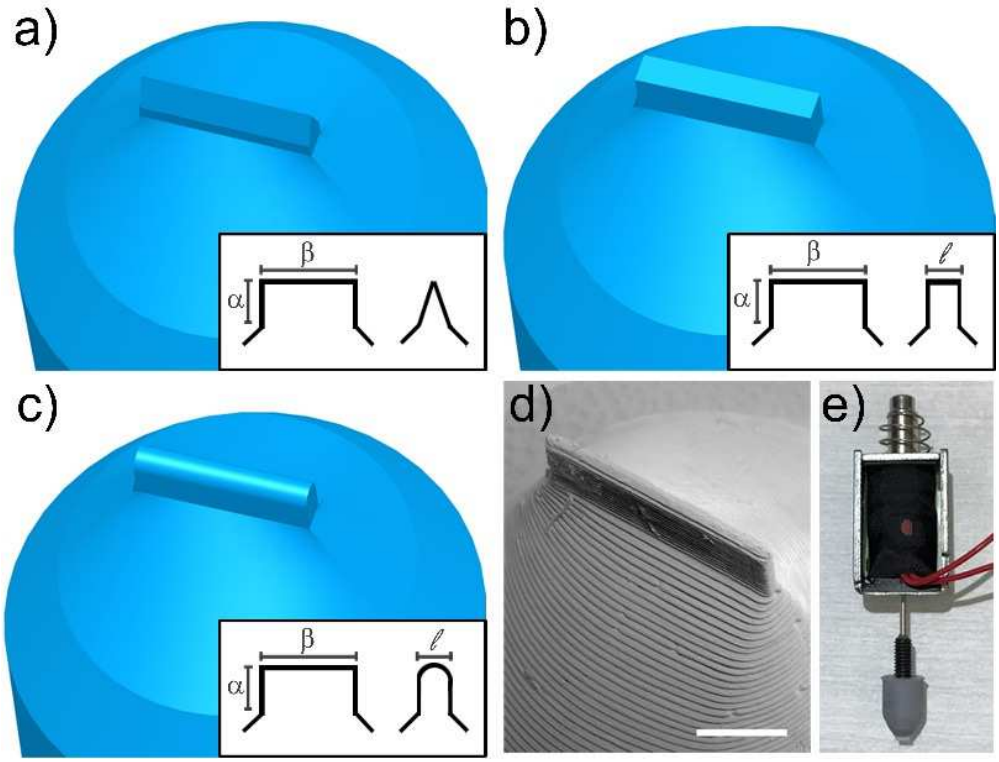

Figure 1: Three tested designs for the 3d printed tips: (a) triangular, (b) square and (c) hemispherical. *The dimensions α, β, ℓ represented in the insets are the same for all the geometries: α=0.6mm, β=3 mm and ℓ=0.25. (d) SEM image of the optimized hemispherical actuator tip (scale bar 1mm). (e) Picture of the frame-solenoid with the tip installed at one end of the plunger and with a spring fixed on the other side.*

2.2.2 Back-flow volume evaluation by numerical simulation

The minimization of the area of actuation represents a necessary but not sufficient condition to make the back-flow volume negligible. Another factor influencing the process is the diameter and the mechanical properties of the tubing in which the liquid flows. In pinch valves, this tubing is usually made of soft materials and its hyperelastic deformation[24], due to the stress applied by the tip, influences the closing profile of the tubing and plays an important role in the resulting displaced volume during the valve actuation. In order to gauge

the extent of these contributions, 2D finite element simulations (Comsol Multiphysics) of the median longitudinal cross-section of the system were performed, as shown in Fig. 2a. In particular, a time-dependent simulation of the closing process has been set, fixing the optimized design for the actuating tip as presented above. In addition, a two parameters Mooney-Rivlin model[25,26] is considered to describe the hyperelastic behavior of typical silicon-rubber tubing (whose walls are represented in light blue in Fig. 2a,b), as described in [27]. The solid mechanics simulation is run for a defined tip displacement in the y direction, as indicated by the blue arrow in Fig. 2a. The initial (dashed line) and final (solid line) configurations of the actuation process are represented in Fig. 2a,b. The displaced volume generated by the actuation was evaluated as a function of the tubing diameter (ranging from 10 to 350µm), integrating the displaced domain resulting from the simulation (represented in red in Fig. 2b) over the cylindrical geometry of the tubing. As expected, the results show an increase in the displaced volume as a function of the tubing diameter (Fig. 2c). Interestingly, a back flow volume smaller than a few tens of nanoliter is numerically achieved in the working range of tubing diameter between 10 µm and 100 µm (see yellow background region in Fig. 2c). Unfortunately, to the best of our knowledge, the smallest soft tubes commercially available are used for medical applications (HelixMark by Freudenberg Medical) and present diameters down to hundreds of microns, causing thus a large back flow volume (see blue background region in Fig.2c). This fact represented an incentive for developing a microfabrication protocol to produce soft material tubing having diameters in this optimal working range, leading to negligible back-flow conditions in pinch valve applications.

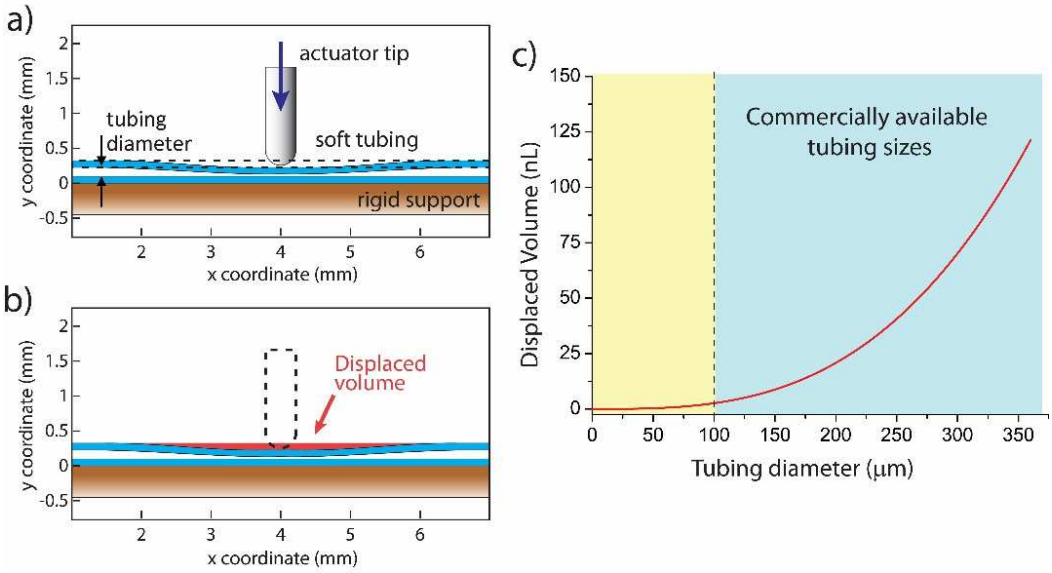

Figure 2: Numerical simulation of the actuation process. *(a) A median longitudinal cross-section of the system is considered and the simulation is performed for a fixed actuator displacement (blue arrow). The actuator tip (in grey) acts by clumping the soft tubing (walls represented in blue), placed on top of a rigid support (in brown). The initial configuration of the system is represented by a dashed line. (b) The displaced domain resulting from the simulation (in red) is integrated over the cylindrical geometry of the tubing in order to obtain the displaced volume. (c) Resulting displaced volume as a function of the inner tubing diameter. An optimal working range is defined, leading to a negligible displaced volume (yellow background area), as opposed to the large one predicted for commercially available tubing sizes (blue background area).*

2.2.3 Optimization of the PDMS tubing-like device microfabrication

Based on the simulations results described above and having identified a need for small diameter tubing, we proposed a new approach for the fabrication of

tubing-like devices composed by channels having customized diameters in the range of tens of microns.

Since soft-lithography is considered to be one of the simplest and most widely available microfabrication strategies[20], we based our protocol on this technology, in order to make our work available in most laboratories. Due to its hyperelastic properties, PDMS also fulfills the need of a material that can sustain numerous deformation cycles without showing plastic deformations. Additionally, in order to avoid any delamination and un-bonding problems during the application of the mechanical stresses, which easily occur with multilayer PDMS devices, a monolithic structure is also highly desirable. Therefore, we developed a specific fabrication protocol, taking into account all these constraints. In addition, exploiting the fast prototyping and ease of use strengths of 3D manufacturing, we produced a mold composed by 4 parts, that are screwed together. The central part (see orange part in Fig. 3a) is assembled with two lateral sides (yellow parts in Fig. 3b). The top view of the resulting assembly shows two rectangular grooves connected by a central channel (1.5mm large, 1.1mm deep and 8mm long), crossing longitudinally the surface. This pattern is designed to facilitate the manipulation of the final PDMS device and to accommodate the tubing for external connections (inlet and outlet of the valve).

A tungsten metallic wire is placed in the center of the microchannel defined by the assembly and two PTFE capillaries (few cm in length) are partially inserted around it on both sides of the channel, leaving the section of wire between the grooves uncovered (see Fig. 3c). The PTFE capillaries will act as inlet and outlet of the final valve. During device fabrication, they are filled with a 50:50 (v/v) water/glycerol solution, in order to prevent the diffusion of pre-

polymerized PDMS inside them. This operation was performed manually by using a plastic syringe connected to the tubing extremity placed outside of the mold. PDMS was then poured on the mold and the excess was removed by the doctor blade technique[28] in order to obtain a flat layer having the same height as the mold (see Fig. 3d). After PDMS curing (70°C for 1 hour) the last component of the mold was placed on top and new PDMS was poured on it (Fig. 3e). After degassing and removing the pre-polymer in excess as described before, the whole structure was placed again in the oven at 70°C for 1 hour (Fig. 3f). Once polymerized, the PDMS structure was unmolded and, following a device sonication in iso-propanol for 30 minutes at room temperature, the metal wire was removed. Notably, the sonication step not only permits washing away the glycerol solution but, especially, it slightly swells the PDMS, changing its mechanical properties[29] and lubricating the contact with the metallic wire. In this way, the wire can be easily pulled out of PDMS, leaving the microchannel intact. Optionally, notably for operation at high pressures, epoxy glue can be added externally to better attach the PDMS part to the PTFE tubing. Fig.3g shows the final PDMS tubing-like device. These microfabrication steps, guaranteeing easy unmolding and the fabrication of monolithic devices, were repeated using metallic wire having different diameters (25, 35, 50, 80µm). After that, a 5% (v/v) solution of 1H,1H,2H,2H-perfluorodecyltrichlorosilane (by Sigma-Aldrich) in FC-40 was flowed in the PDMS microchannel to improve the oil wetting, thus the droplet stability[28].

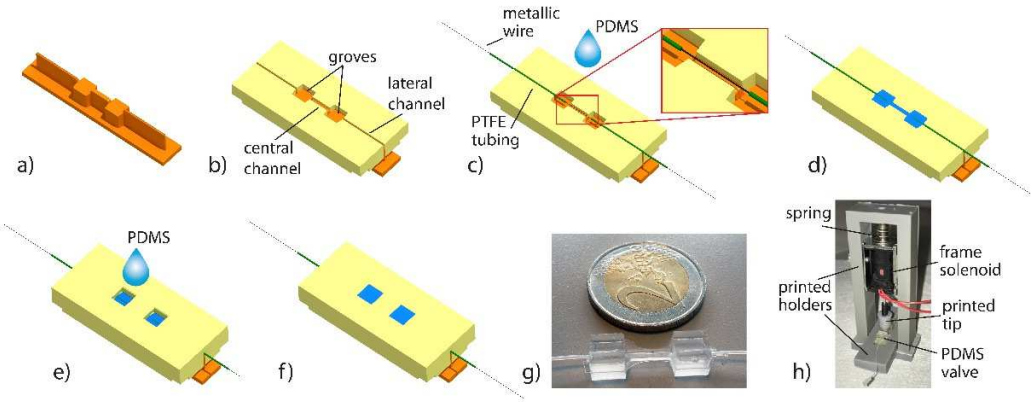

Figure 3: Microfabrication process of the tubing-like PDMS device. *(a-b) After having assembled the central and lateral side parts of the 3D printed mold, (c) the metallic wire (black) is placed in the center of the microchannel defined by the assembly. Two PTFE capillaries (green) are fixed on the lateral portions of the channel and filled with the glycerol solution. (d) Pre-polymerized PDMS is poured on the mold and, after baking, (e) the last top part of the mold is added and new PDMS is poured. Picture of the tubing-like PDMS device, (g) just unmolded and (h) installed in correspondence of the valve actuator.*

Finally, the tubing-like devices resulting from our fabrication protocol were characterized by optical microscopy, to identify any divergence from the expected cylindrical shape. In particular, the diameters of the PDMS channels were found to be slightly smaller than the metallic wire used and, in particular, shrinkages between 2% and 4% were observed. These values are comparable with the data reported in literature for PDMS soft-lithography [30–32]. Despite the shrinkage could be slightly reduced by finely tuning the curing parameters (e.g.: curing temperature, replication geometry, the mixing ratios, layer thickness), the shrinkage variation resulting by our protocol was sufficiently small for the final purpose of the device and therefore this aspect was not further investigated. In addition, several cross-sections for the same device were imaged, showing a uniform circular shape along the tubing length, with a circularity coefficient $f_{circ} = 0.975 \pm 0.006$ ($f_{circ} = 1$ for a perfect circle).

2.2.4 Final valve assembly

The tubing-like PDMS devices were finally placed in correspondence of the solenoid frame actuators equipped with the 3D printed tips presented above. As shown in Fig. 3h, in order to obtain an easy to handle system, both the actuator and the PDMS device were installed in dedicated 3D printed rigid supports. For these parts, much less precision was required, thus the printing layer was fixed at 150µm. As for conventional normally-open pinch valves, when an electric current is applied, the magnetic field pulls the frame solenoid plunger, that clamps the tubing placed in its correspondence and compresses the spring as well. Oppositely, when the current is turned OFF, the spring goes back to its resting position, and the tubing is re-opened. Following the manufacturer specification, our frame solenoid was supplied with a 12V DC electric potential to obtain a continuous 3W power. This produces a magnetic force of about 340mN, providing a plunger displacement of 1.1mm and resulting in a pressure exerted by the actuator tip on the PDMS tubing-like device during the closing process of about 4.5 bar.

2.2.5 Device microfabrication for DoD and droplet sorting applications

As it will be better described in the paragraph 3.2, the produced valves have been coupled with microfluidic devices to implement: i) droplet on demand (DoD) and ii) droplet sorting applications. In both cases, the devices were produced by standard double replica molding with PDMS, starting from a positive brass master prepared by micro-milling (Mini-Mill by Minitech Machinery Corp.) and following the same protocol presented in [28]. The device

for DoD is characterized by a conventional T-junction geometry, with two inlets that, during the experiments, are connected at two the pinch-like valves. Differently, the device dedicated to the droplet sorting includes: i) a sequence of two T-junctions for the continuous generation of droplets containing different water phase liquids, ii) a storage area for the droplets and iii) a Y-junction where droplets can be driven towards two different outlets connected downstream at two valves.

3 Results and discussion

After having established the microfabrication protocol, the properties of the pinch-like microvalve were characterized regarding: i) the back-flow volume, ii) the burst pressure and iii) the durability with regards to multiple open/close cycles.

3.1 Mechanical characterization

As shown in Fig. 4a, in order to evaluate the back-flow volume, we connected one end of the valve to a syringe and the other end to a PTFE tubing, connected to a reservoir at the atmospheric pressure. After having prefilled the microfluidic circuit with the fluorinated oil (see Materials and solvents paragraph), we sucked by the syringe a small amount of distilled water (0.1 µL) and then the same initial oil. In this way, a confined droplet is generated as described in[2]. After that, we observed one of the two droplet menisci while sequentially opening and closing the valve under zero-flow condition. Since the syringe pump is connected upstream of the valve, the displaced volume will be

transported downstream, in the tubing section containing the aqueous droplet. In particular, neglecting the oil lubrication film[9], by measuring the water-oil meniscus displacement ($\Delta L=L-L_0$) with respect to its initial position (L_0) and knowing the internal radius of the tubing (r), we estimated the volume of liquid that is moved during the valve actuation ($V=\Delta L\pi r^2$). The graph in Fig. 4b presents the back-flow volume displaced during the valve actuation as a function of the measured size of the tubing-like device (or tubing diameter). For each tubing diameter, 5 different valves were fabricated and tested. The reported points are obtained by averaging the representative mean values for each of the five series of measurements performed with the same valve. The associated error bars are calculated considering the standard deviations. The resulting values show coefficients of variation ranging between 2% and 5%, indicating the good reproducibility of our fabrication protocol.

Additionally, back-flow volumes smaller than 2 nL were achieved for tubing sizes less than 50 µm. As expected, the smaller is the tubing diameter, the lower is the displaced volume, qualitatively following the same behavior of the simulation results presented above. Additionally, this behavior suggests that by using smaller capillary the back-flow volume would not significantly change. For this reason, and since the reduction of the channel radius (r) brings to a dramatic increase of the hydraulic resistance R of the microfluidic circuit[33] ($R\propto 1/r^4$), we did not investigate smaller PDMS channel diameter. Overall, these results demonstrate the possibility to construct a valve having a displaced volume of a few nL, an important improvement with respect to commercial pinch-valves. This feature makes this type of valves perfectly suitable for any application requiring an extremely small back-flow.

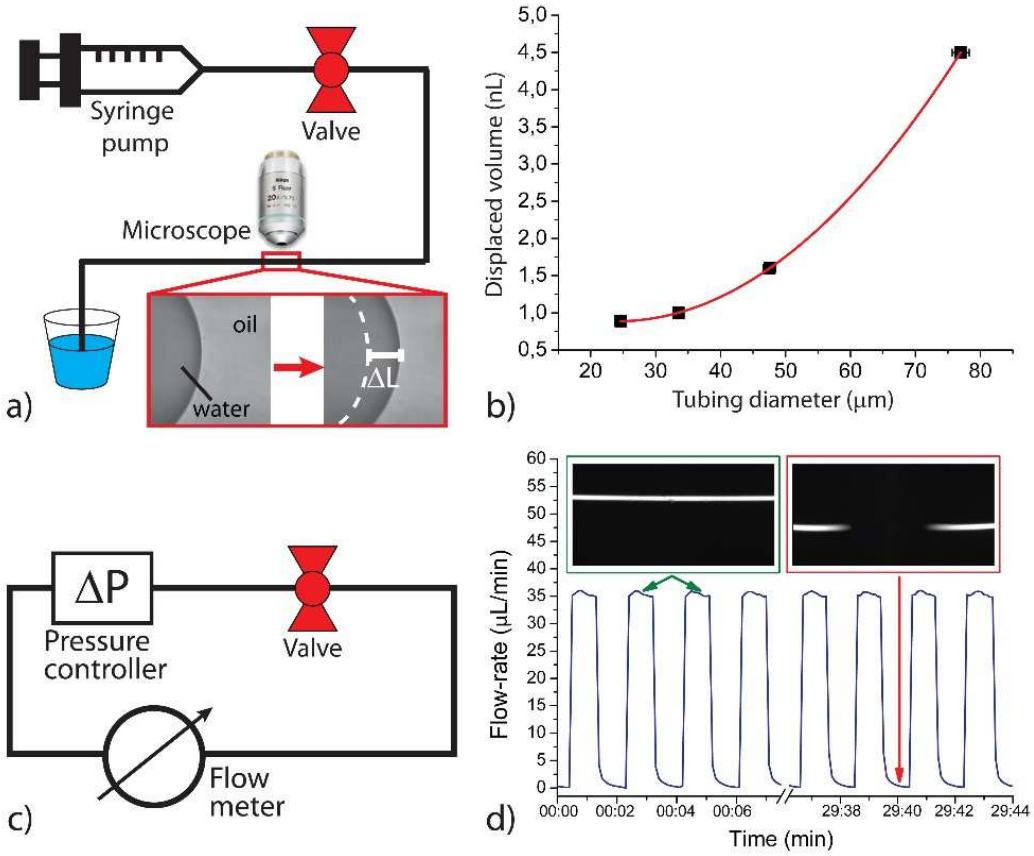

Figure 4: (a) Schematic diagram of the experimental setup for the evaluation of the back-flow volume. *(b) Measured back-volume plotted as function of the channel diameters of tubing-like PDMS devices; the error bars are not visible if they are smaller than the relative black dot. The values are fitted (red line) by a quadratic polynomial equation. (c) Schematic diagram of the setup used to evaluate the mechanical resistance of the valve during several open/close cycles. (d) The flow measured by the flowmeter during sequential valve actuation is plotted as a function of the time and oscillates between a constant value when the valve is open and zero when it is closed. Since the channel was pre-filled with fluorescein, in the insets it is possible to observe the valve in its open (i) and closed (ii) state. Furthermore, in the closed state the dye is completely evacuated from the clamped area, indicating that the valve is perfectly closed.*

In order to evaluate the maximal pressure applicable before bursting the valve[34], we connected the two ends of the valve (nominal diameter 50μm) to a pressure

controller as shown in Fig.4c. As presented in[35], the flowmeter connected in series was used for monitoring the eventual leakages during the experiment. After having pre-filled the entire microfluidic circuit by water, keeping the valve closed, an increasing pressure was applied with steps of 200 mbar every 30 seconds. The system was stable up to 4 bar, when leakage occurred at the tubing connections, while the valve remained intact. Therefore, this valve can support at least 4 bar, and probably more. This was expected considering the monolithic state of the device, due to the optimized fabrication strategy. Since the PDMS is poured and polymerized as a whole, the tubing-like device is completely free from delamination or bonding problems, which represents some of the main limitations of earlier microfabricated valves.

Finally, using the same set-up (Fig. 4c), we verified the durability and correct functionality of the valve under intensive stress conditions, performing sequential open/close cycles every second, for 30 minutes. Applying a pressure of 300 mbar, we could measure a flow of 35.6±0.7 µl/min when the valve is open and a 0.0±0.5 µl/min flow when it is closed (see Fig. 4d). These values are the average results on 900 independent open/close cycles, repeated three times, and demonstrates that our valve closes leak tight. Additionally, filling the circuit with a fluorescein solution (3µM in water), we could clearly and directly observe the region of the PDMS capillary involved in closing and opening operations (insets in Fig. 4d). It is worth noting that, in accordance with the flow-meter measurements, no leakage was observed during the operations and that the dye is completely removed from the clamped region when the valve is in the closed state.

3.2 Proof of concept applications

After having characterized these valves from the mechanical point of view, we exploited their unique properties targeting some specific applications for droplet microfluidics that require precise valve operation.

We first addressed the most demanding problem concerning droplets and valve: the capability of flowing droplets through a valve without droplets splitting, trapping or fusion. Droplets in oil phase (volume V=500pL) were generated by a conventional T-junction geometry, transported towards the valve by using an external PTFE tubing, and flown through the valve while cycles of opening and closing were performed. Fig. 5a shows a bottom view of the PDMS tubing-like device (nominal diameter 50µm). Since the droplets transport is controlled by a pressure-driven flow, when the valve is open, droplets can easily pass through the channel undisturbed (Fig. 5, I-II), while, when it is closed, droplets stop in correspondence of the actuator (Fig. 5, III). Finally, when the valve is re-opened, droplets can continue flowing in the PDMS tubing-like channel, whose integrity is not affected by the clamping process (Fig. 5, IV-VI). These results further reinforce the suitability of our valve for droplets handling, even in the case of limited distance between the droplet and the clamped region. This skill is mainly due to the monolithic state of the valve, its negligible back flow and the elastic fabrication material.

This valving system was then applied to Droplet on Demand (DoD)[36], which consists in an active droplet generation. In fact, in conventional generation approaches, droplets volume and their production frequency are linked parameters, thus one cannot be tuned without influencing the other. Differently, DoD raised the possibility to manipulate droplets independently. Nowadays,

this versatile control is extremely desirable for complex operations, like the formation of predesigned sequences of droplets containing different liquids, which represents a useful practice in many biological protocols[37,38]. Practically, DoD can be achieved by connecting the two inlet channels (for oil and aqueous phases) of a conventional T-junction geometry with two valves that are alternately opened and closed in order to flow oil or water in the main channel. However, from the technological point of view, in order to achieve sufficient precision, the back-flow volume generated during the valves actuation must be carefully managed. In particular, to ensure that the back-volume is not pushed in the microfluidic device, the ratio (ϕ) between the hydraulic resistance upstream and downstream of the valve must be higher than a critical value that depends on the valve itself. For example, in the work proposed by Churski et al.[39], this ratio should be higher than 10^6. In practice, considering two circular channels of equal length, if the one placed downstream of the valve has a diameter of 300µm, the tubing that should be used upstream in order to avoid any back-flow in the device must have a radius of 2cm. Even if this represents an extreme case because large valves had been used in this earlier work, this example emphasizes the difficulty of performing DoD with low volumes using earlier methods. In contrast, due to their small back-flow volume, the new pinch-like valves presented here are extremely valuable for DoD applications. To prove this, we followed the scheme proposed in [36], connecting two of our valves (nominal diameter of 50µm) at the inlets of the T-junction device presented above (see Fig. 5b). Additionally, we carefully adjusted the lengths of the tubing upstream and downstream of the valves in order to have a ratio ϕ of about 1. Therefore, changing the opening and closing time for the valves

(t_o and t_w for the oil and the water phase, respectively) and the pressure applied to control the liquid (p_o and p_w for oil and water, respectively), as expected, we obtained on-demand droplets having different sizes in a range of volumes between 40 nL and 350 nL. In detail, as shown in Fig. 5b, fixing p_w, the droplet size increases linearly by the increase of t_w. In contrast, the droplet size is independent of the opening time t_o of the oil inlet. Additionally, the slopes presented in the graph are directly proportional to p_w (see inset), as shown in [36]. Finally, as typical of DoD systems, we could vary as desired droplets volume generated in the same experiment and in real time. These results are all in perfect agreement with the one proposed in [36], demonstrating that our valves are perfectly suitable for DoD applications and do not require any control on the hydraulic resistance ratio ϕ , as mandatory for conventional DoD systems.

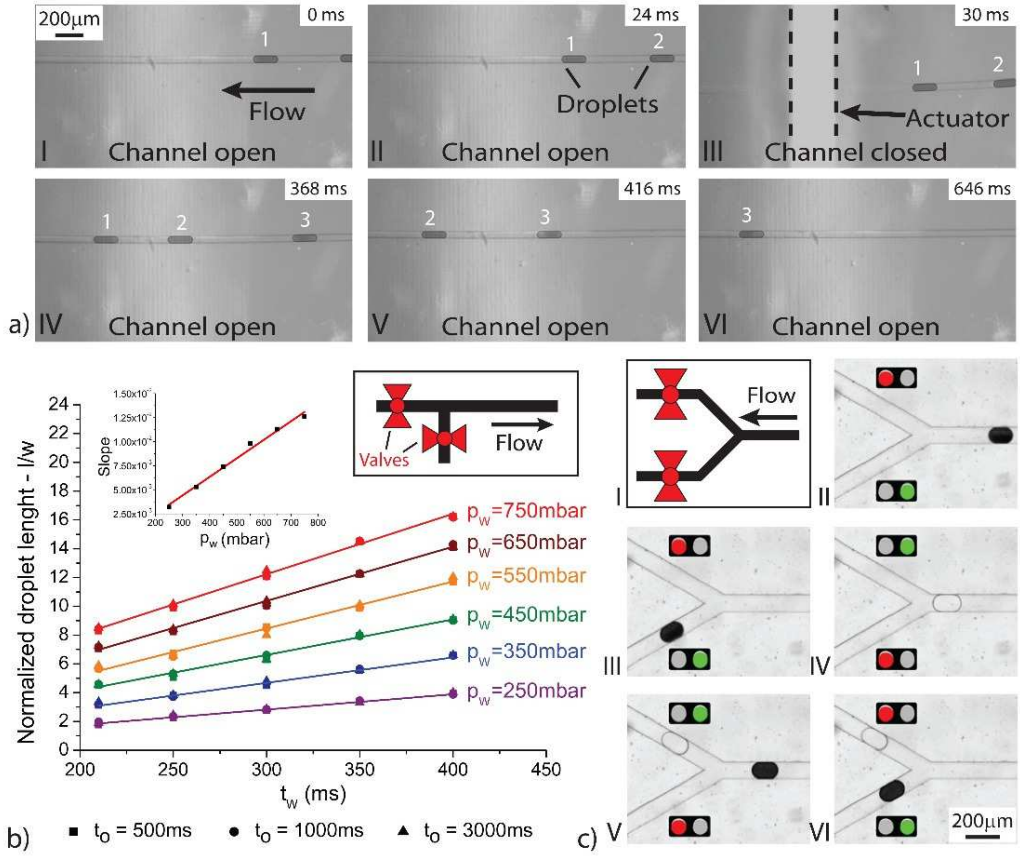

Figure 5: (a) Image sequence showing the droplets flow inside the PDMS tubing-like channel *before (I-II), during (II) and after (IV-VI) the valve actuation. Interestingly, droplets are unperturbed during the whole process. Furthermore, the valve operations do not affect the PDMS capillary integrity. (b) Water in oil emulsion is generated by DoD strategy using two valves connected at the inlets of a T-junction (cross section: 300x300µm, see scheme in the inset). Keeping the oil pressure constant (600mbar), the normalized droplet lengths (l) by the channel width (w) plotted as a function of the opening time of the valve connected to the water inlet (tw) show linear behaviors for different water pressure applied. These slopes are proportional to the water pressure (pw) (see inset). Differently, the droplet size is not influenced by the opening time for the oil inlet (to). Error bars were evaluated as the standard deviation of the average of dozens of droplet lengths (coefficient of variation CV<2%) and are not visible in the graph because they are smaller than the data points. (c) Image sequence of the droplet sorting process by a Y-junction, whose branches are connected with two valves.*

Finally, we tested the valve for droplet sorting which, as recently discussed by Xi et al.[40], represents an important requirement for various lab-on-a-chip applications, especially regarding cells encapsulation and biochemical reactions. In detail, the sorting can be achieved by driving the droplets to a Y-junction where, subjected to an external stimulus, they are deviated in a specific direction. Previous implementations used e.g. a local thermal actuation[41] or dielectrophoresis effects[42]. However, the first requires a laser which must be well focused on a specific point of the device, while the second is optimized only for small and not confined droplets. A simpler approach would be connecting two valves downstream of the outlets of the Y-junction to direct the droplets by controlling the flow. Despite the simplicity of this approach, no examples are presented in literature, mainly due to the impossibility to flow confined droplets through a valve and to the back-flow exerted by the valves, which would strongly perturb the droplets flow. In order to exploit the negligible back-flow volume of the pinch-like valves presented here, we used them for droplets sorting. In particular, as shown in Fig. 5c, water phase droplets (volume about 600pL) having two different colors (dark and transparent) were generated by the double T-junctions and collected in a storage region (see 2.2.5 paragraph). From there, they are guided towards a Y-junction and automatically discriminated according to their color by a dedicated image recognition LabVIEW software.

The presented DoD and sorting experimental setup show a throughput of few Hz, which is, in some cases, slower than other methods mentioned above (between tens and hundreds of Hz). This limitation is mainly due to the chosen electronics (National Instrument card), presenting a maximum output

switching frequency of 5Hz. However, the versatility of our system allows an easy coupling with a different electronics and/or other mechanical actuators in order to achieve a faster response in time. Therefore, this parameter can be tuned according with the final application of interest, while keeping the simplicity of the valves. For example, the PDMS tubing-like device and the 3D printed tip could be combined with a piezoelectric actuator, which would increase the switching rate up to few hundreds Hz[33]. This would be convenient for both droplet sorting and DOD applications.

4 Conclusions

In this work we presented the conception, fabrication and characterization of an external microfluidic valve that shows high resistance to pressure (tested up to 4 bar) and permits droplets handling and in particular their passage through it without any trapping, damaging or perturbation. Additionally, the valve is characterized by zero dead volume, an advantage borrowed from common pinch valves, but differently from them, it shows a back-flow volume of only few nL. For that, after having established a reliable microfabrication process, we demonstrated its compatibility with diffuse droplets protocols: i) the generation of Droplet-on-Demand avoiding the typical limitations of earlier systems concerning the hydraulic resistance ratio downstream and upstream of the valve; and ii) the droplet sorting mediated by a Y-junction, without requiring the use of external equipment, like a laser focusing system.

Therefore, coupling the versatility of 3D printing technology with conventional PDMS soft-lithography, we propose an easy-to-fabricate device, suitable for droplet microfluidics, not requiring any specific equipment or clean-room

facilities. This compact valve can be produced and/or used in both specialized and non-technical environments and, would be suitable for point-of-care applications and compatible with low-resource settings. Finally, it is worth to notice that other fragile colloidal systems such as cells or beads could pass through these valves without being stacked or perturbed during their flow.

References

1 M.T. Guo, A. Rotem, J.A. Heyman, D.A. Weitz, Droplet microfluidics for high-throughput biological assays, Lab Chip. 12 (2012) 2146. doi:10.1039/c2lc21147e.

2 D. Ferraro, J. Champ, B. Teste, M. Serra, L. Malaquin, J.-L. Viovy, P. de Cremoux, S. Descroix, Microfluidic platform combining droplets and magnetic tweezers: application to HER2 expression in cancer diagnosis, Sci. Rep. 6 (2016) 25540. doi:10.1038/srep25540.

3 P. Zhu, L. Wang, Passive and active droplet generation with microfluidics: a review, Lab Chip. 17 (2017) 34–75. doi:10.1039/C6LC01018K.

4 R. Seemann, M. Brinkmann, T. Pfohl, S. Herminghaus, Droplet based microfluidics, Reports Prog. Phys. 75 (2012) 16601. doi:10.1088/0034-4885/75/1/016601.

5 D. Ferraro, Y. Lin, B. Teste, D. Talbot, L. Malaquin, S. Descroix, A. Abou-Hassan, Continuous chemical operations and modifications on magnetic γ-Fe 2 O 3 nanoparticles confined in nanoliter droplets for the assembly of fluorescent and magnetic SiO 2 @γ-Fe 2 O 3, Chem. Commun. 51 (2015) 16904–16907. doi:10.1039/C5CC07044A.

6 Y. Schaerli, R.C. Wootton, T. Robinson, V. Stein, C. Dunsby, M.A.A. Neil, P.M.W. French, A.J. deMello, C. Abell, F. Hollfelder, Continuous-Flow Polymerase Chain Reaction of Single-Copy DNA in Microfluidic Microdroplets, Anal. Chem. 81 (2009) 302–306. doi:10.1021/ac802038c.

7 A.C. Hatch, J.S. Fisher, A.R. Tovar, A.T. Hsieh, R. Lin, S.L. Pentoney, D.L. Yang, A.P. Lee, 1-Million droplet array with wide-field fluorescence imaging for digital PCR., Lab Chip. 11 (2011) 3838–45. doi:10.1039/c1lc20561g.

8 S.A. Vanapalli, A.G. Banpurkar, D. van den Ende, M.H.G. Duits, F. Mugele, Hydrodynamic resistance of single confined moving drops in rectangular microchannels, Lab Chip. 9 (2009) 982–990. doi:10.1039/B815002H.

9 C.N. Baroud, F. Gallaire, R. Dangla, Dynamics of microfluidic droplets, Lab Chip. 10 (2010) 2032. doi:10.1039/c001191f.

10 A.M. Stockton, M.F. Mora, M.L. Cable, P.A. Willis, Design rules and operational optimization for rapid, contamination-free microfluidic transfer using monolithic membrane valves, Sensors Actuators B. 177 (2013) 668–675. doi:10.1016/j.snb.2012.11.039.

11 R. Mohan, B.R. Schudel, A. V. Desai, J.D. Yearsley, C.A. Apblett, P.J.A. Kenis, Design considerations for elastomeric normally closed microfluidic valves, Sensors Actuators B Chem. 160 (2011) 1216–1223. doi:10.1016/j.snb.2011.09.051.

12 C.I. Rogers, J.B. Oxborrow, R.R. Anderson, L.-F. Tsai, G.P. Nordin, A.T. Woolley, Microfluidic valves made from polymerized polyethylene glycol diacrylate, Sensors Actuators B Chem. 191 (2014) 438–444. doi:10.1016/j.snb.2013.10.008.

13 K.W. Oh, C.H. Ahn, A review of microvalves, J. Micromechanics Microengineering. 16 (2006) R13–R39. doi:10.1088/0960-1317/16/5/R01.

14 O. Cybulski, S. Jakiela, P. Garstecki, Whole Teflon valves for handling droplets, Lab Chip. 16 (2016) 2198–2210. doi:10.1039/C6LC00375C.

15 M.A. Unger, H.-P. Chou, T. Thorsen, A. Scherer, S.R. Quake, Monolithic Microfabricated Valves and Pumps by Multilayer Soft Lithography, Science (80-.). 288 (2000) 113–116. doi:10.1126/science.288.5463.113.

16 T. Thorsen, S.J. Maerkl, S.R. Quake, Microfluidic Large-Scale Integration, Science (80-.). 298 (2002) 580–584. doi:10.1126/science.1076996.

17 Solenoid-Driven Slider Valve – Takasago Fluidic Systems, (n.d.). http://www.takasago-fluidics.com/conts/wp-content/uploads/2017/01/Solenoid-driven-Slider-Valve.pdf (accessed August 10, 2017).

18 W. Wang, J.J. Lu, C. Gu, L. Zhou, S. Liu, Performing Isoelectric Focusing and Simultaneous Fractionation of Proteins on A Rotary Valve Followed by Sodium Dodecyl–Polyacrylamide Gel Electrophoresis, Anal. Chem. 85 (2013) 6603–6607. doi:10.1021/ac401470d.

19 S. Waheed, J.M. Cabot, N.P. Macdonald, T. Lewis, R.M. Guijt, B. Paull, M.C. Breadmore, 3D printed microfluidic devices: enablers and barriers, Lab Chip. 16 (2016) 1993–2013. doi:10.1039/C6LC00284F.

20 Y. Xia, G.M. Whitesides, Soft Lithography, Angew. Chemie Int. Ed. 37 (1998) 550–575. doi:10.1146/annurev.matsci.28.1.153.

21 D. Ferraro, C. Semprebon, T. Tóth, E. Locatelli, M. Pierno, G. Mistura, M. Brinkmann, Morphological Transitions of Droplets Wetting Rectangular Domains, Langmuir. 28 (2012) 13919–13923. doi:10.1021/la302854t.

22 A. Yamada, R. Renault, A. Chikina, B. Venzac, I. Pereiro, S. Coscoy, M. Verhulsel, M.C. Parrini, C. Villard, J.-L. Viovy, S. Descroix, Transient microfluidic compartmentalization using actionable microfilaments for biochemical assays, cell culture and organs-on-chip, Lab Chip. 16 (2016) 4691–4701. doi:10.1039/C6LC01143H.

23 R. Bernasconi, C. Credi, M. Tironi, M. Levi, L. Magagnin, Electroless Metallization of Stereolithographic Photocurable Resins for 3D Printing of Functional Microdevices, J. Electrochem. Soc. 164 (2017) B3059–B3066. doi:10.1149/2.0081705jes.

24 D.P.J. Cotton, A. Popel, I.M. Graz, S.P. Lacour, Photopatterning the mechanical properties of polydimethylsiloxane films, J. Appl. Phys. 109 (2011) 54905. doi:10.1063/1.3552917.

25 R.S. Rivlin, D.W. Saunders, Large Elastic Deformations of Isotropic Materials. VII. Experiments on the Deformation of Rubber, Philos. Trans. R. Soc. London A Math. Phys. Eng. Sci. 243 (1951).

26 M. Mooney, M., A Theory of Large Elastic Deformation, J. Appl. Phys. 11 (1940) 582–592. doi:10.1063/1.1712836.

27 M. Shahzad, A. Kamran, M.Z. Siddiqui, M. Farhan, Mechanical Characterization and FE Modelling of a Hyperelastic Material, Mater. Res. 18 (2015) 918–924. doi:10.1590/1516-1439.320414.

28 B. Teste, N. Jamond, D. Ferraro, J.-L. Viovy, L. Malaquin, Selective handling of droplets in a microfluidic device using magnetic rails, Microfluid. Nanofluidics. 19 (2015) 141–153. doi:10.1007/s10404-015-1556-6.

29 C.U. Yu, J.E. Mark, Specific Solvent Effects in Swollen Polymer Networks, Macromolecules. 7 (1974) 229–232. doi:10.1021/ma60038a015.

30 C. Moraes, Y. Sun, C.A. Simmons, Solving the shrinkage-induced PDMS alignment registration issue in multilayer soft lithography, J. Micromechanics Microengineering. 19 (2009) 65015. doi:10.1088/0960-1317/19/6/065015.

31 S.W. Lee, S.S. Lee, Shrinkage ratio of PDMS and its alignment method for the wafer level process, Microsyst. Technol. 14 (2007) 205–208. doi:10.1007/s00542-007-0417-y.

32 M.H. Madsen, N.A. Feidenhans'l, P.-E. Hansen, J. Garnæs, K. Dirscherl, Accounting for PDMS shrinkage when replicating structures, J. Micromechanics Microengineering. 24 (2014) 127002. doi:10.1088/0960-1317/24/12/127002.

33 P. Tabeling, Introduction to microfluidics, Oxford University Press, 2005.

34 E. Piccin, D. Ferraro, P. Sartori, E. Chiarello, M. Pierno, G. Mistura, Generation of water-in-oil and oil-in-water microdroplets in polyester-toner microfluidic devices, Sensors Actuators B Chem. 196 (2014) 525–531. doi:10.1016/j.snb.2014.02.042.

35 M. Serra, I. Pereiro, A. Yamada, J.-L. Viovy, S. Descroix, D. Ferraro, A simple and low-cost chip bonding solution for high pressure, high temperature and biological applications, Lab Chip. 17 (2017) 629–634. doi:10.1039/C6LC01319H.

36 K. Churski, J. Michalski, P. Garstecki, Droplet on demand system utilizing a computer controlled microvalve integrated into a stiff polymeric microfluidic device, Lab Chip. 10 (2010) 512–518. doi:10.1039/B915155A.

37 S. Jakiela, T.S. Kaminski, O. Cybulski, D.B. Weibel, P. Garstecki, Bacterial Growth and Adaptation in Microdroplet Chemostats, Angew. Chemie Int. Ed. 52 (2013) 8908–8911. doi:10.1002/anie.201301524.

38 U. Tangen, G.A.S. Minero, A. Sharma, P.F. Wagler, R. Cohen, O. Raz, T. Marx, T. Ben-Yehezkel, J.S. McCaskill, DNA-library assembly programmed by on-demand nano-liter droplets from a custom microfluidic chip, Biomicrofluidics. 9 (2015) 44103. doi:10.1063/1.4926616.

39 K. Churski, M. Nowacki, P.M. Korczyk, P. Garstecki, Simple modular systems for generation of droplets on demand, Lab Chip. 13 (2013) 3689. doi:10.1039/c3lc50340b.

40 H.-D. Xi, H. Zheng, W. Guo, A.M. Gañán-Calvo, Y. Ai, C.-W. Tsao, J. Zhou, W. Li, Y. Huang, N.-T. Nguyen, S.H. Tan, Active droplet sorting in microfluidics: a review, Lab Chip. 17 (2017) 751–771. doi:10.1039/C6LC01435F.

41 C.N. Baroud, J.-P. Delville, F. Gallaire, R. Wunenburger, Thermocapillary valve for droplet production and sorting, Phys. Rev. E. 75 (2007) 46302. doi:10.1103/PhysRevE.75.046302.

42 J.-C. Baret, O.J. Miller, V. Taly, M. Ryckelynck, A. El-Harrak, L. Frenz, C. Rick, M.L. Samuels, J.B. Hutchison, J.J. Agresti, D.R. Link, D.A. Weitz, A.D. Griffiths, Fluorescence-activated droplet sorting (FADS): efficient microfluidic cell sorting based on enzymatic activity, Lab Chip. 9 (2009) 1850. doi:10.1039/b902504a.

Conclusion and perspectives

In the wide set of functionalities currently available in the droplet microfluidic toolbox (i.e., droplet generation, merging, splitting, sorting, cell encapsulation,…), a robust device allowing the possibility to enrich or extract an analyte of interest from a complex matrix is still under investigation. This step, crucial in many biochemical protocols, is conventionally performed based on the manipulation of a functionalized solid-state support, binding the target molecule.

Many approaches have been proposed in multiphase and droplet microfluidics, exploiting different microfluidics architectures (stationary, digital and continuous). Among them, one of the state of the art technologies are the magnetic tweezers pioneered by our team. Indeed, it represents the only device currently available in continuous droplet microfluidics to perform extraction and redispersion operations in droplet continuously flowing in a capillary. More than five years after its development, this represents a mature and robust technology, whose flexibility led to the implementation of clinical applications in the droplet workflow. In this work, we focused in particular on two recent projects regarding the purification of mRNA from a total RNA sample prior to an RT-qPCR step for cancer gene expression level determination, and the detection of amyloid beta peptides, as biomarkers of interest for Alzheimer disease. On the other hand, this technology does not take full advantages of common continuous droplet microfluidics architectures, being thus limited by the processing velocity, miniaturization and lack of parallelization.

The aim of my PhD work has been to answer the demand for a droplet microfluidic concept combining both the capture/release functionality and the high throughput processing. We thus presented the conception, fabrication and characterization of a novel droplet microfluidic approach based on the

integration of a pair of soft magnetic components placed adjacently to the main droplet flowing microchannel, and activated by an external permanent magnet. This strategy allows to focus the magnetic field lines generating a strong and local magnetic force along the path of the droplet, able to compact the functionalized paramagnetic particles in a cluster and to attract it in the region between the soft magnets. In order to reach the trap, the beads cluster must deform the droplet meniscus, generating a short droplet finger inside the capture region. This magnetically-assisted fingering prevents the droplet to restore its initial shape in the main channel and represents a condition allowing its splitting while the rear droplet meniscus crosses the capture region. As a result, a subdroplet containing the cluster of magnetic particles is generated, while the parent droplet continues its flow in the main channel. Interestingly, the droplet is kept immobile in the continuous oil flow and, switching OFF the soft magnetic components, it can be released, upon merging, in a coming droplet with a negligible carryover of supernatant. This configuration allows purification rates higher than 96% in the range of flows considered (up to 1 µl/s) and extraction rate higher than 95% up to 0.25 µl/s.

We have also demonstrated that the extraction performances of this device can be improved by the generation of a controlled droplet fingering in the capture region, thus avoiding the slow-down of the magnetic particle cluster dynamics towards the trap, due to the droplet interfacial counterforce. With this aim, two strategies were proposed, corresponding to a passive or active control of the droplet fingering process. The former exploits a pressure-driven hyperelastic component, microfabricated and installed in a dead-end channel portion perpendicular to the main one, connected to the capture pocket. This device

allows to control the droplet self-triggered fingering phenomenon in the trap due to the pressure increase in the portion of the main channel beyond the capture region caused by the presence of the droplet crossing the junction. On the other hand, the latter approach is based on the control of the droplet fingering by setting a constant hydraulic resistance ratio between the main and the secondary channel through a pressure controller. Although presenting comparable extraction and redispersion rates (>95% for flow-rates up to 1 µl/s), the latter approach bring an additional functionality to the system, allowing both the clean-up of a target molecule from the original matrix and the possibility to perform further downstream process on the extracted beads cluster (e.g., optical detection, re-encapsulation,…) in a section of the microfluidic network distinct from the main channel. As a first proof-of-concept, these functionalities were exploited for the preparation of nucleic-acids libraries dedicated to NGS, focusing, in particular, on a critical step represented by DNA size selection process. As a matter of fact, this protocol is not of straightforward implementation in a continuous droplet microfluidics architecture, due to the absence of a device integrating both the magnetic separation and the extraction and redispersion steps required. Together with the need for specific functionalities, this protocol is based on the precipitation of target DNA fragments on carboxylic beads in presence of NaCl and PEG, thus involving the manipulation of a viscous fluid in droplet. Consequently, a study on the effect of the dispersed phase viscosity on the extraction performance as a function of the magnetic particle load was performed, for the first time in continuous droplet microfluidics. Preliminary data of size selection and clean-up performed on a DNA ladder sample were presented, showing for the first

time in droplet microfluidics size distribution and recoveries comparable with the ones of conventional methods, but with interesting improvements in reagents volume and automation. Further investigations must be conducted on specific aspects, notably related to the influence and efficacy of the washing steps on the following PCR amplification and sequencing.

Several perspectives are envisioned for the system following both the technological and the application axis. Concerning the technological point of view, the concept developed in this work is suitable for further downscaling, for application requiring smaller volume droplet, like single-cell analysis. However, decreasing the working droplet volume, a resizing in the channel dimensions should be reconsidered in order to keep the droplet in a confined state. Furthermore, despite the droplet fingering phenomenon can always be controlled by setting the hydraulic resistance ratio between the main and the secondary channel, the lower beads load in the droplet causes a decrease in the achieved magnetic force, thus probably affecting the device functionality. For this reason, the material and the related fabrication process should be reconsidered, in order to achieve a sharper magnetic flux density gradient and, therefore, a more intense magnetic force able to counteract the finger retreat process and to maintain the droplet in a magnetically-driven deformed state, allowing the following splitting and extraction. The improvements in droplet processing rate, together with the proposed reduction in droplet volume, require a more adapted and rapid droplet generation system than the currently-used motorized pipettor. In this direction, the optimized pinch valve presented in the last chapter of this work represents an interesting technology for the generation

of deterministic trains of droplets, exploiting, in particular, the Droplet-On-Demand system.

From the applicative point of view, the validation of the clean-up and size selection steps using a nucleic acid sample extracted from NGS control cell line is planned in a short future. Furthermore, as a long-term perspective, the implemented protocols can be integrated with merging and thermal amplification stages in order to develop a sample-in/libraries-out droplet microfluidic platform, suitable for different NGS libraries preparation. Nevertheless, an opening towards the implementation of new bead-based protocol is also suitable, fostered by the robustness of our concept, allowing sequential capture/release processes and clean-up steps with high extraction rate and extremely low carryover of supernatant, and further reinforced by its versatility in terms of magnetic beads concentration and aqueous phase viscosities handled.

Annex 1

SCIENTIFIC REPORTS

OPEN

Microfluidic platform combining droplets and magnetic tweezers: application to HER2 expression in cancer diagnosis

Received: 14 January 2016
Accepted: 18 April 2016
Published: 09 May 2016

Davide Ferraro[1], Jérôme Champ[2], Bruno Teste[1], Marco Serra[1], Laurent Malaquin[3], Jean-Louis Viovy[1], Patricia de Cremoux[2] & Stephanie Descroix[1]

The development of precision medicine, together with the multiplication of targeted therapies and associated molecular biomarkers, call for major progress in genetic analysis methods, allowing increased multiplexing and the implementation of more complex decision trees, without cost increase or loss of robustness. We present a platform combining droplet microfluidics and magnetic tweezers, performing RNA purification, reverse transcription and amplification in a fully automated and programmable way, in droplets of 250nL directly sampled from a microtiter-plate. This platform decreases sample consumption about 100 fold as compared to current robotized platforms and it reduces human manipulations and contamination risk. The platform's performance was first evaluated on cell lines, showing robust operation on RNA quantities corresponding to less than one cell, and then clinically validated with a cohort of 21 breast cancer samples, for the determination of their HER2 expression status, in a blind comparison with an established routine clinical analysis.

The discoveries allowed by large-scale genomics and post-genomics have important outcomes in medicine, giving rise in particular to the development of "precision medicine". This approach is defined by the Food and Drug Administration as the tailoring of medical treatment to the individual characteristics, needs and preferences of a patient during all stages of care, including prevention, diagnosis, treatment and follow-up[1]. To date, advances in genomic sequencing have improved the knowledge of the genetic characteristics of tumor cells and led to the identification of numerous new gene mutations or amplifications that may be appropriate for genomics-driven drug development. The panel of targeted therapies matched to specific patient's tumor genomic alterations is fast increasing. As a consequence, the timely selection of the best therapy for each patient is becoming an increasingly difficult challenge for physicians. In parallel, important efforts are developed in clinical practice to minimize the invasiveness of diagnostic acts, leading, in particular, to a development of micro-biopsies and more generally to a reduction of the typical size of clinical samples. In order to perform assays of increasing complexity on samples of decreasing size, innovative technologies allowing fast and multigene screening analysis from minute sample material are needed[2–4]. We describe here such a method and validate it regarding the specific problem of HER2 (human epidermal growth factor receptor 2) status determination in breast cancer patients.

Breast cancers represent 23% of all cancers and 14% of cancer mortality worldwide. 15~20% of breast cancer patients present an amplification of HER2 and subsequent overexpression in breast cancer is associated with a more aggressive clinical behavior[5]. However, adjuvant humanized monoclonal antibody directed against HER2 (trastuzumab) or HER2-targeted tyrosine kinase inhibitors (e.g. Lapatinib) have dramatically improved survival of breast cancer patients with HER2 overexpression (HER2+), compared with patients without such overexpression (HER2-)[6]. Therefore, a reliable evaluation of HER2 expression level has become a major biomarker in daily clinical practice. The initial diagnosis of breast cancer and risk classification involves pretreatment core needle biopsies, histological diagnosis, hormone receptor and HER2 status. Recommendations for HER2 evaluation

[1]Institut Curie, PSL Research University, Laboratoire Physicochimie, CNRS/UMR 168, Institut Pierre-Gilles de Gennes, MMBM group, Paris, France. [2]APHP Hôpital Saint-Louis, Molecular Oncology Unit, University Paris-Diderot, INSERM/CNRS, UMR944/7212, Paris, France. [3]LAAS-CNRS, Université de Toulouse, CNRS, Toulouse, France. Correspondence and requests for materials should be addressed to P.D.C. (email: patricia.de-cremoux@aphp.fr) or S.D. (email: stephanie.descroix@curie.fr)

methods in breast cancers are published and periodically updated by a panel of experts to improve upon the accuracy and convenience of HER2 testing by immunohistochemistry (IHC) or Fluorescent *In Situ* Hybridization (FISH), which represent the gold standard in clinical practice[7,8]. Recently, we investigated the potential of Quantitative Polymerase Chain Reaction (qPCR) as an alternative to FISH, in a multicentre screening based on 840 cases, in the framework of a prospective project entitled "Support Program for Costly Diagnostic and Therapeutic Innovations" supported by the French Institute of Cancer (INCa)[9]. As a conclusion of this study, qPCR represents a reliable alternative for the quantification of HER2 expression level in cancer classification. This technique is significantly less labor-intensive and more reliable than FISH, but it remains rather expensive, notably due to the cost of reagents, and as all PCR-based diagnosis approaches, it requires rigorous procedures and environments to avoid contamination and false-positives.

A promising technique to fulfil the fast increasing demand for throughput and multiplexing associated with "precision medicine", while reducing costs, is microfluidics. This technology allows volume reduction, automation and confinement[10]. Quake *et al.*[11] developed a Reverse Transcription (RT) -PCR assay in microfluidic devices based on PDMS valves, an approach now commercial available in the Fluidigm IFC device. This device allows outstanding single cell sensitivity and a high throughput, thanks to the parallel processing of numerous samples versus numerous conditions (e.g. 48×48). This format, in which the cost per run is essentially independent of the number of samples processed, yields low cost per data point at full capacity, but is not well adapted to diagnostic screening of gene expression, in which samples arrive at the laboratory at random times, and a short time to answer is required for each sample. Droplet microfluidics, which allows compartmentalization in nanoliter volumes without complex integrated valves, has the potential to overcome this limit and, indeed, proof-of-concept experiments using droplet microfluidics were reported since then[12,13]. However, most droplet based approaches to RT-PCR so far, followed the same spirit as developed for "digital PCR"[14,15], e.g. the generation and pooling of a large quantity of individual droplets from a single liquid sample. Higher programmability was introduced by electro-wetting on dielectric technology (EWOD)[16] and a device performing messenger RNA (mRNA) extraction, purification and transcription has been recently described[17]. EWOD, however, requires complex microfabricated devices with electrodes, bringing back the cost issues mentioned regarding microfabricated valves[11]. It also requires an additional upstream interface for sample and reagents loading.

Here we present a new platform aimed at bringing to the clinical world the advantages of droplet microfluidics, addressing issues relevant to the specific challenges of clinical diagnosis, i.e. reliability, robustness to contamination, high multiplexing potential, versatility, user-friendliness, automation and cost reduction, while maximizing the compatibility and interoperability with currently validated and used protocols and workflows. The front-end of this platform is a simple motorized pipetting arm, which allows the direct sampling of samples and reagents from standard microtiter plates (MTP), for full compatibility with current sample storage strategies and equipment. As a main difference as compared to currently commercialized droplet platforms, such as those used in "digital PCR", all droplets are kept equally spaced by oil in a highly confined state (a format also called "plug microfluidics" in literature)[18,19]. This way, inter-droplet contamination risk is reduced and the "identity" (originating well) of each droplet, built in the sequence of droplets all along the protocol, is known without need for internal tags. These differences alleviate several current limitations of droplet microfluidics[20]. The second original feature of the platform is the "magnetic tweezers" concept (Fig. 1), previously applied to ELISA[21], and applied here for the first time to nucleic acids analysis. This magnetic tweezers approach allows the transfer of functionalized magnetic particles between subsequent droplets, bringing into the droplet microfluidics world the power of solid-state extraction and the flexibility of magnetic beads-based protocols. Here we use it to specifically capture and purify mRNA from a raw sample. Finally, the platform comprises a thermocycler, in which RT and pre-amplification PCR cycles are performed in the droplets. The whole protocol is programmed in a series of "trains" of confined droplets containing all the required reagents and samples. Several trains can be loaded sequentially and travel at constant distance from each other like in real railway. This way, multiple samples can be processed in a fully automated way in a single capillary, without any contact with external environment, reducing labour needs, risks of manipulation errors and/or contamination, in addition to a strong reduction of reagents and samples needs.

Different tests were performed in order to validate the platform, focusing on two genes of interest, the target gene HER2 and a reference gene named TBP (TATA-binding protein). As already introduced, HER2 is a major theranostic biomarker for breast cancer. TBP, a "house-keeping gene" with low variability of expression in breast cancer cells, is usually chosen in clinics as a reference in order to validate the quality of total RNA samples. A first series of experiments was performed with total RNA samples extracted from two human breast cancer cell lines: MCF7, which belongs to the luminal subgroup, has a normal expression level of HER2 and SKBR3, which presents an overexpression of this gene, displays a typical HER2+ status.

The ability of the platform to perform RT and PCR in droplets was evaluated and quantified. The performance of PCR technologies depend on many factors, including thermal control, detection, data analysis and normalization, and algorithms for Cycle threshold (Ct) determination are rather complex and apparatus-dependent. These developments are now integrated in conventional qPCR devices in a way transparent to end-users, and they constitute the frame in which biologists perform their analysis and draw their conclusions. These qPCR platforms have a relatively high sample and reagents consumption, and integrating fluorescence detection directly in the droplet format could induce strong gains regarding cost and sensitivity. However, in this first study of a new microfluidic concept, we wanted to quantify its advantages and possible disadvantages without adding in the comparison other factors, such as the sensitivity and stability of a new detection scheme, the influence of which would combine with the microfluidic part in a way difficult to unravel. Therefore, in order to allow for a more reliable comparison, we chose to perform the final steps of the analysis in a conventional qPCR machine, taking advantage of the possibility offered by the platform to collect after processing individual samples in conventional microtubes or MTP.

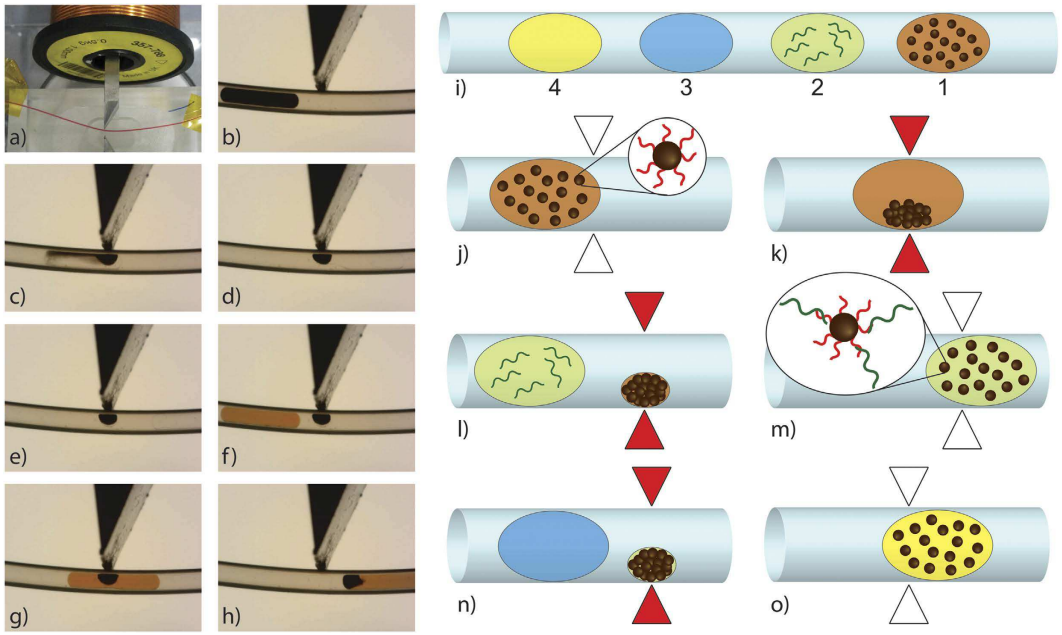

Figure 1. Magnetic tweezers technology and experimental workflow for RT-PCR experiment. (**a**) Picture of the magnetic tweezers with the capillary (highlighted with a red liquid). A second passive magnetic tip, placed opposite to the first with regards to the capillary, contributes to field lines shaping and to the optimization of the magnetic force[21]. (**b**–**h**) Sequence of images showing the extraction and the redispersion of magnetic beads from one droplet to another one (colored in orange), switching ON and OFF the electric current in the coil. (**i**) Scheme of a typical train of droplets used for the RT-qPCR analysis: 1) oligo-dT magnetic beads, 2) total RNA sample, 3) washing buffer and 4) RT-PCR mix. (**j**–**o**) Workflow of beads and droplets manipulation during the protocol.

Then, a clinical validation of the overexpression level of HER2 in breast patient samples was performed thanks to a blind comparison versus the method previously established[9].

Results

Design layout and characterization of the microfluidic platform. The crux of the platform is the magnetic tweezers technology[21] (Fig. 1): a soft ferromagnetic core is positioned with its body in a tunable electric coil and its sharp tip in close contact with a capillary (Fig. 1a). The capillary is filled with fluorinated oil and highly confined aqueous droplets are carried over the tip by the oil flow. Applying an electric current to the coil, a magnetic field is generated, with a peak of about 0, 35T at the tip and a strong gradient within the capillary, able to attract paramagnetic beads suspended in an initial droplet traveling in the capillary (Fig. 1c). The magnetic force is sufficient to extract the beads as a densely packed aggregate against capillary forces and retain it immobile in the oil flow. The beads aggregate is kept within an aqueous subdroplet (Fig. 1d,e), so that it is never in contact with the oil or the channel wall. When a second droplet is carried by the flow over the tip (Fig. 1f), coalescence with the magnetically trapped subdroplet spontaneously occurs. If the magnetic field is turned off, the beads are released and dispersed inside the following droplet (Fig. 1g,h) (see Supplementary Movie 1). Thanks to this, functionalized beads can be used to extract analytes of interest from a complex sample and carry them between different media, with very little carryover of the initial matrix. The procedure can be repeated using series of tweezers so that particles can be sequentially exchanged from one droplet to the other within a droplet train. For the present RT-PCR protocol, the sequence of drops is described in Fig. 1. The first droplet contains oligo-dT magnetic beads in suspension in their storage buffer. They are extracted and released in a second droplet containing the sample of total RNA (Fig. 1j–l); here mRNA is captured on the magnetic beads by hybridization (Fig. 1m). The magnetic beads are captured by a second tweezers after 5 minutes of incubation (set by the distance between tweezers and by the flow velocity), allowing the extraction of the mRNA. The cluster is then washed by a washing buffer droplet (Fig. 1n) and finally redispersed in a last droplet containing the RT-PCR mix (Fig. 1o). The whole train is then transported seamlessly to a serpentine channel in a heated element, where RT and PCR will be performed. In order to achieve full automation, a dedicated program using LabView 2011 (National Instruments) was developed to synchronize magnetic field actuation with the passage of the droplets (see Methods and Supplementary Note 1).

Droplets trains are generated by pipetting the different solutions directly from a MTP. The use of confined droplets, which can travel over long distances keeping their initial order and spacing[22], allows to implement in a flexible way complex protocols, built in the sequence of droplets. This leaves a lot of flexibility for programming, since the order and content of droplets can be customized at will by the end-user, including the possibility to program different protocols into successive trains. The platform, schemed in Fig. 2, is inspired from the work of Chabert *et al.*[23], with some differences aimed at accounting for the specificities of RT and at increasing

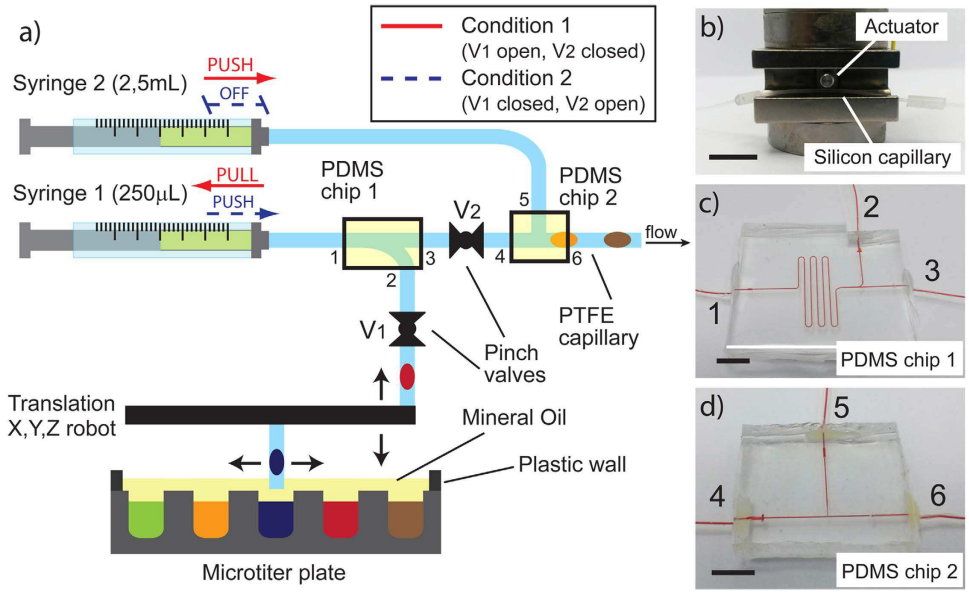

Figure 2. Microfluidic platform for the generation of trains of droplets. (**a**) Scheme of the droplet microfluidic generator module, which combines a MTP plate placed under a motorized pipettor arm (Cetoni), two syringes, two pinch valves (**b**) and two PDMS chips (**c**,**d**). The connections between the PDMS chips inlets and the different parts of the platform are numbered from 1 to 6 and the same numbers are reported on the scheme (**a**). Syringe 1 is connected with inlet 1 of PDMS chip 1 (Fig. 2c) while syringe 2 is connected with PDMS chip 2 (Fig. 2d) at inlet 5; inlets 2 and 3 are connected respectively to the pipettor head and to the PDMS device 2 (inlet 4), thanks to tubing passing through the two valves (V1 and V2). Finally, inlet 6 of the second PDMS chip is connected with the capillary in which droplets are driven between the magnetic tweezers. In order to generate droplets trains, while other droplets are flowing in the rest of the platform, homemade software switches alternatively between two conditions represented by red and blue lines. In condition 1, V1 is open and V2 is closed; syringe 1 is in aspiration mode generating and storing droplets in the PDMS device 1 while syringe 2 is pushing oil in the rest of the circuit. Then, in condition 2 (V1 closed, V2 open), syringe 2 is stopped and syringe 1 pushes the generated droplet train over PDMS device 2; after that, condition 1 is reactivated, and a new droplet train can be generated while the previous one is flowing in the processing system. In order to avoid pinching of a droplet by a valve, 10 mm oil spacers were introduced between droplet trains, and pipetting and valving were synchronized to ensure that valves close only onto these spacers. Each train in the series of trains can be prepared from any arbitrary combination of samples and reagents. The water and oil phase solutions are placed in the MTP, which is covered by a mineral oil film of 2–3 mm for avoiding contaminations or solution evaporations. The length of the scale bar of (**b**–**d**) is 1 cm.

interoperability with current diagnosis platforms. The system involves a high-precision syringe pump (Syringe 1) dedicated to droplets sampling, a high volume syringe pump (Syringe 2) to push trains of droplets at constant velocity (set at 0.1 µl/s) through the device, and a compact 1-arm motorized pipettor allowing programmed sampling from any well in a MTP. Sampling is performed by sequential aspiration of sample or reagents and oil. PDMS microfluidic devices (Fig. 2c,d) are designed to operate as switching and storage junctions in order to create two independent fluidic circuits. Using those and a combination of pinch valves (Fig. 2b), the system is able to generate a train of droplets, while previously generated trains are flowing in the rest of the platform (see Methods). This approach allows a continuous operation, wherein an intermittent pipetting process generates successive trains, while previously generated trains are processed at constant speed. It also allows "on-the-flight" reprogramming, i.e. varying the samples and reagents combination for next trains, while a previously prepared train is studied, without interrupting operation.

In order to avoid any contaminations between different wells by the capillary, the same PTFE capillary was used for sampling and droplets train transport. The carrier oil was fluorinated oil (FC-40, by 3 M) containing a fluorinated surfactant (2% of 1H, 1H, 2H, 2H-perfluoro-1-decanol, by Fluorochem). In such conditions, the surface tension between the oil and the PTFE is low enough to guarantee that a small film of FC-40 is always present at the end of the capillary. Fluorinated oil also reduces the risk of molecules diffusion from the aqueous phase droplet into the continuous oil phase, avoiding cross-contamination problems[24]. This has been demonstrated performing systematically negative control tests, consisting in normal train of droplets where the RNA droplet is replaced by washing buffer, interspaced between positive trains. In particular, a negative control train was systematically included every 7 positive trains and all trains of droplets were treated using the same protocol, from the droplet generation to the qPCR amplification. In all the tests (total of more than 200 for the whole series of experiments presented in this work), the qPCR curves from the negative control droplets did not shown any amplification. An example of this can be observed in Supplementary Fig. 2, which shows raw data obtained of the amplification curves. In contrast with conventional droplet microfluidics, in which surfactants are designed to

prevent droplet merging by maximizing steric repulsion between the surfactant molecules[25], we used here perfluorodecanol, which produces stable water phase droplets in fluorinated oil and prevents wall contamination, but still allows the merging of droplets and subdroplets upon contact in a highly confined state[26].

In order to prevent evaporation problems[27] and to insulate the RNA samples from the external environment, reducing risks of cross-contamination and degradation by ambient RNases , a layer of mineral oil is dispensed over the MTP after having placed the solutions. In contrast with previous work[23], mineral oil was preferred to fluorinated oil: being less dense (0.838 g/mL at 25 °C) than both water (about 1 g/mL at 25 °C) and FC-40 (1.855 g/mL at 25 °C), it stays on top of them during pipetting (Fig. 2a), without requiring the use of specific MTPs. Overall, the droplet size dispersion ranged between 1–2% for droplet volumes between 50–350 nL. During the experimental workflow droplets of 250 nL were used.

After the steps performed in the magnetic tweezers, droplets containing the purified mRNA mixed with reverse transcriptase, polymerase and primers are flown into a temperature controlled module kept at 50 °C for 5 minutes (see Supplementary Fig. 1) and the RT step is performed in the droplets. In order to evaluate the platform's automation capability and robustness, 45 trains of droplets were continuously generated and processed without human intervention in the same experiments. They allowed analyzing two genes of interest from 7 total RNA samples and three negative controls performed in triplicate. The whole automated protocol, from droplets generation to the RT, takes about 4 hours. After that, in a first series of experiments, droplets containing the complementary DNA (cDNA) were collected in standard PCR tubes, pre-loaded with TaqMan mix, to perform the qPCR in a conventional instrument (SmartCycler, by Cepheid). In a second protocol, aimed at demonstrating the possibility to perform RT-PCR seamlessly in the platform, the droplets were subjected to a series of 15 pre-amplification by thermal cycling, before transfer to the conventional qPCR machine.

Optimization and validation of the microfluidic platform with cell lines. *Calibration curves for TBP and HER2.* A first series of experiments was performed to check that the high surface to volume ratio intrinsic to microfluidics does not affect the efficiency of the reaction, e.g. by enzymes adsorption or loss. This was achieved by varying enzymes concentration in the RT-PCR mix (Supplementary Table 1). Increasing the concentration beyond that suggested by the supplier did not yield any decrease of Ct, whereas decrease of enzymes concentration yielded an increase in Ct only for concentrations below 20% of the standard one. This demonstrates that the concentration recommended by the supplier in macroscopic format also corresponds to a robust optimum of efficiency in our platform, so this concentration was used in following experiments.

Then, the capture efficiency of mRNA by the magnetic beads was evaluated by performing sequential capture steps from the same initial sample (see Supplementary Note 2 for details). Parallel tests performed by the droplet microfluidic platform and in conventional PCR tube, using the same protocols, show in both cases an excellent capture efficiency of $95 \pm 2\%$ for the droplet format and $93 \pm 2\%$ for the batch mode. The similarity of the efficiency in both modes demonstrates that the microfluidic format indeed exploits the good capture efficiency of the beads used here to its best extent, and does not yield any specific loss.

The purification efficiency (defined here as the rejection factor for non-messenger RNA) was evaluated by quantifying the total RNA content of the purified droplet and the waste droplet, respectively, and was shown to be better than 100X (see Supplementary Note3 for more details).

Calibration curves for TBP and HER2 genes were then prepared with total RNA quantities ranging from 1.5 ng/drop to 15 pg/drop, corresponding to 6 ng/μl to 60 pg/μl; this range is lower than the typical concentrations used for the routine quality check for clinical samples (6 and 25 ng per assay). The lowest calibration point, about 15 pg, roughly corresponds to the total mRNA content of a single cell or, considering the typical expression level of HER2 in breast cancer lines, between 10 and 1000 copies of target mRNA per droplet. Figure 3a,b show the results obtained for MCF7 and SKBR3 cell lines, respectively. Each curve is the average of a triplicate of the same experiment repeated three times, starting from the same MTP. An example of raw data obtained is provided in Supplementary Fig. 2. The Cts horizontal error bars for the RNA/droplet concentrations are evaluated by the propagation of error on the droplet volume, while the verticals error bars are given by the standard deviation of the triplicate ($CV < 1\%$). Thus, the error bars in Fig. 3 represent the variations due to our new setup and protocol, avoiding possible external sources of error such as degradation of the RNA sample or inaccuracies of MTP preparation. This point will be fundamental for the clinical validation, in which a sample calibrator has to be analyzed at the same time and with the same protocol as the patient samples. Calibration curves in Fig. 3 are linear in the investigated range ($R^2 > 0.96$), demonstrating that the efficiency of mRNA capture and of the RT reaction performed in droplets are not influenced by the initial quantity of mRNA. The efficiencies (E*ff*) of the qPCR, derived by the curves' slope reported in the graphs, are always higher than 97%. As expected, the Cts obtained for TBP do not differ significantly between the two cell lines. For HER2, in contrast, SKBR3 shows Cts about 5units smaller than those of MCF7, in line with the HER2+ and HER2- status of these cell lines.

It is also worth noting that these results confirm the absence of contamination between droplets, already demonstrated by negative controls presented in the first part of the results section, above. All data were derived from different trains of droplets performed in the same capillary, and comprising initial RNA concentrations over two orders of magnitude of concentration. In particular, in some cases, the train at lowest concentration are generated directly followed a train at the highest concentration. If some cross-contamination occurred the measured Ct should have a larger dispersion at low RNA concentrations than at high, disrupting the linearity of the calibration curves.

Finally, the possibility to perform RT-qPCR in a single step in the droplet was evaluated by an additional series of experiments performed on total RNA from MCF7 in which, after RT, the droplets trains are arrested in the temperature unit, and subject to PCR. Ct values in PCR depend to some extent on the apparatus and sensitivity of the detection so, in order to allow for a more quantitative validation, we chose a hybrid method in which 15 temperature cycles are performed in the capillary and the droplets are then transferred to the SmartCycler for

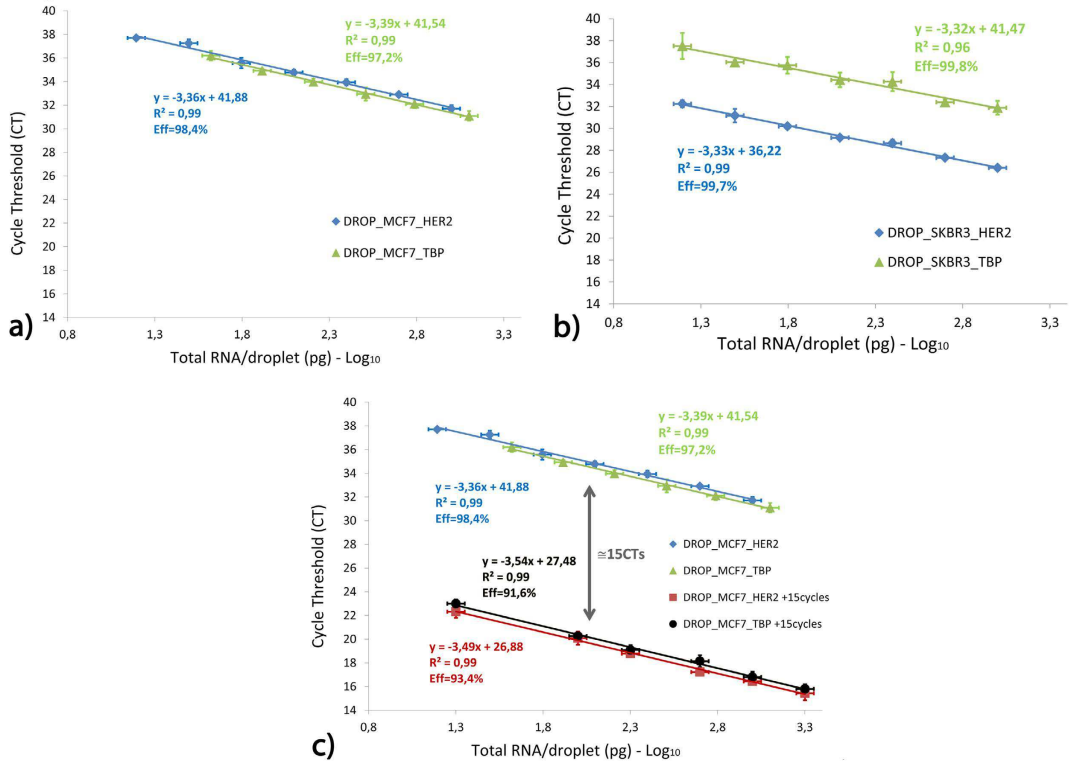

Figure 3. qPCR calibration curves. Calibration curves for (**a**) MCF7 and (**b**) SKBR3 cell lines for genes HER2 and TBP, represented in blue and green, respectively. Cts are plotted in logarithmic scale as a function of the total RNA concentration. The qPCR efficiency E*ff*, reported below the fit parameters, was extracted from the slope of the linear fits. (**c**) Calibration curves for MCF7 without (blue and green points and fits) and with (red and black points and fits) 15 PCR pre-amplifications cycles: as expected, the curves are shifted of about 15 Cts. Error bars are not visible when they are smaller than the point.

final qPCR analysis. The results (Fig. 3c) show that, within experimental error, the calibration curves obtained are shifted by 15 Cts as compared to the previous ones, indicating that the efficiency of the PCR is similar in the droplets and in the conventional thermocycler. Moreover, the slopes of the graphs with and without 15 cycles of pre-amplification are also comparable, suggesting that no additional loss or degradation of enzymes occurred during thermal cycling in the droplet, and that the in-drop amplification provided DNA fragments of a similar quality as those obtained in the SmartCycler. Combined together, these results demonstrate that RT-qPCR can be performed in the highly confined droplets of the platform, without loss of reproducibility, quality and performance and without inter-trains contamination.

Clinical Validation with breast cancer patient samples. Clinical validation was performed in a blind protocol, using 21 samples of total RNA extracted from percutaneous biopsies of breast cancer patients of Saint-Louis Hospital in Paris (France). The samples were analyzed, independently and in parallel, by classical RT-qPCR at the hospital (see Methods) and by the droplet microfluidics platform, using the SmartCycler as end-line quantitative analyzer, as described above for cell lines. The total RNA quantities used for this validation were, respectively, 20 ng per test for the Hospital, and 250 pg per test (or 250 pg/droplet) for the microfluidic platform. All results were analyzed with the $2^{-\Delta\Delta Ct}$ Method[28,29], which is well established for RT-qPCR. This strategy allows the normalization of the expression of the gene of clinical interest (HER2) to a reference having a stable expression level between individuals (in our case TBP) and also with a reference sample without HER2 overexpression (MCF7 cell lines for the droplet platform and a pre-defined set of samples for the hospital platform). This allows to take into account possible differences of RNA or DNA quality and/or amplification between the two genes. The result of this analysis is the Fold difference *Fd*, which quantifies the difference in expression between the patient sample and the control sample: ideally, $Fd \approx 1$ would mean no overexpression and the higher is *Fd*, the higher is the expression of the gene. In practice, however, there is no absolute reference of what is a "normal" expression, both for HER2 and TBP, and measured expression levels depend to some extent on the details of the experimental procedure, so the *Fd* threshold of positivity has to be evaluated on a heuristic basis, for a given platform. In the diagnostic laboratory at Saint-Louis Hospital, the *Fd* cut-off ratio to consider a sample HER2 negative or positive was determined on a tumor training set using univariate partition method (XLSTAT software) and correlation with IHC–HER2 expression. Final result were expressed as a normalized ratio considered as over-expressed if $Fd > 7$[9,30]. The two sets of data with the Ct and *Fd* values are reported in the blue and yellow columns of Supplementary Table 2. *Fd* values obtained on the droplet platform are systematically higher than

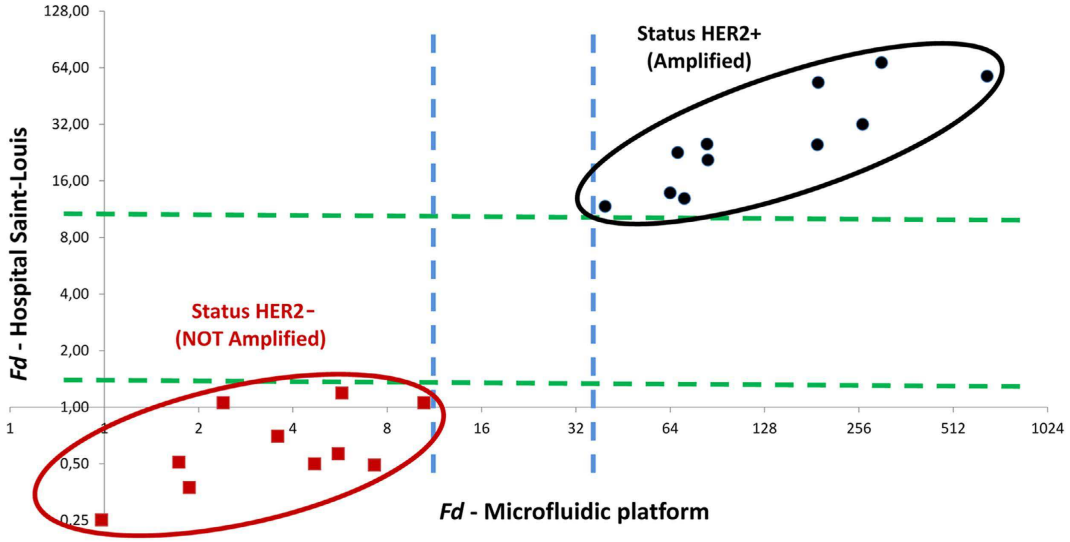

Figure 4. Correlation between hospital and microfluidic platform results. Graph in Logarithm scale (base 2) of the *Fd* obtained by the Saint-Louis Hospital platform versus the *Fd* obtained by the droplet microfluidic platform. Samples disclosed *a posteriori* as HER2- samples are plotted in red, and HER2+ ones in black. The dashed lines help to identify the excluded zone between the two populations: blue for the droplet platform (10.48–39.67), green for the hospital (1.5–11.71).

those obtained at the hospital. Such a discrepancy could be expected considering the relative nature of this parameter and our use of a different reference in the two environments. This complication can be overcome by a correlation analysis, as previously proposed[31]. The linear correlation between the two sets of data yields a Pearson Correlation Coefficient 0.84, showing good correlation. Most importantly regarding diagnosis, the correlation graph (Fig. 4) between the droplet and hospital platforms shows an identical segregation of positive and negative patients, plotted in red and black, respectively. By definition, data from the hospital segregate in two data sets on each side of the $Fd \cong 7$threshold. More specifically, in this cohort, the highest *Fd* of negative patients is at 1.19 and the lowest positive is at 11.71 (green dash line). All data obtained on the microfluidic platform segregate together with the data from the hospital, the highest negative being at 10.48, and the lowest positive at 39.67 (blue dashed lines).

Discussion and Conclusions

We presented a novel droplet microfluidics platform for gene expression quantification by RT-qPCR. As already introduced above, the progress of "precision medicine", in which an increasing number of molecular biomarkers must be tested on the same patient sample, is limited by conventional techniques, in which large quantities of samples and reagents are requested for every single assay. Additionally, gene expression information is carried by mRNA, which only represents 1–3% of the total RNA and is a more fragile and delicate nucleic acid than DNA. Finally, even minimal contamination by post-PCR amplification products from other reactions could easily yield false positives. To overcome these difficulties, very strict, time consuming and space-intensive workflows are required. These requirements, together with the cost of reagents, constitute a hindrance to the spreading of precision medicine approaches in less-favored settings and a cost burden on the health system in more favored countries.

The microfluidic platform developed here provides a path overcoming these limitations, while remaining compatible with the standard equipment and sample storage available in diagnostic laboratories. Starting from total RNA samples distributed in conventional microtiter plates, this droplet platform permits the generation of different trains of droplets allowing mRNA extraction by magnetic beads, washing, redispersion in RT-PCR mix and finally the thermal steps for RT or RT plus pre-amplification cycles of PCR, all in droplet format. Various combinations of samples and RT-PCR mixes can be programmed dynamically from the same set of samples and reagents.

The platform was first validated using total RNA extracted from MCF7 and SKBR3 cell lines. Calibration curves for both TBP and HER2 genes expression levels were found linear between 1, 5 ng and 15 pg of total RNA per droplet. As mentioned above, it is worth noting that the smallest concentration of total RNA used in this series is comparable with the RNA concentration of a single cell (about 20 pg). Therefore, although not relevant to the present clinical application and validation, our platform is suitable to perform RT-qPCR from single cells. Since technologies for single cell encapsulation in droplet exist[13,32], this could open the route to a strong simplification of single cell expression studies.

During these tests, as expected, MCF7 and SKBR3 cell lines showed normal and overexpressed HER2 gene level, respectively, and the same level of TBP expression. Additionally, the curves were found parallel, yielding PCR efficiencies between 97–99%, allowing their relative expression analysis. When 15 cycles of PCR

pre-amplification are performed in the droplet following RT, a shift of 15 cycles in the calibration curves is obtained, showing that the platform allows inline mRNA purification, reverse transcription and DNA amplification with an efficiency comparable to that observed in conventional PCR machines. To date, in the routine analysis developed at Saint-Louis Hospital, total RNA is used to minimize manipulations and risks of contamination. Indeed, mRNA purification is not mandatory for all applications and is often avoided in conventional protocols. In our platform, however, this step can be included without additional sample manipulation or risk of contamination, since it is performed entirely in the microfluidic capillary. Implementing this additional purification is thus a way to increase the robustness of the method, by getting rid of a large majority of spurious RNA, at no additional risk and with negligible increase in the whole process time. Additionally, it is interesting to note that new technologies such as RNA sequencing, require highly purified samples to perform multiplex reactions and tend to use more and more often additional magnetic beads-based purification steps to avoid any non-specific reactions[33]. Therefore, we believe that our platform, performing in "native" mode mRNA extraction by magnetic beads, Reverse Transcription and PCR pre-amplification, will also make it an interesting front-end technique for these new massively parallel technologies[34,35].

A blind test versus an established routine clinical diagnosis was then performed on a cohort of 21 patients for the determination of HER2 amplification status, using the $2^{-\Delta\Delta Ct}$ Method, typical for qPCR analysis. The results show a good quantitative correlation of 0.84 between the *Fd* values. Moreover, in Fig. 4 the two populations of normal and overexpressed HER2 tumors are well identified, demonstrating that all the 21 patient samples studied were well characterized by the microfluidic platform in the blind test.

The platform used here allowed the processing of one sample every 3 minutes, i.e. about 500 samples per day. This is quite sufficient for most clinical diagnosis expression needs. Indeed, in research, experiments can be pooled and synchronized, in order to take advantage of devices processing in parallel many samples, but in clinical diagnosis, the ability to provide a fast response for each patient at a low cost is often as important or more important than theoretical throughput. Strategies involving parallel processing in disposable chips are thus poorly adapted, since the operation cost per chip is essentially independent of the number of samples processed in the chip, so that samples must be pooled up the full capacity of the chip or close to it, before processing to keep costs low. Our system, in contrast, does not use disposable chips, samples are processed sequentially and reagents are well protected under oil in the machine and can be kept for re-use on-demand. Therefore, the typical one hour response time can be maintained without significant cost increase from a single sample per day to the maximum rate of 500 samples per day, making the platform particularly suitable and cost-efficient for situations in which the number of samples to treat per day can vary widely, typically from a few to several hundred. It should be noted, however, that in order to best fulfill clinical requirements, the machine used here was aimed at flexibility but not optimized for speed. For higher throughput applications, the use of a more industrial pipetting stage, for instance, could allow the parallelization of the droplet generation step. Additionally, both valves and magnetic tweezers used here could accommodate more capillaries with little modification, so the throughput of the system could be increased by one or two order of magnitudes without major modifications.

The presented microfluidic platform shares with previous droplet microfluidic systems the use of oil to compartmentalize aqueous media in multiple nanoliter scale microreactors and thus, the possibility to considerably reduce reagents and sample consumption but, besides this, it has very different aims. Current droplet microfluidic systems use high-throughput generation of droplets from one or a few streams, to achieve thousands to millions of independent reactions in discretized samples of the same mix. This has opened, for instance, the route to digital "one molecule per droplet" approaches, leading to spectacular increases in sensitivity in PCR[14], but the cost of analysis per sample remains high. Here, in contrast, we use compartmentalization to increase automation and reduce volume, but remain in the "one reaction per sample" paradigm. In other words, a combination of a single droplet of sample and a single droplet of PCR mix is sufficient for typing the sample regarding to the corresponding sequence. As consequence, sample and reagents consumptions are directly commensurate with the volume ratio between a single droplet and a MTP well. This, combined with the magnetic tweezers permitting droplet-to-droplet extraction, purification and transfer, allows the implementation of essentially any protocol currently implemented in pipetting robots. For instance, in this study, starting from the same liquid samples, we easily introduced in our protocols triplicates assays and negative control tests, which are fundamental in diagnostic analyses. The microfluidic platform also shares with current robotized platforms MTPs as common entry and exit points, allowing easy evolution from existing workflows. However, it presents several advantages as compared to conventional robots, which remain in the MTP format through the whole protocol; at first, the reduction of the sample volume and RT reagents needed to obtain a data point is reduced by a factor between 40 and 200. Even smaller volumes could be sampled with syringes of smaller diameters, but we did not consider this useful here, since a X40 volume reduction, in combination with the absence of microfabricated disposables, and a strong reduction in plastic consumables, are already sufficient to decrease consumables cost to a level negligible as compared to other costs in the workflow, such as blood sampling and labor. Additionally, any sample contained in a single well (typically 20 to 100 μl) can be typed versus up to 100 PCR mixes contained in different wells or, alternately, a single PCR mix of 20 to 100 μl can be used to screen up to 100 samples, in a fully programmable manner and in any combination of samples versus mixes. This opens the route to multi-biomarkers screening from the same sample volume, to costs reductions and to the implementation of diagnostic sequences based on decision trees, without additional manipulation; for instance, a new train of droplets can be prepared from the same sample well with different primers, following the result of a first test, in an operator-decided or automated way. Another advantage is a reduction of risks of human error or contamination, either by RNase (sample degradation) or by DNA (false positives), thanks to the fact that operations are performed under oil all along the protocol. Indeed, the droplet platform was installed in a multi-purpose biochemistry lab, in which various other experiments involving amplification of human DNA were also performed, without pre-PCR and post-PCR segregation, and no event suggestive of contamination was observed during the whole study. This contamination

control advantage works both ways, i.e. it can also increase the protection of users, for the manipulation of potentially infectious samples.

Finally, the microfluidic platform is very versatile regarding protocol development: it can implement in a fully automated manner most existing protocols involving magnetic beads and use existing kits, except for a widely reduced reagents consumption, having an important impact on reagents cost. In the experiments presented here, this advantage is somewhat reduced by the final step, performed in a conventional thermocycler for the sake of clinical comparison. This step still requires the same quantity of polymerases and primers than in conventional methods. However, we have demonstrated that RT and qPCR can be performed in the same droplet. This opens the route to the development of a next generation device, comprising on-chip fluorescent detection, as already demonstrated in several proof-of concept experiments[36–38]. This improvement has the potential to further increase sensitivity, since it will avoid the dilution performed during droplet collection, in the present protocol, and also reduce the consumption of PCR reagents. Thus, either in the form presented here, as a front-end device for the preparation of direct or pre-amplified cDNA, or as a fully integrated device including detection, we believe that the droplet microfluidics and magnetic tweezers technology presented here will bring considerable gain in cost, robustness and simplicity of operation for a multiplicity of nucleic acid analysis applications, in particular in diagnosis.

Methods

Droplet microfluidic platform description:. The flow control part of the platform is designed to generate a train of droplets by sequential pipetting, while other droplets already generated are processed at constant and controlled speed in the rest of the platform. The platform comprises two syringe pumps (Nemesys, by Cetoni GmbH) equipped with 250 μL and 2, 5 mL syringes (by SGE), a motorized pipettor arm (Rotaxys, by Cetoni GmbH), two pinch valves (by NResearch Inc.) that are alternatively open and closed. Two PDMS devices are used for capillary connections (see Fig. 2). A 384-wells MTP is used for reagents and samples storage. A volume of 25 μL of each solution is distributed in individual wells placed below the motorized pipetting arm. Mineral light oil (by Sigma-Aldrich) is then spread on the plate in order to avoid reagents evaporation. The MTP is placed on a home-made holder that can be moved in X, Y, Z directions by a manual stage (Thorlabs). Once the pipetting capillary is aligned with the reference well, software controlling the motion of the pipettor's arm and the syringe is operated. Capillary is moved from one well to the other, pipetting in each one the desired volume of liquid and inserting between each water droplet a fluorinated oil plug. Considering the volume capacity of a single well and the volume of the droplet and oil phases, it is possible to generate from a single solution of 25 μl about 100 droplets of 250 nl.

Figure 2 schematically describes how the different parts of the platform are connected and how the platform allows droplet generation while the previous trains are flowing in the processing system. The pipetting takes about 1 second per droplet. Including the time needed for arm motion and oil pipetting, one train of droplets can be generated and manipulated between the valves and the PDMS devices in about 2–3 minutes. The PDMS connectors were prepared by standard double replica molding techniques, starting from a brass mold made by micro milling (see Supplementary Fig. 3). The pinch valves used operate by clamping an elastic capillary by a tip controlled by an electromagnet (see Fig. 2b). PTFE capillaries used for droplet manipulation cannot be used for this purpose due to their poor elastic proprieties. Therefore, in the valves they were replaced by a silicone capillary having the same internal size than the PTFE one (0.31/0.64 mm ID/OD, by Helix Medical). The connection between the two different capillaries was achieved using a third silicon capillary (ID = 0.50 mm, OD = 1.3 mm, by Deutsch & Neumann). To ensure good wettability by fluorinated oil, PDMS devices and silicone capillaries were treated with a solution of (Tridecafluoro-1, 1, 2, 2-tetrahydrooctyl)trichlorosilane in FC-40 (5% w/w) for 1 h.

When leaving PDMS connector 2, droplets are driven in a single seamless capillary between i) the two magnetic tweezers made of two magnetic coils (copper wire of 71 cm and 1 mm diameter, by Radiospares) surrounding soft ferromagnetic tips (AFK502 alloy, by Aperam) and ii) the thermocycler provided by Prime Techne and further adapted. Two Macro Objective (MLH-10X) mounted on two low cost CMOS Cameras (acA1300–60 gm, by Basler) and white LED back light illumination (by Schott Lighting and Imaging) were used for droplet observation and image analysis for magnetic tweezers control (see Supplementary Note 1). The cameras are connected to the computer by the NI PCIe-8236 card (National Instruments) and the communication between the home made LabVIEW software and the magnetic coils is achieved by the NI USB-6525 interface (National Instrument). Since the droplet generator and the magnetic tweezers modules can work at the same time, after preparation of the samples and reagents MTP, any combination of samples and reagents can be processed in any order and numbers of iterations, until exhaustion of the volume (about 500 analyses per sample for an initial load of 100 μl).

Samples. *Cell lines.* Human breast cancer cell lines SKBR3 (HER2-like phenotype) and MCF7 (luminal phenotype) were acquired from ATCC. They were cultured in DMEM culture medium supplemented with 10% FBS and 2% glutamine without antibiotics. They were harvested every week to amplify enough material for one year use of controls.

Patient cohort samples. The retrospective study was conducted on 21 breast cancer pre-treatment core-needle biopsies. Paraffin-embedded sections of AFA-fixed biopsies, used for the histological diagnosis were assessed by immunohistochemistry (for estrogen receptor ER), progesterone receptor (PR) and HER2 content. Tumours were considered "HER2-positive" if more than 30% of cells showed definite membrane staining. Control by FISH or SISH or qPCR was done for ambiguous cases. Frozen samples were used for the present study. They were processed under RNAse-free conditions. They represent a part of a more extensive protocol analysing diagnosis markers (ER, PR and HER2) and proliferation markers. The protocol and the ancillary studies were reviewed and approved by an ethics committee (CPP Ile de France IV, France, n°2013/27NICB, 30/07/2013).

Total RNA extraction. Cell lines and tumors' nucleic acids were extracted by phenol/chloroform procedure[39] and qualified and quantified using Bioanalyzer (by Agilent Technologies) and Nanodrop 2000 instruments, respectively. Tumor cell purity and presence of *in situ* carcinoma were assessed on adjacent tumor H&E-stained sections, by the referent pathologist[30].

$2^{-\Delta\Delta Ct}$ Method for folding difference (*Fd*) evaluation. The $2^{-\Delta\Delta Ct}$ Method[28,29] was used for the evaluation of the folding difference values starting from the Cts obtained by the droplets platform and the conventional hospital protocols. It proceeds as follows: at first, the ΔCt is defined as the difference in Ct between the gene of interest (HER2) and the reference gene (TBP), both for the sample and for the reference:

$$\Delta Ct_{sample} = Ct_{sample}(HER2) - Ct_{sample}(TBP) \quad (1)$$

$$\Delta Ct_{ref\_sample} = Ct_{ref\_sample}(HER2) - Ct_{ref\_sample}(TBP) \quad (2)$$

where "*ref_sample*" represents the normal control sample. Then, $\Delta\Delta Ct$ is calculated as the difference between the two ΔCt:

$$\Delta\Delta Ct = \Delta Ct_{sample} - \Delta Ct_{ref\_sample} \quad (3)$$

finally, the Fold difference (*Fd*) value is calculated with the following equation:

$$Fd = 2^{-\Delta\Delta Ct}. \quad (4)$$

Quantification of HER2 overexpression RT-qPCR – hospital protocol. First-strand cDNA synthesis was performed with 1 μg total RNA using Superscript II Reverse Transcriptase (Invitrogen Corporation) in a final volume of 25 μL. Quantitative PCR were performed on LightCycler 2.1 instrument (Roche Diagnostics). HER2 overexpression was evaluated by relative quantification using TATA-binding protein as endogen control (TBP) using 20 ng cDNA as previously described[30]. A 5 μL diluted sample of cDNA (20 ng) was added to 20 μL of the PCR mix. The thermal cycling conditions comprised an initial denaturation step at 95 °C for 10 min, 45 cycles at 95 °C for 15 sec, and annealing temperature, 60 °C for 1 min.

Final result were expressed as a normalized ratio *Fd* considered as over-expressed if $Fd > 7$. The cut-off ratio was determined on a tumors training set using univariate partition method (XLSTAT software) and correlation with IHC–HER2 expression as previously published by our group[30].

Preparation of the solutions for RT-qPCR performed in the droplet platform. Before transferring into micro titer plate, total RNA, stored at −80 °C, was quantified & qualified using Nanodrop&BioAnalyzer (Agilent) instruments. Desired total RNA quantities were diluted into Binding Buffer provided with the DynabeadsOligo(dT)25 Kit (61002, Life Technologies) and BSA (B14, Thermo Scientific) was added to a final concentration of 0.4%. For the preparation of the paramagnetic beads solutions for droplet generation, after resuspending Dynabeads in the vial, 100 μL was transfer to a tube and placed in a magnet for 1 min. The supernatant was discarded and Dynabeads were resuspended into 100 μL of Binding Buffer, well mixed and placed in a magnet for 1 min. The supernatant was discarded and Dynabeads were resuspended into a 25 μL mix composed of 23.5 μL Binding Buffer, 0.5 μL 20% BSA, 1 μL SUPERase In™ RNase Inhibitor (AM2694, Life Technologies). Two 1.5 ml tubes containing a 50 μL Washing Mix (48 μL Wash Solution, 1 μL 20% BSA, 1 μL RNase inhibitor) were prepared. CellsDirect™ One-Step qRT-PCR kits (11732, Life Technologies) was used to prepare the Reverse transcription mix as follow: 12.5 μL of 2X Reaction Mix, 1 μL of anchored Oligo(dT)23VN (S1327S, NEB), 1 μL of each Forward and Reverse primers (custom primers to study HER2 or TBP or Actin b from IDT), 1 μL of SuperScript® III RT/Platinum® Taq Mix with RNaseOUT™ Ribonuclease Inhibitor and qsp to 25 μL with DEPC-treated water. Each solution was well mixed by pipetting before transferred into 384-well titer Plate.

After the microfluidic process (mRNA capture, washing, Reverse transcription), droplets containing cDNA were recovered into 1.5 mL tubes with 5 μL of DEPC-treated water. qPCR reactions were performed in the SmartCycler instrument (by Cepheid), with a mix composed of: 12.5 μL of 2X Reaction Mix, 1 μL of each Forward and Reverse primers (custom primers to study HER2 or TBP or Actin b from IDT), 0.5 μL of TaqMan™ Probe (custom probes to study HER2 or TBP or Actin b from IDT) 1 μL of SuperScript® III RT/Platinum® Taq Mix with RNaseOUT™ Ribonuclease Inhibitor, 5 μL of cDNA output and qsp to 25 μL with DEPC-treated water. The thermocycling program was: an enzyme activation step at 95 °C for 120 sec, followed by 50 cycles of 95 °C/15 sec and 60 °C/30 sec.

References

1. Garraway, L. A., Verweij, J. & Ballman, K. V. Precision oncology: an overview. *J. Clin. Oncol.* **31,** 1803–5 (2013).
2. Stahel, R. *et al.* Optimising translational oncology in clinical practice: strategies to accelerate progress in drug development. *Cancer Treat. Rev.* **41,** 129–35 (2015).
3. André, F. *et al.* Comparative genomic hybridisation array and DNA sequencing to direct treatment of metastatic breast cancer: a multicentre, prospective trial (SAFIR01/UNICANCER). *Lancet. Oncol.* **15,** 267–74 (2014).
4. Swanton, C. SAFIR01: steps towards precision treatment in breast cancer. *Lancet. Oncol.* **15,** 242–3 (2014).
5. Wolff, A. C. *et al.* Recommendations for human epidermal growth factor receptor 2 testing in breast cancer: American Society of Clinical Oncology/College of American Pathologists clinical practice guideline update. *J. Clin. Oncol.* **31,** 3997–4013 (2013).
6. Perez, E. A. *et al.* Predictability of adjuvant trastuzumab benefit in N9831 patients using the ASCO/CAP HER2-positivity criteria. *J. Natl. Cancer Inst.* **104,** 159–62 (2012).
7. Wolff, A. C. *et al.* Recommendations for human epidermal growth factor receptor 2 testing in breast cancer: American Society of Clinical Oncology/College of American Pathologists clinical practice guideline update. *J. Clin. Oncol.* **31,** 3997–4013 (2013).

8. Lambein, K., Van Bockstal, M., Denys, H. & Libbrecht, L. 2013 update of the American Society of Clinical Oncology/College of American Pathologists guideline for human epidermal growth factor receptor 2 testing: impact on immunohistochemistry-negative breast cancers. *J. Clin. Oncol.* **32,** 1856–7 (2014).
9. Jacquemier, J. *et al.* SISH/CISH or qPCR as alternative techniques to FISH for determination of HER2 amplification status on breast tumors core needle biopsies: a multicenter experience based on 840 cases. *BMC Cancer* **13,** 351 (2013).
10. Mitchell, P. Microfluidics–downsizing large-scale biology. *Nat. Biotechnol.* **19,** 717–21 (2001).
11. Marcus, J. S., Anderson, W. F. & Quake, S. R. Parallel Picoliter RT-PCR Assays Using Microfluidics. *Anal. Chem.* **78,** 956–958 (2006).
12. Mary, P. *et al.* Analysis of gene expression at the single-cell level using microdroplet-based microfluidic technology. *Biomicrofluidics* **5,** 024109 (2011).
13. Eastburn, D. J., Sciambi, A. & Abate, A. R. Ultrahigh-throughput Mammalian single-cell reverse-transcriptase polymerase chain reaction in microfluidic drops. *Anal. Chem.* **85,** 8016–21 (2013).
14. Vogelstein, B. & Kinzler, K. W. Digital PCR. *Proc. Natl. Acad. Sci.* **96,** 9236–9241 (1999).
15. Pekin, D. *et al.* Quantitative and sensitive detection of rare mutations using droplet-based microfluidics. *Lab Chip* **11,** 2156–66 (2011).
16. Shen, H.-H., Fan, S.-K., Kim, C.-J. & Yao, D.-J. EWOD microfluidic systems for biomedical applications. *Microfluid. Nanofluidics* **16,** 965–987 (2014).
17. Rival, A. *et al.* An EWOD-based microfluidic chip for single-cell isolation, mRNA purification and subsequent multiplex qPCR. *Lab Chip* **14,** 3739–49 (2014).
18. Song, H., Chen, D. L. & Ismagilov, R. F. Reactions in droplets in microfluidic channels. *Angew. Chem. Int. Ed. Engl.* **45,** 7336–56 (2006).
19. Nightingale, A. M., Phillips, T. W., Bannock, J. H. & de Mello, J. C. Controlled multistep synthesis in a three-phase droplet reactor. *Nat. Commun.* **5,** 3777 (2014).
20. Schneider, T., Kreutz, J. & Chiu, D. T. The potential impact of droplet microfluidics in biology. *Anal. Chem.* **85,** 3476–82 (2013).
21. Ali-Cherif, A., Begolo, S., Descroix, S., Viovy, J.-L. & Malaquin, L. Programmable magnetic tweezers and droplet microfluidic device for high-throughput nanoliter multi-step assays. *Angew. Chem. Int. Ed. Engl.* **51,** 10765–9 (2012).
22. Baroud, C. N., Gallaire, F. & Dangla, R. Dynamics of microfluidic droplets. *Lab Chip* **10,** 2032 (2010).
23. Chabert, M., Dorfman, K. D., de Cremoux, P., Roeraade, J. & Viovy, J.-L. Automated Microdroplet Platform for Sample Manipulation and Polymerase Chain Reaction. *Anal. Chem.* **78,** 7722–7728 (2006).
24. Theberge, A. B. *et al.* Microdroplets in microfluidics: an evolving platform for discoveries in chemistry and biology. *Angew. Chem. Int. Ed. Engl.* **49,** 5846–68 (2010).
25. Baret, J.-C. Surfactants in droplet-based microfluidics. *Lab Chip* **12,** 422–33 (2012).
26. Morita, M. *et al.* Interfacial properties and emulsion stability in fluorinated oil—non-fluorinated oil—surfactant(s) systems. *Colloids and Surfaces* **67,** 81–93 (1992).
27. Guttenberg, Z. *et al.* Planar chip device for PCR and hybridization with surface acoustic wave pump. *Lab Chip* **5,** 308 (2005).
28. Livak, K. J. & Schmittgen, T. D. Analysis of relative gene expression data using real-time quantitative PCR and the 2(-Delta Delta C(T)) Method. *Methods* **25,** 402–8 (2001).
29. Schmittgen, T. D. & Livak, K. J. Analyzing real-time PCR data by the comparative CT method. *Nat. Protoc.* **3,** 1101–1108 (2008).
30. Lehmann-Che, J. *et al.* Immunohistochemical and molecular analyses of HER2 status in breast cancers are highly concordant and complementary approaches. *Br. J. Cancer* **104,** 1739–46 (2011).
31. Yuen, T., Wurmbach, E., Pfeffer, R. L., Ebersole, B. J. & Sealfon, S. C. Accuracy and calibration of commercial oligonucleotide and custom cDNA microarrays. *Nucleic Acids Res.* **30,** e48 (2002).
32. Chabert, M. & Viovy, J.-L. Microfluidic high-throughput encapsulation and hydrodynamic self-sorting of single cells. *Proc. Natl. Acad. Sci. USA* **105,** 3191–6 (2008).
33. Zhao, W. *et al.* Comparison of RNA-Seq by poly (A) capture, ribosomal RNA depletion, and DNA microarray for expression profiling. *BMC Genomics* **15,** 419 (2014).
34. Metzker, M. L. Sequencing technologies - the next generation. *Nat. Rev. Genet.* **11,** 31–46 (2010).
35. Shi, X., Chen, C.-H., Gao, W., Chao, S.-H. & Meldrum, D. R. Parallel RNA extraction using magnetic beads and a droplet array. *Lab Chip* **15,** 1059–65 (2015).
36. Kopp, M. U., Mello, A. J. & Manz, A. Chemical amplification: continuous-flow PCR on a chip. *Science* **280,** 1046–8 (1998).
37. Hatch, A. C. *et al.* 1-Million droplet array with wide-field fluorescence imaging for digital PCR. *Lab Chip* **11,** 3838–45 (2011).
38. Miyaki, K. *et al.* Fabrication of an integrated PDMS microchip incorporating an LED-induced fluorescence device. *Anal. Bioanal. Chem.* **382,** 810–6 (2005).
39. Chomczynski, P. & Sacchi, N. Single-step method of RNA isolation by acid guanidinium thiocyanate-phenol-chloroform extraction. *Anal. Biochem.* **162,** 156–159 (1987).

Acknowledgements

This work was supported in part by the Digidiag project (ANR) from the French government, the ARC foundation for young researcher fellowship, European research Council Advanced Grant N°: 321107 "CellO". M.S. was supported by a Curie Institute International PhD fellowship. Some technological elements used in this article are covered by patent WO2013041983, property of Centre National de la Recherche Scientifique.

Author Contributions

D.F., J.C., B.T., L.M., J.-L.V. and S.D. conceived the experiment. D.F., J.C., B.T. and M.S. conducted the experiments. D.F., J.C., J.-L.V., P.d.C. and S.D. contributed to the data analysis and discussions. D.F., J.C., J.-L.V., P.d.C. and S.D. wrote the manuscript, with input from all authors.

Additional Information

Supplementary information accompanies this paper at http://www.nature.com/srep

Competing financial interests: The authors declare no competing financial interests.

How to cite this article: Ferraro, D. *et al.* Microfluidic platform combining droplets and magnetic tweezers: application to HER2 expression in cancer diagnosis. *Sci. Rep.* **6**, 25540; doi: 10.1038/srep25540 (2016).

Annex 2

Sensors and Actuators B 255 (2018) 2126–2135

Contents lists available at ScienceDirect

Sensors and Actuators B: Chemical

journal homepage: www.elsevier.com/locate/snb

Research paper

Single-step immunoassays and microfluidic droplet operation: Towards a versatile approach for detection of amyloid-β peptide-based biomarkers of Alzheimer's disease

Thanh Duc Mai[a,b,c,d], Davide Ferraro[b,c,d], Nacéra Aboud[a], Renaud Renault[b,c,d], Marco Serra[b,c,d], Nguyet Thuy Tran[a], Jean-Louis Viovy[b,c,d], Claire Smadja[a], Stéphanie Descroix[b,c,d,*], Myriam Taverna[a,**]

[a] PNAS, Institut Galien de Paris-Sud, Faculté de Pharmacie, Université Paris-Sud, CNRS UMR8612, 5 rue JB Clément, 92290 Châtenay-Malabry, France
[b] Laboratoire Physico Chimie Curie, Institut Curie, PSL Research University, CNRS UMR168, 75005 Paris, France
[c] Sorbonne Universités, UPMC Univ Paris 06, 75005 Paris, France
[d] Institut Pierre-Gilles de Gennes, 75005 Paris, France

ARTICLE INFO

Article history:
Received 7 June 2017
Received in revised form 7 August 2017
Accepted 1 September 2017
Available online 5 September 2017

Keywords:
Amyloid-β (Aβ) peptides
Alzheimer's disease (AD)
Microfluidic droplet
Magnetic beads
Immunoassays
Capillary isoelectric focusing (CIEF)

ABSTRACT

In this study, single-step magnetic-beads based immunoassays was developed and for the first time adapted to microfluidic droplet operation for sequential determination of well-established amyloid-β peptide biomarkers (*i.e.* monomeric Aβ 1–42 and Aβ 1–40) for molecular diagnosis of Alzheimer's disease (AD). With the developed sandwich assay protocol, the capture antibodies (*i.e.* monoclonal anti-Aβ antibodies that are specific for N-terminus of Aβ 1–42 and Aβ 1–40) grafted onto magnetic beads and the detection antibodies (*i.e.* beta amyloid 1–16 monoclonal antibody labeled with horseradish peroxidase) can simultaneously bind to monomeric β peptides in a single step. Aβ 1–42 and Aβ 1–40 in cerebrospinal fluid (CSF) samples were successfully detected using the developed batchwise immunoassay approach. With the aim at expanding the spectrum of traced Aβ peptides beyond Aβ 1–42 and Aβ 1–40 for more precise diagnostics of AD, the developed sandwich assay was for the first time coupled as a downstream module to peptide fractionation and collection using capillary isoelectric focusing. Demonstration of this methodological combination was carried out with Aβ 1–40, Aβ 1–40 and Aβ 5–40. The immunoassay in batchwise format was downscaled into a purpose-made microfluidic droplet platform allowing significant sample volume reduction and higher throughput. Using a series of 4 programmable magnetic tweezers to manipulate a train of nano-scale confined droplets containing magnetic beads, sample, washing and detection solutions, a sequence of 8 analyses could be realized within 45 min. This droplet based immunoassay was realized in a dedicated platform integrating an in-house-made light emitting diode (LED)-based fluorescent detector, replacing conventional microscopic setup so as to significantly reduce the construction cost and simplify the detection protocol. Using this microfluidic configuration coupled with LED-based detection, information on both Aβ 1–42 and Aβ 1–40 concentrations can be collected in a single sequence with less than 1 μL of sample.

1. Introduction

Molecular biomarkers in the cerebrospinal fluid (CSF) have a central role to diagnose Alzheimer's disease (AD), monitor AD evolution and for drug development as CSF reflects molecular events occurring in the brain thanks to its direct contact with the extracellular brain space [1]. Among all CSF biomarkers, amyloid-β peptide Aβ 1–42 is considered the most well-established and internationally validated one for early diagnosis of AD [2–4]. This peptide belongs to the Aβ peptide "family" having from 37 to 43 amino acids (AA) that are naturally produced via enzymatic proteolysis of the amyloid precursor protein (APP) in body fluids [5]. The determination of Aβ 1–42 alone however is not sufficient for precise discrimination of AD from other neurodegenerative diseases (NDs) because low levels of Aβ 1–42 in CSF may be also associated with other NDs, notably dementia with Lewy body (DLB), Parkinson's

* Corresponding author.
** Corresponding author.
E-mail addresses: stephanie.descroix@curie.fr (S. Descroix), myriam.taverna@u-psud.fr (M. Taverna).

http://dx.doi.org/10.1016/j.snb.2017.09.003
0925-4005/

disease (PDD) or Creutzfeld-Jacob disease (CJD) [6]. For this reason, different biomarker combinations for AD have been proposed, notably the triplex Aβ 1–42, Tau and 181p-Tau proteins that is currently under clinical use [7–9]. In parallel, continued research has been implemented to establish more biomarkers for AD, focusing on Aβ 1–42/Aβ 1–40 ratio [2,9,10], Aβ 1–42, Aβ 1–40 and Aβ 1–38 [11–13], the ratio of Aβ 1–42/(Aβ 1–42 + Aβ 1–40 + Aβ 1–38) [14], Aβ 1–40/Aβ 1–42 and Aβ 1–37/Aβ 1–38/Aβ 1–39 [15,16], Aβ 1–42 and Aβ 2–42 [17] and Aβ 1–42, Aβ 2–40 and Aβ 2–42 [18]. The combination of Aβ 1–42/Aβ 1–40 has been the most frequently cited or recommended for research on AD likelihood prediction as it reflects AD-type pathology better than CSF Aβ 1–42.

Of all the methods for tracing of Aβ peptide-based AD's biomarkers in CSF [3], immunoassays have been the conventional and well-established ones [19–23]. This technique can be divided into wells-based and microbeads-based sandwich assays. The former type includes standard enzyme-linked immunosorbent assay (ELISA) [24] and Meso Scale Discovery (MSD) [25,26], whereas the microbeads-based format can be referred as multi-analyte profiling assay (Luminex xMAP) [27,28] and single molecule array (SiMoA) [29–32]. A modified version of microbeads-based sandwich assay has recently been reported by Pi et al., using quantum dots for the detection of Aβ 1–42 alone [33]. Among these immunoassay approaches, ELISA has been up to now the most practiced one for detection of Aβ peptides. However, within- and between-laboratory variations of the results are very often observed with conventional ELISA due to laborious and manual steps required, which in turn may lead to a large discrepancy in Aβ 1–42 concentrations and misinterpretation of AD diagnoses [34,35]. To avoid these crucial problems, SiMoA and xMAP technologies are normally preferred. Nevertheless, despite the higher automation of the immunoassay protocols and the lower limits of detection achieved, these systems still present important limitations. In particular, they require costly commercial instruments that are not readily accessible to an integration of other customized operations and purpose-made instrumentation. Furthermore, several dozen μL of sample are required for each analysis, which renders the detection of many analytes from the same biological sample not possible if only a limited sample volume (few μL for example) is available. In this context, miniaturization of the conventional batch-based sandwich assays into microfluidic platforms is of significant interest for the development of point-of-care (POC) devices and to increase the quality and accuracy of ELISA methods. Notable positive features of this down-scaled configuration include small required volumes of samples and reagents, the minimized likelihood of contamination, and reduction of the assay time due to the high surface-to-volume ratio and small diffusion distance. An important feature expected from the downscaling is to provide automated procedures that will certainly allow more accurate and precise assays than current classical ELISA.

Efforts to develop microchip-based systems for determination of Aβ peptide-based AD biomarkers have indeed been communicated repeatedly by our groups, using microchip electrophoresis and/or magnetic immunocapture [13,36–40]. Due to (i) the presence of these Aβ peptides in CSF at only trace amounts (generally 0.1–10 nM in CSF) that renders their quantification not trivial and (ii) their close structures that make them difficult to be separated, continued efforts to improve the detection sensitivity and selectivity are still required. In this context, a new approach for selective and sensitive determination of Aβ peptides is to carry out immunoassays in microfluidic droplets. Droplet-based technologies have emerged as new tools for a wide range of applications, notably in diagnostics, drug delivery, molecular imaging *etc.* [41,42]. For the purpose of AD diagnosis, Kim et al. and Park et al. recently implemented ELISA employing microliter scale-droplets in an ELISA instrumental platform. However this method that produced droplets of 30–50 μL in wells of a microtiter-plate was applied to the detection of amyloid β oligomers and not to monomers [43,44]. Their systems can be considered as the transitional configuration between traditional batch-wise (μL – mL ranged) ELISA and microfluidic-droplet-wise (nL – sub μL ranged) one. To the best of our knowledge, the coupling of ELISA with microfluidic (sub μL scaled) droplets for determination of several monomeric Aβ peptides has not been reported yet. This may come, at least partially, from the fact that working with monomeric Aβ peptides is very challenging and require experienced handling because they tend to i) form heterogeneous mixtures in nature, which make them unstable and prompt to self-assemble, oligomerise, aggregate [3] and ii) bind to other molecular partners or surfaces during the analysis process. In addition, dedicated microfluidic systems are needed for such purpose, as it is not readily possible to work with sub μL droplets using a microtiter-plate.

Herein we report a novel magnetic bead-based immunoassay in which capture antibodies grafted onto magnetic beads and detection antibodies can simultaneously bind to monomeric Aβ 1–40 and Aβ 1–42 in a single step. This method was employed for detection of these peptides in CSF samples. With the aim at expanding the spectrum of Aβ peptides to be traced to achieve higher specificity of AD diagnosis, the developed sandwich assay was for the first time coupled as a downstream module to capillary isoelectric focusing (CIEF). Using this technique, Aβ peptides possessing different isoelectric points can be first compartmentalized into different fractions along a capillary filled with a pH gradient under a high electrical field. These fractions were then collected for subsequent detection of Aβ peptides using the developed ELISA method. Demonstration of this methodological combination was carried out with Aβ 1–40, Aβ 2–40 and Aβ 5–40. Towards digital diagnostics and automation of the ELISA protocol, the developed single-step immunoassay was in parallel downscaled to a microfluidic droplet platform with a series of programmable magnetic tweezers (refer to reference [45] for details on these tweezers) coupled with a home-made and low cost fluorescence detector. The objective of the present work is to provide both methodological and instrumental approaches for detection in a flexible manner of established and potential Aβ-based biomarkers for early diagnosis of AD.

2. Experimental

2.1. Chemicals, reagents and samples

Amyloid peptides were purchased from either Anaspec (Fremont, CA, USA) or American Peptide (Sunnyvale, CA, USA). *N*-(3-Dimethylaminopropyl)-*N′*−ethylcarbodiimide hydrochloride (EDC), *N*-hydroxysulfosuccinimide sodium (S-NHS), Tris(hydroxymethyl)aminomethane (Trizma-HCl), hydrochloride triethanolamine (TEA), bovine serum albumin (BSA), phosphate buffered saline (PBS 10X), polyoxyethylenesorbitan monolaurate (tween-20), boric acid, phosphoric acid (85%), formic acid , ammonium hydroxide 28.1% (m/V), sodium hydroxide, dimethyl sulfoxide (DMSO, 99.9% purity), iminodiacetic acid, urea, Pharmalyte 3–10 carrier ampholytes, bicine, 3-((3-Cholamidopropyl)dimethylammonio)-1-propanesulfonate hydrate (CHAPS), 2-(*N*-Morpholino)ethanesulfonic acid hydrate, 4-Morpholineethanesulfonic acid (MES) hydrate and IgG from murine serum (reagent grade, ≥95%), were provided by Sigma (St. Louis, MO, United States). Fluorinert oil FC-40 (ZF-0002-1308-0) was purchased from 3 M (USA). The surfactant 1H, 1H, 2H, 2H – perfluoro-1-decanol was obtained from Sigma Aldrich. Pharmalyte 5–8 and 3–10 carrier ampholytes were acquired from GE Healthcare (Velizy-Villacoublay, France). CIEF gel (polymer solution) and "capillary revival solution" (part number 608082)

were purchased from ABSCIEX (Les Ulis, France). Carboxylate functionalized magnetic micro-particles (Dynabeads MyOne, 10 mg/mL, diameter of 1 μm) were obtained from Invitrogen (Fisher Scientific, Illkirch, France). The capture antibodies, i.e. monoclonal anti-Aβ antibodies 12F4 and G2-10, were purchased from Covance (Emeryville, CA) and Merck Millipore (Molsheim, France). The detection antibody, *i.e.* Aβ 1–16 monoclonal antibody labeled with horseradish peroxidase, (6E10-HRP) was obtained from Eurogentec (Seraing, Belgium). The QuantaRed enhanced chemifluorescent HRP substrate kit was purchased from ThermoFisher (Saint-Herblain, France). All solutions were prepared with deionized water purified with a Direct- Q3 UV purification system (Millipore, Milford, MA, USA). All CSF samples (from AD and healthy patients) were taken by the department of Neurology, university of Ulm (Ulm, Germany), aliquoted and stored at −20 °C until use. The sampling procedure was detailed elsewhere [13,14]. Collection and analysis of CSF samples were approved by the Ethics Committee at the University of Ulm.

2.2. Materials and apparatus

2.2.1. For macroscale protocols

All magnetic beads based immunoassays in batch were carried out in protein LoBind 1.5 mL tubes purchased from Eppendorf (Hamburg, Germany). For retaining magnetic beads, a neodymium magnet purchased from Ademtech (Adem Mag MSV, Bessac, France) was used. Centrifugation was done with a Micro Star 17R centrifuge (VWR, Leuven, Belgium). Shaking of magnetic bead suspensions during the incubation and washing steps was realized with a mixer (Mischer 5432, Eppendorf). Fluorescence detection with the excitation and emission wavelengths of 530 nm and 585 nm respectively were carried out with a FP-750 Spectrofluorometer from Jasco (Lisses, France) using a 40 μL quartz cuvette (Starna Scientific, Essex, England). pH values of solutions were controlled with an inoLab WTW series pH 730 m. All CIEF experiments were implemented with an ABSCIEX PA 800 ProteomLab instrument equipped with a 280 nm UV detector, using PVA-coated capillaries 100 μm id (Agilent, U.S.). Data acquisition and instrument control were realized with the Karat 7.0 software.

2.2.2. For droplet microfluidic operations

The microfluidic droplet platform was inspired from our previous configurations [45,46]. It comprises two syringe pumps (from Nemesys, Cetoni GmbH) equipped with 500 μL and 2.5 mL glass syringes (purchased from SGE) and a motorized pipettor arm (Rotaxys, Cetoni GmbH), used for droplets generation. A 384-well plate (AB-1384, Thermo Scientific) was used for sample storage and reagent solutions. The plate was placed on a purpose-made holder that can be adjusted in the X, Y, Z directions. PTFE tubing with ID of 0.3 mm and OD of 0.6 mm (Z609692-1PAK, Sigma Aldrich) was used to conduct the droplet trains. Fluorinated oil FC-40 mixed with the surfactant (1H, 1H, 2H, 2H – perfluoro-1-decanol, 2% w/w) was used to separate aqueous droplets inside PTFE tubing. In the protocol, four magnetic tweezers, prepared in-house (see refs [45,46]), were used. They are composed of a couple of paramagnetic tips activated by a magnetic coil. Four Macro Objective (MLH-10X) mounted on four low-cost CMOS Cameras (acA1300-60 gm, Basler) and white LED back light illumination (Schott Lighting and Imaging) were employed for droplet observation. Fluorescent detection was carried out with a home-made light-emitting diode (LED) based detector. Signals from the home-made LED detector were recorded with a data acquisition unit (NI USB-6255, National Instrument) and then processed with a purpose-made LabVIEW program.

2.3. Methods

2.3.1. Peptide preparation and storage for immunoassay experiments

Stock Aβ 1–42 was prepared in ammonium hydroxide 0.16% (m/V) whereas other amyloid peptides were dissolved in ammonium hydroxide 0.10% (m/V). Aliquot solutions (10 μL) of individual peptides were prepared at a concentration of 2 mg/mL and subsequently lyophilized to remove all traces of ammonia. These lyophilized aliquots were then stored at −20 °C until use. For preparation of standard solutions (STDs), the lyophilized Aβ peptides were diluted with PBS 1X/BSA 0.1% buffer to obtain desired concentrations. These solutions were freshly prepared and stored at 4 °C for use within one day.

2.3.2. CIEF protocol

For CIEF operation, Aβ peptides, prepared from stock solutions in DMSO (460 μM), were 60-fold diluted in a solution composed of 20 mM bicine, 0.6% CHAPS (pH 7.6, bicine-CHAPS buffer) prior to isoelectric focusing. A CIEF master mix was prepared by combining 70 μL of 4 M urea in CIEF gel, 5 μL of Pharmalyte 5–8, 1 μL of Pharmalyte 3–10 and 1 μL of 200 mM anodic stabilizer. This CIEF master was vortexed for 1 min and centrifuged for 5 min at 1000 rpm. The solution of amyloïd peptides at a define concentration was then added to the CIEF master mix. Bicine-CHAPS buffer was then added to obtain 100 μL of the final sample solution. The catholyte and the anolyte solutions were composed of 10 mM H_3PO_4 (pH 2.4) and 50 mM MES (pH adjusted to 8.3 with a solution of NaOH) respectively. A PVA-coated capillary was used to avoid wall-adsorption of proteins and to suppress the electroosmotic flow. At the beginning of each day the capillary was conditioned with a capillary revival solution at 10 psi for 5 min. Between two successive runs the PVA-coated capillary was rinsed with the capillary revival solution for 2 min at 10 psi and then with water for 2 min at 20 psi. Prior to CIEF, the sample was filled into the capillary at 10 psi for 0.5 min. Focusing was then carried out by application of a 15 kV voltage for 6 min, followed by hydrodynamic mobilization at 0.1 psi under the same voltage. Each Aβ peptide fraction was collected in 10 μL of the catholyte solution (50 mM MES pH 8.3). For collection of Aβ peptide fractions, pressurization from the inlet of the capillary was applied while keeping the high voltage in order to maintain the focalization of Aβ peptide fractions and thereby their resolution.

2.3.3. Protocol for grafting of antibodies onto magnetic beads

Magnetic micro-particles (Dynabeads MyOne Carboxylic Acid, 10 mg in 1 mL) were coated with either 12F4 or G2-10 antibodies according to the optimized protocol. Briefly, the beads from 500 μL of a Dynabeads MyOne suspension (10 mg/mL) were rinsed twice with 1 mL PBS 1X after removal of the suspending solution. 500 μL of an EDC solution (10 mg/mL in PBS 1X) and 500 μL of an S-NHS solution (10 mg/mL in PBS 1X) were then added into the washed beads, followed by the addition of 20 μL of the selected antibodies (either 12F4 or G2-10). The mixture was incubated for 3 h under vigorous shaking at room temperature (RT). The antibody-bound magnetic beads were subsequently washed twice with 1 mL of PBS 1X, followed by an incubation at RT with 1 mL of 50 mM Tris-HCl (pH 7.4) for 15 min in order to quench the non-reacted activated carboxylic acid groups. The antibody-bound magnetic beads were then washed 3 times with 1 mL of PBS 1X/0.1% BSA/0.1% Tween-20 prior to final suspension in 500 μL of this solution. A neodymium magnet was employed to retain magnetic beads during removal or addition of a suspension solution. The concentration of the bead suspension after this antibody-grafting protocol remains unchanged at 10 mg/mL. For grafting of antibodies onto magnetic

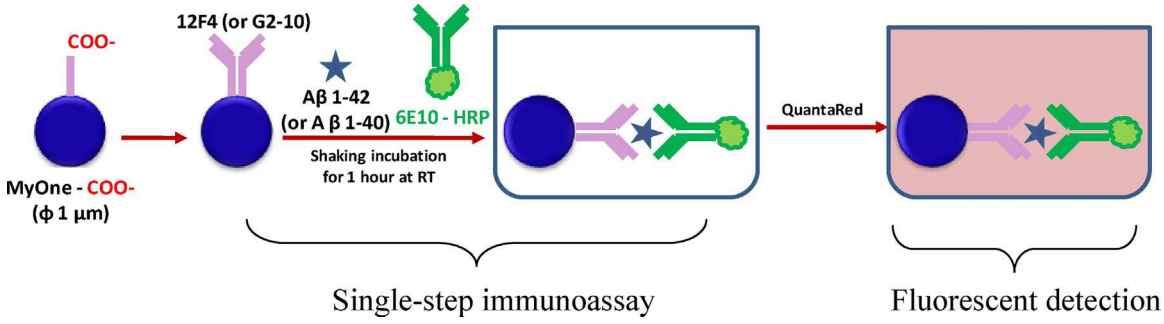

Fig. 1. Protocol of magneticbeads- based immunoassays of Aβ 1–40 and Aβ 1–42 in batch mode.

microbeads pre-coated with IgG (Dynabeads M-280, 10 mg in 1 mL) refer to the protocol reported elsewhere [36].

2.3.4. Magnetic-beads based immunoassays in batch mode

For magnetic-beads based immunoassays in batch, a volume of 50 µL of either a STD solution (prepared in PBS 1X/0.1% BSA/0.1% Tween-20) or a CSF sample was incubated with 500 µg of magnetic beads coated with the desired antibodies (MyOne – 12F4 or MyOne – G2-10) and 5 µL of 6E10-HRP 0.4% in PBS 1X on a mixer at RT for 1 h. Beads were then washed carefully three times (15 min each time) with PBS 1X/0.1% BSA/0.1% Tween-20. After removal of the washing solution, 50 µL of the QuantaRed solution was added to the beads and allowed to react on shaking for 15 min, followed by addition of 5 µL of the QuantaRed stop solution. The color intensities of the obtained solutions after the incubation with the QuantaRed reagent were measured at the respective excitation and emission wavelengths of 530 nm and 580 nm.

2.3.5. Magnetic-beads based immunoassays realized in the microfluidic droplet platform

A robotic arm and a 500 µL syringe were used to automatically pipette the droplets from different reservoirs into a PTFE tubing. A train of 5 droplets (200 nL each) is needed to complete one droplet-based immunoassay. It includes: i) one droplet of antibody-bound magnetic beads prepared in PBS 1S/0.1% BSA/0.1% Tween-20, ii) one droplet of a standard/sample solution, iii-iv) two droplets of the washing solution (PBS 1S/0.1% BSA/0.1% Tween-20) and v) one droplet of the detection solution (QuantaRed). In between the droplets, a small air bubble (50 nL) was generated as a spacer to avoid any merging of droplets [47]. In a sequence, a series of 8 trains was manipulated at a flow-rate of 0.13 µL/s. Beads were trapped out of one droplet and released into another by ON/OFF triggering of magnetic tweezers by using a dedicated software [45]. The detector was situated after the last tweezers to record the fluorescent signals emitted from the detection droplets (refer also to Fig. S1 in the Electronic Supplementary Information (ESI) and Section 3.2 for more details on instrumental design).

3. Results and discussion

3.1. Single-step magnetic-beads-based immunoassays

3.1.1. Batchwise protocol development

In conventional ELISA, several (manual) operations are involved to separately implement i) trapping of antigens (i.e. Aβ peptides) onto a solid support (i.e. magnetic beads) grafted with capture antibodies and ii) binding of the detection antibodies onto the immobilized Aβ peptides. For adaptation of batch-based ELISA into a microfluidic platform, simplification of such a protocol is needed to facilitate the operation and minimize error accumulation. We therefore first developed single-step batch-wise magneto-immunoassays for detection of Aβ 1–40 and Aβ 1–42 from standard solutions. The protocol, illustrated in Fig. 1, is straightforward and can be realized using a modest infrastructure without recourse to costly commercial instruments like SiMoA or xMAP ones. In our approach, we propose to simultaneously carry out two aforementioned operations in a single step. By avoiding additional washing steps in-between these operations, this helps significantly reduce the operation time and step number, thus rendering it more adaptable to subsequent down-scaling into a microfluidic device (see Section 3.2). This protocol exploits two different epitopes on Aβ peptides that are available for binding to capture antibodies (*i.e.* 12F4 for C-terminus of Aβ 1–42 and G2-10 for Aβ 1–40 respectively) and detection one (6E10-HRP for N-terminus of both Aβ 1–42 and Aβ 1–40). Detection was then carried out using the enzymatic reaction of the HRP with 10-acetyl-3,7-dihydroxyphenoxazine (ADHP) in the QuantaRed substrate to produce the highly fluorescent and soluble product resorufin. It was found that detection antibody 6E10-HRP can easily adsorb non-specifically onto bead surface, leading in turn to false positive signals (see Fig. S2 in the ESI). The choice of magnetic beads and the composition of the washing solution are thus of importance to eliminate this problem. Different types of magnetic beads were investigated, *i.e.* Dynabeads M-280 grafted with different capture antibodies according to [36] and Dynabeads MyOne grafted with 12F4 or G2-10 antibodies. The latter exhibited the least non-specific adsorption of 6E10-HRP (data not shown). We found that using buffers containing simultaneously BSA (protein blocker) and Tween-20 (non-ionic detergent blocker) allows to decrease drastically the non-specific adsorption of the 6E10-HRP on the bead surface (see Fig. S3 in the ESI). The 6E10-HRP concentration during the incubation step was also tuned to avoid the difficulty in removing its excess from the bead surface. It was found that for the optimized mixture of 6E10-HRP (0.04% v/v) and beads (10 mg/mL), 1-h incubation followed by washing steps with a solution composed of PBS 1X/0.1% BSA/0.1% Tween-20 (washing for 3 times, 15 min each) removed efficiently the residual 6E10-HRP from the beads. Compared to conventional immunoassays in which incubations are implemented overnight with gentle shaking at 4 °C, our procedure takes much shorter time and is compatible with microfluidic operation at RT (see Section 3.2). The correlation between Aβ 1–42 concentrations and the achieved detection signals are illustrated in Fig. 2. The color intensity reached the saturation state at the Aβ 1–42 concentrations over 10 nM. A similar observation was made for Aβ 1–40 concentrations (at 15 nM). To evaluate the specificity of the method, two experiments were performed in the study and the results were exploited: i) capture of Aβ 1–40 (10 nM) onto magnetic beads grafted with G2-10 antibodies in the presence of Aβ 1–42 (1 nM) and ii) capture of Aβ 1–42 (10 nM) onto magnetic beads grafted with 12F4 antibodies in the presence of Aβ 1–40 (10 nM). The tested peptide concentrations were selected based on the fact that the concentration of

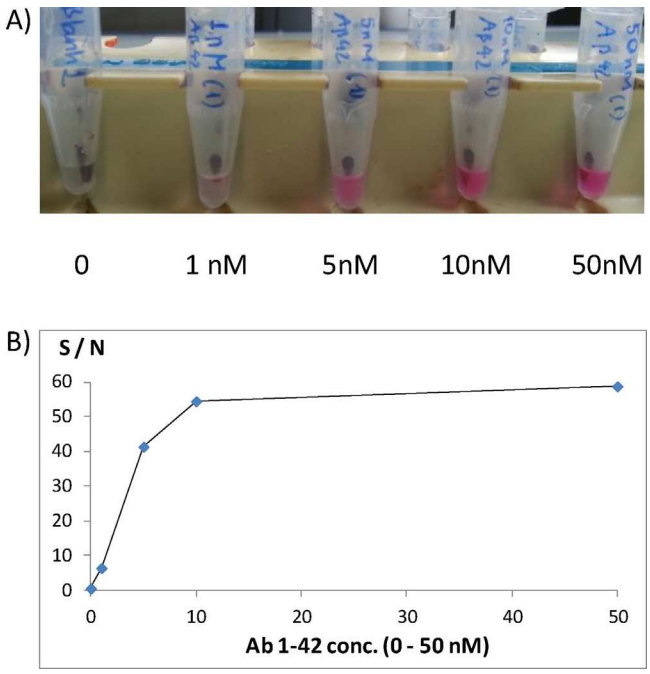

Fig. 2. The correlation between Aβ 1–42 concentrations and the color intensities of the detection solutions (A) and the achieved fluorescent signals (B). Refer to Section 2.3 for details on experimental conditions.

Aβ 1–40 is much higher than that of Aβ 1–42 in CSF. No observable change of the signal was detected in the former and there was only a slight signal decrease by 8% in the latter. The developed method is thus considered fully specific for Aβ 1–40 and about 90% specific for Aβ 1–42 under the tested conditions. In order to eliminate the signal bias caused by such slight competitive capture, and minimize the signal mismatch issue induced by the matrix difference between standard solutions and CSF samples, the standard addition method was preferred. In this case, by keeping the same CSF matrix for all measurements of each sample spiked with different defined Aβ peptide concentrations, the signal bias is subtracted during the result extrapolation. The developed batch-based immunoassays were then applied for detection of Aβ 1–42 and Aβ 1–40 in CSF samples collected from one AD patient and one healthy person. For determination of Aβ 1–40 or Aβ 1–42 in each CSF sample, three 50 μL CSF aliquots were spiked with a known amount of the two Aβ peptides and concurrently subjected to the same series of immunoassays. Based on the linearity of the obtained fluorescent signals (Fig. S4 in the ESI), the concentrations of Aβ 1–42 and Aβ 1–40 were extrapolated to be 0.04 nM and 2.5 nM for the AD patient's CSF and 0.71 nM and 28 nM, respectively for the healthy person's one. As expected, the concentration of Aβ 1–42 as well as the ratio of Aβ 1–42/Aβ 1–40 were found to be much lower in the AD patient, in agreement with the literature [11]. A total volume of 300 μL was needed for determination of Aβ 1–42 and Aβ 1–40 in each CSF sample with this standard addition method.

3.1.2. CIEF based compartmentalization of Aβ peptides as a fore-front of magnetic beads- based immunoassays

More performing AD diagnosis could be achieved by considering a wider spectrum of Aβ peptides beyond Aβ 1–42 and Aβ 1–40. In this context, extended detection of several other Aβ peptides, considered as complementary potential AD biomarkers, rather than limiting at only the established ones (Aβ 1–42 and Aβ 1–40) is desirable. This objective nevertheless could not be easily realized with the immunoassay approach due to the lack of antibodies that are specific to all targeted Aβ peptides. This limitation on the other hand can be overcome by coupling the developed immunoassay with pH-gradient-induced compartmentalisation of peptides under a high electrical field (*i.e.* CIEF). The integration of this electrokinetic method as a forefront module prior to immunoassays allows resolute separation of amyloid peptides based on their pI differences without the need of organic solvents that can denature or oligomerise the analytes. In detail, demonstration was implemented with Aβ 1–40, Aβ 2–40 and Aβ 5–40. During CIEF, Aβ peptides are focalized and concentrated into different zones along the capillary as soon as they reach the pH corresponding to their pI. Three zones were formed after this process, with Aβ 1–40 in the first (pI = 5.33), Aβ 2–40 in the second (pI = 5.98) and Aβ 5–40 in the last one (pI = 6.46) [48]. Each of these fractions was then collected by pressure mobilization to the detection end of the capillary and subjected to a beads-based immunoassay in batch mode. For the first time an off-line CIEF coupling to magnetic beads – based immunoassays was demonstrated for Aβ peptides. Indeed in the present work, fraction collections were performed along a closed microchannel, whereas in the work reported recently by Mikkonen et al. a perpendicular CIEF collections of Aβ peptides from an opened channel followed by MS detection was employed [49]. Compared to the commercially available setup for fraction collection and detection after isoelectric focusing [50], significant reduction of the working volume (from 150 μL down to some μL only) can be achieved with our approach. Moreover, the capture antibody G2-10, grafted on magnetic beads, which is specific to the C-terminus of all Aβ x-40, can be conveniently used to trap either Aβ 1–40, Aβ 2–40 or Aβ 5–40 previously compartmentalized in different fractions (see Fig. S5 for demonstration of good capture and detection of Aβ 1–40, Aβ 2–40 or Aβ 5–40). Magnetic beads – based immunoassay in this case serves as an efficient, simple and inexpensive tool to visualize peptides and monitor the collection operation. It is shown in Fig. 3A the distribution of Aβ 1–40, Aβ 2–40 and Aβ 5–40 in different fractions after the CIEF process, monitored by this immunoassay approach. The concentration of these Aβ peptides was 10 nM in the collected fractions. Note that a four-time dilution occurred during the collection step, indicating that the Aβ peptides' concentration inside the capillary after the CIEF focalization step was 40 nM. The focusing of intact Aβ 1–40, Aβ

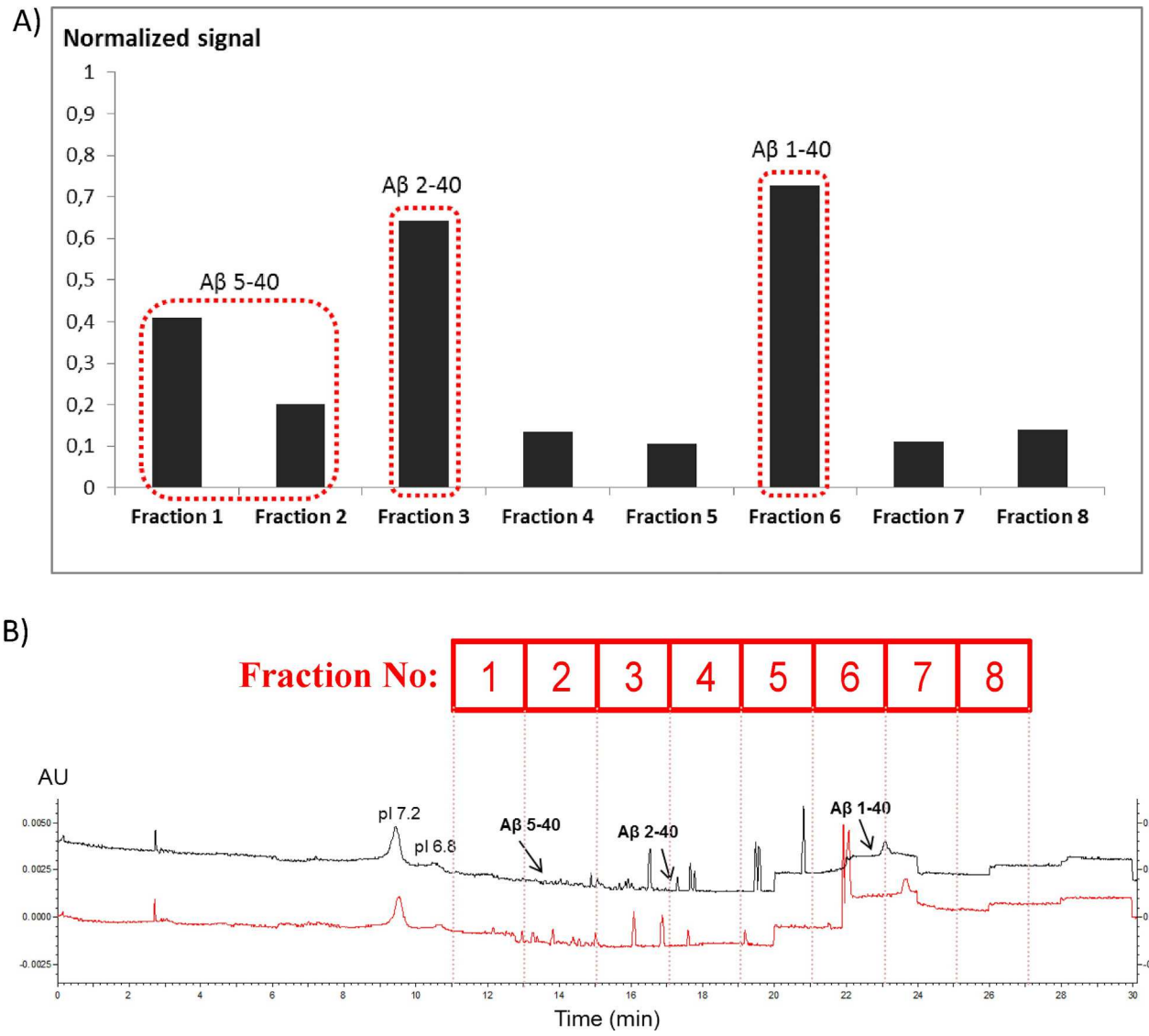

Fig. 3. Distribution of Aβ 1–40, Aβ 2–40 and Aβ 5–40 fractions after CIEF process, visualized with the developed batchwise immunoassay (A) and on-capillary UV detection (B). Black profile for Aβ peptide concentration inside the capillary of 40 nM; Red line: CIEF blank. Refer to Section 2.3 for details on experimental conditions. (For interpretation of the references to colour in this figure legend, the reader is referred to the web version of this article.)

2–40 and Aβ 5–40 at this concentration cannot be visualized with conventional UV detection (the black electropherogram in Fig. 3B). The positions of these Aβ peptides could only be traced with UV detection at concentrations over 150 nM (see Fig. S6). The traceable range with UV detection however was far higher than the expected levels of Aβ peptides (0.1–10 nM) in CSF samples.

3.2. Magnetic beads-based immunoassays of Aβ peptides in a microfluidic droplet platform

3.2.1. Instrumental design and operation optimization

To offer higher degree of automation to minimize manual operations inducing errors, significant reduction of sample/reagent volumes and drastic diminution of operation time, the developed batch-wise immunoassays were then translated into a microfluidic droplet platform, making a step forward in the molecular AD diagnosis. The optimized instrumental setup is shown in Fig. 4. An overview of a typical sequence with parameters for each operation is given in Table 1. The protocol starts with an uptake of droplet trains from the reservoirs which are then delivered through the magnetic tweezers and mixing plates towards the detector. By on/off triggering of the magnetic tweezers, the beads were transferred from the initial droplet to the sample droplet in the sample incubation step, then to two washing droplets during the steps of washing 1 and washing 2, and finally dispensed in the detection droplet in the step of sample detection (see Table 1 and Fig. 4). In each step, the beads stayed in droplets for a certain time (*i.e.* incubation time) while the droplets were moving with the flow inside the tubing over a certain distance (*i.e.* droplet travel distance). During the sample incubation step, the beads were dispensed in a droplet

Table 1
Typical operation sequence of the immunoassay protocol.

Operation	Flowrate (μL/s)	Incubation time (min) [a]	Droplet travel distance (m) [b]
Sample incubation	0.13	15	2.0
Washing 1	0.13	7.5	1.0
Washing 2	0.13	7.5	1.0
Sample detection	0.13	10	1.3

[a] The duration that the beads stay in a selected droplet.
[b] The tubing length between two pairs of tweezers, over which the droplets are delivered.

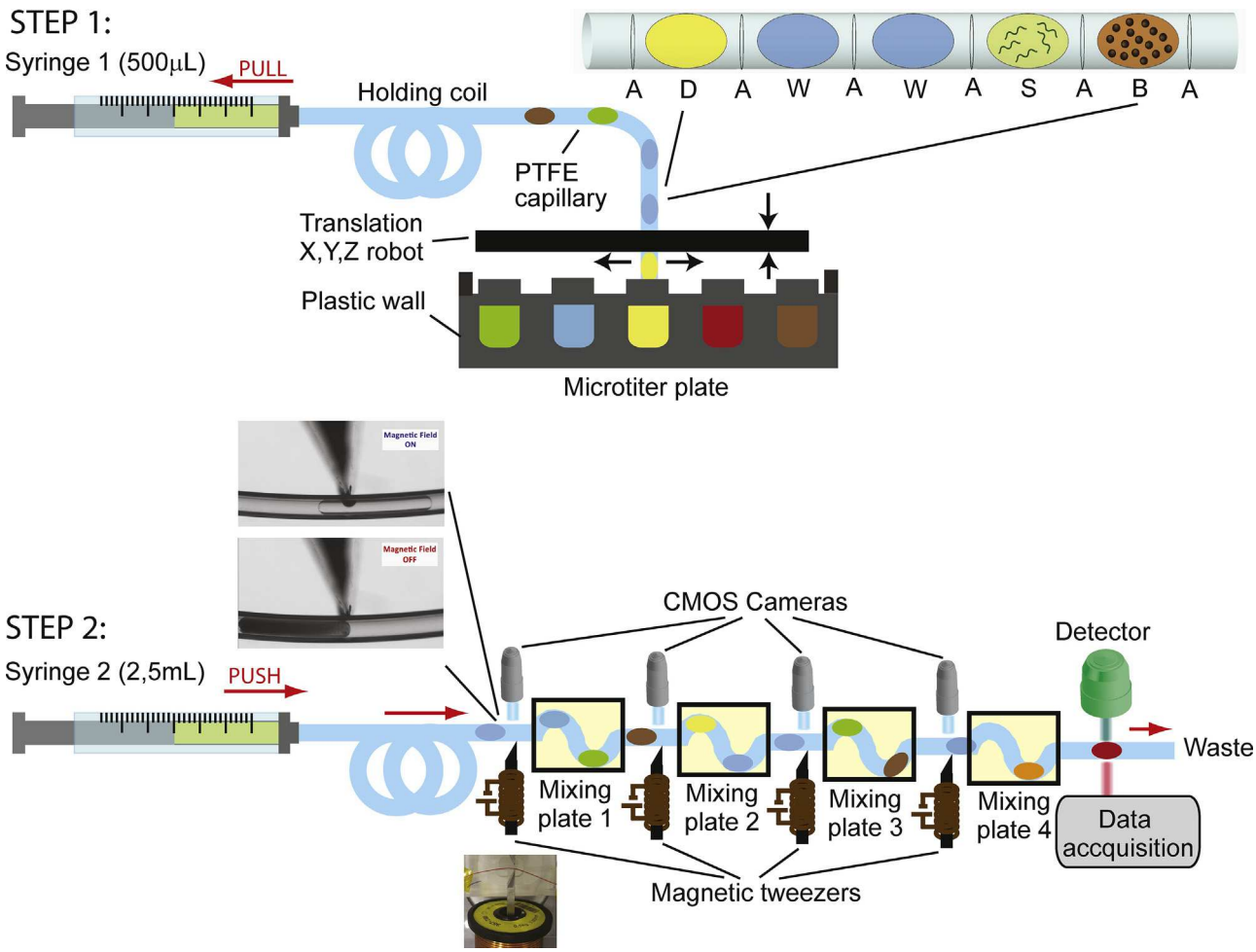

Fig. 4. The schematic drawing of the microfluidic droplet setup. D: detection droplet; W: washing droplet; S: sample droplet; B: magnetic bead droplet; A: air bubble. Droplets are separated by oil.

containing the sample (i.e. Aβ peptides) and the detection antibodies. The residual (non-specifically bound) detection antibodies were then washed away from the beads in the steps of washing 1 and 2. Subsequently in the step of sample detection, the washed beads were transferred into the detection droplet containing the substrate for enzymatic reaction followed by fluorescent detection. The distance between the tweezers and the flowrate were adjusted in order to achieve an optimal incubation time in each step (see Table 1). To adapt the microfluidic droplet platform to the developed ELISA protocol, new features were implemented compared to our previous versions of the setup [45,46]. First, four pairs of magnetic tweezers were synchronized to allow the trains to move in one direction while transferring the beads from the bead droplet to the sample one (for single-step immunoassay), then to two washing droplets and finally into the detection droplet that contains the enzymatic substrate. Without this multi-tweezers setup, the droplet trains had to move back and forth in the tubing several times through a single pair of magnetic tweezers [46,51]. This back and forth movement led to unwanted prolongation of operational time. Second, in order to improve the mixing of the beads inside the droplets, the PTFE capillary was placed in metallic holders, named hereafter mixing plates, which preset a winding configuration [52]. The design and dimensions of the mixing plate are shown in Fig. S1 of the ESI. Four mixing plates were inserted between magnetic tweezers to help the beads recirculate efficiently in the droplet. Indeed, it was observed that without these mixing plates, the beads stayed at the rear of moving droplets and were not well mixed, resulting in mediocre efficiencies of immunoassay and bead washing. Last, a low cost and purpose-made LED-based detector was integrated at the downstream of the droplet trains for facile monitoring of the fluorescent signals from detection droplets. The detector, whose construction materials (excluding the filter set) cost ~$50, is composed of a green LED for excitation, a silicon photodiode as primary light detector, basic optics, 3D-printed parts, and a custom-made lock-in amplifier (see Fig. S7 in the ESI). Fluorescence readings were recorded with a data acquisition unit and an in-house-made LabView-based program. By emitting the excitation light (at 530 nm) and recording the emission one (at 570 nm) at a pre-defined frequency (10 kHz), the obtained signal/noise could be significantly amplified by the lock-in circuit. With this detector, the detection protocol is much simplified as the user just needs to collect all proceeded data from an excel file for quantification or graph demonstration. Note that in our previous version where conventional epifluorescence microscope equipped with a translation stage and a camera was employed [46], manual and tedious conversion of the captured images into digital data had to be implemented, which in turn renders the detection operation less straightforward compared to the present setup. Moreover, the use of a conventional fluorescent microscope, would increase considerably the construction cost of an eventual prototype of the global microfluidic platform.

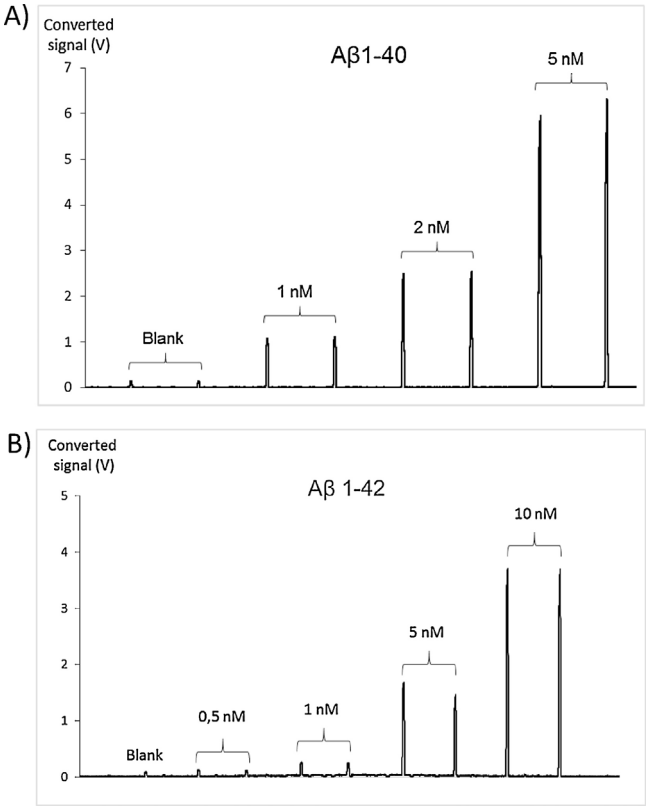

Fig. 5. Fluorescent signals for Aβ 1–40 (A) and Aβ 1–42 (B) on passage of detection droplets through the LED-based detector. Refer to Section 2.3 for details on descriptions of instrumental setup and operational protocol on the microfluidic droplet platform.

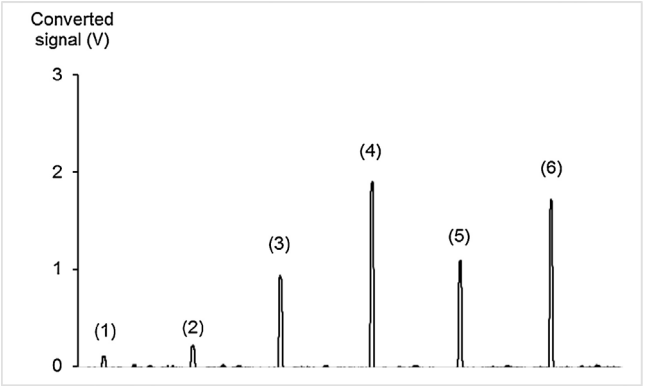

Fig. 6. Fluorescent signals for sequential determination of Aβ 1–40 and Aβ 1–42 (2 nM each) spiked in an artificial CSF sample. Detection of (1) a blank droplet (artificial CSF) with MyOne-12F4, (2) a blank droplet with MyOne-G2-10, (3, 5) the spiked artificial CSF with MyOne-12F4 and (4, 6) the spiked artificial CSF with MyOne-G2-10. Refer to Section 2.3 for details on descriptions of instrumental setup and operational protocol on the microfluidic droplet platform.

3.2.2. Performance

The volume required for each droplet operation was significantly reduced from 50 μL in the batch mode to only 200 nL with the droplet-based platform. Accordingly, remarkable reduction of the amounts of samples and reagents consumed could be achieved in this droplet-based immunoassay. The overall operation time was also significantly reduced for throughput improvement, with a sequence of 8 assays performed in less than 1 h instead of 2 h per assay in batch mode. Moreover, operator's intervention was minimized thanks to a high degree of automation. Fluorescent signals for Aβ 1–40 and Aβ 1–42 on passage of detection droplets through the LED-based detector are shown in Fig. 5A and 5 B respectively. The detection limits are in the order of 0.5–1 nM, which are quite closed to the expected range of 0.1 nM for Aβ 1–42 in CSF samples. Very good linearity was achieved for both for Aβ 1–40 and Aβ 1–42 (r^2 of 0.9973 and 0.9949, respectively).

To demonstrate the possibility of sequential determination of both Aβ 1–40 and Aβ 1–42 from the same sample in a single run, the protocol was modified to allow aspiration of two droplets, one of which contains MyOne-12F4 beads and the other contains MyOne-G2-10 ones, in two consecutive trains. Detection of Aβ 1–40 and Aβ 1–42 (2 nM each) spiked into an artificial CSF sample is illustrated in Fig. 6, with replicate measurements of 2 separated sample droplets carried out for each peptide. The signal increase was clearly observed between artificial CSF samples with and without spiking of Aβ peptides and both peptides could be detected with the same response factor.

4. Conclusions and perspectives

We have for the first time developed a straightforward single-step method of magnetic beads- based immunoassay that can be operated into a microfluidic droplet platform for sensitive and selective detection of the two well-established Aβ peptide biomarkers for AD (Aβ 1–40 and Aβ 1–42). The significance of microfluidic droplet coupled with LED-based technology has been demonstrated for high throughput ELISA sample detection. Compared to conventional ELISA, our microfluidic droplet protocol offers automation, reduction of sample and reagent volumes (down to 200 nL) and significant diminution of operation time, thus making a step forward in the molecular diagnosis of AD. The use of a sequence of tweezers allows a continuous droplet movement in one direction, which in turns offer a significant reduction in operational time and improvement of analysis throughput. The detection limits found by our microfluidic approach was in the order of 0.5 nM, which is close to the detection limit needed for detection of Aβ peptides, especially Aβ 1–42, in CSF samples. The purpose-made LED-based detector can be employed not only for the measurement of fluorescence intensity in droplets in this particular case, but also for other microfluidic applications, for instance to detect fluorescent signals emitted from cells or nanoparticles. In order to expand the spectrum of Aβ peptides (i.e. Aβ 1–40, Aβ 2–40 and Aβ 5–40) being determined with the aim at improving AD diagnostic specificity, the marriage between magneticbeads-based immunoassay and CIEF as a preparative sample fractionation was exploited and successfully demonstrated. In our opinion, more investigation should be done for down-scaling the CIEF protocol in the microdevice format. By doing so, Aβ peptides could be first focused in discrete droplets for compartmentalization and much enrichment before quantification with the microfluidic droplet approach could be obtained. Such instrumental development is envisaged so as to open the door for production of a miniaturized device for sensitive and selective detection of a wider number of Aβ peptides.

Acknowledgements

This work, the post-doctoral fellowship for Dr. Thanh Duc Mai and the PhD scholarship of Nacéra Aboud have been financially supported by the French Investissements d'Avenir program (DIGIDIAG project) under the grant agreement ANR-10-NANO-02. The post-doctoral fellowship for Dr. Davide Ferraro was supported by the Arc fondation for young research fellowships. The PhD program of Marco Serra was supported by a Curie Institute International PhD fellowship. Some technological elements used in this article are covered by the patent WO2013041983, property of the 'Centre National de la Recherche Scientifique' (CNRS, France). The authors thank IPGG LABEX/EQUIPEX for infrastructure support.

Appendix A. Supplementary data

Supplementary data associated with this article can be found, in the online version, at http://dx.doi.org/10.1016/j.snb.2017.09.003.

References

[1] E.R. Peskind, R. Riekse, J.F. Quinn, J. Kaye, C.M. Clark, M.R. Farlow, et al., Safety and acceptability of the research lumbar puncture, Alzheimer Dis. Assoc. Disord. 19 (2005) 220–225.
[2] J. Wiltfang, P. Lewczuk, M. Otto, Biomarkers for dementia and other neurodegenerative diseases. Current developments, Nervenarzt 87 (2016) 1305–1309.
[3] Y.L. Zhou, L.T. Liu, Y.Q. Hao, M.T. Xu, Detection of a beta monomers and oligomers: early diagnosis of alzheimer's disease, Chem. Asian J. 11 (2016) 805–817.
[4] C. Humpel, Identifying and validating biomarkers for Alzheimer's disease, Trends Biotechnol. 29 (2011) 26–32.
[5] J. Kang, H.G. Lemaire, A. Unterbeck, J.M. Salbaum, C.L. Masters, K.H. Grzeschik, et al., The precursor of alzheimers-disease amyloid-A4 protein resembles a cell-surface receptor, Nature 325 (1987) 733–736.
[6] B. Mollenhauer, H. Esselmann, S. Roeber, W. Schulz-Schaeffer, C. Trenkwalder, M. Bibl, et al., Erratum to: different CSF β-amyloid processing in Alzheimer's and creutzfeldt jakob disease, J. Neural Transm. 118 (2011) 1261–1262.
[7] B. Dubois, H.H. Feldman, C. Jacova, H. Hampel, J.L. Molinuevo, K. Blennow, et al., Advancing research diagnostic criteria for Alzheimer's disease: the IWG-2 criteria, Lancet Neurol. 13 (2014) 614–629.
[8] K. Blennow, H. Hampel, CSF markers for incipient Alzheimer's disease, Lancet Neurol. 2 (2003) 605–613.
[9] P. Lewczuk, H. Esselmann, M. Otto, J.M. Maler, A.W. Henkel, M.K. Henkel, et al., Neurochemical diagnosis of Alzheimer's dementia by CSF ab 1–42, ab 1–42/Ab 1–40 ratio and total tau, Neurobiol. Aging 25 (2004) 273–281.
[10] N.R. Graff-Radford, J.E. Crook, J. Lucas, et al., ASsociation of low plasma Ab1-42/Ab1-40 ratios with increased imminent risk for mild cognitive impairment and alzheimer disease, Arch. Neurol. 64 (2007) 354–362.
[11] S. Janelidze, H. Zetterberg, N. Mattsson, S. Palmqvist, H. Vanderstichele, O. Lindberg, et al., CSF Aβ42/Aβ40 and Aβ42/Aβ38 ratios: better diagnostic markers of Alzheimer disease, Ann. Clin. Transl. Neurol. 3 (2016) 154–165.
[12] V. Welge, O. Fiege, P. Lewczuk, B. Mollenhauer, H. Esselmann, H.-W. Klafki, et al., Combined CSF tau, p-tau181 and amyloid-beta 38/40/42 for diagnosing Alzheimer's disease, J. Neural Transm. 116 (2009) 203–212.
[13] K. Mesbah, R. Verpillot, M. Chiari, A. Pallandre, M. Taverna, Neutral polymers as coatings for the high resolution electrophoretic separation of A[small beta] peptides on glass microchip, Analyst 139 (2014) 6547–6555.
[14] R. Verpillot, H. Esselmann, M.R. Mohamadi, H. Klafki, F. Poirier, S. Lehnert, et al., Analysis of amyloid-β peptides in cerebrospinal fluid samples by capillary electrophoresis coupled with LIF detection, Anal. Chem. 83 (2011) 1696–1703.
[15] J. Wiltfang, H. Esselmann, M. Bibl, A. Smirnov, M. Otto, S. Paul, et al., Highly conserved and disease-specific patterns of carboxyterminally truncated Aβ peptides 1–37/38/39 in addition to 1–40/42 in Alzheimer's disease and in patients with chronic neuroinflammation, J. Neurochem. 81 (2002) 481–496.
[16] J. Wiltfang, H. Esselmann, A. Smirnov, M. Bibl, L. Cepek, P. Steinacker, et al. β-amyloid peptides in cerebrospinal fluid of patients with Creutzfeldt–Jakob disease, Ann. Neurol. 54 (2003) 263–267.
[17] M. Bibl, M. Gallus, V. Welge, H. Esselmann, S. Wolf, E. Rüther, et al., Cerebrospinal fluid amyloid-β 2–42 is decreased in Alzheimer's, but not in frontotemporal dementia, J. Neural Transm. 119 (2012) 805–813.
[18] H. Esselmann, T.W., Groemer, J., Kornhuber, P., Lewczuk, J.M., Maler, J. Wiltfang, US Patent Application, 13/639, 866(2011) 13/639, 866.
[19] J.-H. Kang, M. Korecka, J.B. Toledo, J.Q. Trojanowski, L.M. Shaw, Clinical utility and analytical challenges in measurement of cerebrospinal fluid amyloid-beta(1–42) and tau proteins as alzheimer disease biomarkers, Clin. Chem. 59 (2013) 903–916.
[20] S. Lista, H. Zetterberg, B. Dubois, K. Blennow, H. Hampel, Cerebrospinal fluid analysis in Alzheimer's disease: technical issues and future developments, J. Neurol. 261 (2014) 1234–1243.
[21] P. Gagni, L. Sola, M. Cretich, M. Chiari, Development of a high-sensitivity immunoassay for amyloid-beta 1–42 using a silicon microarray platform, Biosens. Bioelectron. 47 (2013) 490–495.
[22] N. Xia, L. Liu, M.G. Harrington, J. Wang, F. Zhou, Regenerable and simultaneous surface plasmon resonance detection of a beta(1–40) and a beta(1–42) peptides in cerebrospinal fluids with signal amplification by streptavidin conjugated to an N-Terminus-Specific antibody, Anal. Chem. 82 (2010) 10151–10157.
[23] M. Ammar, C. Smadja, L.G.T. Phuong, M. Azzouz, J. Vignerond, A. Etcheberry, et al., A new controlled concept of immune-sensing platform for specific detection of Alzheimer's biomarkers, Biosens. Bioelectron. 40 (2013) 329–335.
[24] D.R. Lachno, B.A. Evert, K. Maloney, B.A. Willis, J.A. Talbot, M. Vandijck, et al., Validation and clinical utility of ELISA methods for quantification of amyloid-beta peptides in cerebrospinal fluid specimens from alzheimer's disease studies, J. Alzheimers Dis. 45 (2015) 527–542.
[25] H.W. Klafki, H. Hafermann, C. Bauer, U. Haussmann, I. Kraus, J. Schuchhardt, et al., Validation of a commercial chemiluminescence immunoassay for the simultaneous measurement of three different amyloid-beta peptides in human cerebrospinal fluid and application to a clinical cohort, J. Alzheimers Dis. 54 (2016) 691–705.
[26] N. Mattsson, I. Zegers, U. Andreasson, M. Bjerke, M.A. Blankenstein, R. Bowser, et al., Reference measurement procedures for Alzheimer's disease cerebrospinal fluid biomarkers: definitions and approaches with focus on amyloid beta 1–42, Biomark Med. 6 (2012) 409–417.
[27] A. Olsson, H. Vanderstichele, N. Andreasen, G. De Meyer, A. Wallin, B. Holmberg, et al., Simultaneous measurement of beta-amyloid((1–42)), total tau, and phosphorylated tau (Thr(181)) in cerebrospinal fluid by the xMAP technology, Clin. Chem. 51 (2005) 336–345.
[28] J.-H. Kang, H. Vanderstichele, J.Q. Trojanowski, L.M. Shaw, Simultaneous analysis of cerebrospinal fluid biomarkers using microsphere-based xMAP multiplex technology for early detection of Alzheimer's disease, Methods 56 (2012) 484–493.
[29] S. Janelidze, E. Stomrud, S. Palmqvist, H. Zetterberg, D. van Westen, A. Jeromin, et al., Plasma beta-amyloid in Alzheimer's disease and vascular disease, Sci. Rep. 6 (2016) 26801.

[30] L. Song, D.R. Lachno, D. Hanlon, A. Shepro, A. Jeromin, D. Gemani, et al., A digital enzyme-linked immunosorbent assay for ultrasensitive measurement of amyloid-beta 1–42 peptide in human plasma with utility for studies of Alzheimer's disease therapeutics, Alzheimer's Res. Ther. 8 (2016) 58.
[31] D.H. Wilson, D.M. Rissin, C.W. Kan, D.R. Fournier, T. Piech, T.G. Campbell, et al., The simoa HD-1 analyzer: a novel fully automated digital immunoassay analyzer with single-molecule sensitivity and multiplexing, J. Lab Autom. 21 (2016) 533–547.
[32] H. Zetterberg, E. Mortberg, L. Song, L. Chang, G.K. Provuncher, P.P. Patel, et al., Hypoxia due to cardiac arrest induces a time-dependent increase in serum amyloid beta levels in humans, PLoS One 6 (2011).
[33] J. Pi, Y. Long, N. Huang, Y. Cheng, H. Zheng, A sandwich immunoassay for detection of Abeta 1–42 based on quantum dots, Talanta 146 (2016) 10–15.
[34] N. Mattsson, U. Andreasson, S. Persson, M.C. Carrillo, S. Collins, S. Chalbot, et al., CSF biomarker variability in the Alzheimer's Association quality control program, Alzheimer's & Dementia: J. Alzheimer's Assoc. 9 (2013) 251–261.
[35] N. Le Bastard, P.P. De Deyn, S. Engelborghs, Importance andX impact of preanalytical variables on alzheimer disease biomarker concentrations in cerebrospinal fluid, Clin. Chem. 61 (2015) 734.
[36] T.D. Mai, I. Pereiro, M. Hiraoui, J.-L. Viovy, S. Descroix, M. Taverna, et al., Magneto-immunocapture with on-bead fluorescent labeling of amyloid-[small beta] peptides: towards a microfluidized-bed-based operation, Analyst 140 (2015) 5891–5900.
[37] M.R. Mohamadi, Z. Svobodova, R. Verpillot, H. Esselmann, J. Wiltfang, M. Otto, et al., Microchip electrophoresis profiling of a beta peptides in the cerebrospinal fluid of patients with alzheimer's disease, Anal. Chem. 82 (2010) 7611–7617.
[38] Z. Svobodova, M.R. Mohamadi, B. Jankovicova, H. Esselmann, R. Verpillot, M. Otto, et al., Development of a magnetic immunosorbent for on-chip preconcentration of amyloid beta isoforms: representatives of Alzheimer's disease biomarkers, Biomicrofluidics 6 (2012) 024126.
[39] M.R. Mohamadi, R. Verpillot, M. Taverna, M. Otto, J.-L. Viovy, Microchip electrophoresis, with respect to profiling of Abeta peptides in the cerebrospinal fluid of patients with Alzheimer's disease, Methods Mol. Biol. (Clifton, NJ) 869 (2012) 173–184.
[40] R.M. Mohamadi, Z. Svobodova, Z. Bilkova, M. Otto, M. Taverna, S. Descroix, et al., An integrated microfluidic chip for immunocapture, preconcentration and separation of beta-amyloid peptides, Biomicrofluidics 9 (2015).
[41] T.S. Kaminski, O. Scheler, P. Garstecki, Droplet microfluidics for microbiology: techniques, applications and challenges, Lab Chip 16 (2016) 2168–2187.
[42] W.-L. Chou, P.-Y. Lee, C.-L. Yang, W.-Y. Huang, Y.-S. Lin, Recent advances in applications of droplet microfluidics, Micromachines 6 (2015) 1249–1271.
[43] J.A. Kim, M. Kim, S.M. Kang, K.T. Lim, T.S. Kim, J.Y. Kang, Magnetic bead droplet immunoassay of oligomer amyloid Abeta for the diagnosis of Alzheimer's disease using micro-pillars to enhance the stability of the oil – water interface, Biosens. Bioelectron. 67 (2015) 724–732.
[44] M.C. Park, M. Kim, G.T. Lim, S.M. Kang, S.S.A. An, T.S. Kim, et al., Droplet-based magnetic bead immunoassay using microchannel-connected multiwell plates (mu CHAMPs) for the detection of amyloid beta oligomers, Lab Chip 16 (2016) 2245–2253.
[45] D. Ferraro, J. Champ, B. Teste, M. Serra, L. Malaquin, J.L. Viovy, et al., Microfluidic platform combining droplets and magnetic tweezers: application to HER2 expression in cancer diagnosis, Sci. Rep. 6 (2016).
[46] A. Ali-Cherif, S. Begolo, S. Descroix, J.-L. Viovy, L. Malaquin, Programmable magnetic tweezers and droplet microfluidic device for high-throughput nanoliter multi-step assays, Angew. Chem. Int. Ed. 51 (2012) 10765–10769.
[47] D.L. Chen, L. Li, S. Reyes, D.N. Adamson, R.F. Ismagilov, Using three-phase flow of immiscible liquids to prevent coalescence of droplets in microfluidic channels: criteria to identify the third liquid and validation with protein crystallization, Langmuir 23 (2007) 2255–2260.
[48] U. Haussmann, O. Jahn, P. Linning, C. Janssen, T. Liepold, E. Portelius, et al., Analysis of amino-terminal variants of amyloid-beta peptides by capillary isoelectric focusing immunoassay, Anal. Chem. 85 (2013) 8142–8149.
[49] S. Mikkonen, J. Jacksén, J. Roeraade, W. Thormann, A. Emmer, Microfluidic isoelectric focusing of amyloid beta peptides followed by micropillar-matrix-assisted laser desorption ionization-mass spectrometry, Anal. Chem. 88 (2016) 10044–10051.
[50] Agilent, 3100 OFFGEL Fractionator, https://www.agilent.com/en-us/products/offgel-electrophoresis/offgel-electrophoresis-systems/3100-offgel-fractionator.
[51] D. Ferraro, Y. Lin, B. Teste, D. Talbot, L. Malaquin, S. Descroix, et al., Continuous chemical operations and modifications on magnetic [gamma]-Fe2O3 nanoparticles confined in nanoliter droplets for the assembly of fluorescent and magnetic SiO2@[gamma]-Fe2O3, Chem. Comm. 51 (2015) 16904–16907.
[52] M.R. Bringer, C.J. Gerdts, H. Song, J.D. Tice, R.F. Ismagilov, Microfluidic Systems for Chemical Kinetics That Rely on Chaotic Mixing in Droplets, 2004, pp. 1087–1104.

Biographies

Thanh Duc Mai is an assistant professor in analytical chemistry at the Faculty of Pharmacy, University Paris-Sud, France. His main research interests are microfluidics and electrokinetic methodologies in pharmaceutical science.

Davide Ferraro was a postdoctoral researcher at the Institute Curie and Institute Pierre-Gilles de Gennes, France. His main research interest is droplet microfluidics for bioanalytical applications.

Nacéra Aboud was a PhD student at the Faculty of Pharmacy, University Paris-Sud, France. Her main research interests are capillary electrophoresis and microchip electrophoresis in pharmaceutical science.

Renault Renaud was a postdoctoral researcher at the Institute Curie and Institute Pierre-Gilles de Gennes, France. His main research interests are artificial intelligence, neural network and microfluidics.

Marco Serra is a PhD student at the Institute Curie and Institute Pierre-Gilles de Gennes, France. His main research interest is droplet microfluidic instrumentation for biochemical analysis.

Nguyet Thuy Tran is an associate professor in analytical chemistry at the Faculty of Pharmacy, University Paris-Sud, France. Her main research interests are monolithic synthesis in micro-channels and electro-kinetic methodologies in pharmaceutical science.

Jean-Louis Viovy is a research director at the Institute Curie and Institute Pierre-Gilles de Gennes, France. He is the leader of the group 'Macromolecules and Microsystems in Biology and Medicine' at the Institute Curie. His main research interests are organs on chips and lab-on-chip technologies.

Claire Smadja is a full professor at the Faculty of Pharmacy, University Paris-Sud, France. Her main research interests are analytical chemistry, biochemistry and nanotechnology in pharmaceutical science.

Stéphanie Descroix is a research director at the Institute Curie and Institute Pierre-Gilles de Gennes, France. Her main research interests are organs on chips and lab-on-chip technologies.

Myriam Taverna is a full professor at the Faculty of Pharmacy, University Paris-Sud, France. She is the leader of the group 'Protein and Nanotechnology in Analytical Science' at the institute Galien Paris-Sud, France. Her main research interests are analytical chemistry, microfluidics and nanotechnology in pharmaceutical science.

Résumé

La microfluidique de gouttes est un domaine en pleine essor et ce grâce à ses caractéristiques particulières (faible consommation d'échantillon et de réactifs, diminution des temps d'analyse) qui en font un candidat de choix pour les applications bioanalytiques. Cet engouement est également lié aux différentes fonctionnalités disponibles en microfluidique de gouttes, telles que la génération de gouttes, leur fusion, leur brisure, leur tri ou l'encapsulation d'objet en leur sein. Ces différentes fonctionnalités ont notamment permis de réaliser de nombreuses réactions en phase liquide.

Récemment, des stratégies innovantes ont été proposées afin d'introduire une phase solide dans les gouttes et ce via la manipulation de particules magnétiques. Différentes approches ont ainsi été reportées dans la littérature, mais à ce jour aucune approche microfluidique n'a été développée qui permettrait d'extraire et de préconcentrer un analyte d'intérêt présent dans une matrice complexe le tout avec des performance comparables au format conventionnel mais avec un temps d'analyse plus court et dans un format intégré.

Dans ce contexte, nous avons conçu, microfabriqué et caractérisé un nouvelle approche de microfluidique de gouttes basée sur l'intégration de structures magnétiques adjacentes au microcanal principal qui permettent de générer une force magnétique importante localement lorsque ce structures sont activées par un aimant extérieur. Notre nouvelle approche permet notamment de combiner des étapes de capture/relargage mais aussi de clean-up et ce à haut débit. Nous avons ainsi montré que cette nouvelle approche permet l'intégration de processus multi-étapes complexes. Nous l'avons illustré en mettant en œuvre cette approche pour la préparation de librairies pour le séquençage nouvelle génération.

Mots Clés

Microfluidique de goutte, Separation magnetique, Analyses Biochimiques

Abstract

Droplet microfluidics systems are experiencing a growing relevance in the bioanalytical-related fields, especially due to lower sample/reagents consumption, increased sensitivity and faster reaction time of its derived bioassays. This is due to the wide set of functionalities currently available in the droplet microfluidic toolbox (i.e., droplet generation, merging, splitting, sorting, cell encapsulation,…), fostering the implementation of homogeneous (liquid/liquid) processes. Recently, innovative strategies for the development of heterogeneous (typically solid/liquid) reactions have been proposed, based on the manipulation of functionalized magnetic solid-state support to target specific entities. Different microfluidic principles have been presented for the manipulation of such support, however a robust device allowing the possibility to enrich or extract an analyte of interest from a complex matrix with performances comparable with those of lab-scale methods but guaranteeing faster processing times is still highly desired.

To answer these needs, in this work, we present the conception, fabrication and characterization of a novel droplet microfluidic approach based on the integration of a pair of soft magnetic components, placed adjacently to a microchannel and able to generate along the path of the droplet a strong and local magnetic force. Our concept combines both the capture/release and the clean/up functionality with the high throughput processing, including thus all the skills required for the implementation of multi-steps protocol. In particular, the size selection of nucleic acid libraries in next generation sequencing (NGS) application will be presented as a first proof of concept of our device.

Keywords

Droplet microfluidics, Magnetic separation, Biochemical analysis